Synthesis and Characterization of Co-free Ni-rich Single Crystalline Positive Electrode Materials for Li-ion Batteries

by

Aaron Liu

Submitted in partial fulfilment of the requirements
for the degree of Doctor of Philosophy

at

Dalhousie University
Halifax, Nova Scotia
August 2021

© Copyright by Aaron Liu, 2021

To the ones who push me to be better, through support or challenge.

Table of Contents

List of Tables vii
List of Figures viii
Abstract xii
List of Abbreviations and Symbols Used xiii
Acknowledgements xvii
Chapter 1 – Introduction 1
1.1 – Motivation to Study Lithium Ion Battery Technology 1
1.2 – Lithium-ion Batteries 3
1.3 – Positive Electrode Materials 7
1.4 – Negative Electrode Materials 11
1.5 – Electrolyte Systems 13
Chapter 2 – Ni-rich Positive Electrode Materials 17
2.1 – Background 18
2.1.1 – Crystallographic Structure of Ni-rich Materials 18
2.1.2 –Electronic Structure of Ni-rich Materials 19
2.1.3 – Synthesis of Ni-rich Materials 22
2.2 – Issues with Lithium Nickel Oxide (LNO) 24
2.2.1 – Degradation of LNO During Cycling 25
2.2.2 – Safety of LNO when Delithiated 28
2.2.3 – Impact of Li content on the Synthesis of LNO 29
2.3 – Metal Substitution of LNO 31
2.3.1 – Al, Co, Mg and Mn Substitution 31
2.3.2 – Other Metal Substitution 33
2.3.3 – Co-free Ni-rich Materials 35
2.3.4 – Impact of Composition on Ni-rich Materials and the Unavoidable Challenge 36
2.4 – Ni-rich Single Crystalline (SC) Materials 38
2.4.1 – Synthesis of SC Materials 40
2.4.2 – Polycrystalline versus Single Crystalline Materials 41
2.4.3 – Ni-rich SC Materials 43

2.5 – Kinetic Hindrances to Li Diffusion and Irreversible Capacity in Ni-rich Materials 44
2.5.1 – Factors that Affect the Kinetic Hindrances to Li Diffusion in Ni-rich Materials 45
Chapter 3 – Experimental 47
3.1 – Synthesis of Ni-rich Positive Electrode Materials 47
3.2 – X-ray Diffraction (XRD) 48
3.2.1 – Rietveld Refinement of XRD Patterns 50
3.2.2 – XRD Data Collection 54
3.3 – Scanning Electron Microscopy (SEM) 56
3.4 – Particle Size Analysis (PSA) 58
3.5 – Residual Li Impurity Determination by the Pour Method then Acid-Base Titration 58
3.6 – Inductively Coupled Plasma – Optical Emission Spectrometry (ICP-OES) 59
3.7 – Fabrication of Coin Cells 62
3.7.1 – Separation of Single Crystalline Particle Aggregates 62
3.7.2 – Electrode Preparation 63
3.7.3 – Coin Cell Assembly 64
3.8 – Electrochemical Characterization 66
Chapter 4 – Investigating the Effects of Mg Substitution in Various Ni-rich Positive Electrode Materials for Lithium Ion Batteries 68
4.1 – Experimental Design 69
4.2 – Results and Discussions 71
4.2.1 – Material Characterization 71
4.2.2 – Initial Cycles of Coin Cell Testing 75
4.2.3 – Long Term Coin Cell Testing 77
4.3 – Conclusions 84
Chapter 5 – Synthesis of Co-Free Ni-Rich Single Crystalline Positive Electrode Materials for Lithium Ion Batteries: Part I – Two-step Lithiation Method for Al- or Mg-substituted $LiNiO_2$ 86
5.1 – Experimental Design 88
5.2 – Results and Discussions 89
5.2.1 – Heating NiAl and NiMg Samples with No or Low Li in Air as the First Step 89

5.2.2 – Topping up the Li content of NiAl and NiMg Samples in O_2 as the Second Step 94

5.2.3 – 850°C for 5 h with More Li as the First Step, Topped Up Li and 700°C for 20 h as the Second Step 100

5.2.4 – Same First Step at 850°C, but a Higher Temperature Second Step at 750°C 104

5.2.5 – Electrochemical Characterization of NiAl and NiMg Samples Heated at 850°C then 750°C 108

5.2.6 – Comparison of Polycrystalline and Single Crystalline NiMg 110

5.3 – Conclusions 114

Chapter 6 – Synthesis of Co-Free Ni-Rich Single Crystalline Positive Electrode Materials for Lithium Ion Batteries: Part II – One-Step Lithiation Method of Mg-substituted $LiNiO_2$ 115

6.1 – Experimental Design 117

6.2 – Results and Discussions 118

6.2.1 – Heating NiMg Samples to Various Temperatures 118

6.2.2 – Heating NiMg Samples with Various Li/TM Ratios 121

6.2.3 – Separation of Particle Aggregates 124

6.2.4 – Summary of XRD and PSA Results 128

6.2.5 – Impact of Mg Content 130

6.2.6 – Impact of a Low Temperature Step 132

6.2.7 – Electrochemical Comparison of Various SC NiMg and PC NiMg Samples 135

6.2.8 – Investigation into the Capacity Reduction of SC Materials 138

6.3 – Conclusions 141

Chapter 7 – Miscellaneous Investigations of Ni-rich Positive Electrode Materials 143

7.1 – Factors that Affect Capacity in the Low Voltage Kinetic Hindrance Region of Ni-Rich Positive Electrode Materials 143

7.1.1 – Experimental Design 144

7.1.2 – Results and Discussions 146

7.1.3 – Follow up: Li Diffusion Coefficient Measurements by N. Phattharasupakun 155

7.1.4 – Conclusions 158

7.2 – Tracking the Fate of Excess Li in the Synthesis of Various $Li_y[Ni_{1-x}Mn_x]O_2$ Positive Electrode Materials under Different Atmospheres 158

7.2.1 – Experimental Design 161

7.2.2 – Results and Discussions 163
7.2.3 – Conclusions 179
Chapter 8 – Conclusions and Future Work 181
8.1 – Conclusions 181
8.1.1 – Mg Substitution in Ni-rich Materials 181
8.1.2 – Synthesis of Co-free Ni-rich Single Crystalline Materials 182
8.1.3 – Electrochemical Performance of Co-free Ni-rich Single Crystalline Materials 183
8.1.4 – Miscellaneous Investigations of Ni-rich Materials 184
8.1.5 – Main Conclusions from this Thesis 186
8.2 – Future work 186
8.2.1 – Improving the Electrochemical Performance of Co-free Ni-rich Single Crystalline Materials 187
8.2.2 – Further work on Co-free Ni-rich Single Crystalline Materials 190
8.2.3 – Diffusion Studies of Ni-rich Materials 193
8.2.4 – Lowering the Costs of Co-free Ni-rich Material Synthesis 194
8.2.5 – Pushing the Performance of Co-free Ni-rich Materials 196
References 199
Appendix – Copyright Permissions 220

List of Tables

Table 2.1: Cost of some metals used in positive electrode materials. 17

Table 4.1: The synthesized samples, their compositions and the final heating step used for the synthesis. 70

Table 7.1: The synthesized samples, separated by series, and their unit cell lattices, calculated unit cell volume and amount of Ni in the Li layers. 148

Table 7.2: Elemental analysis of the unrinsed and rinsed samples using ICP-OES. Atomic ratios were normalized to Ni + Mn = 1..... 166

List of Figures

Figure 1.1: Schematic of a Li-ion cell with a $Li[Ni_xCo_yAl_z]O_2$ positive electrode and a graphite negative electrode on charge and discharge. 4

Figure 1.2: Voltage versus capacity (normalized to the full cell capacity) plots of $LiNi_{0.90}Co_{0.05}Al_{0.05}O_2$ and graphite half cells and a full cell composed of the two electrode materials. 6

Figure 1.3: The three common structure schemes (layered, spinel, olivine) for positive electrode materials. 8

Figure 1.4: Chemical structure of the electrolyte system components in this thesis. 15

Figure 2.1: The electronic structure and typical electron configurations in a typical layered Ni-rich material. 20

Figure 2.2: Cell voltage as a function of capacity for LCO, NMC111, NCA and LNO. 25

Figure 2.3: An in-situ XRD experiment on LNO. 26

Figure 2.4: Cross-sectional scanning transmission electron microscope images of various Ni-rich materials containing various metals. 34

Figure 2.5: In-situ XRD experiment results and capacity retention as a function of lithium content or specific capacity for various material compositions. 37

Figure 2.6: SEM images of a polycrystalline and single crystalline material and various examples of cross-sectional SEM images, band contrast EBSD maps and EBSD orientation maps of single crystalline materials. 39

Figure 2.7: Theoretical calculations of the energy barrier for Li migration in the presence of one or two vacant neighbouring sites. 45

Figure 3.1: A diagram of X-ray diffraction, as described by Bragg's Law, due to the ordered planes of a sample. 49

Figure 3.2: A schematic and a picture of the D8 Bragg-Brentano goniometer. 55

Figure 3.3: A diagram and a picture of the components inside a coin cell. 65

Figure 4.1: SEM images of samples in the NCAM 90/5/5 series and the NCAM 88/9/3 series. 72

Figure 4.2: XRD patterns of samples in the NM, NAM, NCAM 90/5/5 and NCAM 88/9/3 series. 73

Figure 4.3: XRD Rietveld refinement results for the NM, NAM, NCAM 90/5/5 and NCAM 88/9/3 series. 74

Figure 4.4: Coin cell data for the samples in the NM, NAM, NCAM 90/5/5 and NCAM 88/9/3 series. 76

Figure 4.5: First cycle capacities as a function of Mg content and as a function of Al + 2*Mg content (a2-c2) for the NM, NAM, NCAM 90/5/5 and NCAM 88/9/3 series.... 77

Figure 4.6: Cycling performance for the samples in the NM, NAM, NCAM 90/5/5 and NCAM 88/9/3 series. 78

Figure 4.7: Capacity retention as a function of substituent content and as a function of x in $Li_{1-x}MO_2$ for the samples. 80

Figure 4.8: Differential capacity as a function of cell voltage for the samples in the NM, NAM, NCAM 90/5/5 and NCAM 88/9/3 series. 83

Figure 5.1: SEM images of samples after heating NiAl or NiMg at various temperatures for 5 h with 0Li or 0.5Li. 90

Figure 5.2: XRD patterns of samples after heating NiAl or NiMg at various temperatures for 5 h with 0Li or 0.5Li. 92

Figure 5.3: SEM images of NiAl and NiMg samples after the second heating step at 700°C for 20 h. 95

Figure 5.4: XRD patterns of NiAl and NiMg samples after the second heating step at 700°C for 20 h. 97

Figure 5.5: XRD Rietveld refinement results for NiAl and NiMg samples after the second heating step at 700°C for 20 h. 99

Figure 5.6: SEM images of NiMg samples after the first heating step at 850°C for 5 h and after the second heating step at 700°C for 12 h. 101

Figure 5.7: XRD patterns of NiAl and NiMg samples after the first heating step at 850°C for 5 h and second heating step at 700°C for 12 h. 102

Figure 5.8: XRD Rietveld refinement results for NiAl and NiMg samples after the first heating step at 850°C for 5 h and second heating step at 700°C for 12 h. 103

Figure 5.9: SEM images of NiAl and NiMg samples after the heating steps at 850°C for 5 h and then at 750°C for 12 h. 105

Figure 5.10: XRD patterns of NiAl and NiMg samples after the first heating step at 850°C for 5 h and second heating step at 750°C for 12 h. 106

Figure 5.11: XRD Rietveld refinement results for NiAl and NiMg samples after the first heating step at 850°C for 5 h and second heating step at 750°C for 12 h. 107

Figure 5.12: Coin cell data for the NiAl and NiMg samples after the second heating step at 750°C for 12 h.. 109

Figure 5.13: Comparison of a PC NiMg sample with a SC NiMg sample. SEM images, XRD patterns and XRD Rietveld refinement results of the samples. Coin cell data and cycling performance for the samples. 111

Figure 6.1: SEM images of $LiNi_{0.975}Mg_{0.025}O_2$ samples after heating for 12 h at various temperatures and Li/TM ratios. 119

Figure 6.2: XRD patterns of $LiNi_{0.975}Mg_{0.025}O_2$ samples after heating for 12 h at various temperatures with a Li/TM ratio of 1.05 or 1.10. 120

Figure 6.3: SEM images of $LiNi_{0.975}Mg_{0.025}O_2$ samples after heating for 20 h at 775°C with various Li/TM ratios. 122

Figure 6.4: XRD patterns of $LiNi_{0.975}Mg_{0.025}O_2$ samples after heating with various Li/TM ratios at 775°C or 800°C. 123

Figure 6.5: SEM images of $LiNi_{0.975}Mg_{0.025}O_2$ samples after heating for 20 h at 775°C with a Li/TM ratio of 1.02 and undergoing various particle separation methods. 125

Figure 6.6: PSA results of $LiNi_{0.975}Mg_{0.025}O_2$ samples undergoing various particle separation methods. 126

Figure 6.7: Coin cell data and cycling performance for $LiNi_{0.975}Mg_{0.025}O_2$ samples undergoing various particle separation methods. 127

Figure 6.8: Summary of Ni content in the Li layers and D50 as a function of heating temperature and as a function of the Li/TM ratio. 129

Figure 6.9: XRD patterns and Rietveld refinement results for $LiNi_{0.975}Mg_{0.025}O_2$ and $LiNi_{0.95}Mg_{0.05}O_2$ samples heated at 775°C with a Li/TM ratio of 1.02 or 1.05. Coin cell data and cycling performance for the samples. 131

Figure 6.10: XRD patterns and Rietveld refinement results for $LiNi_{0.975}Mg_{0.025}O_2$ samples heated first at 825°C for 12 h then 750°C for 5 h with a Li/TM ratio of 1.10 or 1.20. SEM images of the samples and summary of Ni content in the Li layers and D50 as a function of heating temperature and as a function of the Li/TM ratio. 133

Figure 6.11: Comparison of the coin cell data and cycling performance for a PC and SC $LiNi_{0.975}Mg_{0.025}O_2$ material. 136

Figure 6.12: Coin cell data for PC and SC $LiNi_{0.975}Mg_{0.025}O_2$ samples synthesized using different precursor sizes and heated to different temperatures. Coin cell data for PC and SC samples cycled at different temperatures. 139

Figure 7.1: XRD patterns of samples in the NiMg 18 µm, NCA 90/5/5 and NiMg 97.5/2.5 3 µm series. 147

Figure 7.2: Coin cell data and an expanded view of the low voltage region for the samples in the NiMg 18µm, NCA 90/5/5 and NiMg 97.5/2.5 3µm series. SEM images of select samples of the NiMg 97.5/2.5 3µm series. 149

Figure 7.3: Coin cell data for the samples in the NCA 90/5/5 and NiMg 97.5/2.5 3µm series cycled at 30°C and 55°C. 152

Figure 7.4: Coin cell data for NiMg 97.5/2.5 samples cycled at 30°C and 55°C and cycled to different lower cutoff voltages. 154

Figure 7.5: Li chemical diffusion coefficient as a function of voltage and SEM images of NiMg-SC and NiMg-PC. 156

Figure 7.6: XRD patterns and Rietveld refinement results for NiMn-CS, NiMn 80/20 and NiMn 50/50 samples synthesized under different atmospheres. 164

Figure 7.7: SEM images of NiMn-CS and NiMn 80/20 synthesized under different atmospheres. 165

Figure 7.8: Acid titration curves of solutions extracted using the "pour method" from NiMn-CS, NiMn 80/20 and NiMn 50/50 samples and the initial pH and residual Li content as plotted by synthesis atmosphere and material. 169

Figure 7.9: Coin cell data for NiMn-CS and NiMn 80/20 samples synthesized under different atmospheres and differential capacity for NiMn-CS, NiMn 80/20 and NiMn 50/50 cells cycled to a higher cutoff voltage. 173

Figure 7.10: Normalized TGA data NiMn 37.5/62.5 samples heated to 1050°C in air with a Li/TM ratio of 1.2, the maximum amount of Li a material can take in if all the Ni are oxidized to Ni^{3+} as a function of the Mn content and a summary of the Li ratio of materials before heating, after heating (850°C 12h, 800°C 5h) and after rinsing for materials synthesized under different atmospheres. 176

Figure 7.11: A simple summary of expected behaviour for materials synthesized with a Li/TM ratio of 1.15 and heated to 850°C for 12 h then 800°C for 5 h. 180

Abstract

To lower the cost and increase the energy density of Li-ion batteries, a common approach is to use positive active electrode materials that are higher in Ni and lower in Co than currently used. However, a set of challenges face the use of Ni-rich materials, including poor cycling lifetime, low thermal stability and sensitivity to ambient atmosphere. Some of these challenges, such as poor cycling lifetime, are believed to stem from volume changes that exert anisotropic stress within a polycrystalline particle. Therefore, this thesis focuses on the development of Co-free Ni-rich single crystalline positive electrode materials.

The thesis first systematically studies the impact of Mg substitution in various Ni-rich compositions. The study demonstrates that Co-free materials can have comparable performance to materials with Co, but the compositional study supports that capacity retention is correlated with capacity and the resulting volume changes.

The thesis then focuses on the development of Co-free Ni-rich single crystalline materials containing either Al or Mg. The synthesis of single crystalline materials is investigated using either the one-step or two-step lithiation method. These studies help achieve understanding of several factors that impact grain growth and the trade-offs of parameters such as heating temperature. This thesis shows that the synthesis of Co-free Ni-rich SC materials that meet physical specification targets is achievable via various synthesis routes. However, the electrochemical performance of the synthesized SC materials is subpar, and this has been shown to mainly be a Li diffusion issue. It is expected that the rate capability and capacity of Co-free Ni-rich SC materials will be inherently limited by the large primary particles. Advances overcoming these limitations will be needed before Co-free Ni-rich SC materials become viable.

List of Abbreviations and Symbols Used

(h,k,l)	Miller indices
a,b,c	Unit cell lattice parameters
AMID	Atlung method for intercalant diffusion
ARC	Accelerating rate calorimetry
BET	Brunauer-Emmett-Teller
C/n	C-rate, where n is the hours needed to fully charge
CCCV	Constant current-constant voltage
CCD	Charge coupled device
CEI	Cathode electrolyte interphase
d	Atomic plane spacing
D_c	Li chemical diffusion coefficient
DEC	Diethyl carbonate
DMC	Dimethyl carbonate
DW	Debye-Waller factor
EBSD	Electron backscatter diffraction
EC	Ethylene carbonate

EDS	Energy-dispersive X-ray spectroscopy
EV	Electric vehicle
F	Geometric structure factor
FEC	Fluoroethylene carbonate
f_n	Scattering factor for the atom n
HS	High spin
ICP-OES	Inductively coupled plasma - optical emission spectrometry
IRC	1st cycle irreversible capacity
L	Lorentz factor
LCO	$LiCoO_2$
LCV	Lower cutoff voltage
LDH	Layered double hydroxide
LFP	$LiFePO_4$
LiBOB	Lithium bis(oxalato)borate
LiTFSI	Lithium bis(trifluoromethanesulfonyl)imide
LMO	$LiMn_2O_4$
LNO	$LiNiO_2$

LS	Low spin
LTO	$Li_{4/3}Ti_{5/3}O_4$
M	Multiplicity of (*h,k,l*) planes
NCA/NCAxyz	$Li[Ni_xCo_yAl_z]O_2$
NMC/NMCxyz	$Li[Ni_xMn_yCo_z]O_2$
NMP	N-methyl-2-pyrrolidone
P	Fraction of turbostratically misaligned graphite layers
P	Polarization factor
PC	Polycrystalline
PSA	Particle size analysis
PVDF	Polyvinylidene fluoride
Q	Specific capacity
r	Ionic radius or particle radius
R_B	Bragg R-factor
SC	Single crystalline
SEI	Solid electrolyte interphase
SEM	Scanning electron microscopy

SWCNT	Single-walled carbon nanotubes
TGA	Thermogravimetric analysis
TM	Transition metal or other metal filling the transition metal role
TSH	Tetrahedral site hop
USD	United States dollar
V	Voltage
XRD	X-ray diffraction
θ	Scattering angle
θ_m	Angle between monochromator and the diffracted beam
λ	Wavelength
μ_{Li}^{n}	Change of the free energy of the negative electrode with lithium content
μ_{Li}^{p}	Change of the free energy of the positive electrode with lithium content

Acknowledgements

First and foremost, I would like to thank my supervisor Dr. Jeff Dahn for his guidance, feedback, and insights. The opportunities I got here in this lab and in Halifax have produced many valuable learning experiences. I remain thankful for my co-op supervisors at Moli for sparking my interest in this field and pointing me to Jeff. I would like to thank my committee members Drs. Kevin Plucknett, Peng Zhang and Josef Zwanziger for providing feedback on my work and this thesis.

Many thanks go to the Dahn lab group for the great working environment and many fruitful discussions. I am grateful to Hongyang Li, Ning Zhang, Marc Cormier and Nutthaphon Phattharasupakun for all the collaborations and discussions on positive electrode materials. I appreciate the contributions from Julie Inglis, Jamie Stark, Phillip Arab and Ronald Väli. I would also like to thank Mike Johnson and Jessie Harlow for keeping the lab and network going smoothly.

I would like to thank Patricia Scallion, Alicia Oickle and Catherine Whitman for their support with SEM and ICP-OES experiments. I would also like to thank Lea Gawne for all the administrative support throughout this program.

I would like to thank my friends and social circles who helped keep my life balanced. I hope to get it rebalanced after this crazy pandemic. To my partner Catherine and my one big family, I am ever thankful for all the love and support you provide.

Chapter 1 – Introduction

1.1 – Motivation to Study Lithium Ion Battery Technology

Since the 1990's, lithium ion (Li-ion) batteries have been increasingly utilized to power laptops, cell phones and other portable electronics. With the disruptions and impacts of global climate change already upon us and accelerating,[1] there is an urgent need to reduce our greenhouse gas emissions. Electrifying transportation and switching to renewable energy are important steps to transitioning society away from fossil fuel reliance. For applications such as electric vehicles (EV) and grid energy storage, Li-ion battery technologies are widely used due to their competitive advantage in specific energy, energy density, specific power, self-discharge rate and cycle life.[2]

The growth of the Li-ion market has been blistering, driven largely by performance improvements and a significant decrease in costs. The amount of energy sold as Li-ion batteries have gone from < 2 GWh in 2000 to ~230 GWh in 2020 and is projected to grow to ~1.3 TWh in 2030.[3] In terms of costs (in USD), Li-ion cells have gone from ~$2,600/kWh in 2000 to ~$400/kWh in 2010 to ~$120/kWh in 2020, with pack level costs being ~$150/kWh in 2018.[2,3] Costs are projected to decrease still but at a slower pace going forward. The majority of the growth is being pushed by the EV sector since the early 2010's and moving forward. Most major automakers have introduced or plan to introduce numerous electric vehicles to their lineup and are investing heavily in the infrastructure needed.

The main research focuses for Li-ion battery manufacturers and researchers are increasing the energy density, improving the lifetime, improving the safety and reducing

the costs of the technology.[4] Tesla's entire current model lineup (Models S, 3, X and Y) have configurations capable of driving more than 500 km per charge,[5] which is already suitable for most consumer requirements. However the costs remain untenable for many people and any improvements from the aforementioned areas of focus will make the products more attractive, encouraging widespread adoption of electric vehicle technology. Increasing the energy density of Li-ion cells will decrease the number of cells needed in the battery pack, allowing for more EVs to be manufactured with the same number of cells. This and other strategies of reducing the costs of cells will allow for the lowering of EV prices. Longer cell lifetimes and safety improvements lead to better warranties and product reliability, improving customer satisfaction and alleviating potential consumer concerns.

The positive electrode makes up about a quarter of the cost of a typical Li-ion cell, which is the single largest slice of the cost structure.[3] This mainly stems from the use of metals such as Ni and Co in the active material of the positive electrode. A common approach to lower the cost of the active electrode material is to use materials higher in Ni and lower in Co. This thesis details work on the development of Ni-rich positive electrode materials, with a focus on Co-free Ni-rich single crystalline materials. Chapter 1 gives a brief introduction to the Li-ion cell and major components. Chapter 2 provides a review of the literature on Ni-rich positive electrode materials. Chapter 3 covers the synthesis and characterization methods and techniques used in this thesis. Chapter 4 investigates the effects of substituting Mg into various Ni-rich compositions. Chapter 5 studies the synthesis of Co-free Ni-rich single crystalline materials containing either Al or Mg using a two-step lithiation method. Chapter 6 then focuses on the

synthesis of the Mg-containing material from Chapter 5 using a one-step lithiation method. Chapter 7 details some miscellaneous investigations that arose from the work done in Chapters 4 to 6. Chapter 8 summarizes the findings from this thesis and suggests some ideas for further studies.

1.2 – Lithium-ion Batteries

Li-ion cells contain 4 main components: the positive electrode, the negative electrode, the separator and the electrolyte. The positive electrode and negative electrode are sometimes referred to, by others, as the cathode and anode, respectively. Generally, an aluminum foil serves as the current collector for the positive electrode, and the positive electrodes are coated double sided on the foil. Likewise, negative electrodes are coated double sided on copper foils. The electrodes are then rolled or stacked together in a "jelly roll" manner in between layers of the separator and placed in the cell. Separators are usually a thin, porous, electronically insulating polyolefin film soaked with electrolyte that allow Li^+ ions to travel through but not electrons. The exact jelly roll shape and dimensions will depend on the cell hardware, and design types include cylindrical, pouch, prismatic and coin cells.[2] The electrolyte solution is injected into the cell before the cell is sealed to prevent exposure to ambient atmosphere.

Figure 1.1 shows a schematic of $Li[Ni_xCo_yAl_z]O_2$ (NCA, the subscripts x, y, z denote the composition of the NCA material)/graphite Li-ion cell operation. During cell operation, Li^+ ions and electrons are reversibly inserted and removed from the electrode materials, in a process called intercalation or deintercalation, respectively. Li atoms in the positive electrode are more stable than Li atoms in the negative electrode, and so Li

atoms in the positive electrode will have a lower chemical potential. When the cell is being charged, Li atoms are deintercalated from the positive electrode and intercalated into the negative electrode. When the cell is charging, a current is applied to the cell and Li^+ ions move through the electrolyte and separator to the negative electrode, with an equal amount of electrons moving through the external circuit. Once charged, the Li atoms in the negative electrode want to return to the positive electrode, but are unable to do so if there is no connected circuit for the accompanying electrons to travel through. When a load is connected, then the Li^+ ions spontaneously deintercalate from the negative electrode and reintercalate back into the positive electrodes while the corresponding electron current flows through the circuit, doing work.

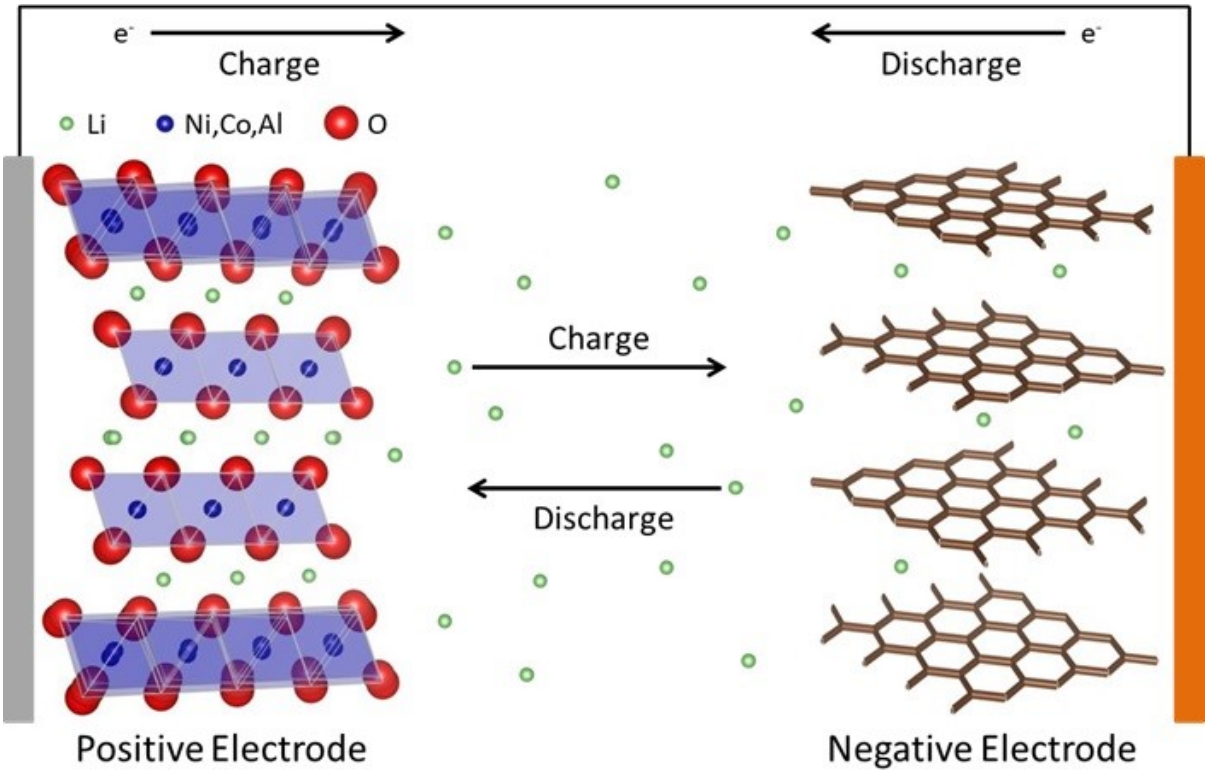

Figure 1.1: Schematic of a Li-ion cell with a $Li[Ni_xCo_yAl_z]O_2$ positive electrode and a graphite negative electrode on charge and discharge. The electrolyte and separator are omitted.

The charge and discharge processes occurring for the cell shown in Fig. 1.1 are given by the following equations:[2]

Positive electrode: $$Li[Ni_aCo_bAl_c]O_2 \underset{discharge}{\overset{charge}{\rightleftharpoons}} Li_{(1-x)}[Ni_aCo_bAl_c]O_2 + xLi + xe^- \quad (1.1)$$

Negative electrode: $$yC + xLi + xe^- \underset{discharge}{\overset{charge}{\rightleftharpoons}} yLi_{\frac{x}{y}}C \quad (1.2)$$

Overall cell: $$Li[Ni_aCo_bAl_c]O_2 + yC \underset{discharge}{\overset{charge}{\rightleftharpoons}} Li_{(1-x)}[Ni_aCo_bAl_c]O_2 + yLi_{\frac{x}{y}}C, \quad (1.3)$$

where the subscripts a, b, c denote the composition of the NCA material and x and y are selected based on the molar capacity of the two electrode materials. Equations 1.1-3 omit the Li^+ ions or electrons consumed in other processes between the positive and negative electrode, which is not the case in reality and will be discussed later.

The difference in chemical potential between the positive electrode and negative electrode gives rise to a voltage, given by

$$V = -\frac{\mu_p - \mu_n}{F}, \quad (1.4)$$

where F is the Faraday constant and p and n designate the positive and negative electrode, respectively. However, the chemical potentials of the two electrodes vary depending on the material as well as the Li content in the material. Figure 1.2 shows a typical voltage versus capacity curve of the cell shown in Fig. 1.1 during charging. The NCA and graphite curves were measured in separate experiments using Li metal foil as the counter and reference electrode, known as half cell experiments. Half cells are useful for evaluating only one electrode material at a time, as the process that occurs on the Li

metal foil occurs at a constant potential. Half cell potentials in this thesis are reported vs. Li/Li^+, while full cell voltages are reported as the potential difference between the positive and negative electrode.

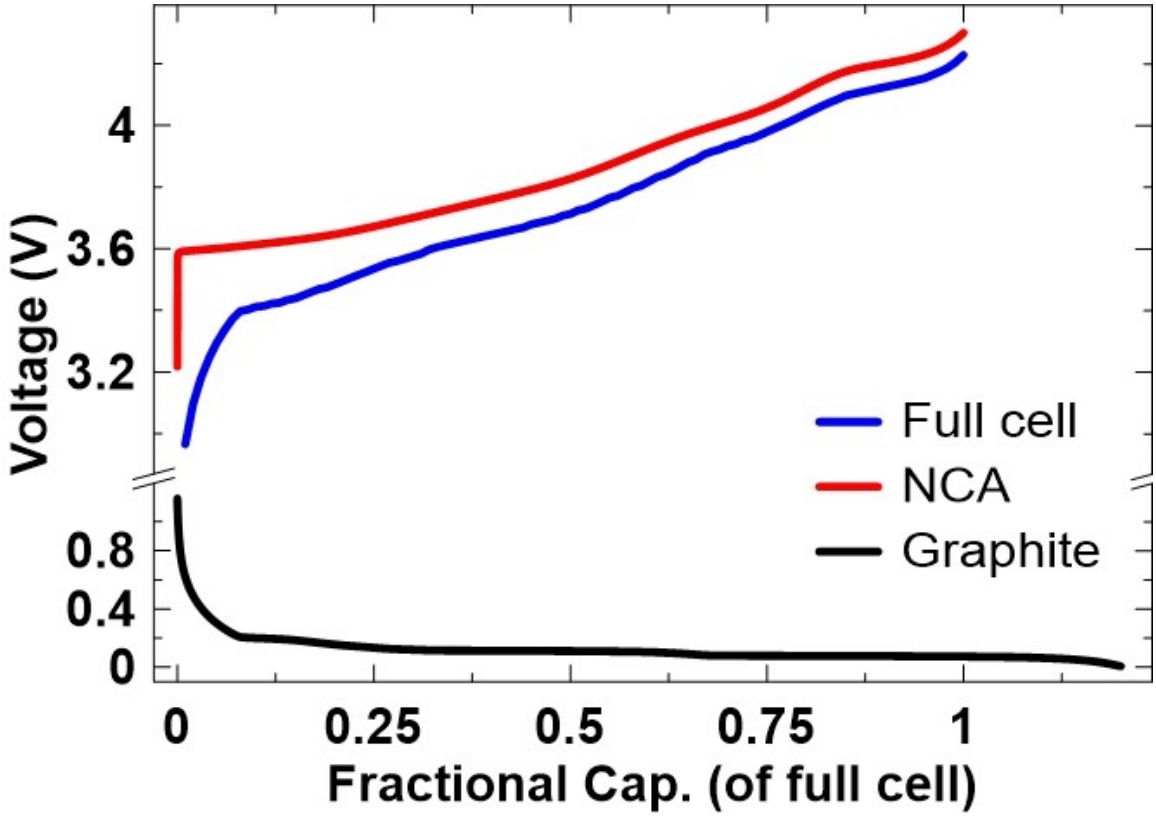

Figure 1.2: Voltage versus capacity (normalized to the full cell capacity) plots of $LiNi_{0.90}Co_{0.05}Al_{0.05}O_2$ and graphite half cells and a full cell composed of the two electrode materials. Half cells were assembled using Li foil as the counter/reference electrode.

The choices of positive and negative electrode materials, as well as electrolyte solutions, all significantly impact the various characteristics of the cell. This will be discussed in the following sections as well as in Chapter 2.

1.3 – Positive Electrode Materials

In the previous section, the positive electrode was referred to as NCA. However, there are actually several different components in the positive electrode. NCA is the active material, which participates in the electrochemical operation of the cell. Binders, such as polyvinylidene fluoride (PVDF), adhere the electrode materials to the current collector after coating. Conductive agents, such as carbon black, maintain a connected network so the conductivity of the electrode remains adequate.

Positive electrode research generally focuses on the active material. Positive electrode active materials need to reversibly accommodate the insertion/extraction of Li at a chemical potential lower than the negative electrode. Another consideration for active material research is the amount of Li the material can accommodate, which is its specific capacity and is given by

$$Q = \frac{nF}{M}, \tag{1.5}$$

where Q is the specific capacity and n is the number of Li per formula unit participating in the electrochemical reaction, F is the Faraday constant (using the units Ah/mol) and M is the molar mass. The number of times the material can undergo the repeated charge/discharge processes helps determine its lifetime, which is another important consideration. Other aspects such as density, safety, Li diffusion rate and cost of the materials (including synthesis and processing steps) all have to be taken into account when deciding on the active material.

Candidates for positive electrode active materials generally come in the layered, spinel or olivine structures. Most Li-ion positive electrode materials will come in the

form of Li[Transition Metal]Anion. Not all cations in the transition metal role have to be transition metals, but there must be atoms that can exist in several oxidation states. For convenience, all non-Li metals filling this transition metal role are generally referred to as transition metals by the battery field, although metals such as Al, Mg and B are not transition metals. In this thesis, metals filling this transition metal role will be referred to as "transition metals and other metals", "non-Li metals", "other metals" or simply just "metals", where applicable. Figure 1.3 shows the three common structure schemes. Different structures will influence the material properties including energy density, Li diffusion capabilities and safety of the material.

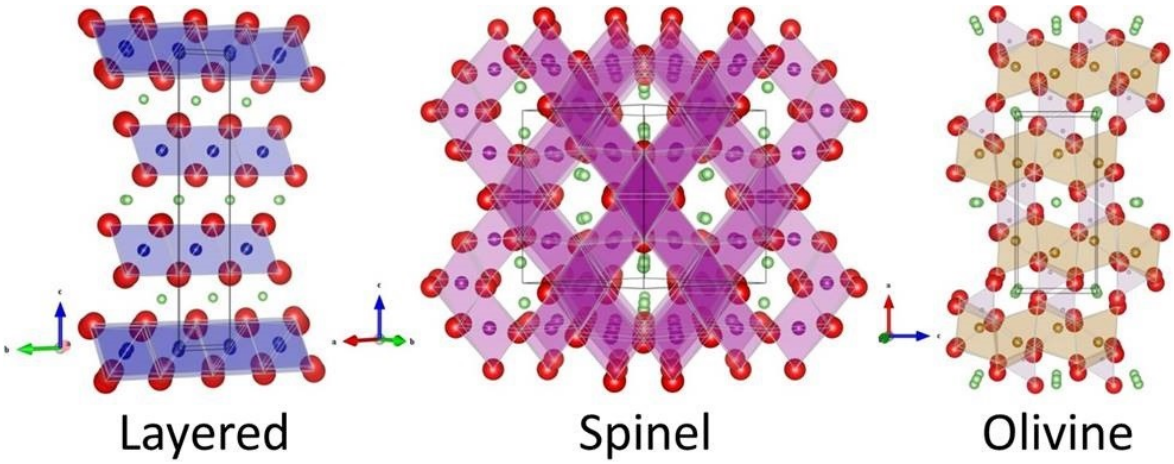

Figure 1.3: The three common structure schemes (layered, spinel, olivine) for positive electrode materials.[6–10]

The most common structure scheme is the layered structure, usually a Li metal oxide (layered materials have a combined market share of 75% as of 2020[3]). It consists of Li, metal and O all arranged into separate layers with the Li located in between layers of O-metal-O (shown by the shaded polyhedra in Fig. 1.3). The diffusion of the Li is two dimensional within the Li layer when the cell is operating. The densities of layered materials are quite high due to their compact layered structure, and layered electrode

materials generally have competitive energy densities. Unfortunately, a serious issue with layered materials is their thermal instability when delithiated to a high degree.[11–31]

Layered $LiCoO_2$ (LCO) was demonstrated to be a good candidate as a positive electrode material by the Goodenough group in 1980,[7,32] and the first commercial Li-ion batteries from Sony utilized LCO as the positive electrode material.[33] LCO has a very competitive energy density owing to the respectable capacity (~160-190 mAh/g, depending on the voltage cutoff) and high density of the material. Additionally, the synthesis of LCO is generally simple and LCO can cycle reversibly for hundreds of cycles.[2,33–37] Unfortunately, the use of LCO in cells also has some drawbacks, the most serious issue being the thermal instability of the material when charged which could lead to safety issues.[11,12,38,39] Another disadvantage of LCO is the use of cobalt, which is toxic and comes with economic and ethical challenges, such as scarcity, higher prices, price volatility, supply chain instability and reports of child labour.[40–45] The drawbacks of using Co are weakening LCO's market presence recently (27% of market share in 2015,[46] down to 10% of market share as of 2020[3]).

With the disadvantages of using Co, there has been lots of research on finding alternative metals, usually transition metals, that can replace cobalt but retain the layered structure. The successful replacement of 2 Co^{+3} with Ni^{+2} and Mn^{+4} to form $Li[Ni_xMn_xCo_{1-2x}]O_2$ (NMC, or NMCxyz for specific compositions/ratios of $Li[Ni_xMn_yCo_z]O_2$) was first demonstrated in 2001[47,48] and have since become a popular positive electrode material (55% of market share as of 2020[3]). Depending on the transition metal ratio of NMC, improvements can be made to the safety, capacity or lifetime, and at a lower cost than LCO.[2,14,15,17,22,37,49–53]

Another layered material in commercial use today is $Li[Ni_{1-x-y}Co_xAl_y]O_2$ (NCA) which has 10% of the market share as of 2020,[3] mainly driven by the use of NCA in Tesla vehicles. Research on NCA originated from $LiNiO_2$ (LNO), but it was found that the material has lower thermal stability than even LCO, and also experienced severe capacity fading upon cycling.[54–58] NCA was then formed from the substitution of Ni with Co to stabilize cycling performance and Al to improve thermal stability.[2,14,15,17,22,37,49,53–55,59–65] The work in this thesis focuses on Ni-rich layered materials, and a more thorough discussion on Ni-rich materials can be found in the next chapter.

Another class of layered materials is Li-rich materials, which have been researched heavily but have not been commercialized yet. Li-rich materials have more Li than transition metals and other metals in the material and some of the Li occupy sites on the transition metal (TM) layer. The material can be thought of as a solid solution between $LiMO_2$ (M = Ni, Mn, Co) and Li_2MnO_3.[37,51,66–74] While Li-rich materials are attractive due to their ability to access oxygen redox capacity and attain very high capacities in the beginning (> 300 mAh/g is possible, but more commonly ~250 mAh/g), the energy density fades quickly due to a high 1st cycle irreversible capacity and both capacity and voltage fade during cycling.[37,51,66,67,69,70,72,73,75] Many studies have been conducted to understand and mitigate the voltage fade but the issues are as yet unsolved. These outstanding challenges so far preclude the commercialization of Li-rich materials.

Materials with the spinel structure have the fastest Li diffusion when compared to other structure schemes due to three dimensional Li diffusion. $LiMn_2O_4$ (LMO)[9,76] is sometimes used for power applications which require high current densities, but is being replaced by layered materials in the market. Drawbacks such as short lifetime and

middling energy density have limited its market presence (market share of 3% as of 2020[3]).

Materials with an olivine structure, such as $LiFePO_4$ (LFP),[77] are very stable and can withstand cycling for longer than most other positive electrode materials. Furthermore, the low costs of olivine materials with iron or manganese as the transition metal have attracted lots of attention (LFP has a market share of 22% as of 2020[3]). The main disadvantage of olivine materials is the presence of bulky phosphate ions, decreasing the energy density. Another disadvantage is that Li diffusion is slow due because diffusion only occurs in one dimensional tunnels, but the rate capability of the material can be improved by reducing the particle size.[78]

1.4 – Negative Electrode Materials

Like the positive electrode, there are other components in the negative electrode other than graphite. Binders and conductive agents are also used in the negative electrode. However, some materials such as graphite are conductive already and do not require conductive agents.

The first commercial Li-ion batteries from Sony utilized petroleum coke as the negative electrode material.[33] Nowadays, graphite is the most common negative electrode material (with a market share of 89% as of 2020[3]) due to its low cost, long lifetime and good energy density. Graphite consists of graphene sheets stacked on top of each other in an arrangement of either 2 alternating sheets (2H, stacking sequence of ABABAB) or 3 alternating sheets (3R, stacking sequence of ABCABC).[2] Both arrangements have the same spacing between graphene sheets (3.36 Å) and between

carbons in the same graphene sheet (1.42 Å). However, real world graphitic materials generally have some stacking faults where a sheet is randomly shifted or rotated, termed turbostratic misalignment. Layers that are turbostratically misaligned are not able to accommodate Li in between the layers. It was shown that the amount of turbostratic misalignment in the material directly correlates with the capacity of the material, as given by

$$Q = 372(1 - P), \tag{1.6}$$

where Q is the specific capacity of the graphitic material in units of mAh/g, 372 is the theoretical capacity of graphite in units of mAh/g and P is the fraction of layers that are turbostratically misaligned.[79] Therefore, materials with high capacity can be made by minimizing stacking disorder of the graphene sheets, which is why graphite became widely used. However, graphite can only accommodate a maximum of 1 Li atom for every 6 carbon atoms, meaning other materials that can accommodate more Li per unit atom may have higher energy densities.

Attention has been given to alloying compounds and materials such as silicon or tin can alloy more than 3 Li per atom, dramatically increasing the theoretical capacity. The increased capacity comes at a cost though, and the alloys swell to a much larger size than the unalloyed material. Graphite will also swell and shrink slightly, but not to the harmful extent of silicon or tin alloys. The repeated swelling and shrinking of the material damages the electrode and will shorten the lifetime of the cell. The large volume changes also contribute to a large irreversible capacity and low capacity retention. A common approach is to blend the alloys with graphite or an inactive component to reduce the detrimental impact of the volume change, and this has led to commercial cells

containing some amount of alloy materials.[80,81] Negative electrodes containing Si composites have a market share of 4% as of 2020, but are projected to grow to a market share of 12% by 2030.[3]

Another negative electrode material is $Li_{4/3}Ti_{5/3}O_4$ (LTO), which has a very long lifetime due to chemical compatibility with the electrolyte.[82] LTO has a spinel structure and cycles between the composition $Li[Li_{1/3}Ti_{5/3}]O_4$ and $Li_2[Li_{1/3}Ti_{5/3}]O_4$ unlike the positive electrode materials discussed earlier. LTO has been shown to cycle without undergoing volume change, minimizing mechanical degradation and contributing to the long lifetime of the material.[83] Additionally, the Li intercalation potential is around 1.5 V vs Li/Li^+, which is quite high for a negative electrode. This allows for high charging currents without the worry of Li plating but the energy of the cell is reduced. LTO has a market share of 4% as of 2020.[3]

1.5 – Electrolyte Systems

Typical Li-ion cells use an electrolyte solution made up of a lithium salt dissolved in organic solvents. There is work on the use of aqueous electrolytes or solid electrolytes to lower costs or enable the use of lithium metal as the negative electrode, but these technologies are not yet widely adopted and will not be discussed in this thesis.

Lithium salts, when dissolved in the solvent, act as the pathway by which Li ions can move between the electrodes during cycling. In order to perform this function, Li salts should be able to fully dissolve and dissociate in the solvent, be inert to the inactive cell components (separator, current collector, cell casing) and to the electrolyte and be stable against oxidative decomposition at the positive electrode and against thermally

induced reactions.[84] Lithium hexafluorophosphate ($LiPF_6$) is the most commonly used Li salt because it fulfills these multi-faceted requirements and provides high conductivity and acceptable safety.[2] However, $LiPF_6$ is very sensitive to moisture and reacts with water to form HF, so handling must occur in a dry room or glovebox. Some other Li salts have been investigated to serve as an alternative solution to $LiPF_6$, such as lithium tetrafluoroborate ($LiBF_4$), lithium bis(oxalato)borate (LiBOB) and lithium bis(trifluoromethanesulfonyl)imide (LiTFSi).[2,84,85] However, they are still not able to provide a better balance of properties than $LiPF_6$ yet.

The electrolyte solvent also needs to balance multiple requirements simultaneously, and these include being able to dissolve Li salts to an appropriate concentration (high dielectric constant), having a low viscosity to promote ion transport and increase conductivity, having a wide potential range at which the solvent remains electrochemically stable, having a large temperature range over which the solvent remains liquid, being inert to cell components (including charged electrode surfaces), being safe (non-toxic and high flashpoint) and being cheap.[84,85] However, unlike the case with Li salts, there is no one compound able to fulfill all these requirements, and Li-ion cells typically utilize a combination of 2 to 5 different solvents.[2,84,85] Ethylene carbonate (EC) is a cyclic carbonate that is the most common component of electrolyte packages because EC imparts a high dielectric constant and helps to form an effective protective layer on the graphite.[86] However, EC is solid at room temperature and needs to be combined with other solvents to lower the freezing temperature and viscosity of the electrolyte. Fluoroethylene carbonate (FEC) can also contribute to a beneficial protective layer but also relies on other solvents to improve the aforementioned solution properties.[2]

Figure 1.4 shows the chemical structure of the Li salt and organic solvents used as the electrolyte systems in this thesis. The properties of $LiPF_6$, EC and FEC have been discussed already. Diethyl carbonate (DEC) and dimethyl carbonate (DMC) are linear carbonates which have a low viscosity.

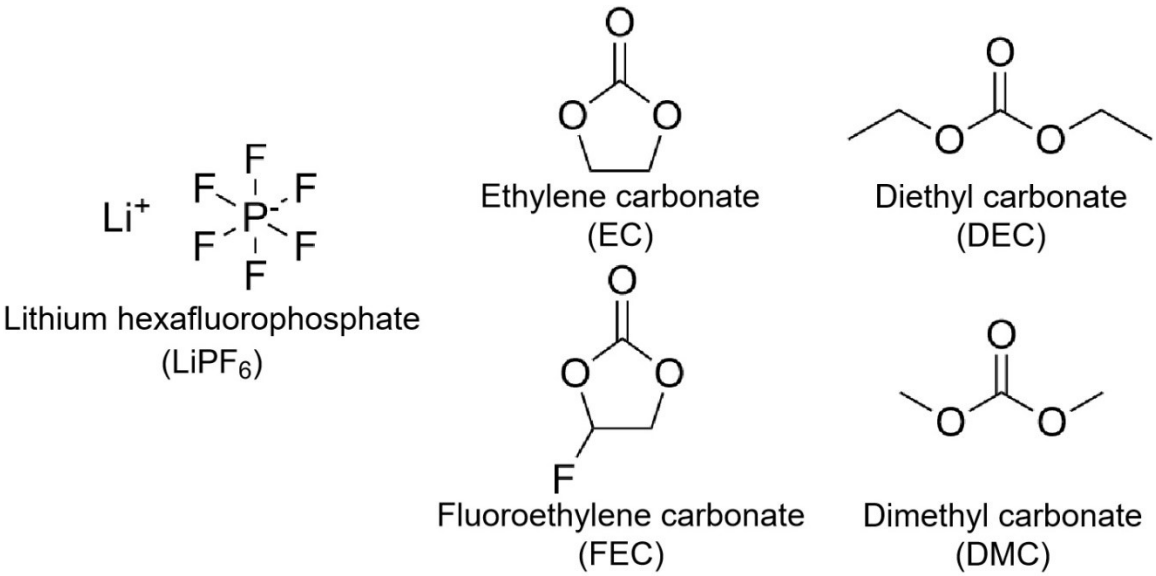

Figure 1.4: Chemical structure of the electrolyte system components in this thesis.

Interestingly, Li-ion cells operate at voltage ranges where lithiated graphite and most other negative electrode materials are not stable in the electrolyte. Fortuitously, the initial reactions between the negative electrode and the electrolyte form a passivating layer on the surface of the electrode. This passivating layer shields the electrode from further reaction, similar to an oxide layer for many metals. This passivating layer is called the solid electrolyte interphase (SEI)[86–88] and Li^+ ions still have the ability to diffuse through, allowing the cell to continue operating. The formation of the SEI will consume electrolyte and Li and contribute to irreversible capacity because the consumed Li can no longer contribute to cell operation. SEI formation occurs mostly in the beginning but also throughout the lifetime of the cell at a slower rate due to breakdown of

the SEI (from cyclic volume changes of the electrode material, for example) requiring further SEI formation to reinforce the SEI layer. Additionally, the type of electrolyte can influence the composition of the SEI, as mentioned earlier regarding EC and FEC being beneficial. Some compounds have been shown to help form a robust SEI even when used in small amounts (< 5%), and strategic use of electrolyte additives can form SEI species that lengthen the lifetime of the cell.[2,84,85,89–99]

Chapter 2 – Ni-rich Positive Electrode Materials

LNO and LCO were demonstrated to be possible candidates as a positive electrode material by the Goodenough group in the 1980's.[7,32,100–102] Sony used LCO as the positive electrode of the first commercial Li-ion batteries[33] and LCO cells continue to be used even now. On the other hand, to the author's knowledge, LNO has never been commercialized, for reasons that will be discussed later.

Recently, LCO cells have been losing market presence, from a market share of 27% in 2015[46] to 10% as of 2020.[3] This is due to markets trying to reduce the use of cobalt. Cobalt is the most expensive metal out of those commonly used in positive electrode materials[42,43,45,103,104] and a cost comparison of several metals commonly used in positive electrode materials is shown in Table 2.1. Cobalt is also toxic and there are issues with sourcing cobalt. Certain regions of the Democratic Republic of Congo, which accounted for ~70% of the world's cobalt production in 2020,[43] have reported cases of human rights abuses, including hazardous working conditions and child labour.[40]

Table 2.1: Cost of some metals used in positive electrode materials.[43,103,104]

Metal	**Price in 2019[43] (USD/kg)**	**Price in 2020[104] (USD/kg)**	**Price in Jun. 2021[103] (USD/kg)**
Lithium	12.70	14.66	16.50 (2018)
Aluminum	2.19	2.65	2.08
Cobalt	37.29	37.15	33.00
Iron	0.093	N/A	0.162
Magnesium	2.43	2.52	N/A
Manganese	N/A	1.61	2.06 (2018)
Nickel	13.90	20.51	18.58

In response to a decreasing LCO market presence, more attention has been focused on cells utilizing Ni-rich positive electrode materials, such as NMC and NCA. For the purposes of this thesis, materials with 80% Ni or higher in the transition metal role are considered Ni-rich materials, but the Ni-rich label has been applied, by others, to materials with a lower Ni content such as NMC622. Unlike LFP, the other positive electrode material surging into the gap created by LCO reductions, Ni-rich materials are comparable to LCO in energy density which is important for EV applications. Aims to improve energy density and reduce costs of NMC and NCA can be achieved by increasing the Ni content of the material, and the compositions of the two materials will invariably converge towards LNO.

2.1 – Background

2.1.1 – Crystallographic Structure of Ni-rich Materials

Figures 1.1 and 1.3 show the structure of LNO and Ni-rich materials. LNO is a layered structure with the rhombohedral $R\bar{3}m$ space group, with Li, Ni and O all arranged into separate layers as discussed in Section 1.3. Li ions occupy the 3a sites (Li layer) while the 3b sites (TM layer) contain Ni ions and 6c sites contained oxygen ions. For Ni-rich materials, like NMC and NCA, the Ni, Mn, Co and Al ions are randomly distributed in the TM layer sites.

The Li and the other metals generally stay segregated in their respective layers, but there are occasions where a non-Li metal ion moves into the Li layer or vice versa. The separation into Li and TM layers is driven largely by steric effects, which occur because of a difference in the ionic radii, and by minimizing the interaction energy

between neighbouring sites through ordering into alternating Li and TM layers.[22,105] Li^+ (0.76 Å) is larger than Ni (0.69 Å, 0.56 Å, 0.48 Å for the +2 to +4 oxidation states, respectively), Mn (0.64 Å, 0.53 Å for the +3 and +4 oxidation states), Co (0.54 Å, 0.53 Å for the +3 and +4 oxidation states) and Al^{3+} (0.54 Å).[106] However, Ni^{2+} is quite close in size to Li^+, so the barrier for Ni^{2+} to move to the Li layer is not as high as for the other metal ions, facilitating the Li and Ni to swap places. This is known as cation mixing. Ni can also exist in the Li layer when the material is synthesized as Li-deficient $Li_{1-x}Ni_{1+x}O_2$, the extra x Ni will occupy sites within the Li layer.[22,101]

In a NMC material with equal amounts of Ni, Mn and Co (NMC111), the transition metals have been found to exist as Ni^{2+}, Co^{3+} and Mn^{4+}.[107] The Mn^{4+} necessitates the formation of Ni^{2+}, but a high Co content has been shown to reduce the amount of Ni in the Li layer.[50] However, cation mixing still occurs in LNO, where it is expected that Ni is in the +3 oxidation state.[22,108–111] This is due to difficulty fully oxidizing all the Ni to the +3 oxidation state, leading to some amount of Ni^{2+} and Li deficiency. Another contribution to the formation of Ni^{2+} is thought to occur due to a disproportionation reaction of 2 Ni^{3+} to Ni^{2+} and Ni^{4+}.[22,37]

2.1.2 –Electronic Structure of Ni-rich Materials

The deintercalation/intercalation of Li ions during cell operation is accommodated by redox reactions of the transition metals. The electrons accompanying the Li ions make their way in/out of the 3d orbitals of transition metals. As discussed above and in Section 1.3, the transition metals are situated in the TM layer and each site is coordinated to 6 oxygen atoms (3 oxygens in the O layer above, 3 in the O layer below). The

octahedral coordination to the oxygen produces a crystal field, which splits the five 3d orbitals of the transition metal into two sets, one with a higher energy than the other. The higher energy orbitals (labeled e_g), d_{z^2} and $d_{x^2-y^2}$, have the orbital lobes pointing towards the oxygens, increasing electrostatic repulsion. The lower energy orbitals (labeled t_{2g}), d_{xy}, d_{xz} and d_{yz}, have the orbital lobes pointing between the oxygens. Figure 2.1a shows the geometry of the five 3d orbitals as split into the e_g and t_{2g} sets.[37]

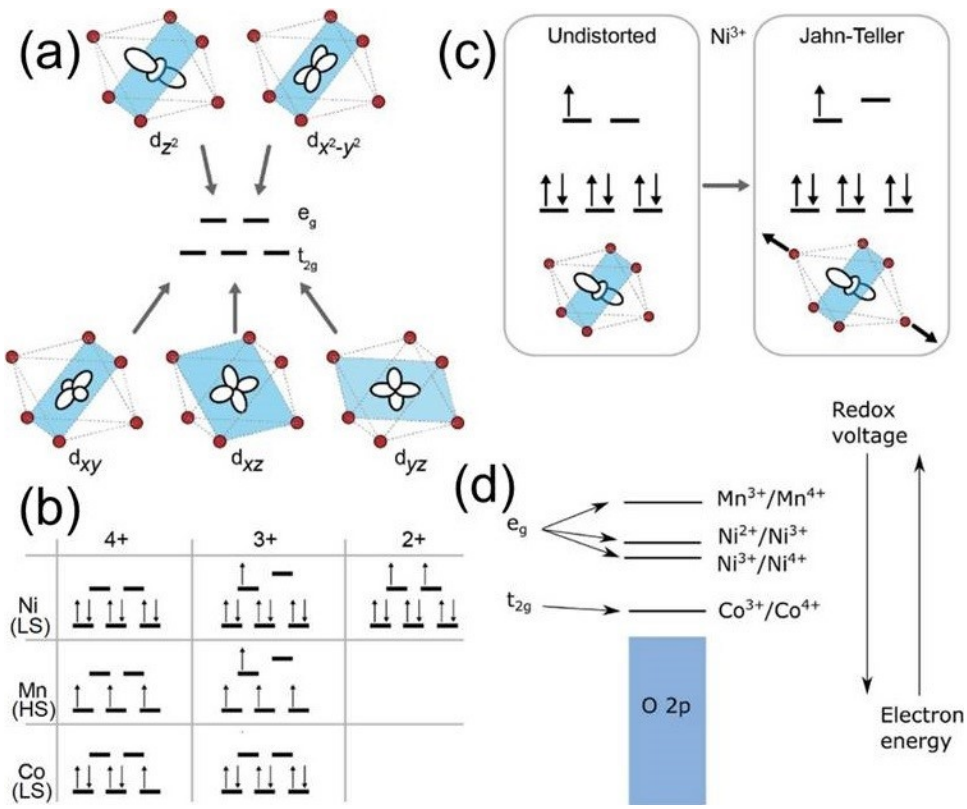

Figure 2.1: (a) Crystal field splitting of the five 3d orbitals of a transition metal in a typical layered Ni-rich material, (b) typical electron configurations of Ni, Mn and Co in layered materials (LS and HS denote low and high spin), (c) splitting of the Ni^{3+} e_g levels due to Jahn-Teller distortions and (d) qualitative position of energy levels of Ni, Mn and Co in layered materials. All panels reproduced with permission from Adv. Energy Mater.[37] Copyright (2017) John Wiley and Sons.

Figure 2.1b shows the electron configurations of the typical Ni, Mn and Co oxidation states observed in Ni-rich materials.[37] As mentioned above, Ni^{2+}, Co^{3+} and Mn^{4+} are present in pristine NMC111, while LNO has mainly Ni^{3+} in the pristine state. When charging, electrons are removed from the Ni and the Co to oxidize them to a maximum of a +4 oxidation state if fully delithiating to MO_2 (M = Ni, Mn, Co). The Mn remains electrochemically inactive as Mn^{4+} except for certain situations involving Li-rich materials accessing the Mn^{3+}/Mn^{4+} redox couple.[37,51,70,72] For Ni^{3+} (and Mn^{3+}), there is only one electron in the e_g set, making it susceptible to a Jahn-Teller distortion that breaks the e_g degeneracy. Fig. 2.1c shows a Jahn-Teller distortion elongating the bonds along one of the octahedral axes so the occupied orbital becomes lower in energy.[37] However, Ni in $LiNiO_2$ does not have a Jahn-Teller distortion, perhaps due to incomplete oxidation to Ni^{3+}, disproportionation reactions to form some amount of Ni^{2+} and Ni^{4+} or other reasons.[22]

Figure 2.1d shows the qualitative positions of energy levels of the 3d orbitals of Ni, Mn and Co and the 2p orbital of oxygen in a typical NMC material.[37] A lower energy level indicates that an electron is more stable, corresponding to a higher voltage needed to deintercalate/intercalate the Li. Redox in Co involves an electron in a t_{2g} orbital which is more stable, hence the lower energy level/higher voltage. The Mn^{3+}/Mn^{4+} redox couple is higher in energy than the Ni^{2+}/Ni^{3+} redox couple, enabling the spontaneous donating of electron from Mn^{3+} to Ni^{3+}, resulting in the Ni^{2+} and Mn^{4+} typically observed in NMC111.[59,107]

2.1.3 – Synthesis of Ni-rich Materials

An early report detailed the solid state synthesis of $Li_yNi_{1-x}Mn_xO_2$ using carefully selected reactants, thorough grinding, and heating of the reactants.[112] Today, it is more popular to carry out the syntheses of NMC, NCA and other lithium mixed metal oxides in two steps.[2,59] A common first step is to synthesize hydroxide precursor materials by co-precipitation. The co-precipitation step produces materials that are atomically mixed in the form of $M(OH)_2$ (M = divalent metals) which alleviates the potential concerns of non-uniform distribution of metals in the electrode material. The second step is to heat the precursor material with a lithium compound to produce the final lithiated electrode material.

The syntheses of hydroxide precursor materials are well understood if the metals are divalent in the hydroxide, such as in NMC precursors.[52,113–118] However, the introduction of Al^{3+} for Al doped materials such as NCA complicates the synthesis of hydroxide precursors and affects the products significantly. Some issues from synthesizing Al doped hydroxides include the product morphology and the formation of a new layered double hydroxide (LDH) phase. For the most part, these issues have been addressed to some extent from advances in synthesis and processing procedures.[119–127]

Putting the lithium into the hydroxide precursor requires mixing a Li compound with the precursor then heating the mixture to high temperatures. As the temperature increases to ~200-300°C, the hydroxide precursor decomposes into the oxide with some small uptake of Li to form Li-deficient rocksalt phases, then Li uptake accelerates above 400°C and the material orders into alternating Ni-rich layers and Li-rich layers starting

~650°C.[105,111,128–130] For LNO, the temperature required to optimally order the cations into a Li and TM layer is around 700°C,[59,111,128–130] while higher temperatures are needed for materials with less Ni.[21,26,27,126,131] As higher heating temperatures are used, the amount of Li lost increases.[99,131–139] Increasing the heating temperature further will promote Li/oxygen loss in the material, lowering the average oxidation state of the Ni and increase the Ni content in the Li layer.[140–143]

Historically, layered positive electrode materials were synthesized mostly in air but as the compositions become increasingly Ni-rich, syntheses need to be carried out in oxygen.[27,59,126,131,132,144–148] As the Ni content increases, a higher proportion of Ni needs to be in the +3 oxidation state to accommodate Li uptake and so synthesis in oxygen promotes the oxidation of Ni^{2+} to Ni^{3+}. There are few reports closely studying when the switch to synthesis in oxygen is needed,[27] although there are more reports studying Ni-rich samples synthesized in different atmospheres[126,132,144,145] or varying oxygen pressures or flow rate.[131,146–148] These studies show that the synthesis of Ni-rich materials in oxygen will generally lead to better performing materials.

While the synthesis temperature and atmospheres are the main factors involved in making good Ni-rich materials, there are some other variables that have been shown to impact the synthesized product as well. Compositions with higher Ni contents require a lower temperature to order well, so $LiOH{\bullet}H_2O$ is often used as the Li source instead of Li_2CO_3 due to a lower decomposition temperature.[21,26,27,59,111,126,128–131] However, $LiOH{\bullet}H_2O$ comes in larger crystals that are harder to grind and mix well with the precursor. A preheat step is often used to melt the LiOH and increase the uniformity of Li distribution.[21,131,149] For the purposes of this thesis, most of the focus on synthesis will

be on the second step (heating step). Mentions in later chapters regarding one- or two-step lithiations do not count the precursor co-precipitation step or the preheat step, although the presence or absence of the preheat step will usually be noted.

Another parameter that will influence the synthesis is the amount of Li used during synthesis. Ideally, a Li to transition metal or other metal (Li/TM) ratio of 1 would be used to fully lithiate the material and reduce Li waste. However, as discussed above, Li loss occurs during synthesis and increases with higher temperature.[99,131–143] Therefore, it is common to use some amount of excess Li during synthesis to ensure the material is not Li-deficient.

2.2 – Issues with Lithium Nickel Oxide (LNO)

LNO was actually under consideration, along with LCO, as the positive electrode for the first Li-ion cells. Due to nearly identical atomic weights, LCO and LNO have essentially the same theoretical specific capacity of 274 mAh/g if all the Li is utilized. However, LNO can extract more Li than LCO at a given voltage (~0.95 Li for LNO and ~0.58 Li for LCO at 4.3 V vs Li/Li^+),[37,110,150–152] so LNO has a higher specific capacity than LCO at that voltage. Figure 2.2 shows the voltage curves of LCO, NMC111, NCA and LNO.[37] As the amount of Ni increases and amount of Co decreases, the amount of capacity at a given voltage increases. This was explained in Fig. 2.1, the Co redox occurs at a higher voltage, so having more Ni means there is more capacity occurring at a lower voltage. LNO is also less costly than LCO, as shown in Table 2.1. However, there are still issues plaguing LNO and preventing LNO from being commercialized even now.

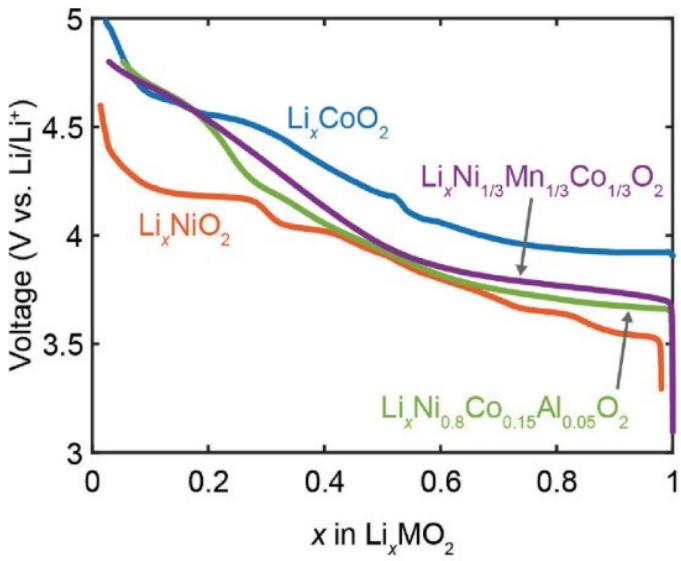

Figure 2.2: Cell voltage as a function of capacity for LCO, NMC111, NCA and LNO. Reproduced with permission from Adv. Energy Mater.[37] Copyright (2017) John Wiley and Sons.

2.2.1 – Degradation of LNO During Cycling

Delithiation/lithiation has significant impacts on LNO, which largely stem from structural changes. Li_xNiO_2 has four different structure configurations, but three phases have what is known as the O3 structure.[14,22,37,59,108–110,153] This signifies that the Li and Ni occupy the octahedral sites and that the unit cell contains 3 layers (usually the NiO_2 layers) before repetition. Since all three phases are the O3 structure, they were designated as the 1st, 2nd, and 3rd hexagonal phases (H1, H2 and H3, respectively) based on the order observed when delithiating the material, so H1 has the highest Li content. The other configuration is the monoclinic phase, which occurs in between the H1 and H2 phases. It has been proposed that the monoclinic phase stems from the ordering of the Li and Li vacancies which break the hexagonal symmetry or from the Jahn-Teller distortion of the Ni^{3+}.[22,108–110,154,155] Figure 2.3 shows an in-situ XRD experiment that continuously

obtained diffraction patterns of the LNO positive electrode during cycling.[110] The phase transitions involving the monoclinic phase as well as the H2 to H3 phase transitions were all observed clearly.

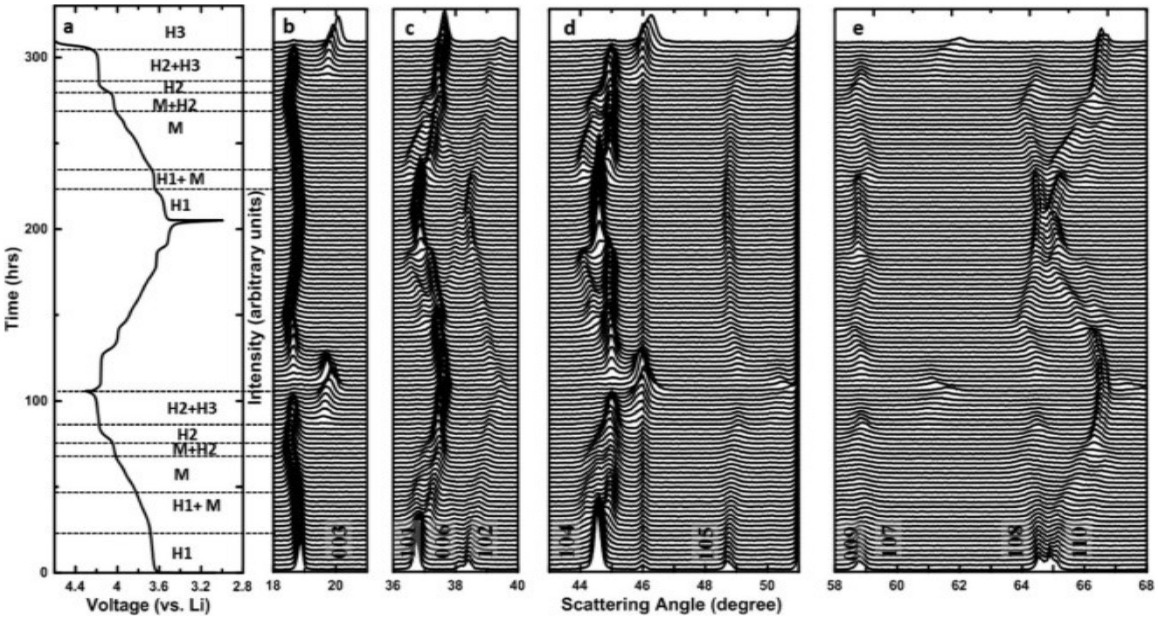

Figure 2.3: An in-situ XRD experiment on LNO. Cell voltage as a function of time (a) are aligned with the diffraction patterns (b-e), of which selected scattering angle regions are shown. The cell was cycled between 3.0–4.3 V for 1 cycle and then charged to 4.6 V, all at a rate of ~C/100. Reproduced with permission.[110]

LNO can cycle reversibly through most of its phases, but there are concerns that transitioning to the H3 phase may be detrimental. As the material transitions from H2 to H3, it experiences a large volume reduction of around 7%.[22,108–110,155] This volume change stems from the contraction of the *c* lattice as Li layers are emptied, which can be observed in Fig. 2.3, especially the (003) reflection (Fig. 2.3b). LCO also experiences a volume change at low Li content, and the O3 to O1 transition for LCO brings a significant reduction in the lifetime of the material.[37,150–152] While the H2 to H3 transition for LNO does not involve a parallel shift of the NiO_2 layers like the O3 to O1

transition for CoO_2 layers in LCO does, the volume change may still be contributing to the poor lifetime of LNO. It is believed that the large volume change causes mechanical stress in the material, forming microcracks in the material. Microcracking in the material opens up new areas inside the particle for electrolyte to infiltrate into as well as forming some electrically disconnected areas, and impedance growth and active material loss have been correlated with microcracking.[15,17,22,37,42,49,53,155–161]

As alluded to above, electrolyte infiltrating to new electrode surfaces will increase the impedance of the material by reacting with the surface. Electrolyte reactions with the positive electrode are exacerbated at high voltage, promoting the oxidation of the electrolyte. These reactions break down electrolyte and consume Li, producing gas and forming a film on the positive electrode analogous to an SEI (often called a cathode electrolyte interphase, CEI).[22,37,49,84,85,89,98,159,162,163] On the positive electrode surface side, the material is quite delithiated at high voltage and contains lots of Ni that are oxidized to the +4 oxidation. Ni^{4+} is unstable and reactive, and reacts with the electrolyte to form more stable Ni^{2+}. This reaction converts the layered material to a spinel and/or rock salt material and is referred to as surface reconstruction.[14,15,17,18,22,37,49,53,156,164,165] The rock salt material is expected to contain some amount of Li so Li diffusion still occurs albeit hindered, but is electrochemically inactive. Surface reconstruction is accompanied by the release of oxygen (the stoichiometry goes from MO_2 to MO, M = Li, Ni) which can also react with the electrolyte.[14,15,17,18,22,37,49,53,159,162–164]

2.2.2 – Safety of LNO when Delithiated

The safety of Li-ion batteries is a big concern for manufacturers and consumers. In general, heat generated from normal operation of well-designed cells and batteries can be safely dissipated to the environment.[166] However, this may not be the case when a short circuit occurs, especially if it is an internal short circuit. In that situation, a large current flows through the short, generating a large amount of heat in a short time. If the cell cannot dissipate the generated heat quickly enough, the cell overheats. As the internal temperature of the cell rises, it triggers several reactions.[12,16,19,20,31,167] Around and above 80-90°C, the metastable components of the negative electrode SEI decompose and the intercalated lithium at the negative electrode reacts with the electrolyte. Both these reactions are exothermic and release flammable gases, further increasing the temperature and pressure inside the cell. Separators melt at around 130°C, which shuts down the current flow and resulting heat generation, but does not stop the heat generation from SEI and negative electrode reactions. Should the cell temperature continue to rise, the delithiated positive electrode material decomposes when heated sufficiently. This exothermic reaction also releases oxygen, which reacts further with the electrolyte to release more heat and causing more decomposition. This positive feedback loop is known as a thermal runaway, and the temperature and pressure rises uncontrollably. Thermal runaway is the major contributor to Li-ion battery safety incidents, as the rapidly rising temperature and pressure may result in cells catching fire and/or exploding. Cell manufacturers have engineered safeguards such as the separator shutdown and pressure-triggered safety vents, which have reduced but not eliminated safety incidents.

The thermal instability of charged LNO contributes to its safety issues. Multiple studies have shown that charged LNO and Ni-rich derivatives are more thermally unstable than other materials such as LCO, LMO and LFP.[11–16,19–21,23,24,31] The thermal instability increases as Ni content increases.[12,13,15,18,26–28,30] This may be due to the reactivity of Ni^{4+} and also because materials with more Ni have more capacity at a given voltage (Fig. 2.2). However, the state of charge, or degree of delithiation, also factors into the decomposition temperature.[11,12,14,18,24,25,29]

Charged LNO, LCO and LMO have similar stoichiometry, but decompose in different ways. When fully delithiated, layered NiO_2 will decompose to the rocksalt NiO and release $\frac{1}{2}O_2$.[11,13,18,23,25,168] On the other hand, fully delithiated layered CoO_2 will decompose to the spinel Co_3O_4 and release $\frac{1}{3}O_2$[11,168,169] and fully delithiated spinel λ-MnO_2 will decompose to the spinel-like Mn_2O_3 and release $\frac{1}{4}O_2$.[11] So not only does charged LNO decompose at a lower temperature, it also releases more oxygen to react with the electrolyte.

2.2.3 – Impact of Li content on the Synthesis of LNO

LNO is sensitive to the Li content during synthesis, and making good, stoichiometric material is not easy. If the stoichiometry is Li deficient, Ni exists in both the +2 and +3 oxidation states to balance the charge and some of the Ni^{2+} will migrate to the Li layer due to Ni^{2+} being a similar size as Li^{+}.[106] The presence of Ni in the Li layer is undesirable since Li diffusion, reversible capacity and rate capability are all negatively impacted.[14,15,17,37,59,110,128,131,140–142,154,170,171] Ni^{2+} in the Li layer does not participate in redox reactions, decreasing the capacity.[21] Since Ni in the Li layer does not intercalate or

deintercalate, the Ni serves as an obstacle in the Li layer which hinders Li diffusion and reduces the rate capability. Regardless of the Li stoichiometry, it is believed that the presence of Ni^{2+} in the material cannot be avoided, perhaps due to disproportionation reactions of 2 Ni^{3+} to Ni^{2+} and Ni^{4+}, and LNO will always have some amount of Ni in the Li layers.[14,37,56,57,59,108,110,128,140–142,154,170,171]

On the other hand, if excess Li is present during sintering, there will be residual Li compounds that remain on the surface as impurities. These surface impurities, such as LiOH and Li_2CO_3, have been shown to reduce the capacity, rate capability and capacity retention of materials.[110,131,157,172–182] A large enough presence of residual Li impurities is also detrimental to the processing of the material into electrodes, as it will cause the gelation of the slurry, making the slurry clumpy and less adhesive to the current collector, or even uncoatable. Similar to the presence of Ni in the Li layer, even with perfect stoichiometry some amount of residual Li compounds will form from reactions of the surface with the ambient atmosphere due to the reactivity of LNO with water and CO_2 in the air.[14,174–176,178,179,181–183]

One common method to remove the residual Li impurities from the material is via a washing step. While washing with water has been generally accepted to be capable of removing the residual Li impurities, it has been found that materials become more sensitive to ambient atmosphere and prone to form more residual Li impurities after a washing step.[172,173,178] The materials are often heated after the washing step to combat this sensitivity and to improve the performance of the material, but the performance depends greatly on the temperature used.[99,178,182] Another concern of the washing process

is the occurrence of ion exchange between the H^+ in solution and the Li in the material, which will reduce the available capacity of the material.[172,174,175,182–184]

2.3 – Metal Substitution of LNO

With the disadvantages of LNO preventing its commercialization, there has been considerable research on finding approaches that can mitigate the disadvantages of LNO. One popular approach has been to substitute some portion of the Ni with other metals.

2.3.1 – Al, Co, Mg and Mn Substitution

The substitution of some portion of the Ni with other metals such as Mn, Co and Al resulted in the commercialization of NMC and NCA, as discussed in Section 1.3. While NMC originated as the substitution of 2 Co^{3+} with Ni^{2+} and Mn^{4+}, the advancement of NMC compositions towards high Ni contents resemble more the replacement of Ni with Co and Mn. Depending on the transition metal ratio of NMC, improvements can be made to the safety, capacity or lifetime.[2,14,15,17,22,37,47–50,52,53] NCA was formed from the substitution of Ni with Co to reduce the amount of Ni in the Li layer and stabilize cycling performance and with Al to improve thermal stability.[2,14,15,17,22,37,49,53–55,59–65]

Metal substitution of Ni with Al, Co and Mn has resulted in commercialized materials such as NMC and NCA, but some of the issues plaguing LNO can still be seen in these materials. Thermal instability of the charged material[13–15,17,21,24,28,30,185] and sensitivity to the Li content[15,17,26,37,52,128,140–142,171,178,179,181] leading to Ni migration to the Li layer and residual Li compounds are issues that can still be observed, albeit to a lesser degree than LNO.[14,17,21,22,37,53,149,157] The issues are more noticeable for materials with

higher Ni contents such as NMC811 or typical NCA, both of which have 80% Ni in the transition metal role.

Besides Al, Co and Mn, research has tried substituting Ni with many different metals. Mg has repeatedly come up as a beneficial dopant from positive electrode material doping studies that try to improve material cycling performances. Mg has been shown to improve cycling performances of various positive electrode materials including LCO,[36,151,152,186–189] NMC,[190–192] NCA[63,149,193,194] and other Ni-rich materials[21,149,195–197] when doped into the material in small amounts. It has been shown that a Mg content of as low as 1-2% can still improve cycling of the material.[149,151,194–197]

The functions of Al, Co, Mg and Mn substitution of Ni has been investigated and discussed in length. All 4 metals are capable of suppressing the LNO phase transitions at high enough substitution concentrations.[14,15,17,21,37,198,199] Co is the only electrochemically active substituent of the 4, participating with the Co^{3+}/Co^{4+} redox couple and maintaining the high specific capacity of the material. The conventional understanding is that the presence of Co reduces the amount of Ni migration into the Li layer,[14,15,37,50,59,61] but this has been debated.[21,27] The inclusion of Co in the composition also benefits the rate capability of the material.[14,15,21,37,42,61,200,201]

With electrochemically inactive substitutes, the specific capacity of the material is reduced. Mg, Al and Mn are all low cost substitutes and generally exist in the material with an oxidation state of +2, +3 and +4, respectively. Mn substitution is known to improve the cycling performance and thermal stability of the material.[14,15,21,24,27,37,64,201,202] Al substitution has been shown to stabilize impedance

growth as well as improve the cycling performance and the thermal stability.[14,15,17,21,37,61,62,64,65,198,199] Mg can also stabilize impedance growth, improve cycling performance and improve thermal stability, but at a higher capacity cost than Al or Mn.[15,17,21,24,56,57,61,149,193–197] The use of Al and Mg dopants comes with some minor drawbacks. With electrochemically inactive substituents, the specific capacity of the material is reduced. Mg and Al generally exist in the material with an oxidation state of +2 and +3, respectively, so the same fraction of Mg reduces the capacity of the material more than Al due to the formation of a Ni^{4+} for charge balance.[21,149]

The inclusion of Al and/or Mg reduces the capacity of the material and thus there is a ceiling to how much of the substituent should be included in the material, generally 5% or less.[14,15,17,21,22,24,37,42,49,53,65,149,151,194–197] Mn is an interesting substituent that, while electrochemically inactive, is less detrimental to the material capacity because some Ni are reduced to Ni^{2+} to compensate for Mn^{4+}.[21,59,107] Therefore, there is no real limit on the amount of Mn in the material and this is demonstrated by the abundance of different NMC and $LiNi_xMn_{1-x}O_2$ compositions.[14,15,17,21,22,26,27,37,42,48,64,201–204] The increase in Ni^{2+} population will result in more Ni content in the Li layer for Mn-substituted LNO materials. Coupled with the absence of Co, the rate capability of the material can be quite poor.[21,27,42,201,203]

2.3.2 – Other Metal Substitution

Many different metals have been studied as substitutions for Ni to various degrees of success.[14,17,21,22,37,42,49,53,149,157,196,197,205–209] While there are too many to discuss in detail, there have been recent advances using certain metals in small amounts to control

the microstructure of the material. The resulting microstructure results in primary particles that are long, thin and radially aligned. The formation of this radial rod-like microstructure seems to stem from the use of substituents like Ta, W, B, and others.[42,49,158,207,208] Figure 2.4 shows the cross-sectional images of 5 different materials to illustrate the impact of using these metals compared to Mn and Al.[208] These radial rod-like primary particles have been attributed to the significant reduction of microcracking after long term cycling, contributing to materials with very impressive capacity retention.[42,49,158,207,208]

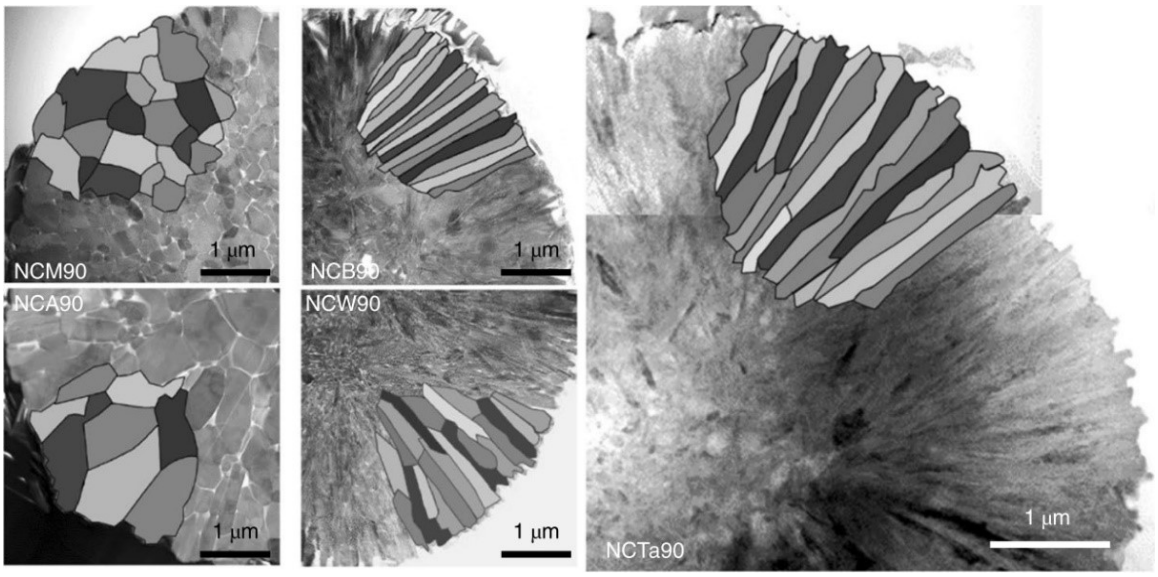

Figure 2.4: Cross-sectional scanning transmission electron microscope images of various Ni-rich materials containing various metals and the corresponding schematic of the primary particle morphology. Reproduced with permission from Nat. Energy.[208] Copyright (2020) Springer Nature.

An interesting question to consider is whether these metals actually act as substituents in the material or not. It is expected that Ta and W exist in the material as Ta^{5+} and W^{6+}. This would drive multiple Ni to the +2 oxidation or limit Li uptake just to balance the charges, without even considering size or charge compatibility of the metals

within a layered structure. It has been found that some metals with a high oxidation state are mainly confined near the surface of the particle.[196,208] This may be due to a slow diffusion of the metal into the material or formation of a secondary phase on the particle surface. More work confirming this and studying this class of "substitution" could be valuable in further improving Ni-rich materials, but will not be the focus of this thesis.

2.3.3 – Co-free Ni-rich Materials

The motivation to eliminate Co from the positive electrode materials stems from cost and sourcing issues. The use of Co comes with economic and ethical challenges, such as scarcity, higher prices, price volatility, supply chain instability and reports of child labour.[40–45,103,104] However, the inclusion of Co in the material has been shown to ease the synthesis and benefit the performance of the material by reducing the cation disorder, maintaining or reducing the irreversible capacity and increasing the rate capability.[14,15,21,27,37,42,50,59,61,200,201]

The costs that come with using Co have generally been justified by the benefits Co imparts, but recent advances in synthesis and materials have demonstrated that Co may not be necessary for Ni-rich materials to perform adequately.[21,24,27,42,149,157,184,196,197,201,202,204–206,210–213] In particular, recent work studying the impact of 5% and 10% doping of Al, Mg, Mn or Co in LNO have questioned the necessity of having Co in the material, showing that Ni migration to Li layers and capacity fading can also be reduced with Al and Mg doping, and that phase transitions and thermal instability can be suppressed with Al, Mg and Mn doping.[21,24]

Besides Co-free Ni-rich materials, there are some alternative solutions to eliminate Co from Li-ion cells. Olivine materials (Section 1.3) are very low cost since they generally use iron and/or manganese as the transition metal. LFP is a Co-free positive electrode material that is already commercially available. LFP is very safe, very stable and can withstand cycling for longer than most other positive electrode materials in mild conditions.[77,78,214] However, the energy density of LFP is not competitive with layered materials owing to the bulky phosphate anions. Li-rich materials are another alternative solution that have been researched heavily but have not been commercialized yet. Li-rich materials are Mn-rich and attractive due to a high energy density, but the large irreversible capacity and concurrent capacity and voltage fading reduce the energy density too quickly.[37,51,66,67,69,70,72,73,75] With the increasing uptake of Ni-rich materials, it is projected that the abundance of high purity Ni will dwindle and costs of Ni will rise.[3,44,215] Therefore, continued work on Co-free Ni-poor/free materials such as olivine materials or Mn-rich Li-rich materials could help alleviate the upcoming concerns.

2.3.4 – Impact of Composition on Ni-rich Materials and the Unavoidable Challenge

Due to the amount of metal substitutions studied, it may be hard to compare the effects of each substituent. However, reports summarizing the impact of compositional changes of Ni-rich materials have similar messages. They found that as the Ni content of the material increases, the capacity increases but at the cost of cycling performance and thermal stability.[14,15,17,22,26,27,42,49,157,216] Figures 2.5c and 2.5d show this relationship for Ni-rich materials containing Mn, Co, Al and Mn substituents (Fig. 2.5c) and NMC and NM materials (and LFP) (Fig. 2.5d).[42,157]

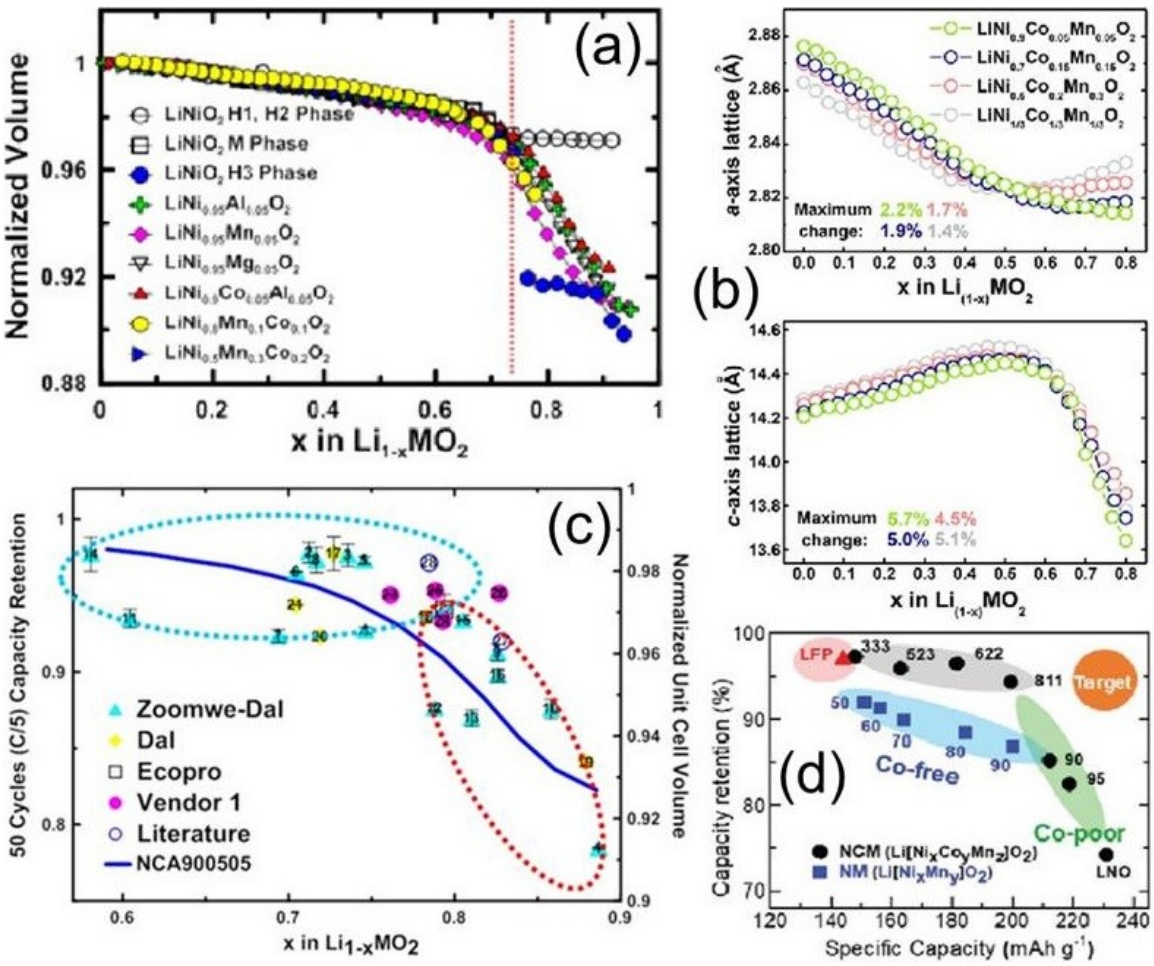

Figure 2.5: In-situ X-ray diffraction experiment results showing the normalized volume (a) or the *a* and *c* lattice parameters (b) as a function of lithium content for various material compositions.[157,217] Capacity retention as a function of lithium content (c) or specific capacity (d) for various material compositions.[42,157] Panels (a) and (c) reproduced with permission from Chem. Mater.[157] Copyright (2019) American Chemical Society. Panel (b) reproduced with permission from JACS.[217] Copyright (2019) American Chemical Society. Panel (d) reproduced with permission from Energy Environ. Sci.[42] Copyright (2021) Royal Society of Chemistry.

Figures 2.5a and 2.5b show the normalized volume/lattice parameters of various compositions as a function of the lithium content.[157,217] Recent work found that the unit cell volume change can be related to the cycling performance and the study proposed that a main failure mode for Ni-rich materials stem from the anisotropic volume change

compromising particle integrity.[157] The unit cell contraction of the Ni-rich electrode was found to be a universal behavior that is dependent on the degree of delithiation, regardless of chemical composition, and this was summed up as "an unavoidable challenge". The benefits of metal substitution to the cycling performance are mainly due to reducing the capacity (degree of delithiation) of the material and thus reducing the volume change, and the choice of substitute may not be significant.[157,217] The volume change is expected to be the main degradation mode for typical Ni-rich positive electrode materials, known as polycrystalline (PC) materials, that have many small individual grains (primary particles) agglomerated in a larger structure (secondary particle). The volume change causes anisotropic stresses and strains on polycrystalline materials because the primary particles are randomly oriented. This causes microcracking of the material and the accompanying electrolyte reactions, surface reconstruction and oxygen release issues as discussed in Section 2.2.1. This was summed up as an "unavoidable challenge" because the volume change is intrinsically linked to the degree of delithiation of the material, so increasing the capacity of the material will invariably bring about more volume change and more degradation.

2.4 – Ni-rich Single Crystalline (SC) Materials

Since the volume change causes anisotropic stresses and strains on PC materials, single crystalline (SC) materials may be able to preserve particle integrity by undergoing isotropic volume change within a particle. Figure 2.6a shows the morphological differences between a PC (UC-532) and SC (SC-532) NMC532 material.[97] SC materials consist of individual primary particles that are not agglomerated into a secondary particle.

This is usually done by growing the primary particles to the micron scale, for the materials discussed in this thesis.

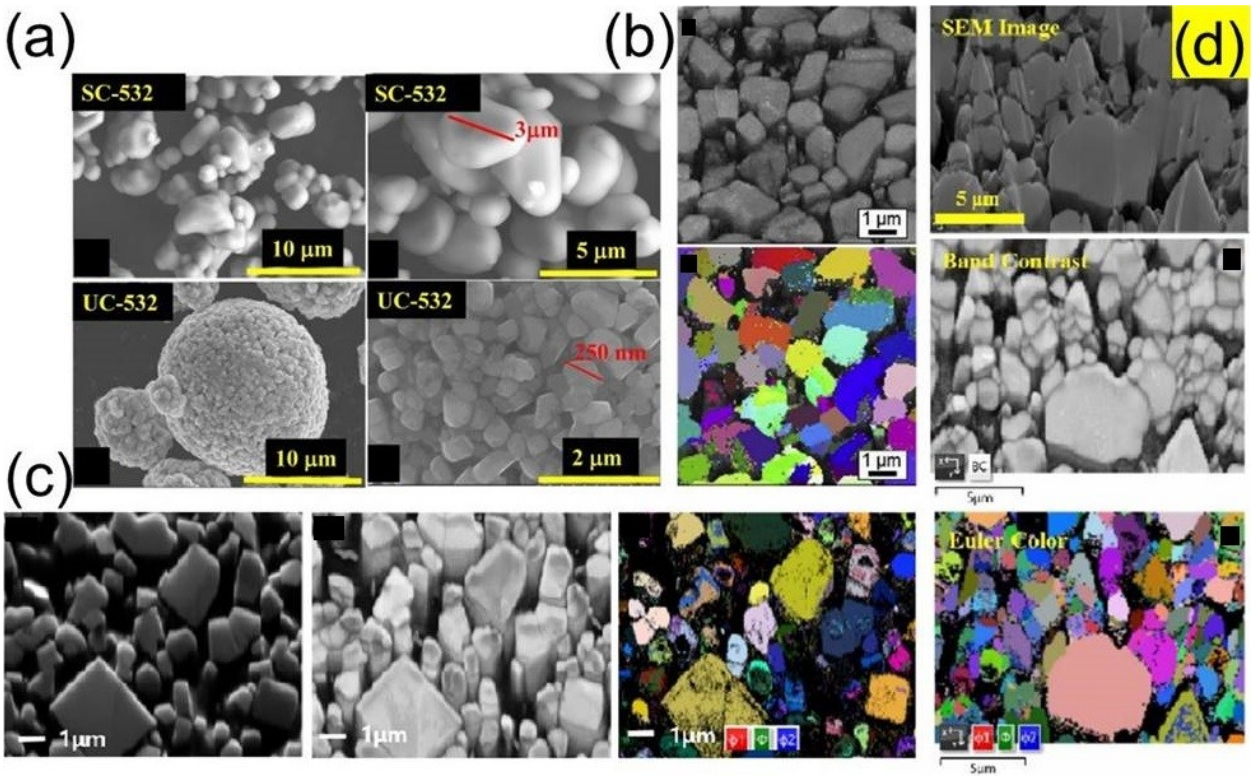

Figure 2.6: Scanning electron microscope (SEM) images (a) of a polycrystalline (UC-532) and single crystalline (SC-532) material.[97] Various examples of cross-sectional SEM images, band contrast EBSD maps and EBSD orientation maps (b-e) of single crystalline (b) NMC622,[137] (c) NMC91/3/6[218] and (d) NCA 88/9/3.[90] Panel (a) reproduced with permission.[97] Panel (b) reproduced with permission from Energy Storage Mater.[137] Copyright (2020) Elsevier. Panel (c) reproduced with permission from Mater. Lett.[218] Copyright (2020) Elsevier. Panel (d) reproduced with permission.[90]

In this thesis, the phrase "single crystalline" is used because the materials look to be individual grains, another suitable term to use is "monolithic". In order to confirm that the material actually consists of single crystals, the primary particles need to be characterized by techniques such as electron backscatter diffraction (EBSD) to confirm the lack of grain boundaries within a primary particle. Figs. 2.6b-2.6d show some

examples of EBSD characterization of SC materials.[90,137,218] While primary particles do not have grain boundaries for the most part, there are still some particles that do (Fig. 2.6b).

2.4.1 – Synthesis of SC Materials

The synthesis of SC materials occurs by grain growth of particles, which are accelerated by some parameters. The first parameter is temperature, which is crucial for promoting grain growth. For various Ni-containing compositions, the temperature at which grain growth is accelerated has been reported to be generally 40-100°C higher than the temperature used to synthesize PC materials with the lowest Ni content in the Li layer.[90,97,99,130,133–135,137–139,218–228] This may be due to the difference in thermal energy required for the ordering of cations into a Li and TM layer[105,111,128–130] versus enabling enough mass transport to facilitate increased grain growth at the particle surface.[138,229] Lattice formation has been suggested to mainly rely on oxygen and lithium migration.[138,230] As discussed in Section 2.1.3, a higher temperature will promote Li/oxygen loss in the material, which may further facilitate mass transport.[138,140–143]

The amount of excess Li has also been reported to promote grain growth of materials.[97,99,130,133,134,137,138,218,221–224,229] Increasing the amount of Li in the synthesis may increase Li migration and improve mass transport. However, it has been found that the impact of Li/TM ratio on grain growth may not be as significant at lower temperatures in the grain growth regime.[99,133,227]

Another way to promote grain growth of materials is to use a fluxing agent.[134,137,138,218,222,225,229,231] The use of a fluxing agent can enable grain growth at lower

temperatures than otherwise needed. The use of a fluxing agent also enables greater control on the morphology of the synthesized SC materials, allowing careful studies of the performance of different surface facets.[134,138,229,231]

The two common SC synthesis methods are solid state reaction and using a salt flux. The solid state reaction is simply the second step of typical positive electrode material synthesis as discussed in Section 2.1.3. However, a higher temperature and sometimes a higher Li/TM ratio are used compared to typical PC material synthesis. The morphology of SC materials synthesized via the solid state reaction is inherited from the precursor morphology, and sometimes the secondary structure of the material can still be observed when inadequate grain growth occurs during the synthesis.[90,97,133,138,139,219,226,227] As mentioned, synthesis using a salt flux enables a greater flexibility and control of the synthesized SC materials.[134,138,229,231] Using a salt flux should also require a lower temperature to promote grain growth, but it is uncertain if any reports have compared the temperatures required for the two methods to attain similar particle sizes. A disadvantage to using the salt flux synthesis method is the requirement of a washing step to remove the fluxing agent. However, solid state reactions using a large amount of Li excess will also require a washing step to remove the remaining excess Li.

2.4.2 – Polycrystalline versus Single Crystalline Materials

There are many reports comparing PC and SC materials of a given composition. When compared against PC counterparts, SC materials have been consistently found to improve the cycling performance.[17,53,92,97,135,137,162,218,223,224,229,232–235] Li-ion cells with SC materials can have further improved cycling performance when appropriate electrolyte

additives are used.[90–92,97,99] SC materials also have better performance at high temperature[97,135,137,223,232,234] and high voltage.[17,97,223,235] Additionally, the thermal stability of charged SC materials has been shown to be better than charged PC counterparts, indicating a greater degree of safety.[17,53,162,223,229,234] The density of SC materials after electrode calendaring is higher than its PC counterpart, and a strategy of combining SC and PC materials in the same cell has been utilized to increase the electrode density even further.[92,229,235]

There seems to be various contributions as to why SC materials experience less degradation than PC materials. SC materials have been reported to reduce parasitic side reactions between positive electrode and electrolyte[92,135,219,224,229] and reduce the degree of microcracking[17,53,135,137,218,223,224,228,229,232,234,236] when compared against PC materials. Most recently, SC materials have been shown to be more tolerant to air exposure compared to PC materials.[183] These findings point to lower surface reactivity of SC materials as well as less mechanical degradation due to volume change as discussed in Section 2.3.4.

However, SC materials are not perfect and there are some drawbacks to using SC materials. SC materials are reported to have less specific capacity than their PC counterparts.[17,90,97,99,135,218,223,224,228,235] The rate capability of SC materials is also generally lower than PC materials, largely owing to the diffusion of Li over larger distances.[99,123,228,234,235] For this reason, SC material syntheses generally have a target particle size in the 2-6 micron range, instead of trying to grow as large particles as possible.

2.4.3 – Ni-rich SC Materials

The majority of studies on SC materials have been on NMC grades with less Ni but increasing amounts of work on Ni-rich materials have been reported recently.[90,92,130,134,135,139,218,221,223,224,228,229,232,233,235,236] The Ni content in SC material studies lags behind those of materials in metal substitution studies,[21,149,157,196,197,205,206] likely due to difficulties in synthesis. Grain growth of particles is promoted by increasing the temperature, increasing the Li/TM ratio or by adding a fluxing agent, but a washing step is often required to remove the excess Li or fluxing agent.[17,99,134,137,138,218,222,225,229,231] With Ni-rich materials, their sensitivity to moisture suggests that a washing step will deteriorate the performance and should be avoided.[17,99,110,131,157,176,178,179,181–183]

NCA materials have been reported to form Li_5AlO_4 at high temperatures and with excess Li,[90,131] so a two-step lithiation method was introduced to synthesize SC NCA.[90] This method consists of a first step that heats the precursors to high temperatures but a deficient amount of Li to grow particles and a second step at lower temperature to fully lithiate the material. Well grown single crystal NCA particles without Li_5AlO_4 impurity were made using this method.[90]

A number of Ni-rich SC materials have been reported to have less capacity than the PC counterparts.[90,135,218,223,224,228,235,237] Though not often reported, looking at a plot of differential capacity as a function of cell voltage may be helpful in observing where the capacity is lost. For NCA 88/9/3, the capacity reduction was observed to occur around the 3.5 V voltage region as well as the ~4.2 V region.[90] While not explicitly discussed, some works on SC Ni-rich materials corroborate the occurrence of lower

capacity in those regions.[139,218,223,224,228,237] These regions have been associated with kinetic hindrances related to Li diffusion, and Li diffusion has been observed to decrease at low and high states of charge.[37,228,238–240]

2.5 – Kinetic Hindrances to Li Diffusion and Irreversible Capacity in Ni-rich Materials

One issue with LNO and Ni-rich materials that is less prevalent as a research focus is the high 1st cycle irreversible capacity (IRC) compared to LCO. Early work ascribed the IRC to shrinkage of the interslab space due to Li deficiency,[241] formation of inactive domains[242] or Ni in the Li layer.[200] However, the discovery that the irreversible capacity can be recovered shifted the focus onto kinetics as the cause for the IRC.[238,243–245] It was observed that Li diffusion is reduced at low and high states of charge.[37,228,238–240]

The kinetic hindrance at low state of charge can be explained by the diffusion mechanism proposed by Van der Ven *et al*.[37,239] Theoretical calculations predict that the tetrahedral site hop (TSH) mechanism is more energetically favorable and thus expected to be the predominant mode for Li diffusion. The TSH mechanism relies on divacancies which become dilute at a low state of charge. As the activation barrier increases due to the lack of divacancies, Li cannot fully diffuse into the material before reaching the set lower cutoff voltage (LCV), leading to the high IRC.

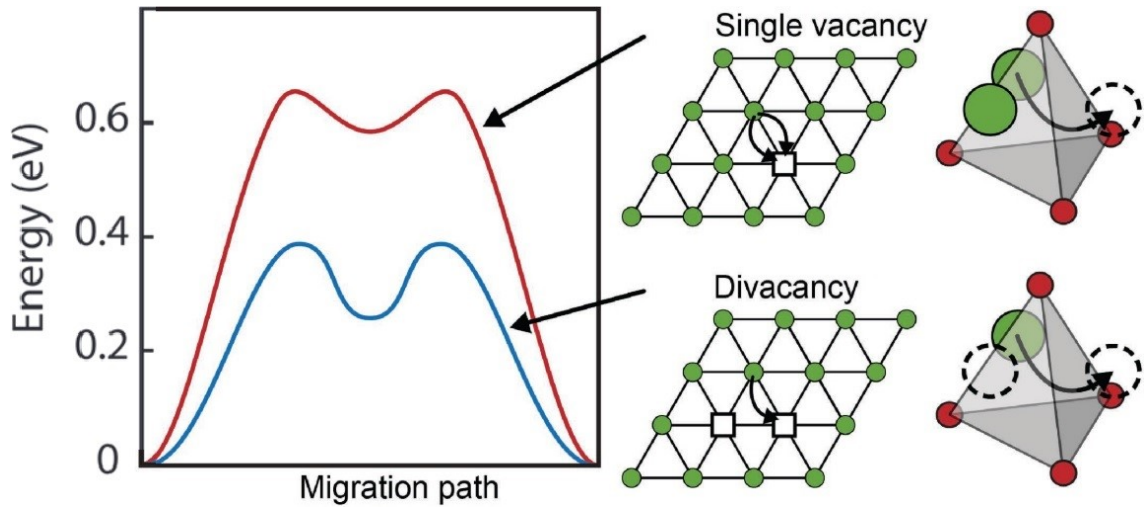

Figure 2.7: Theoretical calculations of the energy barrier for Li migration in the presence of one or two vacant neighbouring sites. Reproduced with permission from Adv. Energy Mater.[37] Copyright (2017) John Wiley and Sons.

The kinetic hindrance at high state of charge occurs due to the structural changes at low lithium content. As discussed in Section 2.2.1 and observed in Fig. 2.5, as Li gets removed from the positive electrode material, the volume change becomes large.[108–110,157,217] Specifically, the contraction of the *c* lattice parameter would shrink the interlayer spacing and create a migration barrier for Li.[37,239] As shown in Fig. 2.5, the collapse of the interlayer spacing seems to be a universal behaviour of Ni-rich materials regardless of composition.

2.5.1 – Factors that Affect the Kinetic Hindrances to Li Diffusion in Ni-rich Materials

The IRC of the material increases quite linearly as the substituent content of LNO increases, except when Co is the substituent.[21,149,200,205] Previous work has shown that substituents for Ni change the potential energy landscape of Li.[21] For example, the energies of two Li sites at opposite vertices from a Mg atom are lowered, "locking" them

in place. Once occupied, these sites no longer participate in Li diffusion, instead they act as pillars that must be circumvented by other diffusing Li ions. This hinders the collective diffusion of Li within the layer, forcing the particle surface to fill with Li at a lower average concentration, reducing the discharge capacity and thereby increasing the IRC. The degree of kinetic hindrance may plateau above a certain substituent threshold, since studies on materials with 80% Ni or below have found negligible effect on the IRC from varying Ni content.[238,245,246]

The effect of kinetic hindrance on IRC is also found in SC materials. As discussed in Section 2.4.3, there have been multiple reports of capacity reductions in Ni-rich SC materials when compared to their PC counterpart. These capacity reductions have been observed to occur at the regions associated with kinetic hindrances to Li diffusion.[90,139,218,223,224,228,237] However, not all of these capacity reductions led to higher IRCs, since some of the SC materials had less charge capacity as well. The kinetic hindrances to Li diffusion are likely exacerbated in SC materials due to the increased Li diffusion length in and out of the larger grains. As research continues to increase the Ni content of SC materials, the capacity reductions and increased IRC will become more significant, therefore further understanding of kinetic hindrances related to Li diffusion are important.

Chapter 3 – Experimental

3.1 – Synthesis of Ni-rich Positive Electrode Materials

The synthesis of Ni-rich materials was discussed in Section 2.1.3. Hydroxide precursors of Ni-rich materials in this thesis were provided by Guizhou Zoomwe Zhengyuan Advanced Material Co., Ltd. (Zoomwe). Zoomwe precursors were co-precipitated using a continuously stirring tank reactor, but the exact synthesis procedure and post-synthesis processing was not shared. The Zoomwe precursors are spherical, come in various secondary particle sizes (D50 ~3-18 μm) and are expected to have similar primary particle sizes, but primary particle sizes were not measured.

A solid state synthesis process was used to lithiate the precursor materials and produce the final $LiNi_{1-x}M_xO_2$ (M = Al, Mg, Mn and/or Co) electrode materials.[21,131,157,247] The hydroxide precursor materials were mixed with a Li source, either $LiOH{\bullet}H_2O$ (FMC Corporation, 99.8%) or Li_2CO_3 (Alfa Aesar, 99%), in a chosen Li to transition metal or other metal (Li/TM) ratio to obtain 2.5 g of each mixture. The mixtures were then ground together by mortar and pestle and placed in alumina heating "boats".

For samples mixed with $LiOH{\bullet}H_2O$, a preheat step was used to increase the uniformity of Li distribution as discussed in Section 2.1.3. The samples were first preheated in a furnace for 3 h at 480°C before another round of grinding. The samples were then placed back in the furnace and heated for 2 h at 480°C then at a higher synthesis temperature for a specified amount of time. For samples mixed with Li_2CO_3, no preheat step is needed and the samples were simply heated to the synthesis

temperature. In this thesis, synthesis temperatures ranged from 700-1000°C and held at the top temperature for 5-20 h. A heating rate of 10°C/min was used for all preheat and synthesis steps. When the heating step was finished, the furnace was naturally cooled, and the cooling rate was neither controlled nor measured. For syntheses involving a lower temperature step after calcination, the furnace was programmed to cool down to the lower temperature at a rate of 10°C/min and held for 5 h. In reality, the furnace cooled naturally at a rate that was probably slower than 10°C/min and so the dwell time at the lower temperature is slightly less than 5 h. After the heating process, lithiated samples were weighed and ground once more before characterization.

Samples were heated in a box furnace or tube furnace depending on the synthesis atmosphere of choice. The majority of syntheses in this thesis occurred in an oxygen atmosphere using a tube furnace (4.6 cm diameter). The tube furnace was kept under an oxygen (Praxair, 99.993%) flow rate of 60 sccm for the entirety of the heating step. Preheat steps were also carried out in an oxygen atmosphere. Syntheses in air were done using a box furnace. The tube furnace was also used to flow extra dry air (Praxair, < 2 ppm H_2O and < 0.5 ppm CO_2) at a flow rate of 60 SCCM in Chapter 7, and this is denoted as synthesis in dry air.

3.2 – X-ray Diffraction (XRD)

X-rays have wavelengths (λ) in the range of 10 nm to 0.01 nm, which are comparable to the size of atoms. This makes X-rays useful for probing structural arrangements and compositions of phases present in a sample. X-rays interact with materials in various ways, including elastic scattering, inelastic scattering, and absorption

of the X-rays. XRD is a technique that uses elastic scattering to gain information about the phases present, their structure, and lattice parameters in a sample.

When an X-ray beam probes a sample, the X-ray photons interact with the electrons of the sample.[248,249] Elastic scattering occurs when the ensuing X-ray photons retain the same wavelength, but the momentum changes. Like a wave of water encountering an object, the photons are scattered in all directions. In samples with a periodically repeating arrangement of atoms, which include Li-ion positive electrode materials (Section 1.3) of interest in this thesis, X-rays are scattered off all the atoms interacting with the X-ray beam. While the majority of the scattered X-rays interfere destructively with each other, constructive interference may occur when the scattered X-rays are in phase. Figure 3.1 shows a depiction of X-ray diffraction. In order for the two X-rays to remain in phase after diffraction, the extra distance travelled by the lower X-ray must be a multiple of the wavelength.

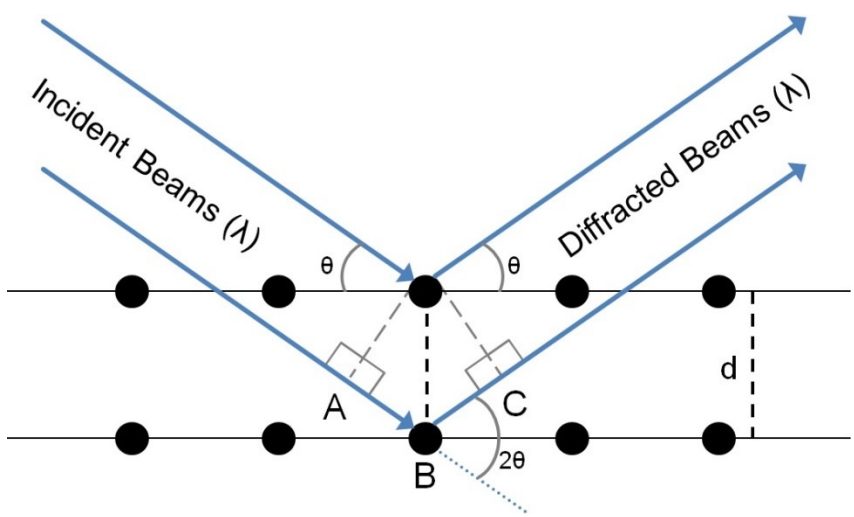

Figure 3.1: A diagram of X-ray diffraction, as described by Bragg's Law, due to the ordered planes of a sample.

The extra distance is depicted as the distance AB + BC in Fig. 3.1, but can also be denoted generally as 2 x d sin(θ). Thus, the constructive interference of X-ray scattering is governed by Bragg's Law,

$$n\lambda = 2d\ \sin\theta, \tag{3.1}$$

where n is an integer, λ is the X-ray wavelength, d is the spacing between particular planes, and θ is the incident angle of the X-ray with respect to the plane of the sample.

Crystalline samples, which have an ordered arrangement of atoms, contain numerous planes which will satisfy Bragg's Law. This gives rise to diffraction peaks that occur at different scattering angles (2θ). XRD patterns show the intensity of diffraction peaks as a function of the scattering angles and can be used to determine the arrangement of atoms in the sample. The arrangements can only occur in a limited number of ways, and space groups are used to designate the symmetry of the sample. Once the space group of the sample is known, diffraction peaks can be assigned a known (*h,k,l*) plane, known as Miller indices, and unit cell parameters can be determined. Since XRD patterns are affected by a multitude of factors, the fitting of powder diffraction patterns to extract information is generally accomplished through "Rietveld refinement".[250]

3.2.1 – Rietveld Refinement of XRD Patterns

Samples with a consistent structure will generate characteristic XRD patterns. Analysis of these patterns can extract a wide range of information, but many factors affect the patterns. The Rietveld refinement method, a least-squares refinement procedure, was used in this thesis to calculate XRD patterns through the software Rietica 2.1 for Windows (Rietica).[250–253]

In order to calculate and fit XRD patterns, parameters such as the space group and approximate lattice parameters, atomic positions, and site occupations are required to begin refinement. Phases can be identified using software like Match!,[254] which was used in this thesis, that compares experimental patterns with those in diffraction pattern databases such as PDF-4+.[255] Approximate structural information can be found for identified phase(s).[256] The intensity of a diffraction peak is given by

$$I(2\theta) = I_0\, P(2\theta)\, L(2\theta)\, F^2(h,k,l)\, M(h,k,l)\, DW(h,k,l), \tag{3.2}$$

where I_0 is the intensity of the incident beam, P is the polarization factor, L is the Lorentz factor, F is the geometric structure factor, M is the multiplicity of the (h, k, l) planes, and DW is the Debye-Waller factor.[249]

The polarization factor accounts for the difference in X-ray scattering depending on electric field polarization. The polarization factor is defined as

$$P(2\theta) = \frac{1}{2}(1 + cos^2 2\theta\, cos^2 2\theta_m), \tag{3.3}$$

where θ_m is the angle between the monochromator and the diffracted beam. The Lorentz factor accounts for the random orientation of planes in the sample. Only a fraction of scattered X-rays will be detected, and the Lorentz factor takes the form of

$$L(2\theta) = (4\, sin^2\theta\, cos\theta)^{-1}. \tag{3.4}$$

The geometric structure factor is the sum of the scattering power of all the atoms to the particular (h, k, l) plane, and is given by

$$F(h,k,l) = \sum_1^N f_n\, e^{2\pi i\,(hx_n + ky_n + lz_n)}, \tag{3.5}$$

where f_n is the scattering factor for the atom n with the fractional atomic position (x_n, y_n, z_n). Atomic scattering factors can be found in literature or databases.[248,257] Atomic scattering factors vary depending on the atomic number, Z, since materials with more electrons will experience more interaction with the X-rays.

The multiplicity factor accounts for the number of (h,k,l) planes that will produce a diffracted peak at the same scattering angle.

The Debye-Waller factor accounts for the thermal vibrations of the atoms and is defined as

$$DW(h,k,l) = e^{-B\left(\frac{sin^2\theta}{\lambda}\right)^2}, \tag{3.6}$$

where $B = 8\pi^2u^2$, with u being the root mean square of the thermal displacement of an atom from its equilibrium position.[258] Thermal vibrations increase the effective size of atoms, which increases the probability of destructive interference.

When fitting XRD data, Rietica utilizes Eq. 3.2 as the basis of its calculations, along with a few other parameters such as peak shape, background, preferred orientation, and phase intensities (the functions treating those parameters are given in Chapter 2 of a Rietveld manual[253]). To begin XRD pattern fitting for synthesized samples, parameters for $LiNiO_2$ were used as a starting template. LNO is indexed based on a hexagonal α-$NaFeO_2$ structure with the $R\bar{3}m$ space group.[21,108–110,131] In the $R\bar{3}m$ space group, Li was assumed to occupy the 3a sites (Li layer) while the 3b sites (TM layer) contained Ni, Mn, Co, Al, Mg and/or Li (Section 8.2 only for Li) depending on the material. Oxygen was assumed to occupy the 6c sites. Li (3a) and O (6c) occupancies were assumed to be 1

and 2, respectively, while the TM occupancy was replaced by the TM ratios to sum up to 1.

Initial refinements of phase scale, then the background parameters, were performed before the lattice parameters were refined. The next sets of refinements were to check for cation mixing. The exchange of Ni and Li between 3a and 3b sites was allowed with the constraint of maintaining full occupancy in the Li and TM layers.

After refining for cation mixing, the sample displacement was the next parameter to be refined. Peak shape parameters were then refined carefully by varying parameters individually before collective refinement of the peak shape parameters. The asymmetry of the peak, the preferred orientation, and overall thermal parameters were then refined if necessary, with parameters reviewed to ensure validity (negative thermal parameters are unphysical, for example). The oxygen site position was the final parameter to be refined.

The lattice parameters and Ni content in the Li layer were the main information extracted from Rietveld refinements. The lattice parameters were then used to determine the unit cell volume of each sample. Errors reported for the lattice parameters were generated through Rietica, and the unit cell volume errors were calculated by propagating the lattice parameter errors. The Bragg R-factor (R_B) was used in this thesis to indicate how well the calculated pattern matched the experimental pattern, and is given by

$$R_B = \frac{\sum |I_{ko} - I_{kc}|}{\sum I_{ko}}, \tag{3.7}$$

where I_{ko} and I_{kc} are the observed and calculated integrated intensity of reflection k, respectively. Since the Bragg R-factor only takes the differences between calculated

integrated intensities and observed intensities into account,[118,259] the aim of minimizing R_B only served as a guide for pattern fitting, not a rule.

While it is known that Mg, when present in the material, can also migrate to the Li layer,[56–58,260] XRD refinement would only evaluate the electron density of the respective element so the refinement cannot actually distinguish whether Ni or Mg is the ion migrating to the Li layer. It is expected that the amount of Mg in Li layer would be ~2.3x more than the amount of Ni in Li layer when refining the same pattern due to Ni having ~2.3x more electrons. This has been confirmed for two of the synthesized samples in Chapter 4 (NM 95/5 and NCAM 84/9/3/4, see Table 4.1) and so only Ni in the Li layer will be reported in this thesis to maintain consistency with materials without Mg.

3.2.2 – XRD Data Collection

XRD patterns of synthesized materials were collected with a Bruker D8 diffractometer. The D8 uses Bragg-Brentano θ-θ pseudo-focusing geometry, which situates the X-ray source and detector at a fixed radius from the fixed sample.[261,262] The D8 can detect diffracted X-rays between scattering angles (2θ) of 0°-130°. Figure 3.2 shows the schematic, as well as a picture, of the D8 goniometer. The diffractometer produces X-rays using a copper source. An electron current of 30 mA is produced by thermionic heating of the tungsten cathode. The electrons are then accelerated at the copper target at 40 kV. Electrons in the inner shell (1s) of copper are ejected, and X-rays are emitted when allowed electron transitions from 2p (Cu-Kα, 1.5418 Å) or 3p (Cu-Kβ, 1.3922 Å) fill the 1s electron hole.[257] Exiting through the Be window of the source, the X-ray beam width is defined by the divergent slit before interacting with the sample.

Some of the diffracted beams then reach the scintillation detector after passing through the anti-scatter slit, receiving slit and monochromator. The slits and monochromator reduce noise by removing signals resulting from Cu-Kβ and fluorescence X-rays.[249]

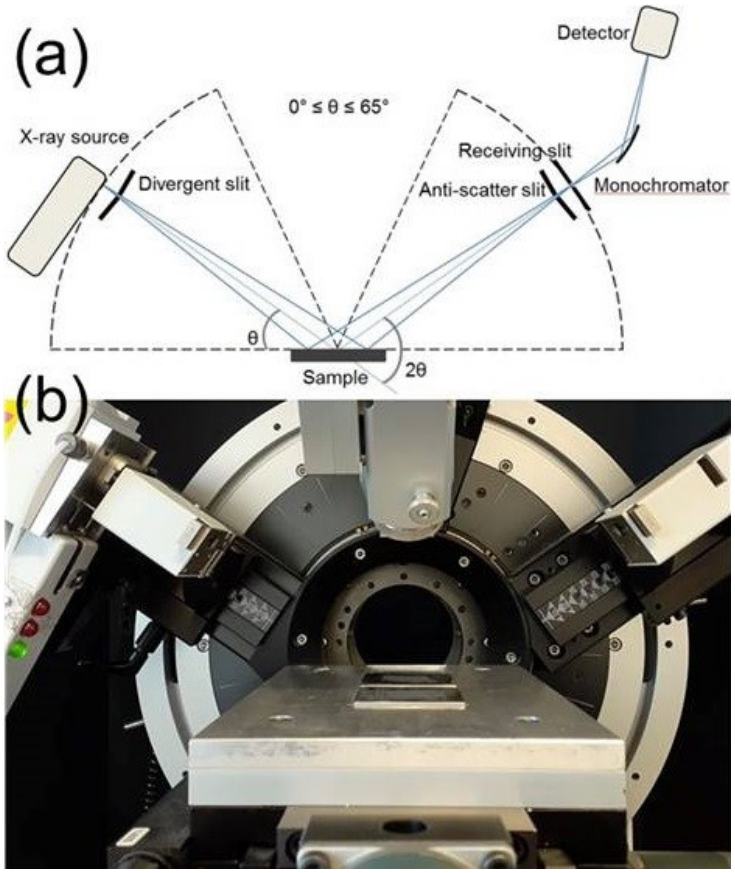

Figure 3.2: A schematic (a) and a picture (b) of the D8 Bragg-Brentano goniometer.

The scattering vector, which bisects the angle between the incident and diffracted beam, is always normal to the sample surface in the Bragg-Brentano geometry. This means that an orientation of a powder grain will only contain one family of planes that are properly aligned to produce diffraction peaks. Therefore, samples should be prepared to ensure that all orientations of powder grains are exposed to the X-ray beam over the range of scattering angles.

Synthesized samples were ground before XRD measurements. Powders were then packed into the well of a stainless steel sample holder and levelled so the sample was flush with the holder. The sample holder was then mounted onto the diffractometer. Samples were measured in the scattering angle (2θ) range of 15-70° for 3 s at intervals of 0.02° per step. A 1° divergent slit, a 1° anti-scatter slit, and a 0.2 mm receiving slit were used.

3.3 – Scanning Electron Microscopy (SEM)

SEM is a common technique used to image the surface topography and particle size of samples. SEM offers better resolution than optical microscopes and requires less intensive sample preparation than transmission electron microscopy, making it suitable to characterize the samples synthesized in this thesis.

SEM imaging of synthesized materials in this thesis was mainly carried out using a NanoScience Phenom G2 Pro Desktop SEM (Phenom Pro SEM). A Hitachi S-4700 SEM (Hitachi SEM, Department of Mechanical Engineering, Dalhousie University) was also sometimes used depending on equipment availability. In an evacuated chamber, the SEM probes the surface of the sample with a focused electron beam.[263,264] The focused electron beam is produced by thermionic heating of a CeB_6 electron source in the Phenom Pro SEM and accelerated at a fixed 5 kV. The Hitachi SEM uses a cold field emission gun and an acceleration voltage range of 0.5-30 kV to produce the electron beam. The electron beam, through a system of condenser lenses and scanning coils, is directed onto the sample and raster scanned across the surface.

The interaction between the electron beam and the sample produces various signals, including the scattering of electrons (both elastic and inelastic) and the emission of photons, which can be detected by specialized detectors. The Phenom Pro SEM uses a backscattered electron detector to detect elastically scattered electrons which are higher in energy (>50 eV). Compositional differences can be detected qualitatively since elements with a higher atomic number backscatter electrons more strongly. The backscattered electron detector lies above the sample in a doughnut shape, allowing the electron beam to shine through the center. The detector is separated into four quadrants, so it can image the topography and composition of the sample based on the signals produced from the different intensities and directions of backscattered electrons. The Hitachi SEM uses a secondary electron detector to detect inelastically scattered electrons which are lower in energy (<50 eV). Secondary electrons are generated from regions near the sample surface and the topographic properties of the sample, such as surface texture and roughness, can be observed.

To prepare powder samples for SEM imaging, samples have to be mounted on a sample stub rigidly so loose powder does not damage the instrument. Samples imaged by the Phenom Pro SEM were prepared by attaching an adhesive carbon tape to the top of the sample stub, then depositing a few milligrams of powder onto the tape. Samples imaged by the Hitachi SEM were prepared by dispensing a drop of conductive graphite paint onto the top of the sample stub, then adhering a similar amount of powder onto the graphite paint and air dried. The stubs were then thoroughly blown with compressed air to remove all loose powder before being placed into the SEM sample holder and imaged.

3.4 – Particle Size Analysis (PSA)

The measurements of the particle size distribution of materials were carried out in this thesis using laser diffraction.[264] The measurements are made by exposing the sample, consisting of dispersed particles, to a beam of light and detecting the angular patterns of light scattered by particles of different sizes. The light will be scattered at small angles relative to the beam of light when the particles are large, whereas the scattering angle will be larger for smaller particles. The scattered light produces angular patterns that are highly characteristic of the particle size, so a mathematical analysis of the scattering patterns can be used to calculate the size distribution of the sample.

PSA was conducted in this thesis using a Partica LA-950V2 laser diffraction particle size distribution analyzer (Horiba). Powders were added into deionized water and sonicated for 4 min before analysis, with samples generally being tested in triplicate. A refractive index value of Ni-rich materials in water of 1.81 (for NCA) was used although it may not be the true value of the materials tested in this thesis. However, PSA measurements were made on the same materials after various separation methods (Section 3.7.1) to compare the impacts of the various methods, so the particle size and degree of separation can be at least taken as quantitative in a relative sense even if the refractive index value used was incorrect.

3.5 – Residual Li Impurity Determination by the Pour Method then Acid-Base Titration

Acid-base titrations have been shown to be a suitable method to determine the amount of residual Li impurity on a Ni-rich sample.[131,172,174,175,177,181–184] LiOH and Li_2CO_3 have well-defined equivalence points and were used to quantitatively determine

the amount of residual Li by species.[131,174,175,177,183,184] However, the exchange of H^+ in solution for Li^+ in the material will occur when immersing samples in water for the duration of the titration.[172,174,175,182–184] This would cause the method to overestimate the amount of residual Li impurities actually present on the sample.

Recent work has reported a suitable solution to minimize the impact of ion exchange using the "pour method".[184] The pour method consists of vacuum filtering 40 mL of deaerated distilled water through about 0.1 g of positive electrode powder and collecting the filtrate for titration analysis. Water used in this characterization was deaerated by boiling to minimize the amount of dissolved CO_2 in solution. The pour method exposes the powder to water for about 5 s, which is enough to dissolve residual Li species but minimizes ion-exchange of Li for H.[182,184] A second pour of 40 mL of deaerated distilled water was performed on each sample to confirm the dissolution of most of the residual Li. Acid titrations of the 40 mL filtrate solutions extracted using the pour method were performed on a Mettler Toledo G20 compact titrator. The acid titration of the filtrate was carried out using 0.0520 M HCl (prepared with deaerated distilled water) as the titrant.

3.6 – Inductively Coupled Plasma – Optical Emission Spectrometry (ICP-OES)

Elemental analysis is a technique used to determine the elemental composition of samples. There are various elemental analysis methods, and ICP-OES measurements were carried out in this thesis using a Perkin Elmer Optima 8000 ICP-OES Spectrometer (Department of Dentistry, Dalhousie University). ICP-OES is a technique suitable for

detecting trace metals, and was used to determine metal atomic ratios of samples synthesized in this thesis.

In ICP-OES, samples are introduced into high temperature argon plasma, with temperatures exceeding 6000 K, which results in the samples ending up as excited atoms and ions.[263,265] The dissolved sample (sample preparation described below) is drawn up using an autosampler and transported into a nebulizer. The nebulizer converts the sample into a fine mist which is then introduced directly into the plasma. The argon plasma then proceeds to cause the sample to undergo a series of processes including desolvation, vaporization, and atomization. The atomized sample then undergoes excitation and/or ionization. The excited atoms and ions emit photons when relaxing to lower energy states, and these photons are emitted at wavelengths that are characteristic of the element. The emissions are then detected by charge coupled device (CCD) photodetectors and converted into electronic signals and processed by a program. By measuring the intensity of radiation of a specific wavelength being emitted, the concentration of an element can be determined with the use of calibration curves. The measured concentrations of elements of interest are then converted into a molar ratio to determine the sample composition.

Sample preparation was performed using Nanopure water (Barnstead Thermo Scientific 18.2 MΩ·cm) and ICP-dedicated glassware to minimize metal contamination for this highly sensitive technique. The standard solutions used to create the calibration curves were prepared from Li, Ni and Mn ICP-grade standards (1000 μg/mL in water with dilute nitric acid, Ultra Scientific). Standard solutions of 0, 0.5, and 1 μg/mL for Li and 0, 1, and 2 μg/mL for Ni and Mn were prepared. This was first done by pipetting 1

mL (Li) or 2 mL (Ni, Mn) of the standard into a 1000 mL volumetric flask and filling a 2% HNO_3 in Nanopure water solution up to the mark to produce the 1 μg/mL (Li) and 2 μg/mL (Ni, Mn) solution. Half of this solution was transferred to a 500 mL volumetric flask. The solution remaining in the 1000 mL flask was then diluted by a factor of 2 (by filling back up to the mark of the volumetric flask) to produce the 0.5 μg/mL and 1 μg/mL solution. The 0 μg/mL blank solution is the 2% HNO_3 solution.

ICP-OES was used to analyze synthesized samples as well as samples rinsed using the pour method described above in Section 3.5. The synthesized samples were used as is for sample preparation and are denoted as unrinsed samples, while the rinsed samples were obtained by air drying the residue from the pour method for less than 1 h. To ensure thorough digestion of the samples, they were dissolved in 2 mL of aqua regia (1:3 HNO_3:HCl (both reagent grade, Sigma Aldrich)) overnight. 8-10 mg of unrinsed samples was dissolved in aqua regia and 10-12 mg of rinsed samples was used to account for residual moisture. 10 μL aliquots of each dissolved sample were then pipetted into 15 mL polypropylene conical tubes (Falcon) and diluted to 12-14 mL with 2% HNO_3. The 3 solutions used to create the calibration curve (blank, 0.5/1 μg/mL, and 1/2 μg/mL) were poured into 50 mL tubes (Falcon) and a large plastic bottle of 2% HNO_3 was prepared as the wash for the ICP-OES measurements.

ICP-OES results (triplicate measurements with an uncertainty of ~2%) were provided in units of mg/L for each element, which were then converted to molarity to determine the metal atomic ratios reported in this thesis. ICP-OES results for lithiated samples were normalized to 2 for the atomic ratios to correspond with the formula unit $Li_xM_yO_2$ ($x + y = 2$, M = Ni, Mn).

3.7 – Fabrication of Coin Cells

3.7.1 – Separation of Single Crystalline Particle Aggregates

SC materials synthesized in this thesis remained aggregated in clusters, similar to a loosely held secondary structure. This may cause issues with connectivity to the individual particles in a cell leading to poor performance, so the aggregates should be separated. SC materials selected for electrochemical characterization underwent separation of the particle aggregates before electrode making and coin cell assembly. Two separation methods were tested and reported in this thesis to understand their ability to separate particle aggregates and the impact of separation on cell performance.

The first separation method utilized a coffee grinder (Black & Decker SmartGrind™) and will be denoted as coffee grinder. The materials were placed inside the coffee grinder and ground for 30 s. The coffee grinder was stopped, and the inner surfaces scraped to reduce caking before grinding again, for a total of 6 x 30 s.

The second method tested utilized a dual-motion planetary mixer (KK-250 S Mazerustar, Kurabo) and will be denoted by the milling medium. The materials were placed in a jar along with either 2 hardened stainless steel balls (6 mm diameter, denoted as 2M balls) or 20 smaller balls (3 mm diameter, denoted as 20S balls) and mixed in the planetary mixer for 100 s. Both milling media were used at a ~3:1 ball:material mass ratio. The jar was then taken out and given a shake to reduce caking before mixing again, for a total of 3 x 100 s.

For chapters studying SC material synthesis, not all characterization methods used SC materials after separation. PSA samples were always separated by 20S balls before characterization. SEM and XRD samples were usually not separated but sometimes were.

3.7.2 – Electrode Preparation

The work of Marks *et al.* helped guide the procedure used in this thesis for electrode preparation.[266] Positive electrodes were prepared by combining the synthesized $LiNi_{1-x}M_xO_2$ (M = Al, Mg, Mn and/or Co), Super-S carbon black (Timcal), and polyvinylidene fluoride (PVDF, Arkema, Kynar 301F) in a ratio of 92:4:4 by weight in a polycarbonate container with 2 zirconia milling beads. A total powder mass of 0.75 g was generally prepared. For 0.75 g of powder, around 0.6 g of N-methyl-2-pyrrolidone (NMP, Sigma-Aldrich, 99.5%) was added into the container to form a slurry, with the exact amount of NMP adjusted based on the viscosity of the slurry. The container was then placed in a planetary mixer and mixed in 3 cycles of 100 s each. If the consistency of the mixed slurry was unsatisfactory, appropriate amounts of NMP were added and mixed for another cycle of 100 s.

A sheet of Al foil (approximately 16 cm x 6 cm, 16 μm thick) was placed on a glass plate and smoothed over using ethanol. The slurry was then coated onto Al foil using a 152 μm notch bar to produce an even coating approximately 4.5 cm wide.[266] The coated foil was then placed in an oven and dried for 1-3 h at 110°C. The dried electrode was then pressed at ~2000 atm with a roller press and punched into discs with a diameter of 1.275 cm. Electrode loadings spanned 7.5-13 mg/cm^2 but were generally around 9-11

mg/cm^2 and electrode densities were generally around 2.2-2.9 g/cm^3, but the thickness of the electrodes was not always measured.

Positive electrode discs were weighed on a microbalance, along with punched discs of the same size of the Al foil. From these masses, along with the masses recorded of the lithiated material, carbon black, and PVDF, the mass of the active component of each electrode disc can be calculated. The electrodes were dried overnight in the evacuated antechamber of an argon filled glovebox (Innovative Technologies) at 110°C then transferred into the glovebox.

3.7.3 – Coin Cell Assembly

Coin cells were fabricated inside the glove box to minimize degradation of the lithium metal negative electrode and the electrolyte. Figure 3.3 shows a diagram and a picture of the coin cell components. The electrolyte used in Chapter 4 contained 1 M $LiPF_6$ (BASF, 99.9%) in a mixture of 1:2 (v/v) ethylene carbonate (EC) and diethyl carbonate (DEC) (BASF, 99.99%). The electrolyte used in Chapters 5 to 7 contained 1 M $LiPF_6$ in a mixture of 1:4 (v/v) fluoroethylene carbonate (FEC, BASF) and dimethyl carbonate (DMC, BASF). Long term cycling of half cell coin cells was found to improve when using the FEC:DMC (1:4 v/v) electrolyte so it was used in later chapters.[155]

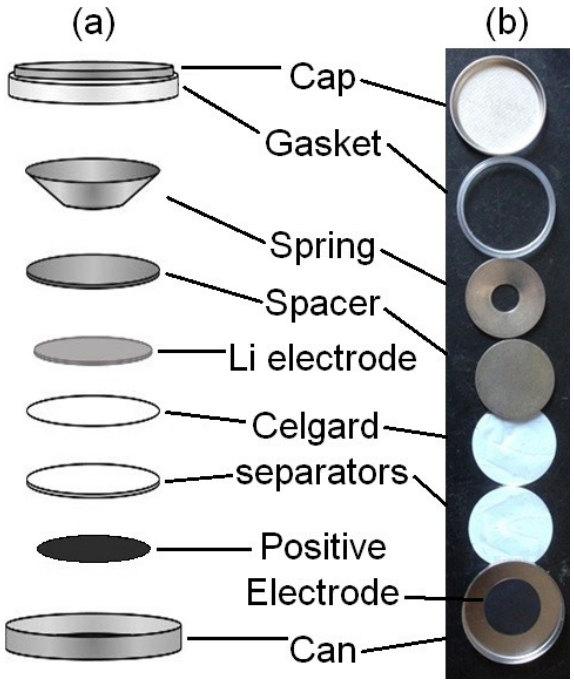

Figure 3.3: A diagram (a) and a picture (b) of the components inside a coin cell. The picture does not show the lithium metal negative electrode, which would be in between the Celgard separator and the spacer.

The positive electrode disc was placed in the stainless steel can before wetting with 5-6 drops (~20 μL per drop) of electrolyte. A Celgard 2300 thin film polypropylene separator (Celgard) was placed on top of the electrode disc and 2-3 drops of electrolyte were added. Next, another Celgard separator was placed on the wet separator and another 1-2 drops of electrolyte were added. A 1.4 cm diameter disc was punched from a 150 μm thick Li metal foil (Chemetall, >99.99%) and placed on the separators, followed by a stainless steel spacer then a stainless steel spring. Care was taken to keep components centered and to avoid contact between the Li foil, spacer and spring with the side of the can to avoid shorting the cell. The stainless steel cap and polypropylene gasket were placed on the spring, making sure the gasket kept the top components from contacting the side of the can. The assembled cell was then sealed with a pneumatic

press, crimping the can edge onto the gasket. The assembled coin cell was then removed from the glovebox.

3.8 – Electrochemical Characterization

Electrochemical characterization is a useful technique in evaluating the performance of a material in an electrochemical cell. Coin cells in Chapter 4 had stainless steel tabs (approximately 2 cm x 0.5 cm) spot welded onto the top and bottom of the cell and the cells were connected to plastic "boats" before connection to a battery charger, which ensures a consistent and stable connection during measurements. Coin cells in Chapters 5 to 7 were connected to clip holders that avoid the need to spot weld tabs onto the coin cells. The majority of electrochemical testing was performed using an E-One Moli Energy Limited Canada (Moli) battery testing system in temperature controlled boxes maintained at 30 ± 0.1°C, while some testing occurred in temperature controlled boxes maintained at 55 ± 0.1°C.

Cells were charged and discharged using a constant current, also known as galvanostatic cycling. The lower and upper voltage cutoffs, as well as the magnitude of the current, can be programmed in the testing protocol. The current rates were chosen by determining the theoretical capacity of the positive electrodes, calculated by multiplying the mass of the active component of each positive electrode disc with the theoretical capacity of the material (Eq. 1.5). However, the theoretical capacity of the material changes based on the cutoff voltages since the material is not being fully delithiated in this thesis. Current rates in this thesis will be stated as a specific capacity (mAh/g) and/or as a C-rate (C/*n*, where *n* is equal to the time, in hours, needed to fully charge or

discharge based on the expected capacity of the first charge). Due to the nature of coin cell fabrication, sets of 2-3 coin cells were cycled for each condition to help ensure reliability of the data collected.

In typical electrochemical testing in this thesis, cells were cycled between 3.0 V and 4.3 V (all voltages reported vs Li/Li^+). The expected capacity of all the materials in this thesis was set to be 200 mAh/g for convenience. A current density of 10 mA/g (~C/20) was used for the first 2 cycles to carefully examine the features of the initial cycles. A current density of 40 mA/g (~C/5) was used for subsequent cycles to evaluate long term cycling performance of the materials. Some materials had more than 200 mAh/g while others had less, so the effective current rate used was slightly different than stated. A total of 54 cycles (50 cycles at C/5 with 2 C/20 cycles before and after) were programmed for each cell, though not all cells were tested using the full protocol. Testing procedures were still being standardized in Chapter 4 so there were some variations in terms of number of C/20 and C/5 cycles. Some electrochemical testing was performed in slightly different conditions, such as at a different temperature or voltage cutoff, and these will be noted in their respective chapters.

The Moli battery charger regularly records the voltage (V), current and time at set time or voltage intervals. Capacity (Q) is calculated by multiplying the current by the time taken to charge/discharge. From these measurements and active component masses, cycling data such as charge capacity, discharge capacity, and 1st cycle irreversible capacity can be determined and plots such as voltage curves (V vs. Q), differential capacity plots (dQ/dV vs. V), and cycling performance plots (discharge capacity (or normalized to the 1st C/5 cycle) vs. cycle number) generated.

Chapter 4 – Investigating the Effects of Mg Substitution in Various Ni-rich Positive Electrode Materials for Lithium Ion Batteries

As discussed in Section 2.3, one popular approach to mitigating issues with LNO has been to substitute some portion of the Ni with other metals, resulting in the development and commercialization of NMC and NCA. Besides Al, Co and Mn in NMC and NCA, substitutions of Ni by many other metals have been tried. Mg has repeatedly come up as a beneficial substituent from positive electrode material doping studies that try to improve material cycling performances. Mg has been shown to improve cycling performances of various positive electrode materials including LCO,[36,151,152,186–189] NMC,[190–192], NCA[63,193,194] and other Ni-rich materials[21,195–197] when doped into the material in small amounts.

The functions of Al, Co and Mg substitutions for Ni have been investigated and discussed at length, which were reviewed in Section 2.3.1. Co is the only electrochemically active substituent of the three, participating with the Co^{3+}/Co^{4+} redox couple and maintaining the high specific capacity of the material. With electrochemically inactive substituents, the specific capacity of the material is reduced. Mg and Al generally exist in the material with an oxidation state of +2 and +3, respectively, so the same fraction of Mg reduces the capacity of the material more than Al due to Mg^{2+} necessitating a Ni^{4+} to compensate and keep charges balanced.[21] Recent work studying the impact of 5% and 10% doping of Al, Mg, Mn or Co in LNO have questioned the necessity of having Co in the material, showing that Ni migration to Li

layers and capacity fading can also be reduced with Al and Mg doping, and that phase transitions and thermal instability can be suppressed with Al and Mg doping.[21,24]

Aims to improve energy density and reduce costs of NCA can be achieved by increasing the Ni content of the material, but at the cost of shorter cell lifetimes and decreased safety. As research continues to increase the Ni content of NCA, the composition will head towards LNO. Additionally, Co is believed by some to reduce the amount of Ni in the Li layer and also to stabilize cycling performance, which are similar benefits that Mg imparts. This chapter studies the effect of Mg substitution in $LiMO_2$ (M = Ni, Ni+Al, Ni+Co+Al, Ni content > 0.8) at a Mg content of less than 5%. The synthesized materials were characterized to understand how Mg affects the materials and whether the presence of Al or Co influences the effects of Mg. The results in this chapter were incorporated into a manuscript published in the Journal of the Electrochemical Society.[149]

4.1 – Experimental Design

Samples were synthesized using metal hydroxide precursors obtained from Zoomwe. All hydroxide precursors used in this chapter have similar particle sizes (D50 ~18 μm). Table 4.1 lists the samples synthesized in this chapter. These samples were a part of one of four composition series, denoted as NM (LNO with Mg substitution), NAM ($LiNi_{0.95}Al_{0.05}O_2$ with Mg substitution), NCAM 90/5/5 and NCAM 88/9/3 (NCA with Mg substitution, with the base material having the specified Ni:Co:Al ratio). The non-Li metal molar compositions are shown in Table 4.1, and samples will be identified by their composition series (just NCAM for both NCAM series) and composition. For

example, NCAM 84/9/3/4 is part of the NCAM 88/9/3 series and has a non-Li metal molar ratio of 84 Ni: 9 Co: 3 Al: 4 Mg. The synthesis procedure was carried out as described in Section 3.1. The precursor materials were mixed with $LiOH{\bullet}H_2O$ in a Li/TM (transition metal or other metal filling the transition metal role) ratio of 1.02 and heated (including preheat steps) with the final heating step as specified in Table 4.1.

Table 4.1: The synthesized samples, their compositions and the final heating step used for the synthesis.

		Composition (%)				**Final heating step**	
Series	**Sample**	**Ni**	**Co**	**Al**	**Mg**	**Temp. (°C)**	**Time (h)**
NM	100/0	100				700	20
	99/1	99			1		
	97.5/2.5	97.5			2.5		
	95/5	95			5		
NAM	95/5/0	95		5		700	20
	94/5/1	94		5	1		
	94/4/2	94		4	2		
NCAM 90/5/5	90/5/5/0	90	5	5		725	20
	90/5/4/1	90	5	4	1		
	89/5/4/2	89	5	4	2		
NCAM 88/9/3	88/9/3/0	88	9	3		735	12
	87/9/3/1	87	9	3	1		
	86/9/3/2	86	9	3	2		
	84/9/3/4	84	9	3	4		

XRD and SEM characterizations were carried out as described in Sections 3.2 and 3.3, respectively. Coin cells were assembled as described in Section 3.7 with 1.0 M $LiPF_6$ in EC:DEC (1:2 v/v) as the electrolyte. Electrochemical testing was carried out as

described in Section 3.8 with the exception of a few samples (NM 100/0 and the NCAM 88/9/3 series) having a slightly different number of slow C/20 cycles before and after 20 C/5 cycles. N. Zhang conducted the material synthesis and characterization of NM 100/0 and NAM 95/0. J. Inglis conducted the electrochemical characterization of some samples in the NAM and NCAM series.

4.2 – Results and Discussions

4.2.1 – Material Characterization

Figure 4.1 shows the SEM images of the samples in the NCAM 90/5/5 series (Figs. 4.1a-4.1c) and the NCAM 88/9/3 series (Figs. 4.1d-4.1g). Figs. 4.1a1-4.1c1 and 4.1d-4.1g show that the spherical secondary particles have similar sizes. Figs. 4.1a2-4.1c2 show that the primary particles do not change significantly with higher Mg content. The lithiated samples all have similar particle sizes and morphology due to consistent precursor syntheses from Zoomwe. Increasing Mg content did not significantly impact the particle size or morphology of the synthesized materials.

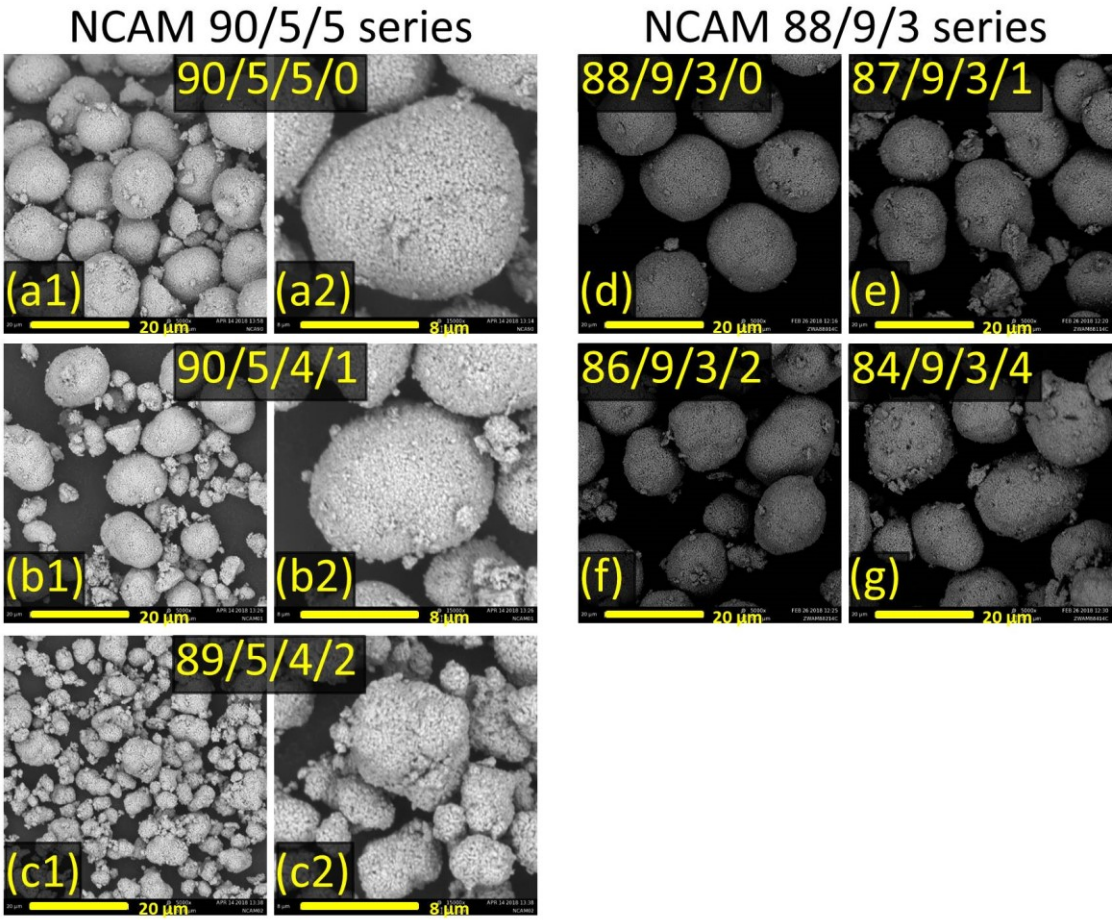

Figure 4.1: SEM images of samples in the NCAM 90/5/5 series (a-c) and the NCAM 88/9/3 series (d-g).

Figure 4.2 shows the XRD patterns of the synthesized materials. An expanded view of the (003) and the (104) reflections is shown in the middle left panels (Figs. 4.2a2-4.2d2), an expanded view of the impurity region is shown in the middle right panels (Figs. 4.2a3-4.2d3) and an expanded view of the region where the strongest MgO reflection would appear is shown in the right panels (Figs. 4.2a4-4.2d4). All materials synthesized were single phase materials. Mg substitution had no significant impact on the patterns although some minor shifts can be seen in the expanded view of the (003) and (104) reflections (Figs. 4.2a2-4.2d2). The reflections shifted to slightly lower angles

with more Mg substitution, indicative of slightly larger unit cells. The expanded view of the impurity region (Figs. 4.2a3-4.2d3) shows that all the synthesized materials did not have an observable (by XRD) amount of surface impurities.[110,131,157,172–182] Figs. 4.2a4-4.2d4 show no observable MgO peaks, indicating that the Mg remained in the materials and did not separate out as MgO.

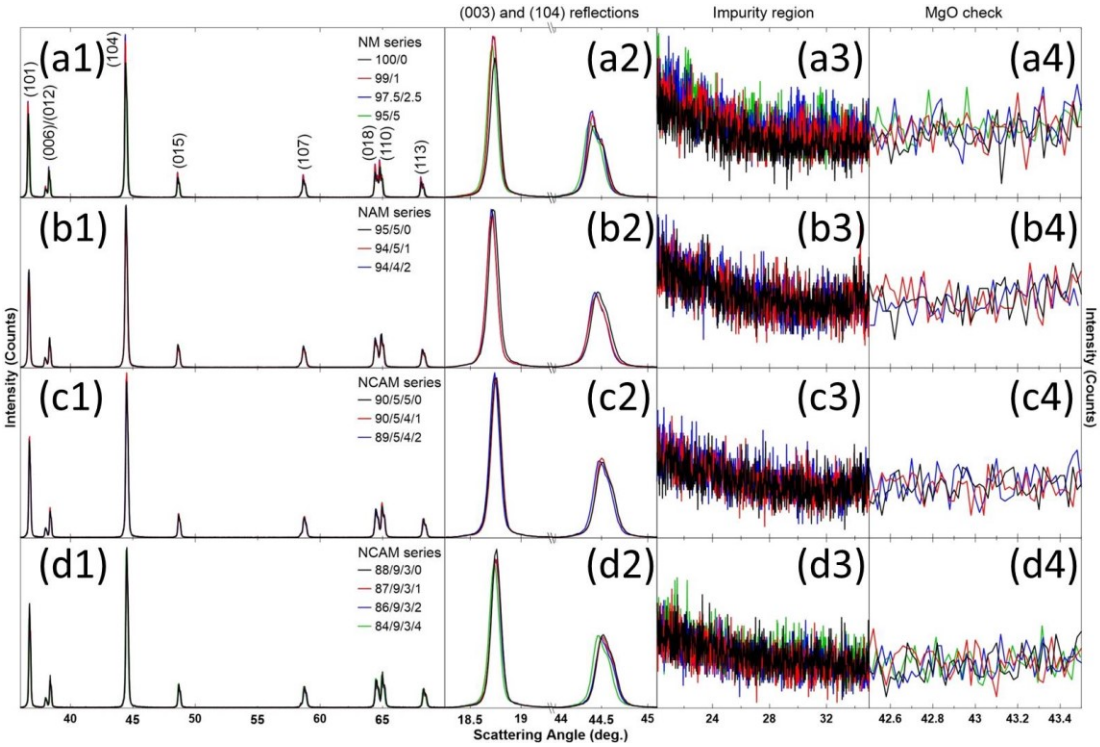

Figure 4.2: XRD patterns (Cu K_α radiation) of samples in the NM, NAM, NCAM 90/5/5 and NCAM 88/9/3 series collected from 35°-70° (a1-d1) along with the expanded views of the (003) reflection (a2-d2), the (104) reflection (a2-d2), the Li impurity region (a3-d3) and the MgO region (a4-d4).

Figure 4.3 shows the Rietveld refinement results for the XRD patterns. The left panels (Figs. 4.3a-4.3b) show the *a* and *c* lattice parameters obtained from the refinements, while the right panels (Figs. 4.3c-4.3d) show the calculated unit cell volume and the amount of Ni in the Li layer. Generally, the unit cell (Fig. 4.3c) increases in

volume as Mg substitution increases, and the increases do not seem to be influenced by the presence of Co or Al. This is reasonable due to the average sizes of the ions involved (radius of Mg^{2+}, $r_{Mg^{2+}} = 0.72$ Å; $r_{Ni^{4+}} = 0.48$ Å; $r_{Ni^{3+}} = 0.56$ Å)[106] and this has been seen in past literature reports.[21,56–58,151,193,194]

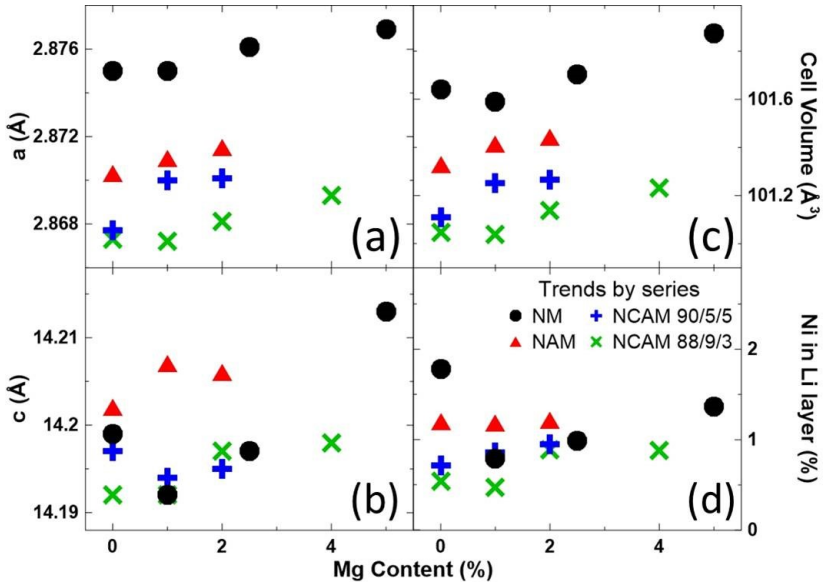

Figure 4.3: Unit cell lattice constants (a,b), the calculated unit cell volume (c) and amount of Ni in the Li layers (d) as a function of Mg content for the NM, NAM, NCAM 90/5/5 and NCAM 88/9/3 series.

Figure 4.3d shows the amount of Ni in the Li layer. Most of the materials synthesized had around 1% Ni in the Li layer or less. Clearly, materials without Co can still achieve low amounts of Ni migration into the Li layer. This goes against the conventional understanding that the presence of Co is needed to reduce the amount of Ni migration into the Li layer[14,15,37,50,59,61] and supports recent work that Co is not required to make decent Ni-rich materials.[21,27] While XRD and Rietveld refinement cannot distinguish between Ni or Mg in the Li layer, the trends seen in Fig. 4.3d seem to agree more with Ni being in the Li layer than Mg, given that the data show no real trend with

regards to Mg content and that LNO made using the same procedure has ~2% Ni in the Li layer or less (Fig. 3d and refs. 21,110,148).

4.2.2 – Initial Cycles of Coin Cell Testing

Figure 4.4 shows the voltage versus specific capacity (V vs. Q, Figs. 4.4a-4.4d) and the differential capacity versus voltage (dQ/dV vs. V, Figs. 4.4e-4.4h) for the synthesized materials as sorted by composition series. Solid and dashed lines represent two duplicate cells. The V vs. Q curves (Figs. 4.4a-4.4d) show that materials with more Mg content achieve less capacity and have higher irreversible capacities. Materials in the composition series containing more Co and Al show more smoothed features in the dQ/dV vs. V curves (Figs. 4.4f-4.4h) due to more suppression of the phase transitions observed in LNO.[21,108–110] For each composition series, the increase in Mg content further smooths the features in the dQ/dV vs. V curves (Figs. 4.4e-4.4h). Significant changes in the dQ/dV vs. V curves due to Mg substitution were observed around 4.2 V for all sample series, ~3.5-3.7 V and ~4 V for the NM series (Fig. 4.4e) and not observed for V < 4.1 V for the NAM and NCAM series (Figs. 4.4f-4.4h).

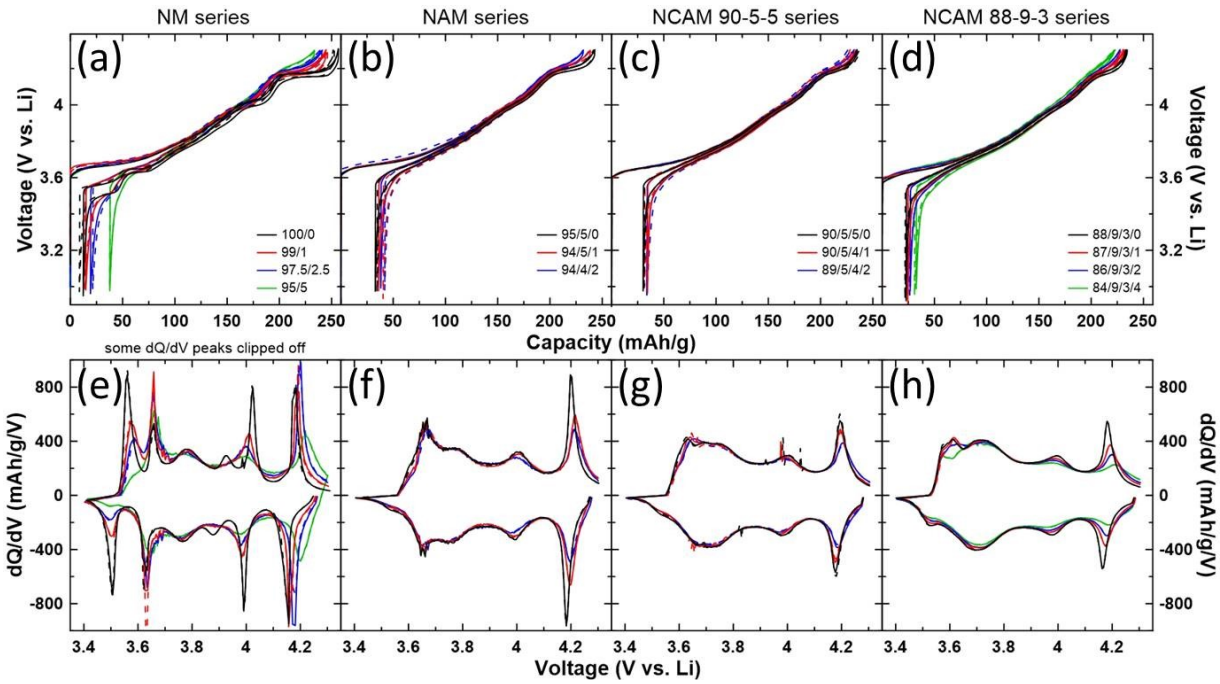

Figure 4.4: Cell voltage as a function of capacity (a-d) and differential capacity as a function of cell voltage (e-h) for the samples in the NM, NAM, NCAM 90/5/5 and NCAM 88/9/3 series.

Figure 4.5 shows the 1st cycle capacity data for the synthesized materials. The data is plotted as a function of Mg content on the left panels (Figs. 4.5a1-4.5c1) and as a function of Al + 2*Mg content on the right panels (Figs. 4.5a2-4.5c2). As noted earlier, increases in the Mg content of the material decrease the charge and discharge capacity as well as the irreversible capacity. This is due to Mg being an electrochemically inactive ion which reduces the amount of available capacity by replacing electrochemically active Ni ions. The impact of Mg content on the capacities of the materials is consistent across composition series and is unaffected by the presence of Co or Al.

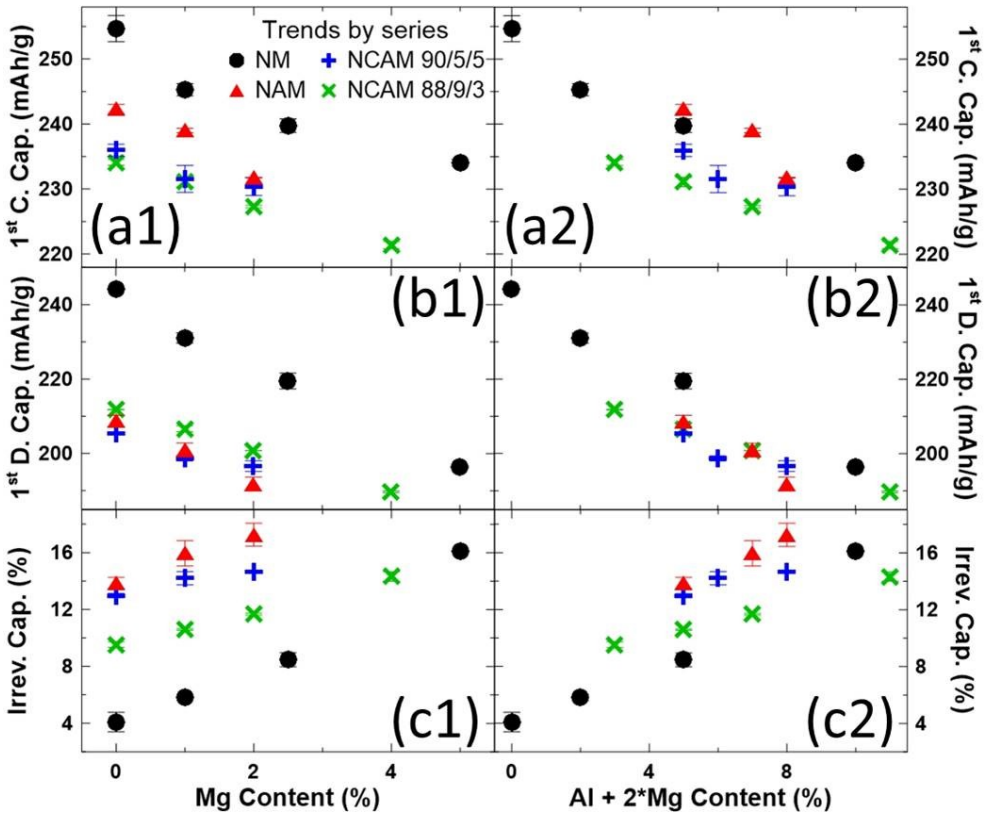

Figure 4.5: First cycle capacities as a function of Mg content (a1-c1) and as a function of Al + 2*Mg content (a2-c2) for the NM, NAM, NCAM 90/5/5 and NCAM 88/9/3 series.

Since Mg is not the only electrochemically inactive ion in the materials, Figs. 4.5a2-4.5c2 account for Al content as well. Al "locks in" one Li ion while Mg "locks in" two Li ions due to the formation of Ni^{4+}.[21] When the capacities are plotted against Al + 2*Mg content in Figs. 4.5a2-4.5c2, all the samples fall along the same linear trend. This indicates that the capacity reductions of all the samples are due to Al and Mg content, with Mg having twice the effect of Al in reducing capacity

4.2.3 – Long Term Coin Cell Testing

Figure 4.6 shows the specific capacity versus cycle number for the synthesized materials as sorted by composition series. Cells were cycled at currents corresponding to

C/5, with several cycles before and after using currents corresponding to C/20. LNO (NM 100/0, Fig. 4.6a) and samples in the NCAM 88/9/3 series (Fig. 4.6d) were cycled 20 times at C/5. It was noted that differences between capacity retention would be easier to discern for more cycles so the rest of the samples were cycled 50 times at C/5. For every series in Fig. 4.6, the sample with no Mg content retained the least capacity during cycling. Samples with higher Mg content started with less capacity but were able to retain the capacity better. This supports previous work that materials with a higher capacity had worse capacity retention during cycling.[14,15,17,22,26,27,42,49,157,216]

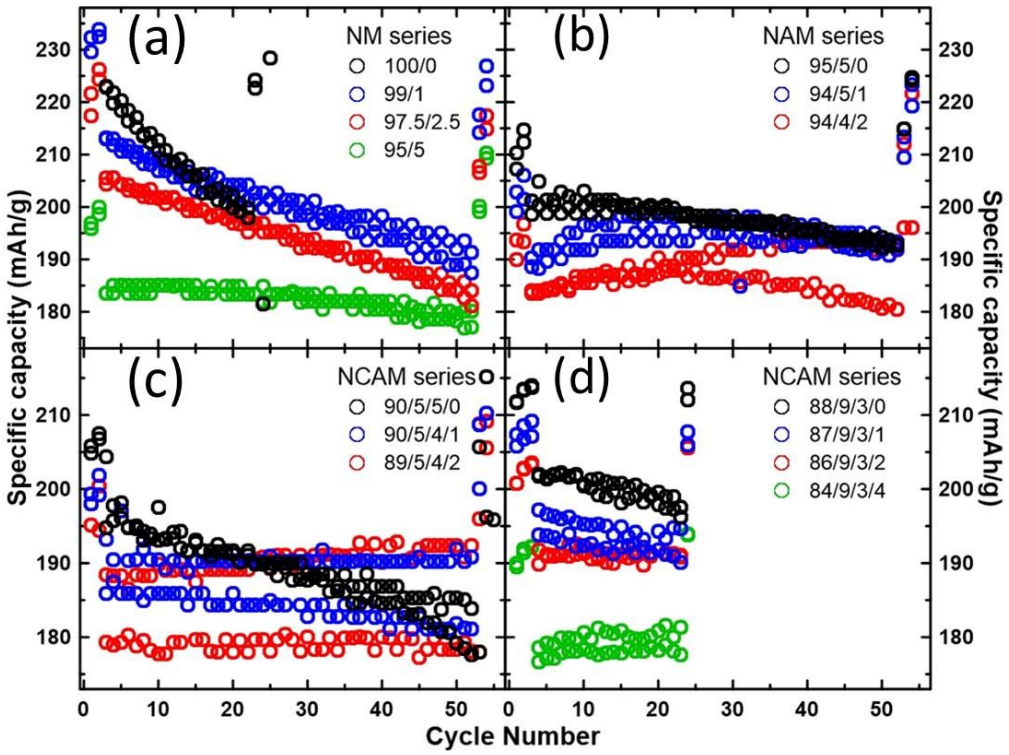

Figure 4.6: Specific capacity as a function of cycle number for the samples in the NM, NAM, NCAM 90/5/5 and NCAM 88/9/3 series.

One interesting phenomenon seen in Fig. 4.6 is that some of the cells had more capacity after several cycles than at the first C/5 cycle. The NAM 94/4/2 sample (Fig.

4.6b) in particular saw one cell increase in capacity for almost the entirety of its cycling. Capacity increases over a few cycles are not uncommon[14,17,21,124,157,161,178,230,267–270] and have been attributed to cracking of the particles.[161] However, capacity increases over so many cycles occurs much more infrequently and it is uncertain if that can also be attributed to particle cracking.[178] These increases in capacity are seen exclusively in half cells, which is reasonable as the Li metal electrode provides an excess of Li to keep intercalating back into the positive electrode. Work on full cell data would be useful to see if capacity simply stays near 100% or if it would drop more quickly, perhaps due to loss of Li to increased SEI formation if particle cracking produces fresh surfaces.

Figure 4.7 shows the capacity retention as a function of substituent content for the synthesized materials. The top row (Figs. 4.7a1-4.7a3) show the capacity retention after 20 C/5 cycles, while the bottom row (Figs. 4.7b1-4.7b3) show the capacity retention after 50 C/5 cycles. Similar to Fig. 4.4, the left column (Figs. 4.7a1-4.7b1) are plotted as a function of Mg content and the right column (Figs. 4.7a3-4.7b3) are plotted as a function of Al + 2*Mg content. Additionally, the middle column (Figs. 4.7a2-4.7b2) are plotted as a function of Al + Mg content to see how capacity retention varies as a function of Ni ions substituted by an electrochemically inactive substituent. The bottom panel (Fig. 4.7c) shows the capacity retention as a function of x in $Li_{1-x}MO_2$, similar to "unavoidable challenge" graphs (Figs. 2.5c and 2.5d).[42,157]

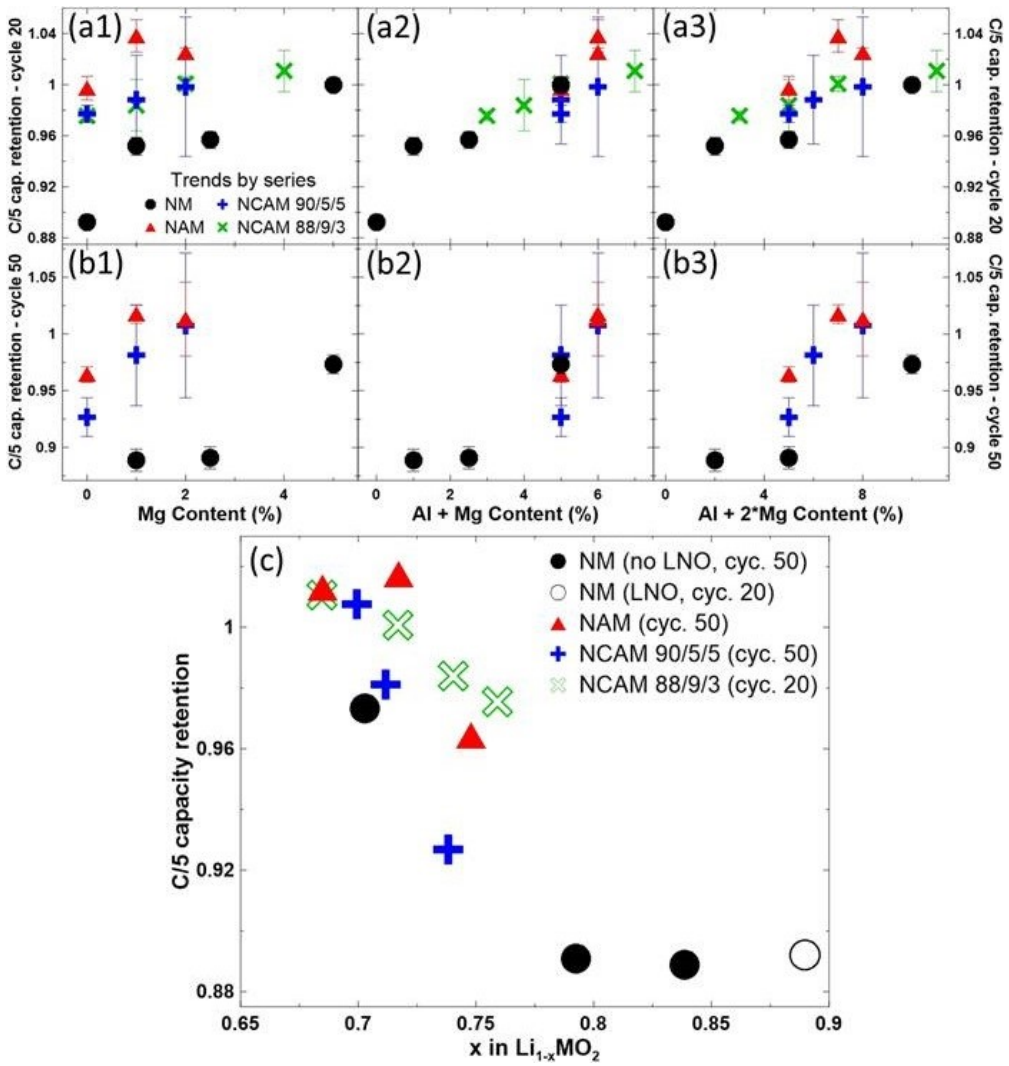

Figure 4.7: C/5 capacity retention at cycle 20 (a1-a3) and cycle 50 (b1-b3) as a function of Mg content (a1-b1), as a function of Al + Mg content (a2-b2) and as a function of Al + 2*Mg content (a3-b3) for the NM, NAM, NCAM 90/5/5 and NCAM 88/9/3 series. Capacity retention as a function of x in $Li_{1-x}MO_2$ (c) for the samples.

Capacity retention increased for every series when increasing substituent content. Capacity retentions at 50 cycles (Figs. 4.7a1-4.7a3) were lower than at 20 cycles (Figs. 4.7b1-4.7b3), but the trend remains. As noted previously, some of the prolonged capacity increases lead to capacity retentions of over 100% after 20 or 50 cycles for some samples with low initial capacity. While the increases were most observable for the NAM series

(Fig. 4.6b), several samples in other composition series also reached over 100% capacity retention.

When capacity retention was plotted against Al + Mg content (Figs. 4.7a-4.7b2) or Al + 2*Mg content (Figs. 4.7a-4.7b3), the samples fall approximately along a linear trend. Samples seemed to more closely follow the linear trend when plotted against Al + Mg content, but this is not overly conclusive. This suggests that amount of Ni ions substituted by an electrochemically inactive substituent may factor more for capacity retention than the amount of "locked in" Li ions. This may have to do with volume change and suppression of phase transitions as it has been shown that LNO doped with 5% Mg and LNO doped with 5% Al both experience very similar volume changes when charged to the same Li content.[21] In fact, cells with NM 95/5 and NAM 95/5/0 have almost the same capacity retention.

While the capacity retention increased for every series when increasing substituent content, it should be noted that increasing the substituent content also decreased the initial capacity (Fig. 4.5). This is very reminiscent of the "unavoidable challenge" behaviour discussed in Section 2.3.4, so a plot akin to the "unavoidable challenge" graphs[42,157] (Figs. 2.5c and 2.5d) was made. Fig. 4.7c shows the capacity retention as a function of the degree of delithiation (1st discharge). Fig. 4.7c clearly shows that the capacity retention decreases as the capacity increases. However, unlike Figs. 2.5c and 2.5d, the decrease in capacity retention occurs at a lower degree of delithiation of ~0.7. This is likely due to the electrolyte used in this chapter (EC:DEC 1:2), which has been found to be worse for cycling performance than FEC:DMC 1:4.[155,157] In fact, the data of some samples of the NM series tested using FEC:DMC 1:4

was included in that study and the samples had improved capacity retention and fit the trend well.[157]

The implication of Fig. 4.7 is that there are at least two options to reach a target lifetime by metal substitution. Considering only the choice between Mg or Al as the substituent, Mg as a substituent will reduce the specific capacity of the material at twice the rate of Al due to the formation of Ni^{4+} to balance the charges. However, substituting the material with Al has difficulties associated with the precursor synthesis from continuous nucleation of $Al(OH)_3$ and/or LDH formation to balance Al^{3+} in the hydroxide material.[119–125,127,271,272] These synthesis difficulties may result in suboptimal particles or more complex processing, which would be avoided if Mg substitution was utilized instead of Al.

Figure 4.8 shows the dQ/dV vs. V curves for the 1st, 20th and 50th C/5 cycle for each of the synthesized materials. Solid and dashed lines represent two duplicate cells. Some dQ/dV peaks were clipped off for some samples in the NM series (Figs. 4.8a1-4.8a3) to maintain a consistent scale that can see features in all the samples. As noted in Fig. 4.4, features in the dQ/dV vs. V curves become more smooth as the composition series become more substituted (moving to the right) and as Mg content increases (moving down).

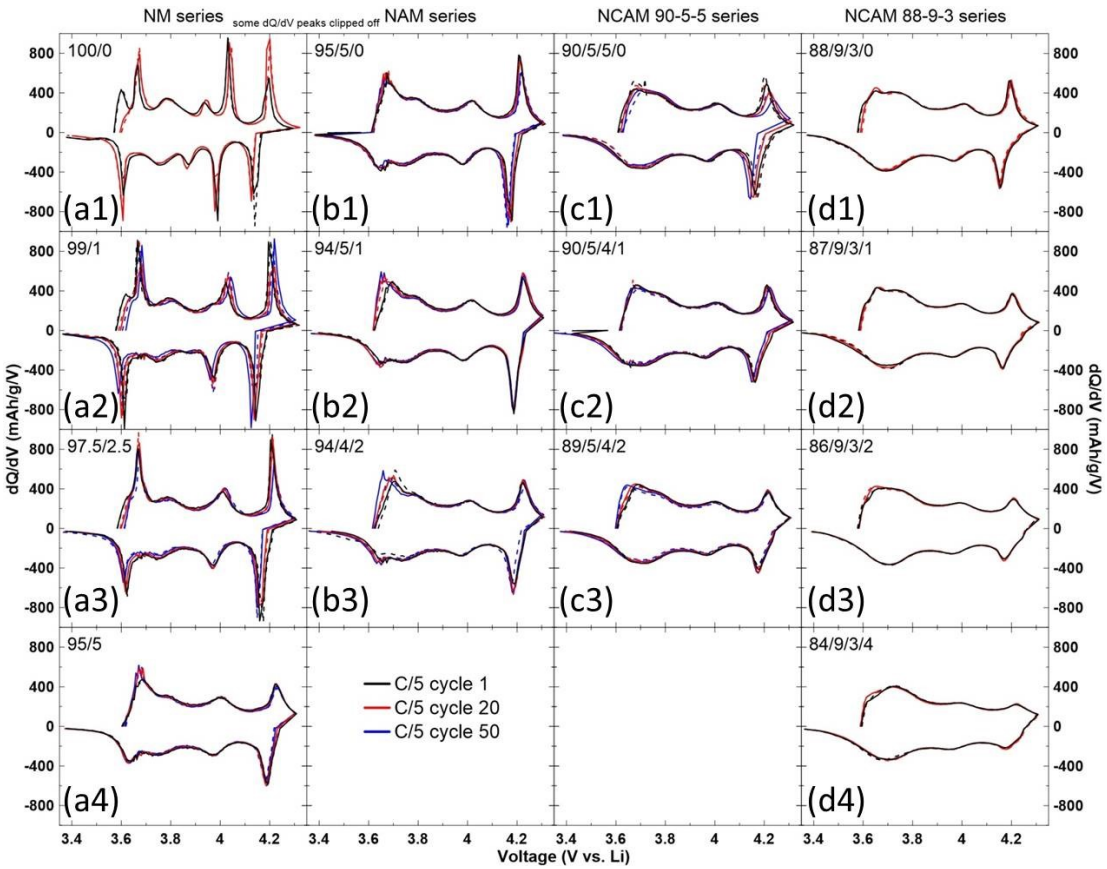

Figure 4.8: Differential capacity as a function of cell voltage at cycles 0, 20 and 50 for the samples in the NM, NAM, NCAM 90/5/5 and NCAM 88/9/3 series.

Figure 4.8 shows that Mg substitution can increase capacity retention of materials by reducing the polarization growth of the material during cycling. This can be most easily observed in the NCAM 90/5/5 series (Figs. 4.8c1-4.8c3) or by comparing NM 95/5 (Fig. 4.8a4) with another sample in the NM series (Figs. 4.8a1-4.8a3). NCAM 90/5/5/0 experiences significant polarization growth, mainly at high V, and the polarization growth is reduced for NCAM 90/5/4/1 and reduced even further for NCAM 89/5/4/2, but so is the reversible capacity. It is hard to see the reduction of the polarization growth when going from NM 100/0 to NM 99/1 and NM 97.5/2.5 but the growth of polarization is dramatically reduced in NM 95/5. Perhaps the NM series, other than NM 95/5, still

undergo the H2-H3 phase transition and thus experience similar volume changes and resulting polarization growth.[21,108–110] On the other hand, the NCAM 90/5/5 series have suppressed the phase transitions, so increasing amounts of Mg decrease the capacity and the volume change of the continuous *c*-axis contraction.[21]

For the cells that experience capacity increases during cycling in Fig. 4.6, their dQ/dV vs. V curves in Fig. 4.8 show an enlarged peak around 3.6-3.7 V. The growth of the peak is more easily observed in the positive (charge) portion of the dQ/dV vs. V curves. The NAM 94/4/2 cell (Fig. 4.8b3) that increases its capacity over most of its cycling also shows an enlarged peak, indicating that its mechanism of capacity increase does not differ from other cells that increase capacity over a few cycles. Each composition series has at least one sample that experienced this phenomenon, although it is most pronounced in the NAM series (Figs. 4.8b2-4.8b3). More work is needed to better understand this phenomenon of capacity increase and why it occurs around 3.6-3.7 V.

4.3 – Conclusions

This chapter studied the effect of Mg substitution in various Ni-rich materials. Materials in four composition series, $LiMO_2$ (M = Ni, Ni+Al, Ni+Co+Al, Ni content > 0.8), were synthesized with a Mg content of 5% or less. All synthesized materials were single phase, contained no appreciable amount of surface or bulk impurities and had reasonably low amounts of Ni in the Li layer, even for materials containing no Co. Increasing the Mg content decreases the initial charge and discharge capacity of the material due to Mg being electrochemically inactive. The decreases in initial capacity are

based on the amount of Li "locked in" by electrochemically inactive Al and Mg substituent, with Mg reducing the capacity twice as much as Al. Features in the dQ/dV vs. V curves were smoothed in materials containing more Co and Al, and increases in Mg content further smoothed those features. Capacity retention of all composition series were improved with increased Mg content. The capacity retention trend of the materials appears to be related to the amount of Ni ions substituted by an electrochemically inactive substituent, unlike the trend for initial capacity reduction. An analysis of dQ/dV vs. V curves show that Mg can improve the capacity retention by reducing the growth of polarization during cycling. Throughout this chapter, the effect of Mg does not seem to be influenced by the presence of Co or Al, so no synergistic effects are observed from co-substitution of Mg with Co and/or Al. This chapter also demonstrates that materials without Co can have comparable performance to materials with Co.

Chapter 5 – Synthesis of Co-Free Ni-Rich Single Crystalline Positive Electrode Materials for Lithium Ion Batteries: Part I – Two-step Lithiation Method for Al- or Mg-substituted $LiNiO_2$

Chapter 4 studied the effect of Mg substitution in several composition series. Chapter 4 was actually a part of a large compositional study carried out in the Dahn lab to study Ni-rich compositions containing Co, Al, Mg and Mn substituents, culminating in a publication summarizing the overlying trends.[157] In general, reports on the impact of compositional changes of Ni-rich materials have similar messages: as the Ni content of the material increases, the capacity increases but at the cost of cycling performance.[14,15,17,22,26,27,42,49,157,216] The Dahn lab compositional study found that the unit cell volume change can be related to the cycling performance and the study proposed that a main failure mode for Ni-rich materials stem from the anisotropic volume change compromising particle integrity.[157] The unit cell contraction of the Ni-rich electrode was found to be a universal behavior that is dependent on the degree of delithiation, regardless of chemical composition, and this was summed up as "an unavoidable challenge". The benefits of metal substitution to the cycling performance are mainly due to reducing the capacity (degree of delithiation) of the material and thus reducing the volume change, and the choice of substituent may not be significant.[157,217] Since the volume change causes anisotropic stresses and strains on polycrystalline (PC) materials, single crystalline (SC) materials may be able to preserve particle integrity by undergoing isotropic volume change within a particle.

The benefits and disadvantages of SC materials were reviewed in Section 2.4.2. There are many reported improvements imparted by SC materials but SC materials have

a slightly lower specific capacity and more complex synthesis. An increasing number of studies on Ni-rich NMCs have been reported recently[90,92,130,134,135,139,218,221,223,224,228,229,232,233,235,236] but studies of SC materials with high Ni content lag behind those of traditional materials in metal substitution studies,[21,149,157,196,197,205,206] likely due to difficulties in synthesis. A washing step is often required to remove the excess Li or fluxing agents commonly used to grow SC materials.[17,99,134,137,138,218,222,225,229,231] With Ni-rich materials, their sensitivity to moisture suggests that a washing step will deteriorate the performance and should be avoided.[17,99,110,131,157,176,178,179,181–183] Additionally, NCA materials have been reported to form Li_5AlO_4 at high temperatures and with excess Li,[90,131] so a two-step lithiation method was introduced to synthesize SC NCA.[90] This method consists of a first step that heats the precursors to high temperatures but with a deficient amount of Li to grow particles and a second step at lower temperature to fully lithiate the material. Well grown single crystal NCA particles without Li_5AlO_4 impurity were made using this method.[90]

Improved energy density and reduced costs of positive electrode materials can be achieved by increasing the Ni content of the positive electrode material but at a trade-off of shorter cell lifetimes. SC materials have been shown to improve the cell lifetime by reducing the degree of material degradation. There have been many studies of Co-free Ni-rich materials[21,24,27,42,130,149,157,184,196,197,201,202,204–206,210–213] but no work on synthesis and electrochemical characterization of Co-free Ni-rich single crystalline materials have been reported as far as the authors are aware. This study investigates the synthesis of single crystalline $LiNi_{0.95}Al_{0.05}O_2$ and $LiNi_{0.975}Mg_{0.025}O_2$ via the two-step lithiation method. The two compositions were chosen based on benefits to thermal stability

compared to LNO, with the substituent content selected to have a similar theoretical capacity.[21,149] The results in this chapter were incorporated into a manuscript published in the Journal of the Electrochemical Society.[226]

5.1 – Experimental Design

Samples were synthesized using metal hydroxide precursors obtained from Zoomwe. There were 3 precursors used in this chapter. $Ni_{0.95}Al_{0.05}(OH)_2$ (Al-substituted materials will be denoted as NiAl) and $Ni_{0.975}Mg_{0.025}(OH)_2$ (Mg-substituted materials will be denoted as NiMg) precursors used to make single crystalline (SC) samples had similar sizes (D50 ~3 μm) while the NiMg precursor used to make the polycrystalline (PC) comparator was larger (D50 ~18 μm), in line with previous work on this composition.[149,157]

The SC synthesis procedure was carried out as described in Section 3.1 with two heating steps (not including preheat). In the first step, the precursor materials were mixed with $LiOH{\bullet}H_2O$ in a lithium/other metal molar ratio of < 1 (a Li/TM ratio of 0 would be just the precursor) and heated at a higher temperature (850°C, 900°C or 950°C) for 5 h. In the second step, additional $LiOH{\bullet}H_2O$ was added to reach an overall Li/TM ratio (1.02, 1.05 or 1.15) and heated at 700°C or 750°C for 12 or 20 h. A preheat step (480°C for 3 h) was included only for samples with significant amounts of added lithium (addition of Li/TM ratio > 0.5 in one step). Samples with an expected Li/TM ratio of 0.9 or higher were heated in oxygen to promote the oxidation of Ni to the +3 state. The PC synthesis procedure was carried out as described in Section 3.1. The NiMg precursor

(D50 ~18 μm) was mixed with $LiOH•H_2O$ in a Li/TM ratio of 1.02 and heated (including preheat steps) at 700°C for 20 h.

XRD and SEM characterizations were carried out as described in Sections 3.2 and 3.3, respectively. SC materials were separated and coin cells were assembled as described in Section 3.7 with 1.0 M $LiPF_6$ in FEC:DMC (1:4 v/v) as the electrolyte. Electrochemical testing was carried out as described in Section 3.8. P. Arab conducted the electrochemical characterization of some samples. P. Scallion conducted the Hitachi SEM imaging of samples.

5.2 – Results and Discussions

5.2.1 – Heating NiAl and NiMg Samples with No or Low Li in Air as the First Step

Figure 5.1 shows the SEM images of NiAl and NiMg samples after the first step. The Li/TM ratios of these samples were either 0 (mixed with no Li, denoted as 0Li) or 0.5 (half the lithium needed to fully lithiate, denoted as 0.5Li) and samples were heated to either 850°C, 900°C or 950°C for 5 h in air.

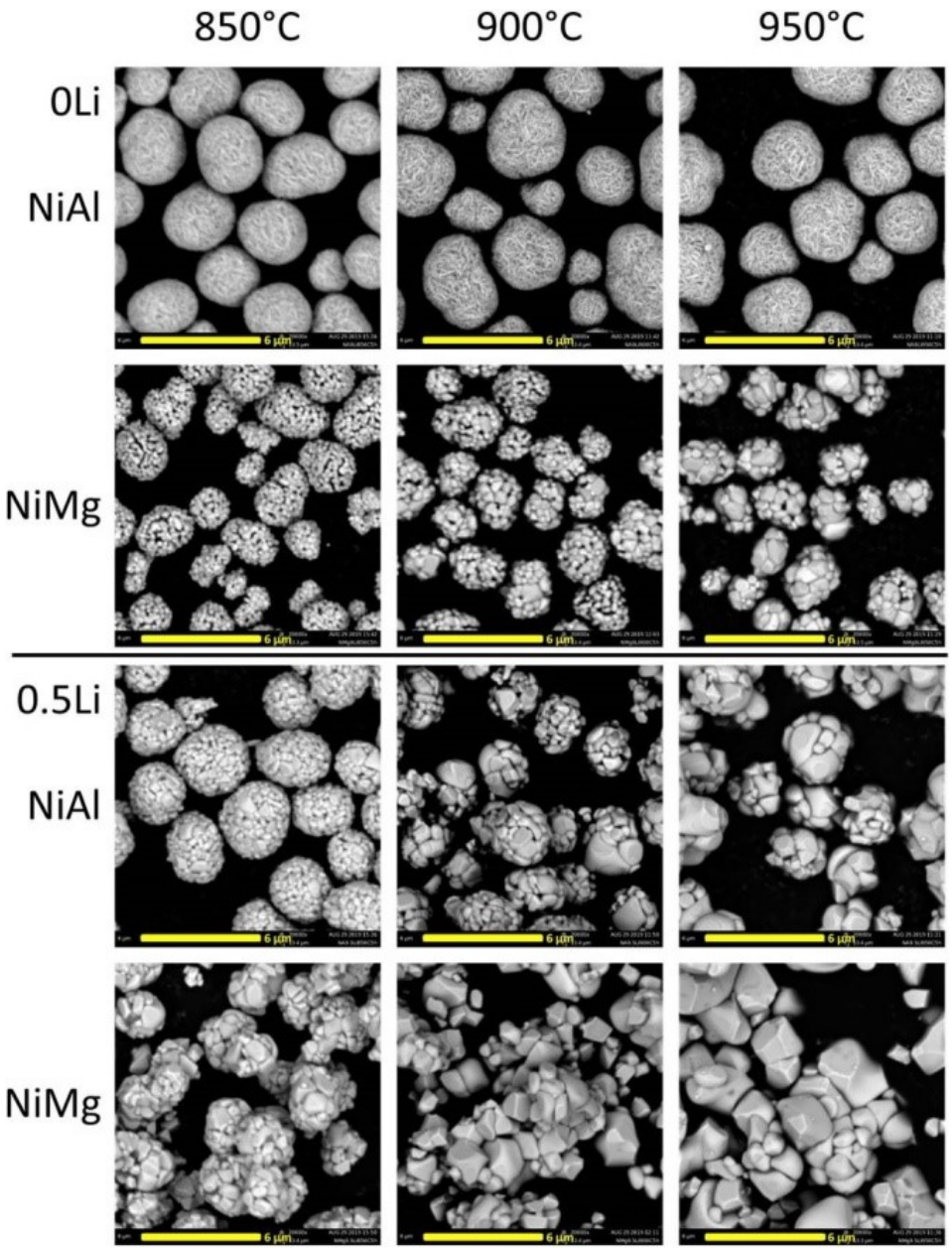

Figure 5.1: SEM images of samples after heating $Ni_{0.95}Al_{0.05}(OH)_2$ (NiAl) or $Ni_{0.975}Mg_{0.025}(OH)_2$ (NiMg) at various temperatures for 5 h with no Li (0Li) or with half the amount of Li needed to fully lithiate (0.5Li).

All NiAl 0Li samples have similar morphology and there were no observable changes when changing the first step heating temperature. Conversely, the NiMg 0Li samples do not have similar morphologies. As the first step heating temperature

increases, primary particle size increases, indicating that grain growth is occurring as temperature increases. This suggests that 2.5% Mg is enough to promote grain growth when heating to 850°C and higher, while 5% Al does not promote grain growth at the same temperatures. Comparing the 0.5Li samples to their 0Li counterparts show that all samples with 0.5Li have more grain growth. Unlike NiAl 0Li samples, NiAl 0.5Li samples heated to a higher temperature had larger particles. NiMg samples with 0.5Li showed even larger particles than the 0Li counterparts. Both Mg and Li are able to promote grain growth, and this growth accelerates as the heating temperature increases. Previous works have reported the importance of Li[97,99,130,133,134,137,138,218,221–224,229] and higher temperatures[90,97,99,130,133–139,218,219,221–225,228] on single crystal growth and Fig. 5.1 corroborates with the literature.

Figure 5.2 shows the XRD patterns of the NiAl and NiMg samples after the first step, along with an expanded view between 42.75°-44.5°. The dominant phase in all these samples is the rocksalt phase, a NiO derivative containing the Al or Mg substituent for 0Li samples and a partially lithiated form for 0.5Li samples. Some amount of ordering of the Li and Ni into Li-rich and Ni-rich layers can be observed in the 0.5Li samples, with the peaks in the 18°-20° range being the signature.[105]

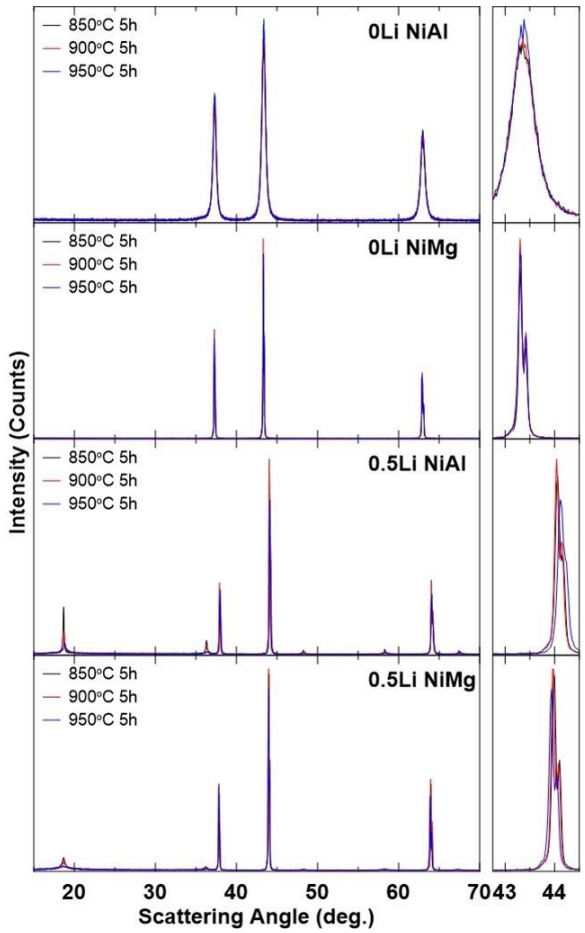

Figure 5.2: XRD patterns (Cu K_α radiation) of samples after heating $Ni_{0.95}Al_{0.05}(OH)_2$ (NiAl) or $Ni_{0.975}Mg_{0.025}(OH)_2$ (NiMg) at various temperatures for 5 h with no Li source (0Li) or with half the amount of Li needed to fully lithiate (0.5Li). XRD patterns were collected from 15°-70°.

Both NiAl and NiMg 0Li samples exhibit only the rocksalt phase with the expected composition being $Ni_{1-x}M_xO$ (x = 0.05 for M = Al and x = 0.025 for M = Mg). The NiAl samples have much broader Bragg peaks than the corresponding NiMg samples. This is due to a lack of grain growth in NiAl samples, and the small grain sizes contribute to peak broadening as described by the Scherrer equation.[249] The NiAl 0Li series of samples are the only samples with broad peaks in Fig. 5.2. This corroborates

with Fig. 5.1 which shows that the NiAl 0Li samples are the only samples that do not undergo grain growth.

The NiAl and NiMg 0.5Li samples show a few differences compared to their 0Li counterparts. One difference is that the reflections are slightly shifted to the right. This can be seen more clearly in the expanded view. This suggests that the unit cells of 0.5Li samples are slightly smaller than the 0Li samples, due to the presence of Li atoms in the structure. The incorporation of Li^{+} will increase the population of Ni^{3+}, which has a smaller ionic radius than Ni^{2+}.[106] The other difference between the 0.5Li samples and the 0Li samples is the presence of alternating Ni-rich layers and Li-rich layers leading to peaks that are not seen in the rock-salt phase.[105] However, as the heating temperature of the first step increases, the peaks associated with this ordering shrink. This may be due to an increase in the amount of Li lost as the temperature increases,[99,131–143] leading to less lithium being incorporated into the material which decreases the amount of layer-type ordering.

Figures 5.1 and 5.2 indicate that both Li and Mg promote grain growth while Al does not promote growth. When Li and/or Mg are present, an increase in temperature will accelerate grain growth. While it is known that Li and high temperatures promote grain growth, the ability for Mg to promote growth has not been reported as far as the authors are aware, and Mg is able to do so at only 2.5%. It seems that the factors that promote growth are factors that facilitate diffusion of ions within the material. Higher temperatures provide more thermal energy for diffusion, but thermal energy is by itself not enough to promote growth in this study as evidenced by the NiAl 0Li series. The inclusion of an ion that can diffuse easily in the material seems to also be required, and

Li^+ and/or Mg^{2+} fill that role. While it is known that Li^+ diffuses in these materials (otherwise the lithiation procedure would fail), there are fewer reports on Mg^{2+} diffusion. Two studies that the authors are aware of both show[273] or suggest[210] that Mg is a better diffuser than Al, corroborating with this chapter. The individual impact of each factor (Li content, Mg content and heating temperature) on grain growth is not probed in this thesis but the grain sizes of the NiMg 0Li sample heated at 950°C for 5 h seem to be qualitatively similar to the grain sizes of the NiMg 0.5Li sample heated at 850°C for 5 h and both seem to be just slightly smaller than the NiAl 0.5Li sample heated at 900°C for 5 h.

5.2.2 – Topping up the Li content of NiAl and NiMg Samples in O_2 as the Second Step

Figure 5.3 shows the SEM images of NiAl and NiMg samples from Figs. 5.1 and 5.2 after the second step. The samples were all heated to 700°C for 20 h in oxygen, with the addition of enough Li to attain an overall Li/TM ratio of 1.05 for 0Li samples and 1.15 for 0.5Li samples to account for the Li loss seen in Fig. 5.2. Samples in this figure are labelled according to their first step conditions. The SEM imaging of the NiAl 0.5Li second step samples was performed using the Hitachi SEM due to equipment availability.

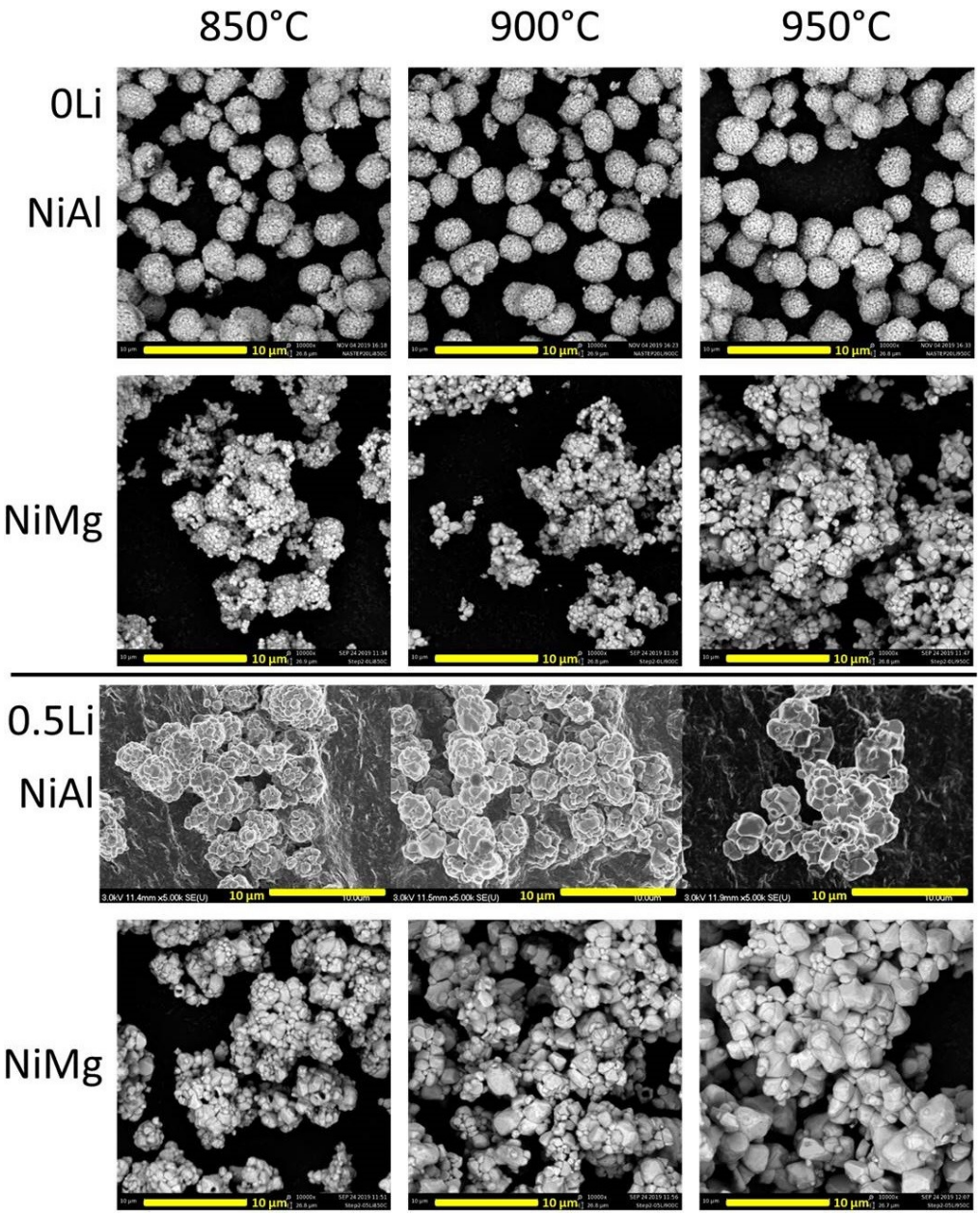

Figure 5.3: SEM images of NiAl and NiMg samples after the second heating step at 700°C for 20 h. Samples are labelled by their first step temperature and Li amount, with 0Li samples being lithiated to a final Li/TM (transition metal or other metal filling the transition metal role) ratio of 1.05 and 0.5Li samples being lithiated to a final Li/TM ratio of 1.15.

The morphology of the samples after second step (Fig. 5.3) follows the same trends as after the first step (Fig. 5.1). The NiAl 0Li series of samples have a similar

morphology after the second step, just like the first step. This is not surprising since there was no grain growth observed in the first step, the second step would be similar to the synthesis procedure for PC materials. The NiAl 0Li particles look similar to other PC samples made from Zoomwe precursors.[131,149,157] The other series of samples produced particles with increasing grain size as the first step heating temperature increased and there was no significant growth seen in between step 1 and step 2. Once again, this is not surprising as the second step heating only reached a temperature of 700°C, which is the temperature used to make PC materials. All synthesized materials produced secondary particles containing primary particles, regardless of primary particle size. The materials with larger primary particles seem more like particle aggregates that can be separated to single crystalline particles and a detailed study of separation methods and their impacts is presented in Chapter 6.

Figure 5.4 shows the XRD patterns of NiAl and NiMg samples from Figs. 5.1 and 5.2 after the second step, along with an expanded view of the (003) reflection, the (104) reflection and the Li impurity region. The dominant phase in all these samples is the layered phase. The NiAl 0Li series of samples were the only series that did not have any impurities. The other series of samples have a rocksalt impurity phase, seen more clearly in the expanded view of the (104) reflection, and the NiAl 0.5Li samples have an observable amount of Li_5AlO_4 (JCPDS #00-027-1209).[254] The formation of the Li_5AlO_4 impurity is undesired because it draws away Li and Al from the material, causing the electrode material to be more Li and Al deficient than targeted.

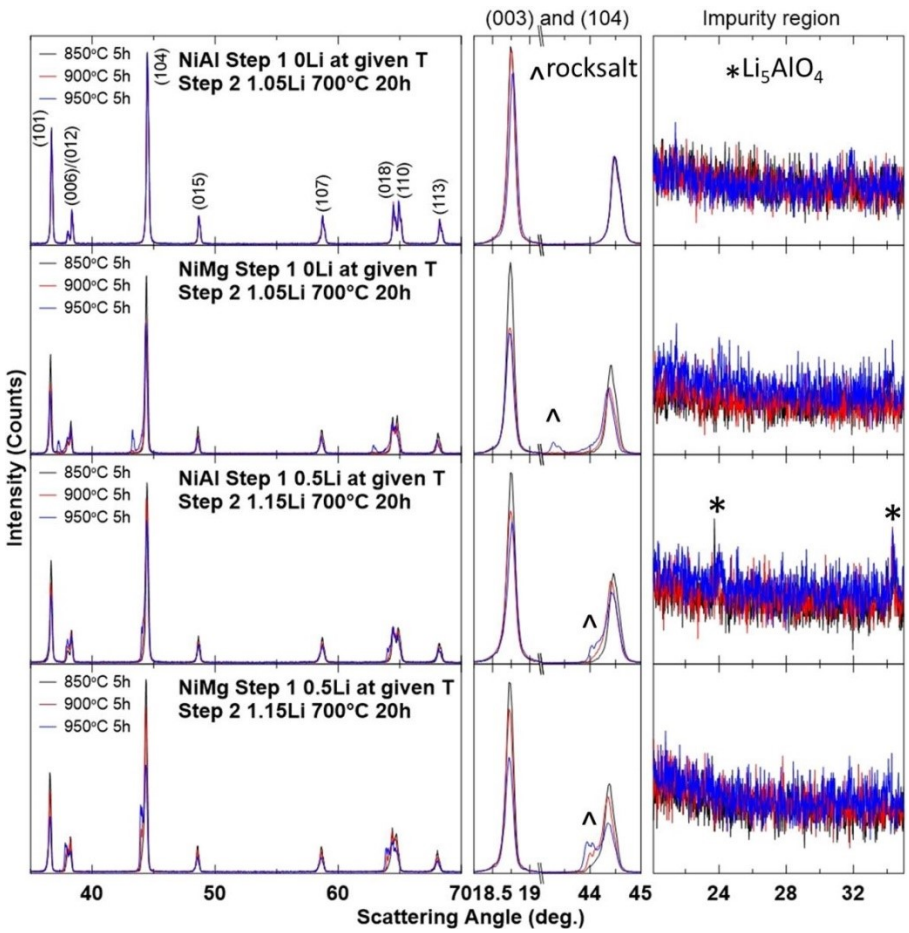

Figure 5.4: XRD patterns (Cu K_α radiation) of NiAl and NiMg samples after the second heating step at 700°C for 20 h were collected from 35°-70° and expanded views of the (003) reflection, the (104) reflection and the Li impurity region are included. Impurity phases are denoted by the ^ (rocksalt phases) and * (Li_5AlO_4) symbols.

The rocksalt impurity phase, as seen in the expanded view of the (104) reflection, is observed in the NiMg 0Li series and the NiAl and NiMg 0.5Li series and is more noticeable at higher first step temperatures. This is likely connected with the degree of grain growth observed in Fig. 5.1. If the Li cannot fully diffuse through the particle and reach the core, there will be portions of the material that remain in the rocksalt structure. The amount of material that the Li cannot reach would increase with larger grain sizes and this is observed in Fig. 5.4. The different scattering angles at which the rocksalt

phase is observed for the NiMg 0Li samples and NiAl and NiMg 0.5Li samples further supports that the rocksalt phase is due to material that did not incorporate further lithium in the second step and not the formation of a new impurity. The formation of a new impurity would be expected to form a phase that has a consistent pattern between all the samples, whereas materials with the same lithium content as after the first step would have reflections at the same scattering angle as observed in Fig. 5.2 and that is the case.

The presence of the Li_5AlO_4 impurity phase in some, but not all, of the NiAl samples suggests that formation occurred during the first step. The observation of the Li_5AlO_4 impurity phase in the NiAl 0.5Li samples is not surprising in the context of the synthesis conditions needed to form single crystalline materials. Previous reports on the synthesis of Al-containing Ni-rich materials have observed this impurity phase.[90,131] These reports have shown that Li_5AlO_4 formation occurs with higher temperatures and higher Li/TM ratios. While the NiAl 0.5Li synthesis temperature of 850°C is within the reported range of Li_5AlO_4 formation (> 800°C), the Li/TM ratio of 0.5 is well below the reported range of Li_5AlO_4 formation (> 0.8-0.9Li). It is uncertain why Li_5AlO_4 formation occurred at such a low Li/TM ratio for these materials. Perhaps the composition plays a role in facilitating Li_5AlO_4 formation since the materials in this chapter are higher in Ni content (95% Ni, 5% Al) compared to the reported works (92% Ni and 3% Al, 90% Ni and 5% Al, 88% Ni and 3% Al).[90,131]

Figure 5.5 shows the Rietveld refinement results as a function of the first step heating temperature for the XRD patterns in Fig. 5.4. The left panels (Figs. 5.5a-5.5b) show the *a* and *c* lattice parameters obtained from the refinements, while the right panels

(Figs. 5.5c-5.5d) show the calculated unit cell volume and the percentage of Ni in the Li layer.

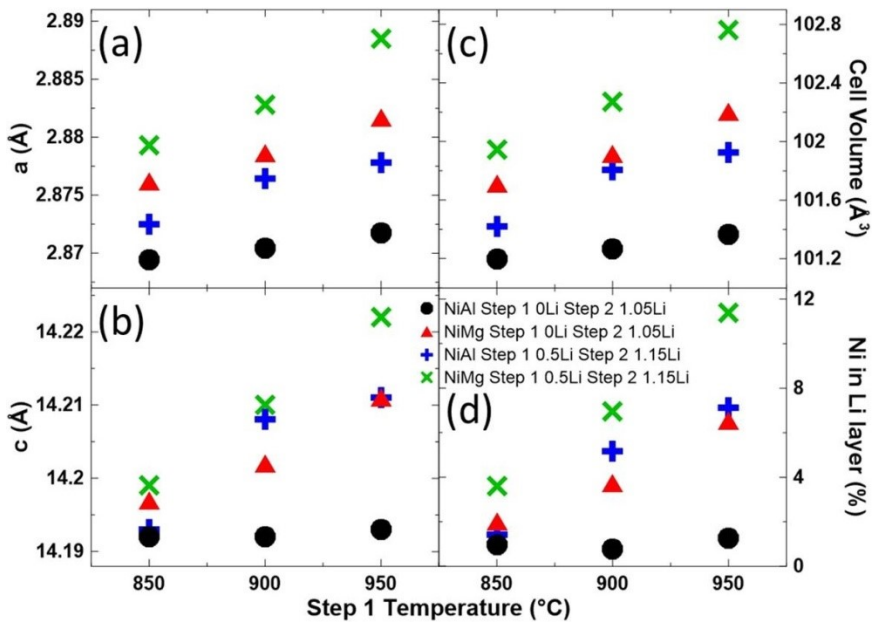

Figure 5.5: Unit cell lattice constants (a, b), the calculated unit cell volume (c) and amount of Ni in the Li layers (d) as a function of the first step heating temperature for NiAl and NiMg samples after the second heating step at 700°C for 20 h.

The unit cell volume (Fig. 5.5c) increases as the first step heating temperature increases for all sample series. However, the NiAl 0Li series shows a smaller increase than the other sample series. A similar trend can be seen for the Ni content in the Li layer (Fig. 5.5d), where samples in a series would have more Ni in the Li layer as the first step temperature increases except for the NiAl 0Li series, which hovered around 1% Ni in the Li layer. The divergence of behaviours between the NiAl 0Li series and the other series may be due to increased diffusivity, by inclusion of Li^{+}, Mg^{2+} and increasing the heating temperature, in the other series. The increased unit cell volume with increasing synthesis temperature has been reported previously and the authors have associated the cell volume increase with cation mixing in that study.[178] This chapter reinforces that correlation and

suggests that Ni content in the Li layer is a larger factor than synthesis temperature to the increase in cell volume, since the NiAl 0Li samples remain relatively stable in the Ni content in the Li layer and the cell volume is only slightly increased as the synthesis temperature increased.

Figures 5.1 to 5.5 showed that the Li content, the Mg content and first step heating temperature are all factors in promoting grain growth. However, some of these factors have drawbacks if relied on heavily to grow particles. Higher temperatures would increase the Ni content in the Li layer as well as increase Li loss (Figs. 2 and 5)[99,131,133–139] and increasing the Mg content would lower the capacity of the material,[21,149] so increasing the Li/TM ratio of the first step was investigated. The additional benefit of increasing the first step Li/TM ratio is that it should avoid the presence of rocksalt impurities, which stem from unlithiated material (Fig. 5.4) as there is enough Li to create a well layered phase in the first step.[90,105]

5.2.3 – 850°C for 5 h with More Li as the First Step, Topped Up Li and 700°C for 20 h as the Second Step

Figure 5.6 shows the SEM images of NiMg samples after the first step and after the second step. Unfortunately, SEM imaging was not available when NiAl samples were synthesized. However, based on a SEM comparison of NiAl samples and NiMg samples shown later, it is expected that the morphology of NiAl samples be similar to NiMg samples due to the abundance of Li. The samples were all heated to 850°C for 5 h in oxygen in the first step, with a Li/TM ratio of 0.9Li, 0.95Li or 0.975Li. The samples were all heated to 700°C for 12 h in oxygen in the second step, with the addition of

enough Li to attain an overall Li/TM ratio of 1.02. Samples in this figure are labelled according to their first step Li/TM ratios.

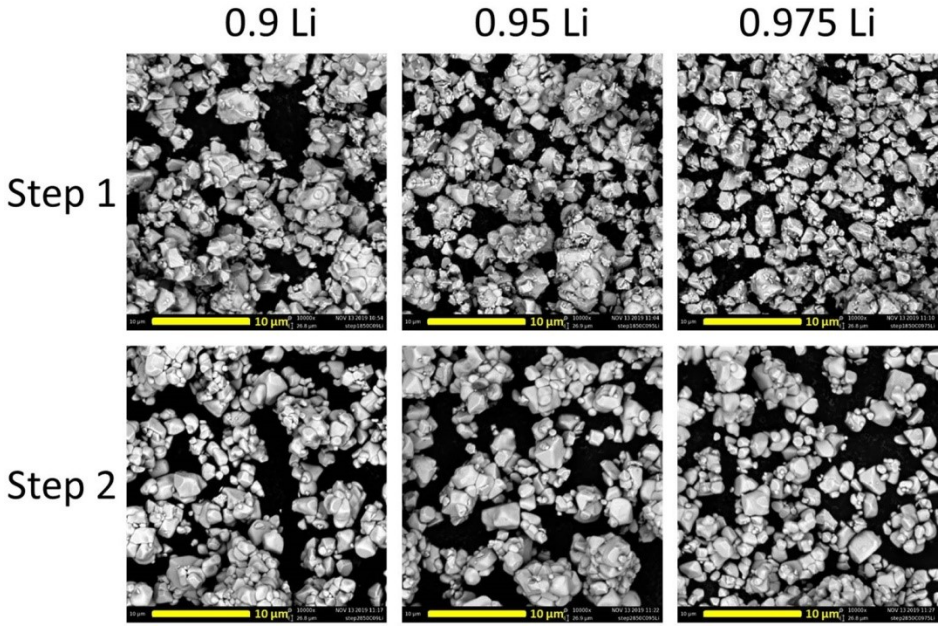

Figure 5.6: SEM images of NiMg samples after the first heating step at 850°C for 5 h and after the second heating step at 700°C for 12 h. Samples are labelled by their first step Li amount, samples are lithiated to a final Li/TM (transition metal or other metal filling the transition metal role) ratio of 1.02 for the second heating step.

The samples look well grown after the first step, with particle sizes slightly larger than the NiMg 0.5Li sample heated to 850°C and slightly smaller than the sample heated to 900°C. There does not seem to be significant morphological differences between the 3 Li/TM ratios at the scale shown in Fig. 5.6. Similar to Fig. 5.3, there was no significant growth seen between step 1 and step 2 due to the lower second step heating temperature, which is the temperature used to make PC materials. Once again, the particles seem like particle aggregates that can be separated to single crystalline particles.

Figure 5.7 shows the XRD patterns of NiAl (Fig. 5.7a) and NiMg (Fig. 5.7b) samples after the first step and after the second step, along with an expanded view of the

(003) reflection, the (104) reflection and the Li impurity region. The samples were heated to 850°C for 5 h in the first step, with a Li/TM ratio of 0.9Li, 0.95Li or 0.975Li, and heated to 700°C for 12 h in oxygen in the second step, with the addition of enough Li to attain an overall Li/TM ratio of 1.02. The dominant phase in all these samples is the layered phase even after the first step. No samples have a rocksalt impurity phase but the NiAl samples still have an observable amount of Li_5AlO_4. In fact, the peaks are even more pronounced, which is not too surprising as the first step now has more Li at 850°C.

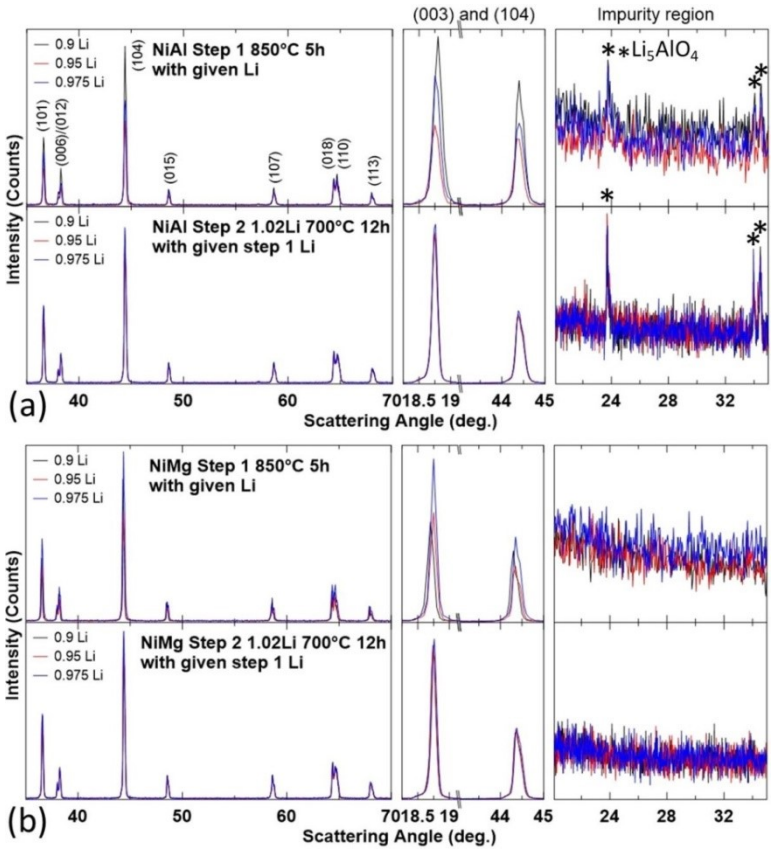

Figure 5.7: XRD patterns (Cu K_α radiation) of NiAl (a) and NiMg (b) samples after the first heating step at 850°C for 5 h and second heating step at 700°C for 12 h. Samples are labelled by their first step Li amount, samples are lithiated to a final Li/TM (transition metal or other metal filling the transition metal role) ratio of 1.02 for the second heating step. XRD patterns were collected from 35°-70° and expanded views of the (003) reflection, the (104) reflection and the Li impurity region are included.

Figure 5.8 shows the Rietveld refinement results as a function of the first step Li/TM ratio for the XRD patterns in Fig. 5.7. The left panels (Figs. 5.8a1-5.8a4) show the refinement results for NiAl samples and the right panels (Figs. 5.8b1-5.8b4) show the results for NiMg samples. From top to bottom, the panels show the *a* (Figs. 5.8a1-5.8b1) and *c* (Figs. 5.8a2-5.8b2) lattice parameters obtained from the refinements, the calculated unit cell volume (Figs. 5.8a3-5.8b3) and the percentage of Ni in the Li layer (Figs. 5.8a4-5.8b4).

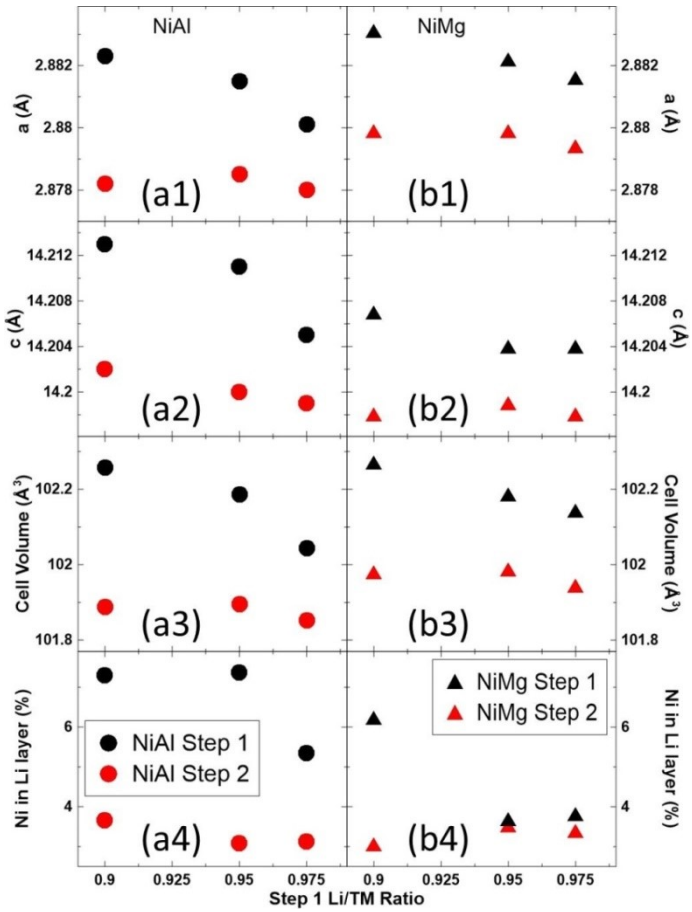

Figure 5.8: Unit cell lattice constants (a1-b1, a2-b2), the calculated unit cell volume (a3-b3) and amount of Ni in the Li layers (a4-b4) as a function of the first step Li amount for NiAl (a) and NiMg (b) samples after the first heating step at 850°C for 5 h and second heating step at 700°C for 12 h. Li/TM is used to denote Li/transition metal or other metal filling the transition metal role.

For almost all the samples, the second step resulted in a sample with a smaller unit cell and less Ni in the Li layer. The only exceptions are the NiMg 0.95Li and 0.975Li samples retaining a similar Ni in Li layer content after the second step. A previous study on the synthesis conditions of NCA has shown that as the Li content in the material approaches 1, both the *c* lattice parameter and the Ni content in the Li layer will decrease.[131] This supports the results seen in Fig. 5.8, as the first step is more Li deficient and the second step has a Li content closer to 1.

Figures 5.6 to 5.8 showed that having a higher Li/TM ratio in the first step (between 0.9-0.975Li) and heating to 850°C for 5 h is a viable approach to making well grown single crystalline materials that avoids rocksalt impurities. However, the final materials all hovered around 3% Ni in the Li layer (Fig. 5.8) while Fig. 5.5 showed that 2% Ni in the Li layer may be attainable. In an effort to lower the Ni content in the Li layer of the final material, a slightly higher temperature was used in the second step.

5.2.4 – Same First Step at 850°C, but a Higher Temperature Second Step at 750°C

Figure 5.9 shows the SEM images of NiAl and NiMg samples after the second step. The samples were all heated to 850°C for 5 h in oxygen in the first step, with a Li/TM ratio of 0.95Li or 0.975Li, and then heated to 750°C for 12 h in oxygen in the second step, with the addition of enough Li to attain an overall Li/TM ratio of 1.02. Samples in this figure are labelled according to their first step Li/TM ratios. The SEM images in Figs. 5.6 and 5.9 were imaged using different SEMs so comparison is not straightforward, but the particles seem to be qualitatively similar in particle size and morphology. This is not too surprising as the first step is the growth step and the

conditions are the same for that step. At these Li/TM ratios for the first step, the 2.5% Mg does not seem to have a significant impact on grain growth, as the particles for the NiMg samples are similar in size as NiAl samples.

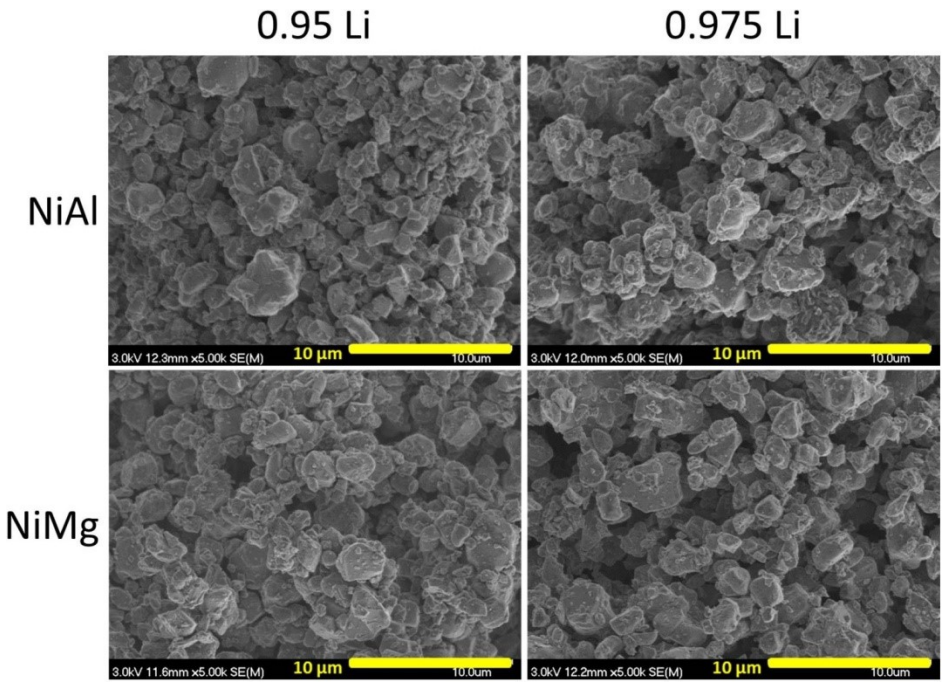

Figure 5.9: SEM images of NiAl and NiMg samples after the heating steps at 850°C for 5 h and then at 750°C for 12 h. Samples are labelled by their first step Li amount, samples are lithiated to a final Li/TM (transition metal or other metal filling the transition metal role) ratio of 1.02 for the second heating step.

Figure 5.10 shows the XRD patterns of NiAl (Fig. 5.10a) and NiMg (Fig. 5.10b) samples after the first step and after the second step, along with an expanded view of the (003) reflection, the (104) reflection and the Li impurity region. The samples were heated to 850°C for 5 h in the first step, with a Li/TM ratio of 0.95Li or 0.975Li, then heated to 750°C for 12 h in oxygen in the second step, with the addition of enough Li to attain an overall Li/TM ratio of 1.02. Similar to Fig. 5.7, the dominant phase in all these

samples are the layered phase. No samples have a rocksalt impurity phase but the NiAl samples still have an observable amount of Li_5AlO_4.

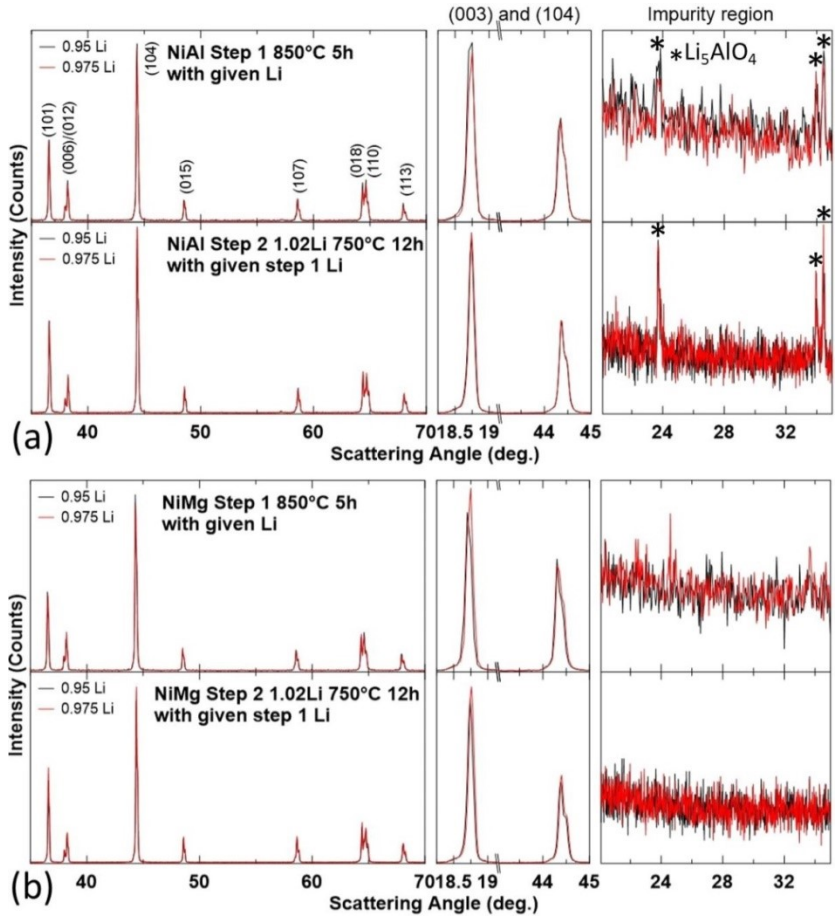

Figure 5.10: XRD patterns (Cu K_α radiation) of NiAl (a) and NiMg (b) samples after the first heating step at 850°C for 5 h and second heating step at 750°C for 12 h. Samples are labelled by their first step Li amount, samples are lithiated to a final Li/TM (transition metal or other metal filling the transition metal role) ratio of 1.02 for the second heating step. XRD patterns were collected from 35°-70° and expanded views of the (003) reflection, the (104) reflection and the Li impurity region are included.

Figure 5.11 shows the Rietveld refinement results as a function of the first step Li/TM ratio for the XRD patterns in Fig. 5.10. The left panels (Figs. 5.11a1-5.11a4) show the refinement results for NiAl samples and the right panels (Figs. 5.11b1-5.11b4) show the results for NiMg samples. From top to bottom, the panels show the *a* (Figs.

5.11a1-5.11b1) and *c* (Figs. 5.11a2-5.11b2) lattice parameters obtained from the refinements, the calculated unit cell volume (Figs. 5.11a3-5.11b3) and the amount of Ni in the Li layer (Figs. 5.11a4-5.11b4). The refinement results of Fig. 5.10 (second step at 750°C) are shown as filled circles and triangles while refinement results of Fig. 5.7 (second step at 700°C, shown in Fig. 5.8) are shown as empty circles and triangles.

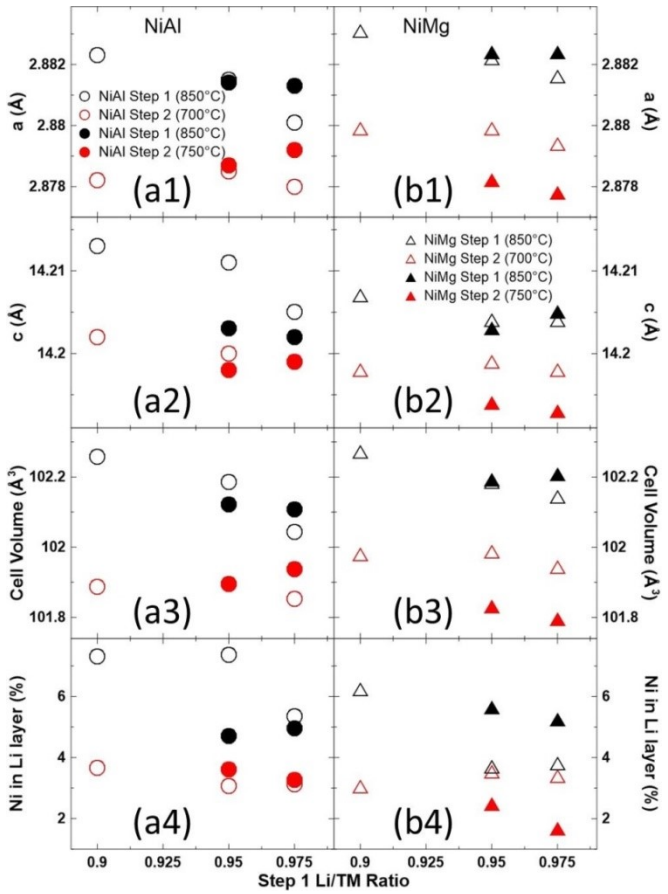

Figure 5.11: Unit cell lattice constants (a1-b1, a2-b2), the calculated unit cell volume (a3-b3) and amount of Ni in the Li layers (a4-b4) as a function of the first step Li amount for NiAl (a) and NiMg (b) samples after the first heating step at 850°C for 5 h and second heating step at 750°C for 12 h along with the results in Fig. 5.8 (second step at 750°C). The refinement results of Fig. 5.10 (second step at 750°C) are shown as filled circles and triangles while refinement results of Fig. 5.7 (second step at 700°C, shown in Fig. 8) are shown as empty circles and triangles. Li/TM is used to denote Li/ transition metal or other metal filling the transition metal role.

Similar to Fig. 5.8, the second step produced samples that have a smaller unit cell and less Ni in the Li layer. For the most part, the samples after the first step have a similar unit cell volume but slightly different Ni content in the Li layer. Heating the second step at 750°C did not have an impact on NiAl samples compared to heating at 700°C. On the other hand, NiMg samples heated to 750°C for the second step had a reduced Ni content in the Li layer (~2%) compared to heating at 700°C (~3%). It is uncertain why the NiMg samples had less Ni in the Li layer when heated to 750°C compared to 700°C but the NiAl samples did not see such a reduction. Perhaps the formation of the Li_5AlO_4 impurity left the sample slightly Li deficient. Since using a second step heating temperature of 750°C resulted in a reduction of the Ni content in the Li layer for NiMg samples and no observable detriment, these NiAl and NiMg samples were selected for electrochemical testing after separation of the particle aggregates (Section 3.7.1).

5.2.5 – Electrochemical Characterization of NiAl and NiMg Samples Heated at 850°C then 750°C

Figure 5.12 shows the voltage (vs Li/Li^+) versus specific capacity (V vs. Q, Fig. 5.12a), the differential capacity versus voltage (dQ/dV vs. V, Fig. 5.12b) and the 1st cycle capacity data (Figs. 5.12c1-5.12c3) for the NiAl and NiMg samples synthesized with a first step temperature of 850°C then a second step temperature of 750°C. Samples in this figure are labelled (Figs. 5.12a-5.12b) or plotted (Figs. 5.12c1-5.12c3) according to their first step Li/TM ratios. Solid and dashed lines represent two duplicate cells for Figs. 5.12a-5.12b.

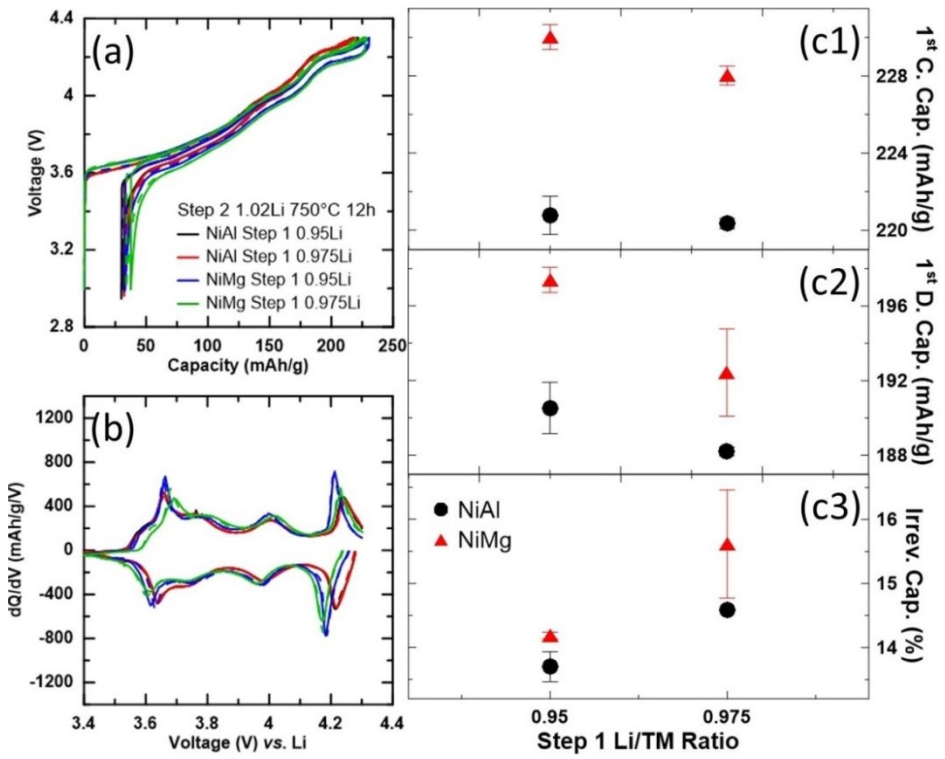

Figure 5.12: Cell voltage as a function of capacity (a) and differential capacity as a function of cell voltage (b) for the NiAl and NiMg samples after the second heating step at 750°C for 12 h. First cycle capacities as a function of the first step Li amount (c1-c3) for the NiAl and NiMg samples. Li/TM is used to denote Li/ transition metal or other metal filling the transition metal role.

Figure 5.12a shows that NiAl cells have a slightly lower 1st charge capacity than NiMg cells and that NiMg 0.975Li cells have a slightly higher irreversible capacity than the other cells, but otherwise the voltage curves look similar. However, dQ/dV vs. V curves (Fig. 5.12b) show that NiAl cells have less capacity at high voltage compared to NiMg cells, resulting in smaller features around 4.2 V (vs Li/Li^+). The NiAl features occur at a slightly higher voltage than NiMg. The NiMg 0.975Li cells also seem to have more polarization than the other cells. Considering the 1st cycle capacities (Figs. 5.12c1-5.12c3), the NiMg cells have more capacity than NiAl cells but have more irreversible capacity.

5.2.6 – Comparison of Polycrystalline and Single Crystalline NiMg

Figure 5.13 compares a selected SC NiMg material (NiMg 0.95Li from Figs. 5.9 to 5.11) with a PC NiMg material of the same composition (97.5% Ni, 2.5% Mg).[157] Fig. 5.13a shows the SEM image of the PC NiMg material and Fig. 5.13b shows the SEM image of the SC NiMg material. Fig. 5.13c shows the XRD patterns of PC and SC NiMg materials, along with expanded views of the (003) reflection, the (104) reflection and the Li impurity region, the calculated unit cell volume and the percentage of Ni in the Li layer. The V (vs Li/Li^+) vs. Q curves (Fig. 5.13d) and the dQ/dV vs. V curves (Fig. 5.13e) of the initial cycles, the cycling performance (Figs. 5.13f1-5.13f2) and the dQ/dV vs. V curves for the initial and final C/20 and C/5 cycles (Figs. 5.13g1-5.13g4) are also shown. Solid and dashed lines represent two duplicate cells for Figs. 5.13d-5.13e. Data for duplicate cells are also shown for Figs. 5.13f1-5.13f2 but not for Figs. 5.13g1-5.13g4 for clarity.

The SEM image of the PC NiMg material (Fig. 5.13a) shows that the synthesized product maintains its secondary particle size with small primary particles, in contrast to the SC NiMg material (Fig. 5.13b) which grows its primary particles to the point where the secondary particle is no longer intact. The XRD patterns of PC and SC NiMg materials (Fig. 5.13c) show similar patterns and no observable Li impurities for either material. The Rietveld refinement results show the SC material has a larger unit cell volume and more Ni content in the Li layer as expected from heating the material to a higher temperature (Fig. 5.5).[178]

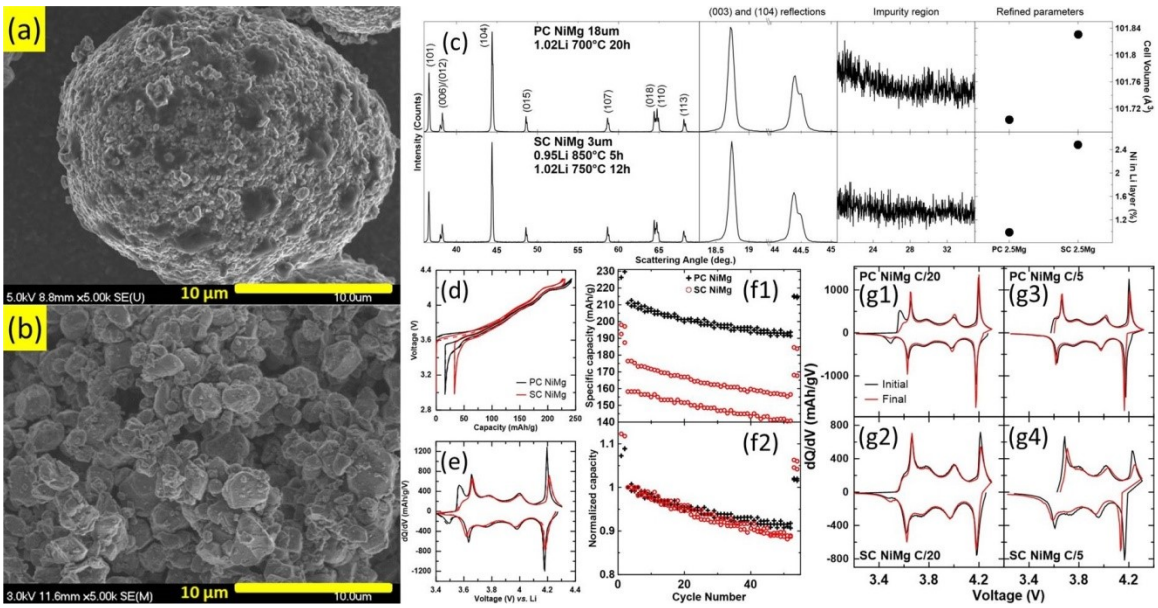

Figure 5.13: Comparison of a polycrystalline (PC) NiMg sample with a single crystalline (SC) NiMg sample synthesized from differently sized precursor particles (d50 ~18µm and ~3µm, respectively). SEM images of (a) the PC NiMg sample and (b) the SC NiMg sample. XRD patterns (Cu K_α radiation) of the samples (c) were collected from 35°-70° and expanded views of the (003) reflection, the (104) reflection and the Li impurity region, calculated unit cell volume and amount of Ni in the Li layers are included. Cell voltage as a function of capacity (d) and differential capacity as a function of cell voltage (e) for the samples. Specific capacity (f1) and normalized capacity (f2) as a function of cycle number for the samples. Differential capacity as a function of cell voltage before and after (g1, g2) or at the beginning and at the end (g3, g4) of the 50 C/5 cycles for the samples.

Comparison of the electrochemical data of the initial cycles shows a significant difference between the capacity of PC and SC NiMg materials. SC NiMg materials have a smaller capacity and a larger irreversible capacity (Fig. 5.13d) than PC NiMg materials. Other studies on SC Ni-rich materials have also reported less capacity compared to their PC counterparts.[17,90,97,99,135,218,223,224,228,235] This loss in capacity in SC NiMg materials can be pinpointed to two regions in the dQ/dV vs. V curves (Fig. 5.13e). SC NiMg

materials lose virtually all capacity around the ~3.5 V region and have smaller features around the 4.2 V region compared to PC NiMg materials. A similar occurrence was reported for SC NCA 88/9/3 but to a lesser degree, perhaps due to a lower Ni content.[90] Although no dQ/dV vs. V curves were reported, voltage curves in several other works on SC Ni-rich electrodes (80-91% Ni) seem to corroborate this occurrence.[139,218,223,224,228,237] Both of these voltage regions have been associated with kinetic hindrances of Li diffusion in the material.[37,240] A more in-depth investigation in the reduction of capacity in SC NiMg materials is included in Chapter 6.

The cycling performances of the NiMg materials (Figs. 5.13f1-5.13f2) indicate that SC NiMg materials do not have any benefits over PC NiMg materials in this study. The PC NiMg cells outperform the SC NiMg materials when considering both specific capacity (Fig. 5.13f1) and normalized capacity (Fig. 5.13f2). This is unexpected since SC materials have generally been reported to experience less capacity fade than PC materials.[17,53,92,97,135,137,162,218,223,224,229,232–235] Examination of the dQ/dV vs. V curves at various cycles (Figs. 5.13g1-5.13g4) suggests that the PC and SC NiMg cells degraded in different ways. The dQ/dV vs. V curves for the initial and final C/20 cycles of PC NiMg cells (Fig. 5.13g1) show the loss of capacity in the ~3.5 V region whereas the dQ/dV vs. V curves for the initial and final C/20 cycles of SC NiMg cells (Fig. 5.13g2) remain quite stable in terms of the features in the curves. A loss of capacity in the ~3.5 V region in the dQ/dV vs. V curves suggests that the main mode of degradation for PC NiMg cells is related to structural change, specifically in the low V kinetic hindrance region. It is hard to pinpoint what the structural change is without further testing, but possibilities include the increase of Ni content in the Li layer hindering Li diffusion or reaction heterogeneity

leading to the filling of the electrode particle surface earlier, reducing the amount of Li that can be intercalated back into the particle.[232] The dQ/dV vs. V curves for the initial and final C/20 cycles of SC NiMg cells show relatively minimal changes, suggesting the structure of the SC material is more stable. Instead, the main mode of degradation for SC NiMg cells seem to be a large increase in the polarization of the cell as evidenced by the dQ/dV vs. V curves for the initial and final C/5 cycles (Fig. 5.13g4). The cause of this polarization growth is uncertain and work is being carried out to try and understand this degradation mechanism. It should be noted that the SC materials underwent particle separation (Section 3.7.1) but some particle aggregates are still present. This will be discussed in the next chapter.

While SC NiAl and NiMg materials have been successfully synthesized in this study, more work is needed to improve these materials. The formation of Li_5AlO_4 impurities for all SC NiAl synthesis conditions tested in this study suggests that the synthesis of SC ultrahigh Ni materials containing Al will lead to a material that is more Li and Al deficient than targeted. SC NiMg synthesis did not experience issues with impurity formation once sufficient lithium was included in the first step, but the SC NiMg materials as synthesized and characterized in this study are not yet competitive when compared to its PC counterpart. These SC NiMg cells have lower capacity, higher irreversible capacity and increased cycling fade than PC NiMg cells. The lower capacity and higher irreversible capacity of SC NiMg cells stems from kinetic hindrances to Li diffusion impacted negatively by larger path lengths for solid state diffusion while the increased cycling fade stems from an increase in cell polarization. More work is needed to understand and address these issues.

The two-step lithiation method was introduced to try and avoid the formation of Li_5AlO_4 in NiAl materials but this chapter has shown that Li_5AlO_4 formation occurred for all tested synthesis conditions for this composition. NiMg did not experience the formation of impurities and is not expected to, even for a one-step lithiation process. As such, Chapter 6 focuses on the synthesis of SC NiMg using a simpler one-step lithiation process. The separation of particle aggregates and the low capacity of the synthesized SC NiMg materials will also be studied in more detail.

5.3 – Conclusions

This chapter studied the synthesis of Co-free single crystalline NiAl (95% Ni, 5% Al) and NiMg (97.5% Ni and 2.5% Mg) materials using a two-step lithiation method. The presence of Li or Mg is required for grain growth and higher temperatures enhance grain growth as well. Grain growth of rocksalt materials in the first step may lead to incomplete lithiation of the material in the second step, resulting in rocksalt impurities, so the first step should contain enough Li to fully convert the material to the layered phase. A first step Li/TM (transition metal or other metal filling the transition metal role) ratio of 0.9-0.975 and heating temperature of 850°C can be used to grow particles to a suitable size. While a second step temperature of 700°C can be used to produce decent materials, a higher second step temperature of 750°C was able to reduce the Ni content in the Li layer down to ~2% for NiMg materials. SC NiAl materials synthesized in this study could not avoid the formation of Li_5AlO_4 impurity even at a Li/TM ratio of 0.5. SC NiMg cells are not yet competitive with PC NiMg cells. Compared to PC NiMg cells, SC NiMg cells have lower capacity, a higher irreversible capacity, and higher cycling fade.

Chapter 6 – Synthesis of Co-Free Ni-Rich Single Crystalline Positive Electrode Materials for Lithium Ion Batteries: Part II – One-Step Lithiation Method of Mg-substituted $LiNiO_2$

In Chapter 5, the use of a two-step lithiation method to synthesize single crystalline (SC) $LiNiO_2$ (LNO) substituted with 5% Al or 2.5% Mg was investigated. The two-step method was introduced as a potential pathway to avoid the formation of Li_5AlO_4 impurities in Al-containing Ni-rich materials,[90,131] and the method consists of a first step that heated the material at high temperatures but with less Li for grain growth and then a second step at lower temperature to fully lithiate the material. The synthesis of single crystalline materials was achieved, but many particles were aggregated into clusters. It was found that the presence of Li or Mg is required for grain growth and higher temperatures enhance grain growth as well. Previous work on SC materials have reported the importance of Li[97,99,130,133,134,137,138,218,221–224,229] and higher temperatures[90,97,99,130,133–139,218,219,221–225,228] on single crystal growth but the impact of Mg on grain growth in these materials was unknown. It was hypothesized that the reason Mg was able to promote grain growth but not Al is due to Mg being a better diffuser in these materials than Al.[210,273] Chapter 5 found that insufficient Li in the first step results in the grain growth of rocksalt materials and may lead to the formation of rocksalt impurities stemming from incomplete lithiation in the second step. A satisfactory procedure was used to grow particles to a suitable size and it was found that a second step temperature of 750°C was able to reduce the Ni content in the Li layer to as low as to ~2% for Mg-substituted materials compared to ~3% Ni in the Li layer for a second step temperature of 700°C. Al-substituted materials synthesized in Chapter 5 could not avoid the formation

of Li_5AlO_4 impurity under all conditions tested, even at a low Li/other metal ratio of 0.5, leading the material to contain less Li and Al than targeted. SC Mg-substituted materials did not experience the formation of impurities and are not expected to form impurities even in a one-step synthesis process.

The electrochemical results from Chapter 5 were below expectations. Cells with SC Mg-substituted materials had lower specific capacity and a higher specific irreversible capacity when compared to their polycrystalline (PC) counterparts. While a lower specific capacity was not unexpected, the reduction in specific capacity was far greater than reported for other SC materials.[17,90,97,99,135,218,223,224,228,235] Al-substituted materials performed even worse in the initial cycles and they were not cycled further nor compared with their PC counterparts. A closer look at the dQ/dV vs. V curves of cells with SC and PC Mg-substituted materials revealed that the initial specific capacity reductions centered mostly around 2 voltage regions. SC cells lost virtually all the capacity around ~3.5 V and some capacity around ~4.2 V compared to PC cells. Both of these voltage regions have been associated with kinetic hindrances of Li diffusion in the material.[37,240] SC cells also experienced a slightly higher capacity fade during cycling than PC cells, which differs from previous reports.[17,53,92,97,135,137,162,218,223,224,229,232–235] Inspection of dQ/dV vs. V curves from the initial and final cycles showed that SC cells seemed to cycle with less low rate capacity loss than PC cells but experienced more polarization growth, suggesting different modes of failure for SC and PC cells.

Building off of Chapter 5, this chapter investigates the synthesis of single crystalline $LiNi_{1-x}Mg_xO_2$ (x = 0.025, 0.05) via a one-step lithiation method. The separation of particle aggregates was studied as well as the use of an adjusted heating

protocol. The low capacity of SC materials was investigated further by varying the starting conditions or the cycling conditions. The results in this chapter were incorporated into a manuscript published in the Journal of the Electrochemical Society.[227]

6.1 – Experimental Design

Samples were synthesized using metal hydroxide precursors obtained from Zoomwe. There were 3 precursors used in this chapter. The majority of this chapter used small (D50 ~3 μm) $Ni_{0.975}Mg_{0.025}(OH)_2$ precursors to synthesize SC samples. Small (D50 ~3 μm) $Ni_{0.95}Mg_{0.05}(OH)_2$ precursors and large (D50 ~18 μm) $Ni_{0.975}Mg_{0.025}(OH)_2$ precursors were used to test the impact of higher Mg content and to compare to its PC counterpart, respectively. When necessary, the small $Ni_{0.975}Mg_{0.025}(OH)_2$ precursor will be designated as 2.5Mg, SC and/or 3μm with the small $Ni_{0.95}Mg_{0.05}(OH)_2$ precursor designated as 5Mg and large $Ni_{0.975}Mg_{0.025}(OH)_2$ precursor designated as PC and/or 18μm, otherwise it should be assumed that the small $Ni_{0.975}Mg_{0.025}(OH)_2$ is the precursor used.

The SC and PC synthesis procedures were carried out as described in Section 3.1. For SC syntheses, the small (D50 ~3 μm) 2.5Mg and 5Mg precursors were mixed with $LiOH{\bullet}H_2O$ in various Li/TM (transition metal or other metal filling the transition metal role) ratios and heated (including preheat steps) at various temperatures for 12 or 20 h. For syntheses involving a lower temperature step after calcination, the furnace was programmed to cool down to 750°C at a rate of 10°C/min and heated for 5 h. In reality, the furnace cooled naturally at a rate that was probably slower than 10°C/min and so the dwell time at 750°C is slightly less than 5 h. For PC synthesis, the NiMg precursor (D50

~18 μm) was mixed with $LiOH{\bullet}H_2O$ in a Li/TM ratio of 1.02 and heated (including preheat steps) at 700°C for 20 h.

XRD, SEM and PSA characterizations were carried out as described in Sections 3.2, 3.3 and 3.4, respectively. Not all characterization methods used materials after separation (Section 3.7.1). PSA samples were always separated by 20S balls before characterization. SEM and XRD samples were usually not separated but sometimes were. SC materials were separated and coin cells were assembled as described in Section 3.7 with 1.0 M $LiPF_6$ in FEC:DMC (1:4 v/v) as the electrolyte. Electrochemical testing was carried out as described in Section 3.8. N. Zhang and J. Stark conducted the material synthesis and characterization of the Li1.05 samples heated at 825°C, 850°C and 875°C. P. Arab conducted the electrochemical characterization of some samples. H. Li suggested the higher temperature cycling experiments. P. Scallion conducted the Hitachi SEM imaging of samples.

6.2 – Results and Discussions

6.2.1 – Heating NiMg Samples to Various Temperatures

Figure 6.1 shows the SEM images of samples with 2.5% Mg (denoted as 2.5Mg) heated to various temperatures for 12 h. The SEM imaging of the samples heated at 825°C was done using the Hitachi SEM due to equipment availability. The Li/TM ratios used for the samples are labelled and the images are organized so that the lower Li/TM ratio of a given temperature is in the top row (Figs. 6.1a-6.1d) and the higher Li/TM ratios are in the bottom row (Figs. 6.1e-6.1h). Higher Li/TM ratios were used for higher temperatures due to concerns about Li loss.[99,128,130–143,274] Samples with lower Li/TM

ratios were synthesized later at the higher temperatures, but no SEM imaging was done due to equipment availability from COVID-19 university closures.

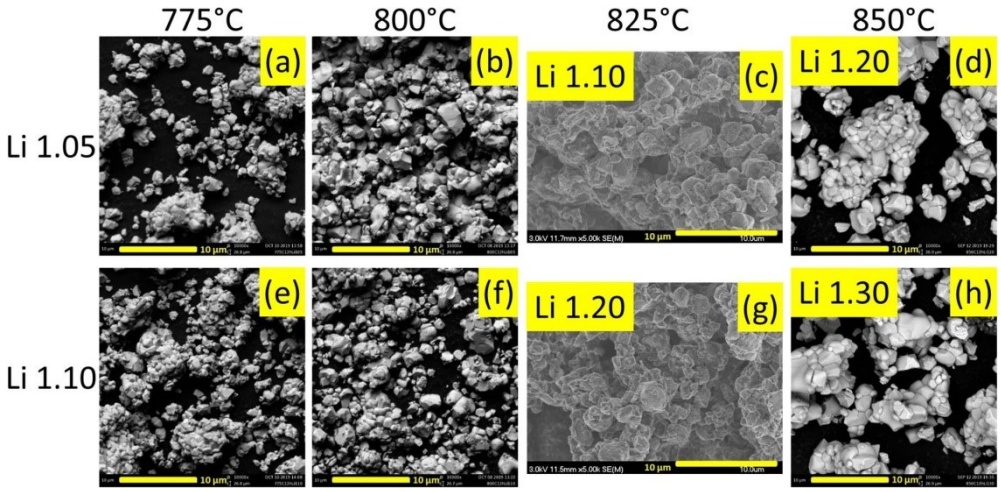

Figure 6.1: SEM images of $LiNi_{0.975}Mg_{0.025}O_2$ samples after heating for 12 h at various temperatures and Li/TM (transition metal or other metal filling the transition metal role) ratios.

Figure 6.1 shows that heating at higher temperatures will result in larger grains. This is not surprising and corroborates with many previous reports.[90,97,99,130,133–139,218,219,221–225,228] A particle size in the micron range is desirable for SC materials.[90,97,99,137–139,221,224,228,231,234,275] The particle sizes of the samples heated at 775°C seem to be slightly undersized and possibly the samples heated at 800°C as well, while the samples heated to a higher temperature were suitable in size. There are no observable differences in particle size or morphology between the Li/TM ratios of 1.05 and 1.10 for 775°C (Figs. 6.1a, 6.1e) and 800°C (Figs. 6.1b, 6.1f), the Li/TM ratios of 1.10 and 1.20 for 825°C (Figs. 6.1c, 6.1g) and the Li/TM ratios of 1.20 and 1.30 for 850°C (Figs. 6.1d. 6.1h) but the impact of varying Li/TM ratios will be explored more in depth in Figs. 6.3 and 6.4.

Figure 6.2 shows the XRD patterns of 2.5Mg samples heated to various temperatures for 12 h (Figs. 6.2a1-6.2e1). An expanded view of the (003) and the (104) reflections (Figs. 6.2a2-6.2e2), an expanded view of the impurity region (Figs. 6.2a3-6.2e3) and Rietveld refinement results (Figs. 6.2f1-6.2f4) are included as well. Samples with a Li/TM ratio of 1.05 are shown in black and samples with a Li/TM ratio of 1.10 are shown in red. The dominant phase in all these samples is the layered phase but a very weak peak corresponding to Li_2O (JCPDS #00-077-2144;[254] a secondary peak around 56° was also confirmed) can be observed in all the samples (Figs. 6.2a3-6.2e3).

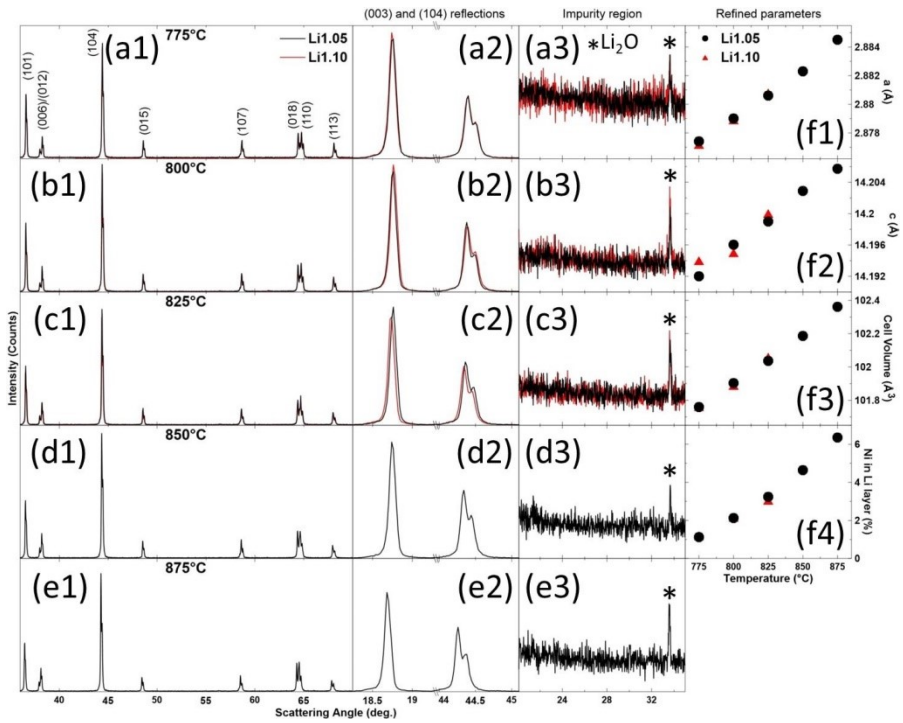

Figure 6.2: XRD patterns (Cu K_α radiation) of $LiNi_{0.975}Mg_{0.025}O_2$ samples after heating for 12 h at various temperatures (a-e) with a Li/TM (transition metal or other metal filling the transition metal role) ratio of 1.05 (black) or 1.10 (red). XRD patterns (a-e1) were collected from 35°-70° and expanded views of the (003) reflection (a-e2), the (104) reflection (a-e2) and the Li impurity region (a-e3) are included. Unit cell lattice constants (f1, f2), the calculated unit cell volume (f3) and amount of Ni in the Li layers (f4) as a function of the heating temperature for the samples.

Rietveld refinement results (Figs. 6.2f1-6.2f4) show a very clear trend with increasing temperature. The individual lattice parameters, the unit cell and the Ni content in the Li layer all increase linearly with increasing temperature. This has been reported previously and corroborated in Chapter 5,[178,226] and the trend is associated with the temperature promoting more Ni into the Li layer and increasing the unit cell volume. The Ni content in the Li layer is just above 1% for both samples heated at 775°C and just above 2% for both samples heated at 800°C. Chapter 5 achieved around 2% Ni in the Li layer for micron-sized SC samples prepared at 850°C (but only 5 h), so it seems that the one-step process may need to utilize lower temperatures than the two-step process. The challenge will be to grow particles of sufficient size while maintaining ~2% Ni content in the Li layer.

6.2.2 – Heating NiMg Samples with Various Li/TM Ratios

Figure 6.3 shows the SEM images of 2.5Mg samples heated at 775°C for 20 h with various Li/TM ratios. The heating time was increased to see if particles could grow larger while maintaining similar Ni content in the Li layer. Qualitatively, these samples seem to be slightly larger than the samples heated for 12 h (Figs. 6.1a, 6.1e) but still mainly in the sub-micron range. Comparing the sample with a Li/TM ratio of 1.02 and the sample with a Li/TM ratio of 1.30, there does not seem to be any significant difference in either the particle size or morphology. There may be some minor differences, but the impact of Li in this chapter is much smaller compared to previous reports on the importance of Li on SC particle growth.[97,99,130,133,134,137,138,218,221–224,229] However, studies that vary both the synthesis temperature and Li/TM ratio show that the

impact of Li/TM ratio may not be significant at lower temperatures[99,133] and this seems to be the case in this chapter.

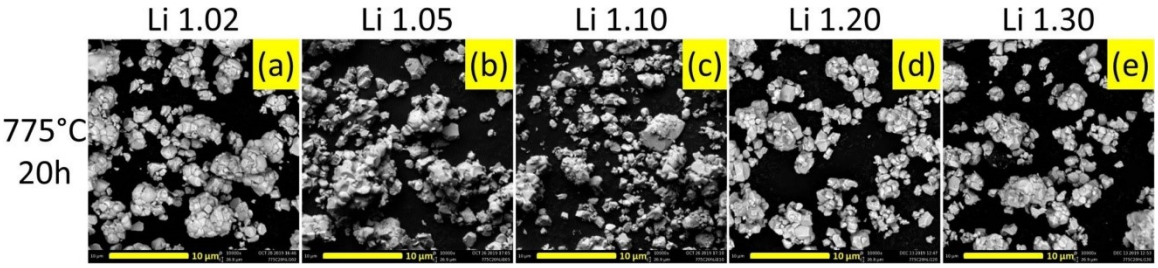

Figure 6.3: SEM images of $LiNi_{0.975}Mg_{0.025}O_2$ samples after heating for 20 h at 775°C with various Li/TM (transition metal or other metal filling the transition metal role) ratios.

Figure 6.4 shows the XRD patterns of 2.5Mg samples heated with various Li/TM ratios (Figs. 6.4a1-6.4e1). An expanded view of the (003) and the (104) reflections (Figs. 6.4a2-6.4e2), an expanded view of the impurity region (Figs. 6.4a3-6.4e3) and Rietveld refinement results (Figs. 6.4f1-6.4f4) are included as well. Samples heated at 775°C for 20 h are shown in black and samples heated at 800°C for 12 h are shown in red. The dominant phase in all these samples is the layered phase but a peak corresponding to Li_2O can be observed in most samples (Figs. 6.4a3-6.4e3). The sample heated at 775°C for 20 h with a Li/TM ratio of 1.02 does not show the presence of Li_2O. Fig. 6.4 shows the impact of synthesis conditions on Li_2O formation much more clearly than Fig. 6.2. Above a Li/TM ratio of 1.02, samples will form Li_2O when heated at 775°C for 20 h. Higher temperatures will also increase the formation of Li_2O, but only below a certain Li/TM threshold as samples at a Li/TM ratio of 1.20 and 1.30 show similar amounts of Li_2O for both heating regimes.

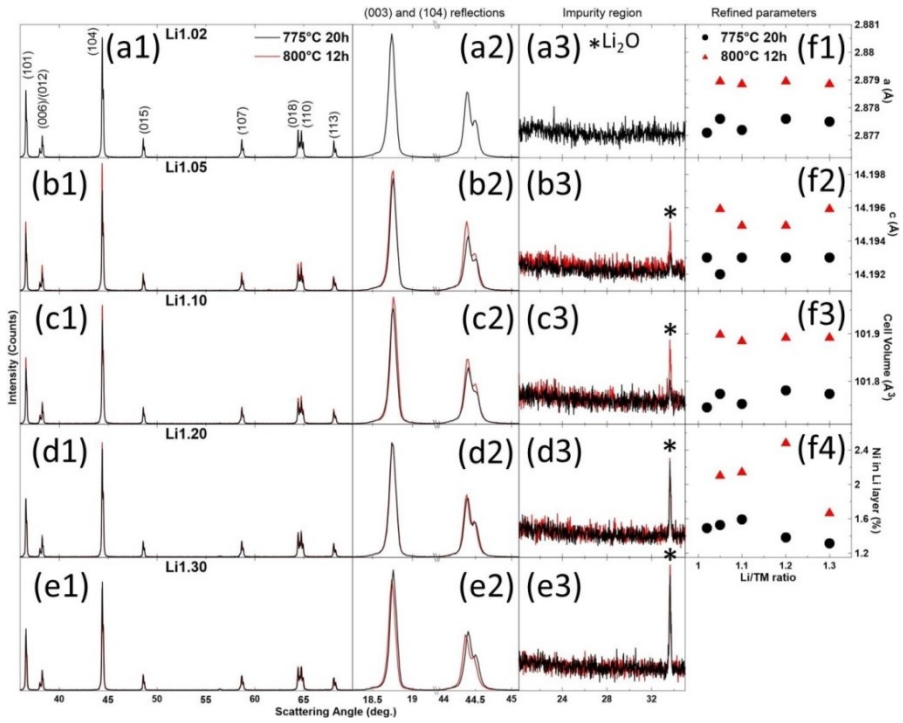

Figure 6.4: XRD patterns (Cu K_α radiation) of $LiNi_{0.975}Mg_{0.025}O_2$ samples after heating with various Li/TM (transition metal or other metal filling the transition metal role) ratios (a-e) at 775°C for 20 h (black) or 800°C for 12 h (red). XRD patterns (a-e1) were collected from 35°-70° and expanded views of the (003) reflection (a-e2), the (104) reflection (a-e2) and the Li impurity region (a-e3) are included. Unit cell lattice constants (f1, f2), the calculated unit cell volume (f3) and amount of Ni in the Li layers (f4) as a function of the Li/TM ratio for the samples.

Rietveld refinement results (Figs. 6.4f1-6.4f4) do not show a significant trend with varying Li/TM ratios. In fact, the impact of heating temperature is highlighted once more as the samples heated at 800°C for 12 h all have larger unit cells and more Ni in the Li layer. Unit cell parameters and volume seem to remain relatively consistent with varying Li/TM ratios. The Ni content in the Li layer seems to peak around a Li/TM ratio of 1.1, with decreasing Ni content in the Li layer as the Li/TM ratio is decreased and also as the Li/TM ratio is increased. It is unsure if this is actually a trend, but this occurs for both heating regimes.

Figures 6.1 to 6.4 demonstrate the impact of varying temperature and Li/TM ratios on the growth of SC materials. Increasing the temperature will increase grain growth but will also increase the Ni content in the Li layer. Increasing the Li/TM ratio does not seem to have an effect on grain growth at lower temperatures (775°C or 800°C) but influences the formation of the Li_2O impurity. The Ni content in the Li layer may also be impacted by the Li/TM ratio. Growing particles of sufficient size while maintaining ~2% Ni content in the Li layer will require a careful balance. Samples heated at 775°C for 20 h with a Li/TM ratio of 1.02 were selected for further testing, as the conditions produced slightly undersized particles but hovered around 1.5% Ni in the Li layer. In terms of the Li/TM ratio, using a lower ratio minimizes Li_2O formation and avoids the use of too much excess Li and could possibly avoid a potentially detrimental washing step as well.[17,99,110,131,157,176,178,179,181–183]

6.2.3 – Separation of Particle Aggregates

Figures 6.1 and 6.3 show that the synthesized samples may experience grain growth but the particles are mainly aggregated in clusters. This may cause issues with connectivity to the individual particles in a cell leading to poor performance, so the aggregates should be separated. This chapter will report on two separation methods, one method utilizing a coffee grinder and the other utilizing a planetary mixer. A third method, sonication in various solvents (NMP, acetone, water), was tested but not reported. Sonication was able to separate aggregates very well, but all attempts resulted in reaggregation of the material after drying or evaporation of the solvent.

Figure 6.5 shows the SEM images of the separation tests of 2.5Mg samples heated at 775°C for 20 h with a Li/TM ratio of 1.02. No separation (Figs. 6.5a1-6.5a2) refers to samples that were hand ground after synthesis with no extra particle separation steps. Coffee grinder (Figs. 6.5b1-6.5b2) refers to samples that were placed in a coffee grinder and ground for 6 x 30 s after hand grinding. 2M balls (Figs. 6.5c1-6.5c2) and 20S balls (Figs. 6.5d1-6.5d2) refer to the use of a planetary mixer utilizing 2 hardened stainless steel balls (6 mm diameter) or 20 smaller balls (3 mm diameter) and mixed for 3 x 100 s. Both milling conditions used a ~3:1 ball:material mass ratio. Low magnification images (Figs. 6.5a1-6.5d1) and higher magnification images (Figs. 6.5a2-6.5d2) are provided so readers can get a sense of the degree of particle separation at two scales.

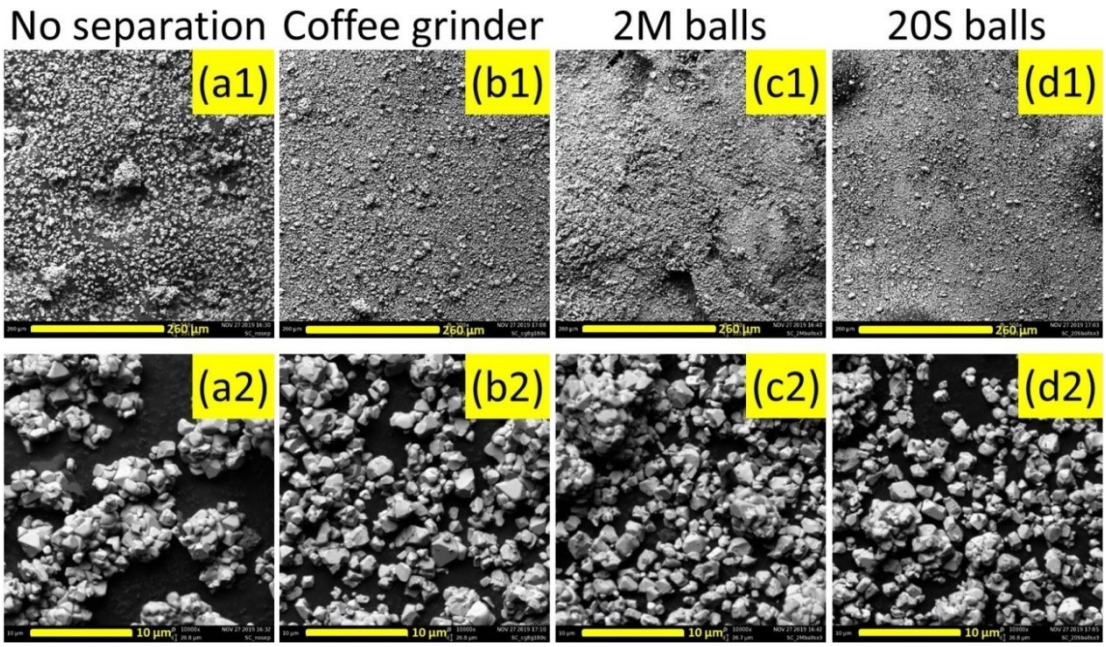

Figure 6.5: SEM images of $LiNi_{0.975}Mg_{0.025}O_2$ samples after heating for 20 h at 775°C with a Li/TM (transition metal or other metal filling the transition metal role) ratio of 1.02 and undergoing various particle separation methods.

Figure 6.5 shows that the reported separation methods succeed to various degrees. Compared to no separation, the size and abundance of particle aggregates were reduced.

However, all images still contained particle aggregates, so no separation method was perfect either. Qualitatively, the coffee grinder method seems to be slightly worse than the planetary mixer methods at lower magnification and similar at higher magnification.

Figure 6.6 shows the PSA results of the separation tests of 2.5Mg samples heated at 775°C for 20 h with a Li/TM ratio of 1.02. Particle size distribution plots are shown on the left (Fig. 6.6a) and D50 values are plotted on the right (Fig. 6.6b). The various lines of a colour represent triplicate measurements for Fig. 6.6a. The 20S balls method of separating particle aggregates is more effective than the 2M balls method and the coffee grinder method. The D50 values suggest that PSA measurements are more indicative of the degree of particle separation rather than the particle size as Fig. 6.5d2 shows that single crystal grains of the 20S balls method are smaller than the measured D50 value of > 4 µm. Therefore, this method should only be taken as a semi-quantitative or even qualitative measure of the degree of particle separation, and a qualitative measure of particle size only for the same method of separation.

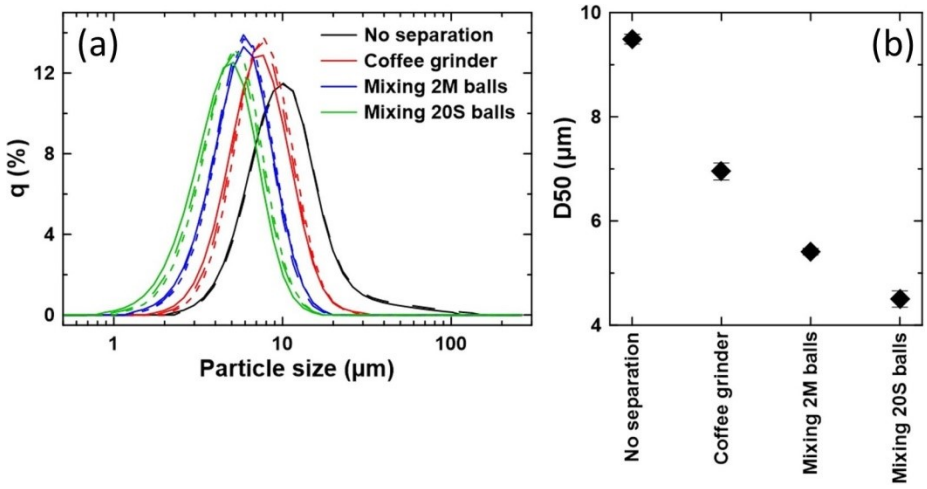

Figure 6.6: Particle size distribution plot (a) and D50 (b) of $LiNi_{0.975}Mg_{0.025}O_2$ samples undergoing various particle separation methods.

Figure 6.7 shows the voltage (vs Li/Li^+) versus specific capacity (V vs. Q, Fig. 6.7a), the differential capacity versus voltage (dQ/dV vs. V, Fig. 6.7b), the 1st cycle capacity data (Figs. 6.7c1-6.7c3) and the cycling performance (Fig. 6.7d1-6.7d2) for the 2.5Mg samples heated at 775°C for 20 h with a Li/TM ratio of 1.02 and separated using different methods. Solid and dashed lines represent two duplicate cells for Figs. 6.7a-6.7b.

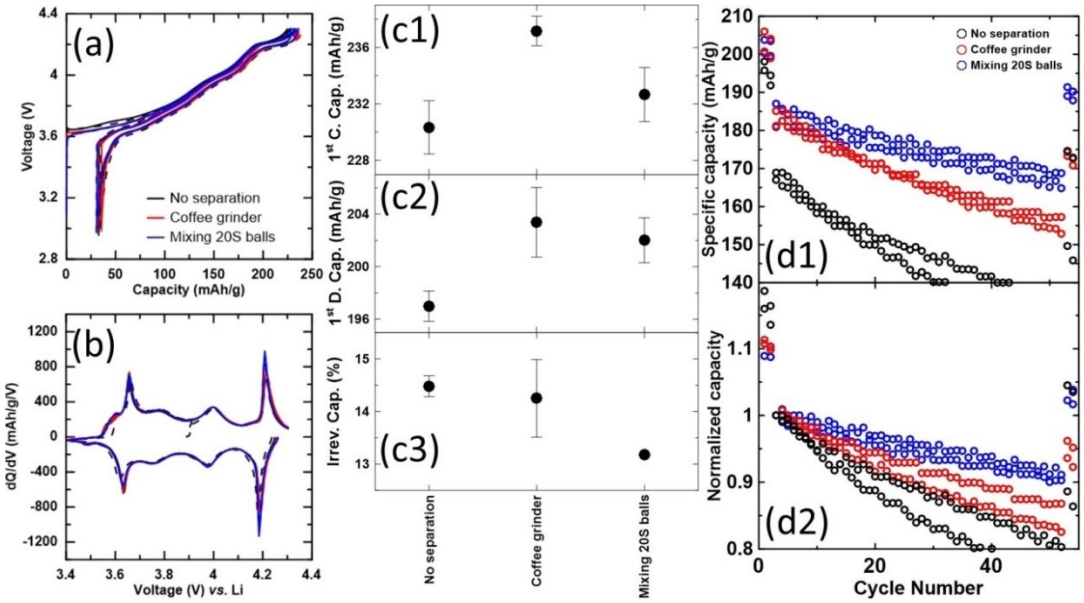

Figure 6.7: Cell voltage as a function of capacity (a) and differential capacity as a function of cell voltage (b) for the initial cycles of $LiNi_{0.975}Mg_{0.025}O_2$ samples undergoing various particle separation methods. First cycle capacities by separation method (c1-c3) as well as specific capacity (d1) and normalized capacity (d2) as a function of cycle number for the samples.

The voltage curves (Fig. 6.7a) and the dQ/dV vs. V curves (Fig. 6.7b) do not show observable differences in the electrochemical behaviour of the samples that were separated differently or not at all. This is not surprising as the base material is the same. However, there are some slight differences between the cells when looking at the capacity data (Figs. 6.7c1-6.7c3). The cells containing unseparated material have slightly

lower capacity, and this can probably be attributed to the poor connectivity to individual particles due to the abundance of particle aggregates. The two separated materials have similar discharge capacities (Fig. 6.7c2) but the coffee ground cells have slightly higher charge capacities (Fig. 6.7c1). Figs. 6.7d1-6.7d2 shows that separation of particle aggregates have a significant impact on cell performance, with the cells containing unseparated material having lower capacity, worse rate retention (going from C/20 to C/5), and worse capacity retention. The cells containing material separated by the coffee grinder have similar capacity, similar rate retention but worse capacity retention when compared to the cells containing the sample mixed with 20S balls. Figs. 6.7d1-6.7d2 is a clear indication that synthesized materials need to be adequately separated in order to cycle well. It may be possible that this material can cycle even better if the separation method is improved, since Figs. 6.5d1-6.5d2 show that the particle aggregates are still present in the sample mixed with 20S balls. Fig. 6.7 also suggests that the lower capacity of SC materials, when compared to PC materials (Chapter 5), do not stem from the particle aggregation, since the cells with separated materials show similar capacity.

6.2.4 – Summary of XRD and PSA Results

Figure 6.8 summarizes the Ni content in Li layer and D50 values of the 2.5Mg samples made throughout the course of this chapter. On the left side of the figure, the Ni content in the Li layer of the samples are plotted as a function of heating temperature (Fig. 6.8a) and Li/TM ratio (Fig. 6.8b). The D50 values are plotted as a function of heating temperature (Fig. 6.8c) and Li/TM ratio (Fig. 6.8d) on the right side of the figure. For the results plotted as a function of heating temperature, the Li/TM ratio of the sample is colour coded and the heating temperature is colour coded for the results plotted as a

function of the Li/TM ratio. Not all samples were characterized by PSA and not all samples were separated when collecting the XRD pattern; XRD patterns of a few samples before and after separation have been collected and no difference was found. There were multiple synthesis conditions that varied in this summary (heating time, scale, Li source, etc.) in addition to heating temperature and Li/TM ratios but the majority of the syntheses utilized similar conditions (except heating time, many samples heated at 775°C were heated for 20 h).

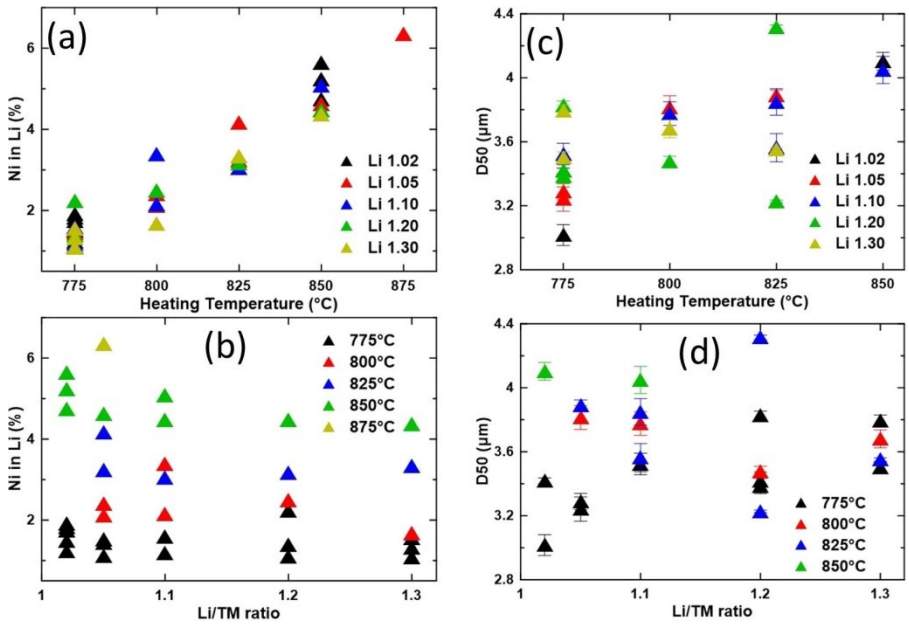

Figure 6.8: Amount of Ni in the Li layers as a function of heating temperature (a) and as a function of the Li/TM (transition metal or other metal filling the transition metal role) ratio (b). D50 as a function of heating temperature (c) and as a function of the Li/TM ratio (d).

Figure 6.8a expands upon the observation from Fig. 6.2f4 that the Ni content in the Li layer is largely defined by the heating temperature when synthesizing SC materials and this supports previous work.[99,131,133–137,139] Chapter 5 found that this trend does not hold if grain growth is not occurring, but grain growth occurs for all these samples due to

the presence of sufficient Li. Compared to heating temperature, varying the Li/TM ratio (Fig. 6.8b) has a much smaller impact, if any, on the Ni content in the Li layers. The relationship between the D50 value and the heating temperature (Fig. 6.8c) is tenuous. It should be noted that the presence of particle aggregates complicates the numerical measurements as discussed in Fig. 6.6. Combining this weak relationship with observations from Fig. 6.1 suggests that heating temperature does impact grain growth and this supports previous work.[90,97,99,130,133–139,218,219,221–225,228] On the other hand, combining observations from Fig. 6.8d and Fig. 6.3 suggests that there is no significant impact on particle size from the amount of Li used and this does not support previous reports on the importance of Li on SC particle growth.[97,99,130,133,134,137,138,218,221–224,229]

6.2.5 – Impact of Mg Content

Figure 6.9 investigates the impact of increasing the Mg content, from 2.5% Mg (denoted as 2.5Mg) to 5% Mg (denoted as 5Mg). Figures 6.9a1-6.9b1 show the XRD patterns of the two materials, along with expanded views of the (003) reflection and the (104) reflection (Figs. 6.9a2-6.9b2), the Li impurity region (Figs. 6.9a3-6.9b3), the calculated unit cell volume (Fig. 6.9c1) and the amount of Ni in the Li layer (Fig. 6.9c2). Samples with a Li/TM ratio of 1.02 are shown in black and samples with a Li/TM ratio of 1.05 are shown in red. The V (vs Li/Li^+) vs. Q curves (Fig. 6.9d) and the dQ/dV vs. V curves (Fig. 6.9e) of the initial cycles, the 1st cycle capacity data (Figs. 6.9f1-6.9f3) and the cycling performance (Figs. 6.9g1-6.9g2) are also shown. The XRD patterns show similar patterns for the two materials, with some Li_2O formation for 2.5Mg Li1.05 (Fig. 6.4b3) and 5Mg Li1.02. It is uncertain why Li_2O forms on 5Mg materials with a Li/TM ratio of 1.02 but not 1.05. Refinement results show that 5Mg materials have a slightly

larger unit cell and slightly more Ni in the Li layer than 2.5Mg materials, and this has been reported before in PC materials.[21,149]

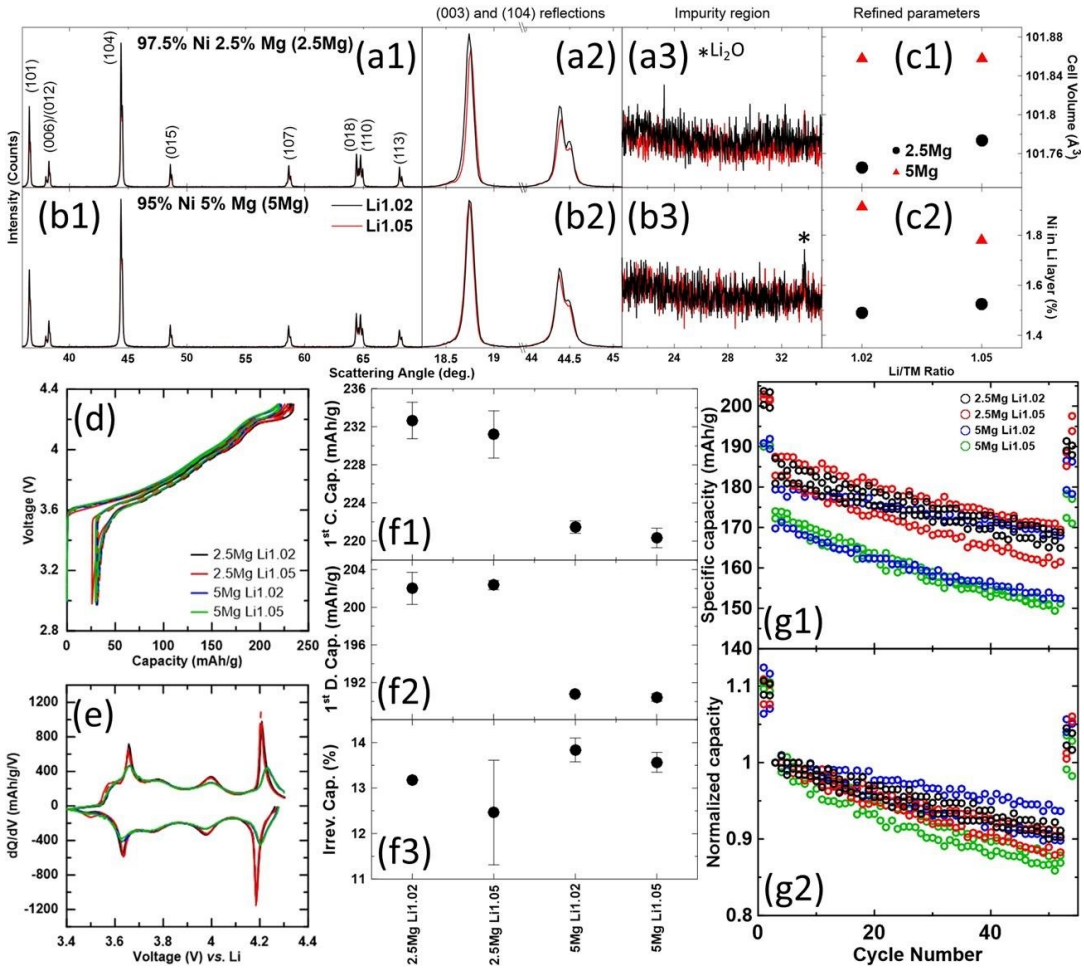

Figure 6.9: XRD patterns (Cu K_α radiation) of $LiNi_{0.975}Mg_{0.025}O_2$ (a) and $LiNi_{0.95}Mg_{0.05}O_2$ (b) samples heated at 775°C for 20 h with a Li/TM (transition metal or other metal filling the transition metal role) ratio of 1.02 (black) or 1.05 (red). XRD patterns (a-b1) were collected from 15°-70° and expanded views of the (003) reflection (a-b2), the (104) reflection (a-b2) and the Li impurity region (a-b3) are included. The calculated unit cell volume (c1) and amount of Ni in the Li layers (c2) as a function of the Li/TM ratio for the samples. Cell voltage as a function of capacity (d) and differential capacity as a function of cell voltage (e) for the initial cycles of the samples. First cycle capacities by sample (f1-f3) as well as specific capacity (g1) and normalized capacity (g2) as a function of cycle number for the samples.

Figure 6.9d shows that the 5Mg cells have less capacity in the initial cycles, and Fig. 6.9e shows that these reductions in capacity occur around 3.6 and 4.2 V, supporting previous reports.[149] Samples of both Li/TM ratios of a material have a relatively similar capacity and 5Mg cells have less capacity than 2.5Mg cells (Figs. 6.9f1-6.9f3). This was expected since it is known that substituting more inactive substituents results in a lower capacity.[21,149] Cycling performance results (Figs. 6.9g1-6.9g2) seem to indicate that the two materials have similar fade, but this is hard to ascertain since the 5Mg cells vary to the point where one cell cycles better and the other cell cycles worse than the 2.5Mg cells. (Fig. 6.9g2) For the most part, 5Mg cells generally start off with a lower capacity with no clear benefit to capacity retention (Fig. 6.9g1).

6.2.6 – Impact of a Low Temperature Step

Figure 6.10 investigates the impact of including a lower temperature step right after the calcination step. The use of a lower temperature step after calcination has been reported to lower the Ni content in the Li layer.[136,143,225,276] Two-step SC syntheses also use a lower temperature to heat the 2nd step to lower the Ni in the Li layer in the process.[90,226] Although it's generally thought that the reduced Ni content in the Li layer stems from topping up the Li/TM ratio to stoichiometry, Chapter 5 revealed that temperature may play a role in this process. Fig. 6.1 shows that micron-sized particles are produced by heating to 825°C, so this was chosen as the calcination temperature and a lower temperature of 750°C was selected due to the success in Chapter 5.

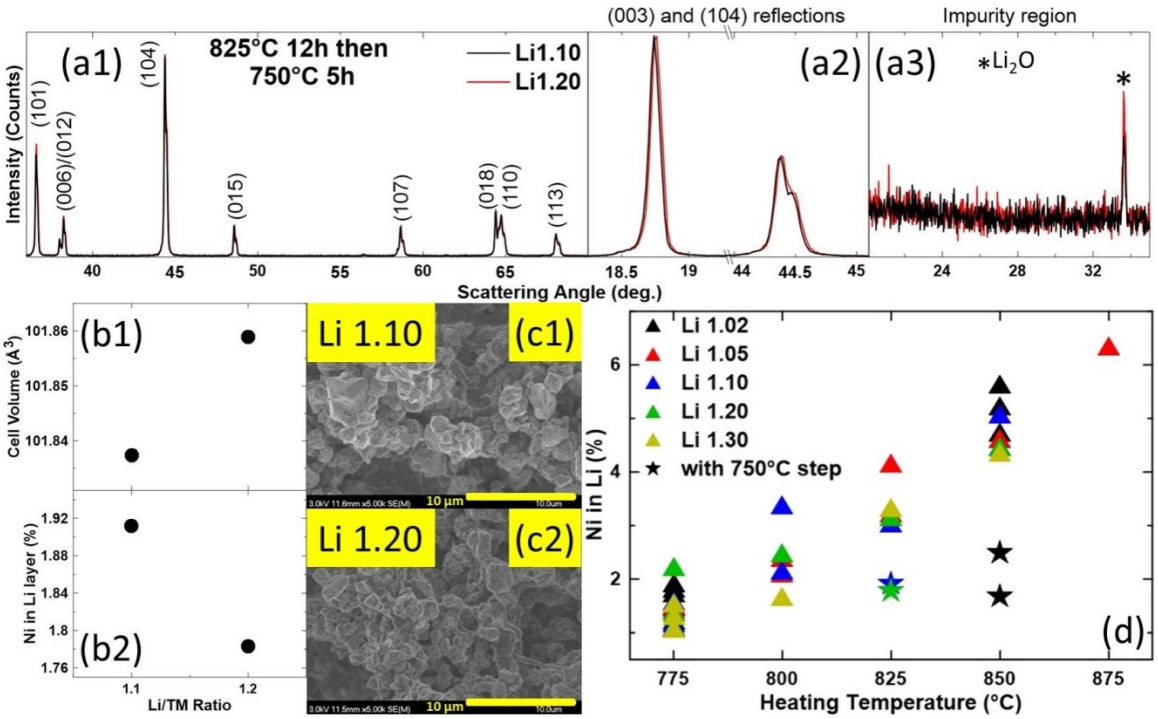

Figure 6.10: XRD patterns (Cu K_α radiation) of $LiNi_{0.975}Mg_{0.025}O_2$ samples heated first at 825°C for 12 h then 750°C for 5 h with a Li/TM (transition metal or other metal filling the transition metal role) ratio of 1.10 (black) or 1.20 (red). XRD patterns (a1) were collected from 15°-70° and expanded views of the (003) reflection (a2), the (104) reflection (a2) and the Li impurity region (a3) are included. The calculated unit cell volume (b1) and amount of Ni in the Li layers (b2) as a function of the Li/TM ratio for the samples. SEM images of the sample with a Li/TM ratio of 1.10 (c1) and 1.20 (c2). Amount of Ni in the Li layers as a function of heating temperature (d) with the inclusion of samples that were synthesized with a 750°C step after calcination (denoted with a star coloured by the Li/TM ratio of the final product).

Figure 6.10a1 shows the XRD patterns of 2.5Mg samples heated at 825°C for 12 h then 750°C for 5 h, along with expanded views of the (003) reflection and the (104) reflection (Fig. 6.10a2) and the Li impurity region (Fig. 6.10a3). Samples with a Li/TM ratio of 1.10 are shown in black and samples with a Li/TM ratio of 1.20 are shown in red. The calculated unit cell volume (Fig. 6.10b1), the amount of Ni in the Li layer (Fig.

6.10b2), SEM images of the samples (Figs. 6.10c1-6.10c2) and a revised plot of Ni content in the Li layer as a function of heating temperature (Fig. 6.10d) are also shown in Fig. 6.10. Fig. 6.10d is simply an updated plot of Fig. 6.8a which includes the Ni in the Li layer values for samples synthesized with a 750°C step after calcination (denoted with a star coloured by the Li/TM ratio of the final product) from this chapter as well as Chapter 5. Note that Chapter 5 samples (the black stars at 850°C) were synthesized by heating at 850°C for 5 h with a Li/TM ratio of 0.90 or 0.95 and taken out of the furnace, then topping off the Li/TM ratio to 1.02 and heating at 750°C for 12 h.

As was expected from heating at 825°C with Li/TM ratios of 1.10 and 1.20, Li_2O can be observed in both samples (Fig. 6.10a3). The sample with a Li/TM ratio of 1.20 had slightly more Li_2O, but otherwise the XRD patterns were similar. The refined Ni contents in the Li layer are under 2% (Fig. 6.10b2), which shows the encouraging impact of including a lower temperature step. It was reported that an annealing step promotes the reorganization of the atoms back to their respective layers but higher temperatures (> 500°C) promote oxygen vacancies which lowers the average oxidation state of the metal atom.[143] This would form more Ni^{2+} and increase the Ni content in the Li layers. It is unclear why the 750°C steps used in Chapter 5 and this chapter were able to reorder the lattice without suffering from increased oxygen vacancies leading to more Ni in the Li layer. Further work on understanding how the low temperature step impacts the Ni content in the Li layer is needed. Comparing the values to Figs. 6.2f1-6.2f4, the unit cell volume and Ni in the Li layer values (Figs. 6.10b1-6.10b2) lie in between the samples heated at 775°C and 800°C, further supporting Chapter 5 findings that unit cell volume is influenced more by the Ni content in the Li layer rather than by heating temperature.

SEM images (Figs. 6.10c1-6.10c2) show micron-sized particles (~1-4 μm), suggesting that this synthesis method can utilize higher temperatures to grow particles while avoiding the increase in Ni content in the Li layer observed in Figs. 6.2f4 and 6.8a. The benefits of this method can be seen in Fig. 6.10d, where samples heated with the inclusion of a lower temperature step can reduce the Ni content in the Li layer by more than 1%.

6.2.7 – Electrochemical Comparison of Various SC NiMg and PC NiMg Samples

With the advent of this new heating protocol, there are now three routes to synthesize SC materials that have around or under 2% Ni in the Li layer. The two-step method in Chapter 5 first heated the precursor at 850°C for 5 h with a Li/TM ratio less than 1 followed by a top up to a Li/TM ratio of 1.02 and heating at 750°C for 12 h. Particles were well grown, but the process requires an extra Li addition, grinding and heating step compared to the one-step process. Figs. 6.1 to 6.4 show that heating the sample at 775°C for 20 h with a Li/TM ratio of 1.02 can also synthesize materials with less than 2% Ni in the Li layer, but the particles are slightly undersized. Fig. 6.10 shows that heating the sample at 825°C for 12 h then 750°C for 5 h may also be suitable. There seems to be fewer drawbacks to this method since the particles are well grown and the furnace can be programmed to cool to 750°C without needing an additional grinding and heating step.

Figure 6.11 shows the voltage (vs Li/Li^+) versus specific capacity (V vs. Q, Fig. 6.11a), the differential capacity versus voltage (dQ/dV vs. V, Fig. 6.11b) and the cycling performance (Fig. 6.11c-6.11d) of the three SC 2.5Mg samples and a PC comparator.

Solid and dashed lines represent two duplicate cells for Figs. 6.11a-6.11b. The three SC samples were synthesized by the three routes to attain around 2% Ni in the Li layer: heating the sample at 775°C for 20 h with a Li/TM ratio of 1.02, heating the sample at 825°C for 12 h then 750°C for 5 h with a Li/TM ratio of 1.02, and a sample from Chapter 5 heated at 850°C for 5 h with a Li/TM ratio of 0.95 then topping up to a Li/TM ratio of 1.02 and heated at 750°C for 12 h.

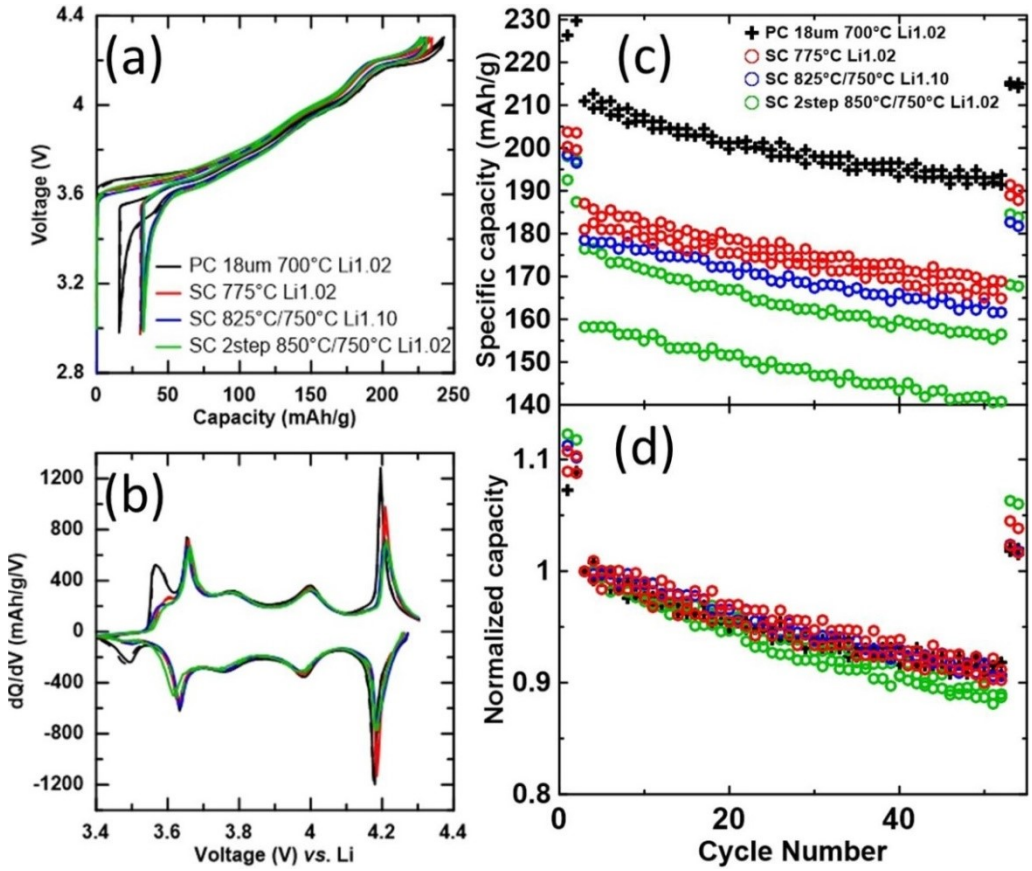

Figure 6.11: Comparison of the electrochemical performance of a polycrystalline (PC) $LiNi_{0.975}Mg_{0.025}O_2$ material synthesized using a larger precursor size (D50 ~18 μm) and single crystalline (SC) $LiNi_{0.975}Mg_{0.025}O_2$ materials synthesized in this chapter and in Chapter 5 (precursor D50 ~3 μm). Cell voltage as a function of capacity (a) and differential capacity as a function of cell voltage (b) for the initial cycles of the samples. Specific capacity (c) and normalized capacity (d) as a function of cycle number for the samples. All SC samples were separated using 20S balls.

Figure 6.11a echoes the observations from Chapter 5, PC materials have higher capacity and lower irreversible capacity than all SC materials tested. Once again, the reductions in specific capacity are far greater than reported for other SC materials.[17,90,97,99,135,218,223,224,228,235] A qualitative method to estimate the amount of residual Li is to look at the 1st charge voltage curve. With more residual Li, a higher voltage can be observed when the cell begins charging.[178–180] Fig. 6.11a suggests that the poor performance of SC materials is not due to residual Li, as slightly more residual Li may be present on the PC material than the SC materials. Like Chapter 5, dQ/dV vs. V curves (Fig. 6.11b) indicate that the capacity reductions of SC cells occur around ~3.5 V (virtually all capacity lost) and around ~4.2 V (some capacity lost), regions associated with kinetic hindrances of Li diffusion in the material.[37,240] Fig. 6.11b also shows that additional capacity is lost around ~4.2 V for the samples heated to 825°C and 850°C. Apart from the aforementioned differences, the dQ/dV vs. V curves of the 4 samples display a very similar electrochemical behavior. Fig. 6.11c suggests a possible trend of lower capacity with higher heating temperature, but more work is needed to confirm this observation. Fig. 6.11d shows that all the materials have similar capacity retention, contrary to previous reports that SC materials experience less capacity fade than PC materials.[17,53,92,97,135,137,162,218,223,224,229,232–235] It should be noted that the SC materials underwent particle separation but some particle aggregates are still present, so the capacity retention can probably be improved further with better separation techniques. In Chapter 5, the analysis of the dQ/dV vs. V curves of PC and SC NiMg materials at the start and end of cycling suggest that the main mode of degradation for PC NiMg cells is related to structural change, specifically in the low V kinetic hindrance region. On the

other hand, the structure of the SC material seems to be more stable and the main mode of degradation for SC NiMg cells seems instead to be a large increase in the polarization of the cell. Fig. 6.11 highlights the need to understand and address the issues with these Co-free Ni-rich SC materials.

6.2.8 – Investigation into the Capacity Reduction of SC Materials

Figure 6.12 shows two experiments to further investigate the lower capacity of SC materials. The first experiment compared SC and PC synthesis conditions using both SC and PC precursors (D50 ~3 μm and ~18 μm, respectively). The PC synthesis conditions are heating the samples at 700°C for 20 h with a Li/TM ratio of 1.02 and the SC synthesis conditions are the same except with a 775°C heating temperature. The second experiment cycled SC materials at different temperature to see if the capacity could be recovered. Due to sample availability at the time of experiment, the sample tested was a suboptimal material with a Ni in the Li layer content of ~2.5%. The V (vs Li/Li^+) vs. Q (Fig. 6.12a) and the dQ/dV vs. V (Fig. 6.12b) of the first experiment are shown on the left side of Fig. 6.12 while the V (vs Li/Li^+) vs. Q (Fig. 6.12c) and the dQ/dV vs. V (Fig. 6.12d) of the second experiment are shown on the right side. Solid and dashed lines represent two duplicate cells. The varying conditions are labelled, with the 2 digit temperatures representing the cycling temperature for the second experiment (Fig. 6.12c-6.12d).

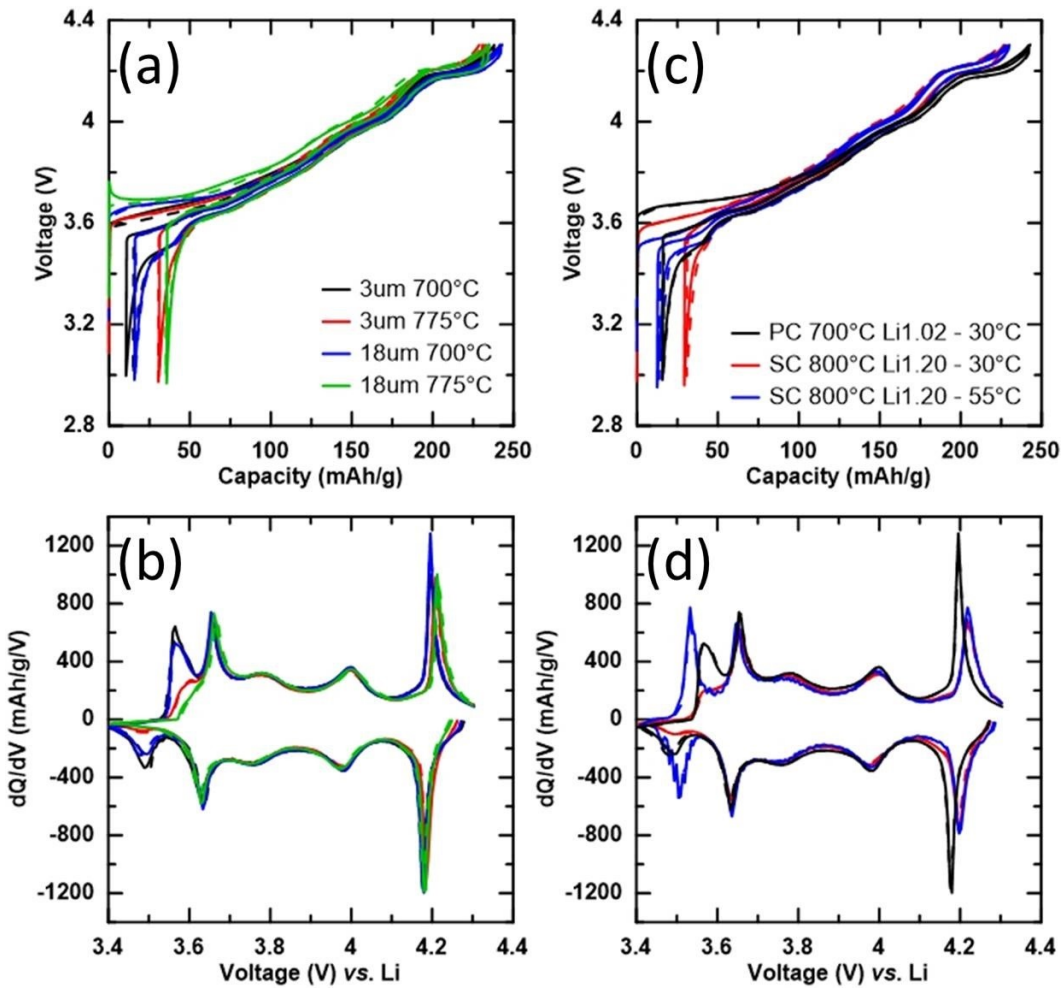

Figure 6.12: Cell voltage as a function of capacity (a) and differential capacity as a function of cell voltage (b) for the initial cycles of PC and SC $LiNi_{0.975}Mg_{0.025}O_2$ samples synthesized using different precursor sizes and heated to different temperatures. Cell voltage as a function of capacity (c) and differential capacity as a function of cell voltage (d) for PC and SC samples cycled at different temperatures.

Figure 6.12a clearly shows that the capacity reductions stem from the use of higher heating temperatures, needed to synthesize SC materials. Materials heated to 775°C showed slightly lower charge capacities and much lower discharge capacities, resulting in higher irreversible capacities. Using smaller precursors reduced the irreversible capacity slightly, but to a smaller extent than heating temperature. Fig. 6.12b

reinforces these observations; materials heated to 775°C having slightly smaller features ~4.2 V during charge and almost no features ~ 3.5 V. No effect of precursor size can be seen in the ~4.2 V features but can be observed in the ~3.5 V features, to a lesser extent than heating temperature again. Figs. 6.12a and 6.12b show that primary particle growth affects the capacity and electrochemical behaviour of the material more than secondary particle size, suggesting that lattice diffusion is slower than grain boundary diffusion.[277–280]

Figure 6.12c shows that cycling SC materials at 55°C cannot recover the lower charge capacity but the discharge capacity is greatly increased, resulting in a similar irreversible capacity for SC materials cycled at 55°C and PC materials cycled at 30°C. The SC cells cycled at 30°C have a discharge capacity of ~196 mAh/g while cells cycled at 55°C have a discharge capacity of ~216 mAh/g. Fig. 6.12d shows that cycling at 55°C does not affect electrochemical activity near 4.2 V but the recovered capacity stems from the ~3.5 V region.

Numerous SC Ni-rich studies have reported a lower capacity of SC materials when compared to the PC counterpart.[17,90,97,99,135,218,223,224,235] SC materials with 80% or more Ni seem to corroborate with Chapter 5 and this chapter that the capacity reductions stem mainly from a loss of capacity near 3.5 V with minor contributions from ~4.2 V.[90,139,218,223,224,226,228,237] Both of these voltage regions have been associated with kinetic hindrances of Li diffusion in the material, with the hindrances being stronger at ~3.5 V.[37,240] As materials become more Ni-rich, there is more capacity in these voltage regions,[21,149,196,205] so this may be why SC materials in this series report a larger capacity reduction than other SC works. This will be explored in more detail in the next chapter.

The kinetic hindrances to Li diffusion at low and high states of charge were discussed in Section 2.5. Theoretical work has shown that the dominant mechanism of Li diffusion is through divancancies and the kinetic hindrance at low states of charge (~3.5 V) stem from the limited number of divacancies available (Fig. 2.7).[37,239] SC materials likely exacerbate this kinetic hindrance due to longer Li diffusion pathways for the Li to diffuse in and out of the larger grains. Larger particle sizes would be more hindered as well, since Li needs to diffuse to and from the surfaces in contact with the electrolyte. This is observed in Fig. 6.12b, with both SC materials and larger particle sizes showing less capacity in the ~3.5 V region. Cycling at higher temperatures would facilitate vacancy migration and increase the frequency of divacancies, lowering the kinetic hindrance. This explains the recovered capacity in Figs. 6.12c-6.12d which has been observed in previous reports on PC Ni-rich materials as well.[21,240] The kinetic hindrance at high states of charge (~4.2 V) has been attributed to the collapse of the interlayer spacing as Li layers are emptied.[37,239] SC materials may experience more kinetic hindrance at this region due to larger primary particle sizes which amplify the effects of the reduction in Li diffusion constant which occurs at high states of charge. The interlayer spacing is heavily dependent on the Li content of the material,[21,157,217] so it may be possible that temperature does not have a significant effect on Li diffusion at this voltage region as observed in Fig. 6.12d.

6.3 – Conclusions

This chapter studied the synthesis of Co-free single crystalline Mg-substituted LNO using a one-step lithiation method. Higher heating temperatures promoted grain growth, but also increased the Ni content in the Li layer. Increasing the Li/TM (transition

metal or other metal filling the transition metal role) ratio does not seem to have an effect on grain growth at lower temperatures (775°C or 800°C) but influences the formation of Li_2O impurity. The separation of particle aggregates is required to improve the cycling performance of the material. Materials with a higher Mg content have less capacity with no clear benefit to capacity retention. The utilization of a lower temperature step after the calcination step can reduce the Ni content in the Li layer below what would be expected at the calcination temperature, and this can be used to grow larger grains while keeping an acceptable amount of Ni in the Li layer. However, all Mg-containing SC materials tested are still not yet competitive with PC materials and have lower capacities, higher irreversible capacities, and similar cycling fade. The lower capacities of SC materials stem from increased kinetic hindrances to Li diffusion at ~3.5 V and ~4.2 V compared to PC materials. The SC cells cycled at 55°C can recover ~20 mAh/g of discharge capacity and have similar irreversible capacity compared with PC cells cycled at 30°C.

Chapter 7 – Miscellaneous Investigations of Ni-rich Positive Electrode Materials

Results from Chapters 4 to 6 sparked some questions and directions to investigate. This chapter discusses two of these miscellaneous studies on topics that may merit more in-depth exploration. Section 7.1 will investigate some factors that affect capacity in the low voltage kinetic hindrance region and Section 7.2 will discuss a method to track the fate of lithium in the synthesis of $Li_y[Ni_{1-x}Mn_x]O_2$ under different atmospheres.

7.1 – Factors that Affect Capacity in the Low Voltage Kinetic Hindrance Region of Ni-Rich Positive Electrode Materials

Chapter 4 and other works observed that the irreversible capacity (IRC) of the material increases quite linearly as the substituent content of LNO increases, except when Co is the substituent.[21,149,200,205] Section 2.5 discusses in detail how the IRC is related to kinetic hindrances to Li diffusion. Previous work has shown that substituents for Ni change the potential energy landscape of Li.[21] For example, the energies of two Li sites at opposite vertices from a Mg atom are lowered, "locking" them in place, acting as pillars that hinder the collective diffusion of Li. This forces the particle surface to fill with Li at a lower average concentration, reducing the discharge capacity and thereby increasing the IRC. A similar phenomenon may occur for some other substituents observed to reduce the capacity in this region.[21,196,205] The degree of kinetic hindrance may plateau above a certain substituent threshold, since studies on materials with 80% Ni or below have found negligible effect on the IRC from varying Ni content.[238,245,246]

The effect of kinetic hindrance on IRC is also found in single crystalline (SC) materials. Chapters 5 and 6 showed that the capacity of SC materials with a composition of more than 95% Ni was significantly lower (~30 mAh/g) than polycrystalline (PC) materials of the same composition. Analysis of differential capacity curves under different conditions show that the capacity reductions mainly stem from the regions associated with kinetic hindrances related to Li diffusion, likely due to the increased Li diffusion length in and out of the larger grains. While not explicitly discussed, several works on SC Ni-rich materials corroborate the occurrence of lower capacity in the kinetic hindrance regions.[90,139,218,223,228,237] As research continues to increase the Ni content of SC materials, the capacity reductions and increased IRC will become more significant, therefore further understanding of kinetic hindrances related to Li diffusion is important.

This section carries out an investigation of factors that affect material capacity in the low voltage kinetic hindrance region (3.0-3.6 V). These factors include: composition, primary and secondary particle sizes, cycling temperature and lower cutoff voltage (LCV). The results in this section make up a portion of a manuscript published in the Journal of the Electrochemical Society.[280]

7.1.1 – Experimental Design

Samples were synthesized using metal hydroxide precursors obtained from Zoomwe. $Ni_{1-x}Mg_x(OH)_2$ (x = 0-0.05, D50 ~18 μm), $Ni_{0.9}Co_{0.05}Al_{0.05}(OH)_2$ (D50 ~3/10/18 μm) and $Ni_{0.975}Mg_{0.025}(OH)_2$ (D50 ~3 μm) precursors were used to make the 3 series of samples in this section. The synthesis procedure was carried out as described in Section 3.1. The precursor materials were mixed with $LiOH{\bullet}H_2O$ in a Li/TM (transition

metal or other metal filling the transition metal role) ratio of 1.02 (unless otherwise stated) and heated (including preheat steps) at 700°C for 20 h (unless otherwise stated).

The first series of samples used $Ni_{1-x}Mg_x(OH)_2$ (x = 0-0.05) precursors and will be denoted as the NiMg 18 µm series, and individual samples will be denoted as NiMg 100-y/y (y = x * 100). The second series of samples used $Ni_{0.9}Co_{0.05}Al_{0.05}(OH)_2$ precursors and will be denoted as the NCA 90/5/5 series, and individual samples will be denoted by the D50 of the precursor (3, 10 and 18 µm). These samples were heated to 725°C for 20 h. The third series of samples used $Ni_{0.975}Mg_{0.025}(OH)_2$ precursors and will be denoted as NiMg 97.5/2.5 3 µm series, and individual samples will be denoted by their heating temperature. The samples heated at 800°C and 850°C used a Li/TM ratio of 1.10 and 1.30, respectively, to help account for Li loss and the samples were heated for 12 h only. Samples in the NiMg 18 µm series have already been discussed in Chapter 4 and some samples in the NiMg 97.5/2.5 3 µm series have already been discussed in Chapter 6. Table 7.1 (below Fig. 7.1) contains a summary of the series and samples within each series.

XRD and SEM characterizations were carried out as described in Sections 3.2 and 3.3, respectively. Samples in the NiMg 97.5/2.5 3 µm series heated to 775°C and above were separated as described in Section 3.7.1 before electrode preparation. Coin cells were assembled as described in Section 3.7 with 1.0 M $LiPF_6$ in EC:DEC (1:2 v/v) as the electrolyte for the NiMg 18 µm series and the NCA 90/5/5 series, and with 1.0 M $LiPF_6$ in FEC:DMC (1:4 v/v) as the electrolyte for the NiMg 97.5/2.5 3 µm series. Electrochemical testing was carried out as described in Section 3.8. N. Zhang conducted the material synthesis and characterization of NiMg 100/0 and NCA 90/5/5 18 µm. E.

Lyle conducted the material synthesis and characterization of NiMg 97.5/2.5 3 µm samples heated at 725°C and 750°C. P. Arab conducted the electrochemical characterization of some samples in the NiMg 97.5/2.5 3 µm series.

7.1.2 – Results and Discussions

Figure 7.1 shows the XRD patterns of the synthesized samples in the 3 series. An expanded view of the (003) and the (104) reflections and an expanded view of the impurity region are shown. The XRD patterns of the samples in the NiMg 18 µm series have already been shown in Chapter 4 and the XRD patterns of some samples in the NiMg 97.5/2.5 3 µm series have already been shown in Chapter 6. The expanded view of the impurity region shows that all the synthesized materials did not have an appreciable amount of surface impurities,[110,131,157,172–182] as could be detected by XRD, except for the samples in the NiMg 97.5/2.5 3 µm series heated to higher temperatures, which showed some traces of Li_2O and perhaps some traces of Li_2CO_3 for the sample heated to 850°C, which used a Li/TM ratio of 1.30.

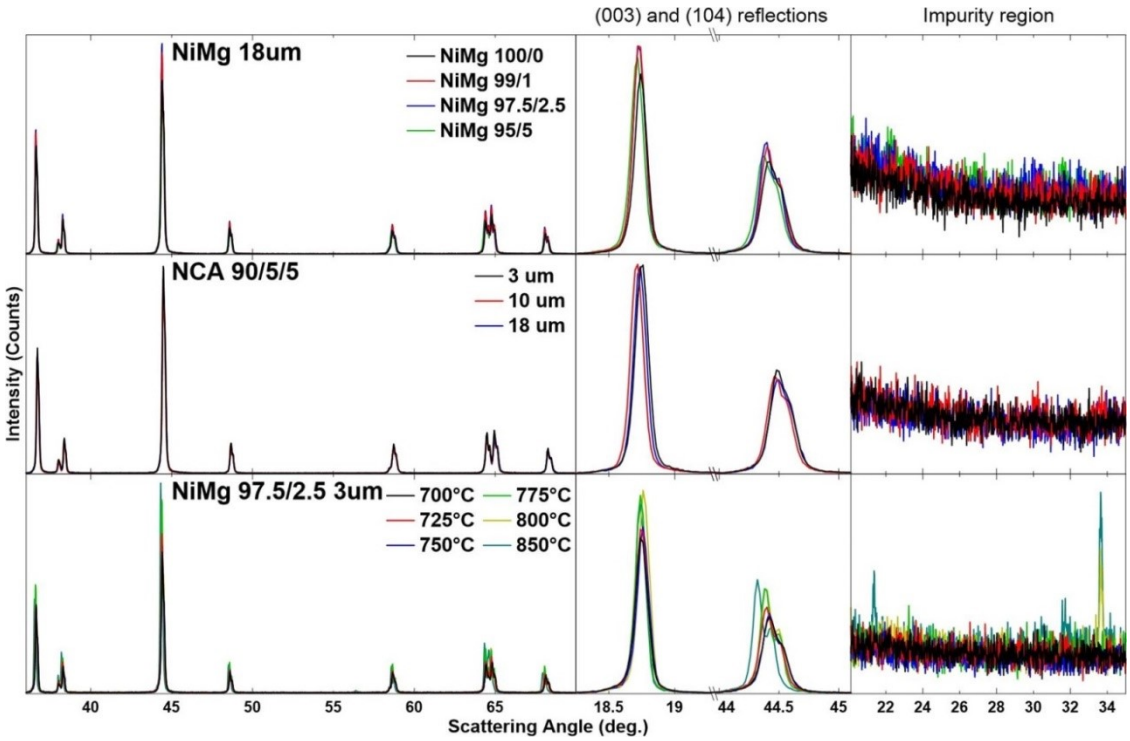

Figure 7.1: XRD patterns (Cu Kα radiation) of samples in the NiMg 18 µm, NCA 90/5/5 and NiMg 97.5/2.5 3 µm series collected from 35°-70° along with the expanded views of the (003) and (104) reflections and the Li impurity region. All samples were synthesized with a Li/TM (transition metal or other metal filling the transition metal role) ratio of 1.02 except for the NiMg 97.5/2.5 3 µm samples heated to 800°C and 850°C, which were synthesized with a Li/TM ratio of 1.10 and 1.30, respectively.

Table 7.1 lists the Rietveld refinement results for the synthesized samples in the 3 series. In general, the unit cell volume increases as the amount of Mg increases and as the heating temperature increases. The amount of Ni in the Li layers stays around 0.4-2% unless the samples are heated to a higher temperature. Varying the particle size has no significant impact on the unit cell volume or the Ni content in the Li layer. More discussion about the impact of Mg content or heating temperature on the refined parameters can be found in Chapters 4 and 6.

Table 7.1: The synthesized samples, separated by series, shown in Figure 7.1 and their unit cell lattices, calculated unit cell volume and amount of Ni in the Li layers.

Series	Sample	a (Å) (±0.0002)	c (Å) (±0.001)	Vol (Å^3) (±0.005)	Ni_{Li} (%) (±0.3)
NiMg 18µm	NiMg 100/0	2.8750	14.199	101.640	1.78
	NiMg 99/1	2.8750	14.192	101.590	0.79
	NiMg 97.5/2.5	2.8761	14.197	101.703	0.99
	NiMg 95/5	2.8769	14.213	101.875	1.36
NCA 90/5/5	3 µm	2.8690	14.192	101.166	0.46
	10 µm	2.8677	14.190	101.060	0.47
	18 µm	2.8677	14.197	101.110	0.71
NiMg 97.5/2.5 3µm	700°C	2.8751	14.194	101.611	0.76
	725°C	2.8776	14.201	101.837	1.99
	750°C	2.8761	14.196	101.696	0.98
	775°C	2.8771	14.193	101.745	1.49
	800°C	2.8789	14.195	101.887	2.16
	850°C	2.8830	14.202	102.228	4.38

Figure 7.2 shows the voltage versus specific capacity (V vs. Q, Figs. 7.2a1-7.2c1), the differential capacity versus voltage (dQ/dV vs. V, Figs. 7.2a2-7.2c2) and an expanded view of the low voltage region of dQ/dV vs. V (Figs. 7.2a3-7.2c3) for the synthesized materials as sorted by series. Data for the NiMg 18 µm series are shown in Figs. 7.2a1-7.2a3, the NCA 90/5/5 series in Figs. 7.2b1-7.2b3 and the NiMg 97.5/2.5 3 µm series in Figs. 7.2c1-7.2c3. Solid and dashed lines represent two duplicate cells. Fig. 7.2d shows the SEM images of NiMg 97.5/2.5 18 µm heated to 700°C and NiMg 97.5/2.5 3 µm heated to 750°C, 775°C and 850°C.

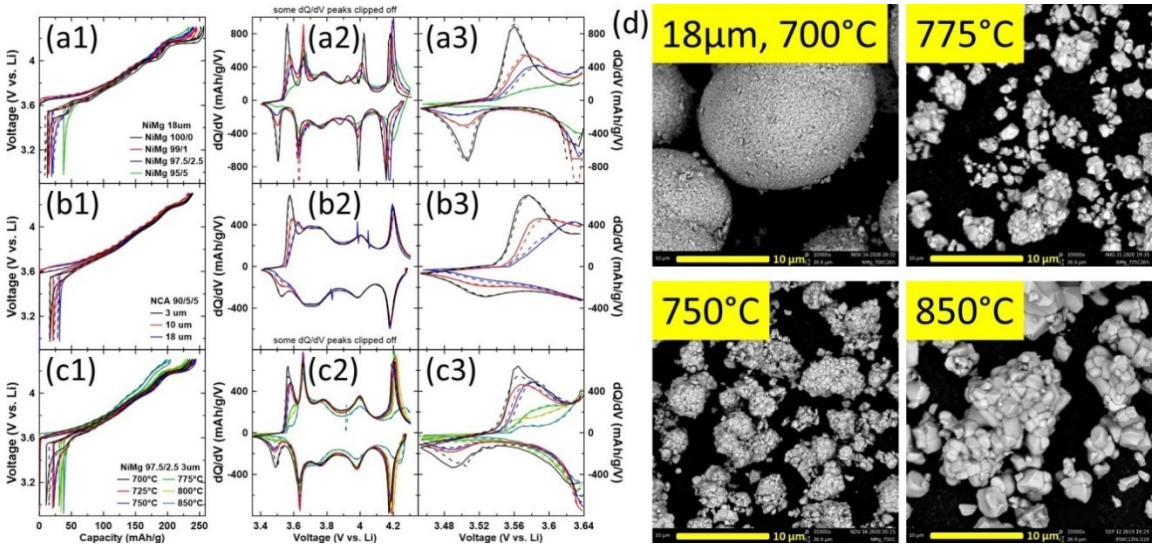

Figure 7.2: Cell voltage as a function of capacity (a-c1), differential capacity as a function of cell voltage (a-c2) and an expanded view of the low voltage region of the differential capacity plot (a-c3) for the samples in the NiMg 18µm, NCA 90/5/5 and NiMg 97.5/2.5 3µm series. SEM images of select samples of the NiMg 97.5/2.5 3µm series (d), except where labelled.

Figure 7.2a1 shows that as the Mg content increases from 0% to 5%, the 1st cycle charge capacity decreases and the irreversible capacity (IRC) increases. Fig. 7.2b1 shows that as the secondary particle size increases from 3 µm to 18 µm, the 1st cycle charge capacity remains the same but the IRC increases. For samples with different secondary particle sizes heated to the same temperature, it is expected that the primary particle sizes remain similar, but was not confirmed.. Fig. 7.2c1 shows that as the heating temperature increases from 700°C to 850°C, the 1st cycle charge capacity decreases and the IRC increases, similar to Fig. 7.2a1.

The impact of the three variables (Mg content, secondary particle size, heating temperature) can be seen more clearly in the dQ/dV vs. V curves (Figs. 7.2a2-7.2c2). Increasing the Mg content (Fig. 7.2a2) smooths out the features in the dQ/dV vs. V

curves stemming from the suppression of the phase transitions observed in LNO, and this has been observed in previous works and with other substituents.[21,149,205] Increasing the secondary particle size (Fig. 7.2b2, no differences in primary particle size expected), on the other hand, only seems to impact the feature in the low voltage region (~3.6-3.8 V) and leaves the rest of the dQ/dV curve virtually unchanged. Increasing the heating temperature (Fig. 7.2c2), which led to increasing primary particle sizes (Fig. 7.2d), seems to impact mainly the features at the low and high voltage regions as observed in Chapters 5 and 6.

Since all three variables affect the features in the low voltage region, expanded views of the dQ/dV vs. V curves are shown in Figs. 7.2a3-7.2c3. It is clear that the dQ/dV features in this region become increasingly small as the variables (Mg content, secondary particle size, heating temperature) increased. In the heating temperature series (Fig. 7.2c3), there is a large reduction in the size of the low voltage region feature going from a heating temperature of 750°C and 775°C. Fig. 7.2d shows the SEM images of the impact of heating temperature on the samples. The samples heated at 700°C and 750°C remain polycrystalline, although there is some primary particle growth observed for the sample heated at 750°C. The sample heated at 775°C shows accelerated particle growth, to the point that the primary particles can be separated into single crystal materials as shown in Chapter 6. The primary particles of the sample heated at 850°C have grown even larger. As the primary particle size increased (Fig. 7.2d), the size of the low voltage region feature in the dQ/dV vs. V curve (Fig. 7.2c3) grew smaller.

Figure 7.2 shows that various factors affect how much capacity can be attained from the low voltage region, and this is correlated with the 1st cycle IRC. The voltage

region shown in Figs. 7.2a3-7.2c3 is affected by kinetic hindrances to Li diffusion.[21,238,240,245] Fig. 7.2a3 shows that capacity in this region increases for increasingly Ni-rich compositions. As discussed in Section 2.5, the Li ions "locked in" by Mg act as pillars that must be circumvented and hinder the collective diffusion of Li within the layer, The second series (Fig. 7.2b3) varied secondary particle sizes and saw a reduction in capacity in this region for larger secondary particles (with no expected difference in primary particle sizes). The third series (Fig. 7.2c3), which varied heating temperatures leading to different primary particle sizes (Fig. 7.2d), also saw a reduction in capacity in the low voltage region as primary particle sizes increased. This indicates that increasing the path length for Li to travel in and out, whether that be from the primary particles to grain boundaries or grain boundaries to the surface of the secondary particles, will reduce the amount of Li that can be reinserted and extracted. The degree of Li reinsertion is dependent on the degree of kinetic hindrance presented by the material. By reducing the kinetic hindrance, such as by lowering the amount of substituents or decreasing the path length for Li to travel, more Li can be reinserted and the IRC is lower. This simple explanation is not complete since it ignores the contribution of other processes, such as cation disorder and SEI formation, but it shows how the low voltage kinetic hindrance region is correlated to IRC. This could mean that the IRC of a material can be reduced if cycling conditions can reduce the degree of kinetic hindrance.

Cycling temperature is a clear choice to test if cycling conditions can reduce the degree of kinetic hindrance. Figure 7.3 shows the V vs. Q curves (Figs. 7.3a1-7.3d1) and the dQ/dV vs. V curves (Figs. 7.3a2-7.3d2) for the NCA 90/5/5 series (Figs. 7.3a1-7.3b2) and the NiMg 97.5/2.5 3 μm series (Figs. 7.3c1-7.3d2) cycled at 30°C (Figs. 7.3a1-7.3a2

and 7.3c1-7.3c2) and at 55°C (Figs. 7.3b1-7.3b2 and 7.3d1-7.3d2). Solid and dashed lines represent two duplicate cells. The 30°C data is the same as in Fig. 7.2 (Figs. 7.2b1-7.2b2 and 7.2c1-7.2c2) and is shown here for ease of comparison.

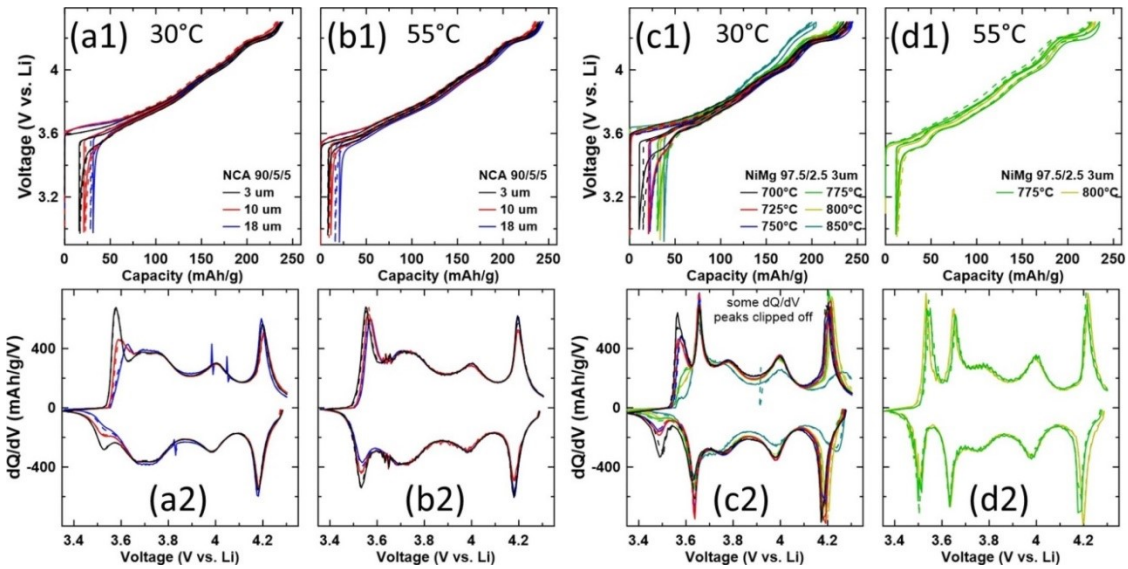

Figure 7.3: Cell voltage as a function of capacity and differential capacity as a function of cell voltage for the samples in the NCA 90/5/5 (a1, a2) and NiMg 97.5/2.5 3µm series (c1, c2) cycled at 30°C. Similar plots for the samples in the NCA 90/5/5 (b1, b2) and NiMg 97.5/2.5 3µm series (d1, d2) cycled at 55°C are shown with the same axes as the 30°C plots.

The impact of cycling cells at 55°C is quite clear. Comparing the V vs. Q curves of the NCA 90/5/5 series (Figs. 7.3a1-7.3b1) shows that cycling cells at 55°C has a negligible effect on the 1st charge capacity but the discharge capacity increases, reducing the 1st cycle IRC. Likewise, the NiMg 97.5/2.5 3 µm series (Figs. 7.3c1-7.3d1) shows that the materials with significant IRC at 30°C can have small IRC when cycled at 55°C. This is seen more clearly when looking at the dQ/dV vs. V curves (Figs. 7.3a2-7.3d2). NCA 90/5/5 materials cycled at 30°C (Fig. 7.3a2) showed remarkably similar dQ/dV vs. V behavior to materials cycled at 55°C (Fig. 7.3b2) except for the low voltage region.

There is more capacity attained in the low voltage region and the differences between the secondary particle sizes are reduced but still present. For the NiMg 97.5/2.5 3 µm series, only materials heated to 775°C and 800°C were cycled at 55°C (Fig. 7.3d2), but both materials had significantly more capacity in the low voltage region cycling and lower IRC at 55°C than at 30°C (Fig. 7.3c2).

Figure 7.4 shows the impact of decreasing the LCV from 3 V to 2 V. The V vs. Q curves (Figs. 7.4a1-7.4b1) and the dQ/dV vs. V curves (Figs. 7.4a2-7.4b2) for a NiMg 97.5/2.5 3 µm material heated to 775°C being cycled at 30°C and at 55°C are shown. Cells cycling to a LCV of 3 V (shown previously in Figs. 7.3c1-7.3d2) are represented by black lines and red lines represent cells cycling to a LCV of 2 V. Solid and dashed lines represent two duplicate cells.

Figures 7.4a1-7.4b1 show that using a LCV of 2.0 V can reinsert slightly more Li into the material and reduce the IRC by a small amount. For clarity, the numbers shown in Figs. 7.4a1-7.4b1 are the capacity at which the cells finish their 1st discharge, which is also the IRC. At 30°C, the IRC for NiMg 97.5/2.5 3 µm heated to 775°C can be reduced by ~6 mAh/g, whereas the IRC reduction is larger (~9.5 mAh/g) when cycled at 55°C, bringing the IRC of the cell down to less than 1%. The dQ/dV vs. V curves (Figs. 7.4a2-7.4b2) show that some of the extra capacity came near 2 V during discharge but was recovered near 3.55 V during charge. This effect has been observed before.[243,244]

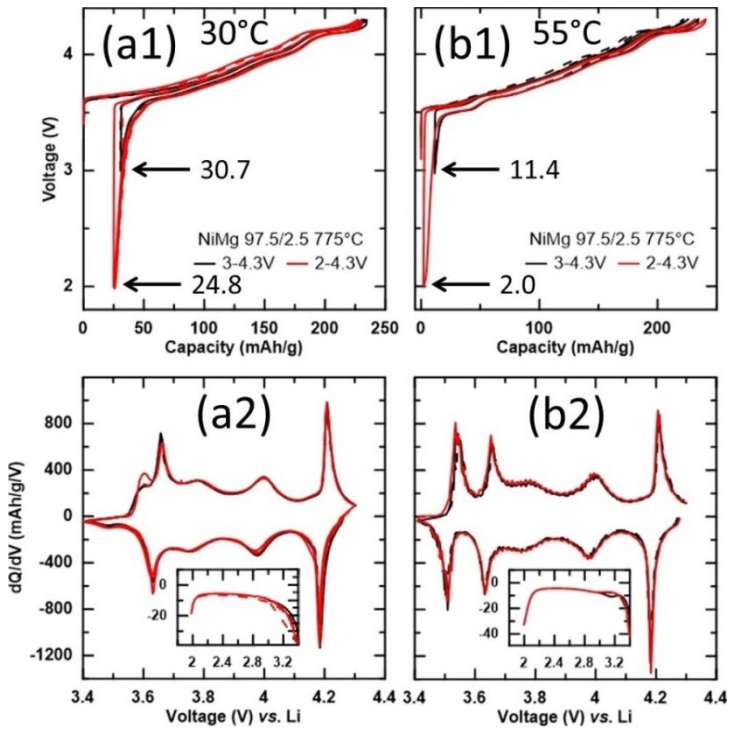

Figure 7.4: Cell voltage as a function of capacity and differential capacity as a function of cell voltage for NiMg 97.5/2.5 samples heated at 775°C cycled at 30°C (a1, a2) and at 55°C (b1, b2) and cycled to different lower cut-off voltages.

Figures 7.3 and 7.4 confirm that the IRC can be reduced by selecting certain cycling conditions. By increasing the cycling temperature, the Li/vacancy migration at low SOC is boosted, allowing more Li to diffuse into the material before the particle surface is filled. The driving force to reinsert the Li is increased by lowering the LCV, allowing more Li to be reinserted before reaching the cut-off voltage, perhaps through the formation of a surface layer of Li-excess metal oxide improving diffusion of lithium into the host as reported by some previous studies.[241,243,244] Although only 2 conditions are reported in this section to reduce the degree of kinetic hindrance and the IRC, these variables (cycling temperature[238,240] and LCV[243,244] as well as rate,[240,243] calendaring[238] and constant current-constant voltage (CCCV) discharge[238,245] have been reported in the literature as being able to reduce the IRC in Ni-rich materials. These variables can all be

understood to reduce the IRC by enhancing the kinetics (cycling temperature, rate), driving force (LCV, CCCV discharge) or reducing the diffusion path length by cracking particles (calendaring). While this section was able to reduce the IRC to as low as 2 mAh/g (<1%), realistically this cannot be utilized since a full cell will have to contend with the IRC of graphite and gaining capacity at ~2 V during discharge but ~3.55 V during charge is not energetically efficient.

7.1.3 – Follow up: Li Diffusion Coefficient Measurements by N. Phattharasupakun

Figures 7.1-7.4 show that understanding the kinetic hindrances of Li diffusion and how to reduce the kinetic hindrances are important to realizing the capacity and rate capability of a material. As such, the ability to measure Li diffusion in a systematic way will be key to further understanding and comparing different Ni-rich materials. The Dahn lab has begun measuring the solid-state Li chemical diffusion coefficient with a method denoted as the "Atlung Method for Intercalant Diffusion" (AMID).[281] The details and procedures of the diffusion studies are outside the scope of this thesis, but more information can be found[280] or will be upcoming.[282,283] An excerpt of the diffusion studies on PC and SC NiMg is included in this section as a follow up on results from Chapters 5, 6 and Section 7.1, and this excerpt makes up some of the other portion of the manuscript published in the Journal of the Electrochemical Society.[280] A. Liu synthesized the materials and N. Phattharasupakun conducted the material characterization in this section, with assistance from P. Scallion for the SEM imaging. M. Cormier devised the fitting procedure to extract the diffusion coefficients for the AMID measurements.

Figure 7.5 shows the Li chemical diffusion coefficient of NiMg 97.5/2.5 SC and PC samples as calculated by the AMID measurements as well as their corresponding

SEM images. The measurements were carried out at 30 and 55°C with two duplicate cells for each condition. The Li chemical diffusion coefficient was higher when cycling at 55°C compared to cycling at 30°C, which is not surprising. The diffusion coefficients as a function of voltage follows similar trends as previously reported,[37,228,238–240] where the diffusion coefficients at low and high states of charge are reduced. As discussed in Section 2.5, the reduction of the diffusion coefficients at low states of charge (3.5-3.6 V) stems from the limited number of divacancies available, reducing the abundance of tetrahedral site hops and forcing more Li atoms to hop through O-O dumbbells, which are less energetically favorable.[37,239] The reduction of the diffusion coefficients at high states of charge (4.2-4.3 V) stems from the contraction of the interlayer spacing, which increases the Li migration barrier. It is important to note that fits below 3.5 V were poor because the available capacity below 3.5 V is negligible; a large fraction of the capacity below 3.6 V lies between 3.5 and 3.6 V.

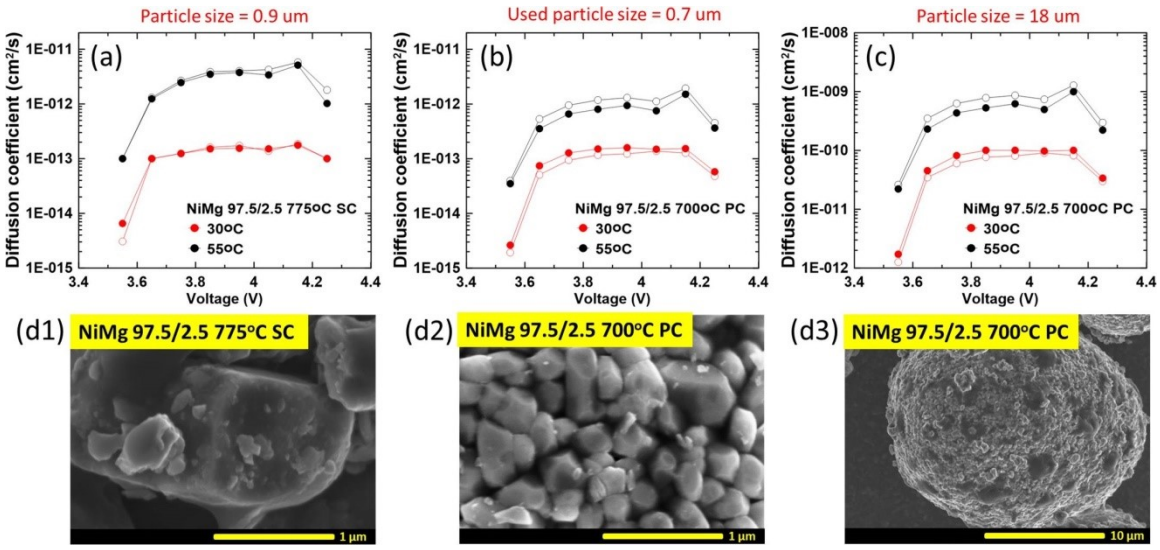

Figure 7.5: Li chemical diffusion coefficient as a function of voltage of (a) NiMg-SC, (b, c) NiMg-PC and SEM images of (d1) NiMg-SC, (d2, d3) NiMg-PC. The particle sizes used in the calculations are shown above the graphs.

Figure 7.5c shows that the Li chemical diffusion coefficients of NiMg PC calculated from the average particle size of 18 μm were several orders of magnitude greater than that of the SC sample calculated with the secondary particle size of 0.9 μm (Fig. 7.5a). The single crystalline particles have larger primary particle sizes and no grain boundaries, so the in-plane lattice diffusion paths are long.[284] This would lead to a large impact of primary particle size on the rate performance of SC materials.[237] On the other hand, the polycrystalline sample contains agglomerated, smaller primary particles. Li diffusion in PC materials occur along primary particle grain boundaries within secondary particles, where there may not be electrode-electrolyte interfaces, and within the lattice of primary particles, which have much shorter diffusion path lengths compared to SC materials. When using an "effective" particle size of 0.7 μm, the fitted diffusion coefficients for the PC cells are in the same order of magnitude as the SC cells. This "effective" particle size is about 3 times larger than the average PC primary particle size of 0.25 μm (Fig. 7.5b and 7.5d2). Previous works reported that grain boundary diffusion of Li is much faster than lattice diffusion,[277–279] which can explain why using the secondary particle sizes resulted in such vastly different diffusion coefficients for the SC and PC samples. Figure 7.5 supports previous reports that grain boundary diffusion is fast, and the rate-limiting process for the Li diffusion of these materials is the bulk lattice diffusion. These results suggest that the primary particle size should be used in the AMID fitting procedure. The abrupt decrease in D_c below 3.6 V for both the SC and PC materials supports the idea that slow Li diffusion is the cause of kinetic hindrance in these materials. Additionally, this AMID measurement raises important questions about the viability of large single crystalline, Co-free Ni-rich materials in Li-ion cells to be used

in typical applications. If D is 10^{-13} cm^2/s, then the characteristic diffusion time, r^2/D, for primary particles that have a radius of 0.5, 1 and 2 microns are 7, 28 and 100 hours, respectively.

7.1.4 – Conclusions

This section studied the impact of various material parameters on the electrochemical performance of the materials, specifically in the low voltage kinetic hindrance region related to Li diffusion. Increasing the amount of substituents, increasing the secondary particle size and increasing the primary particle size were all variables found to decrease capacity in the ~3.4-3.6 V region and increase the 1st cycle IRC. Capacity in the low voltage kinetic hindrance region can be increased significantly when cycling at a higher temperature and when cycling to a lower LCV. Combining the two variables to cycle at 55°C and to a LCV of 2 V reduced the 1st cycle irreversible capacity to 2 mAh/g, or <1%.

7.2 – Tracking the Fate of Excess Li in the Synthesis of Various $Li_y[Ni_{1-x}Mn_x]O_2$ Positive Electrode Materials under Different Atmospheres

As discussed in Section 2.1.3, layered positive electrode materials were mostly synthesized in air in the past, but as the compositions become increasingly Ni-rich, syntheses need to be carried out in oxygen. Reports studying the impact of synthesis atmosphere showed that the synthesis of Ni-rich materials in oxygen will generally lead to similar or better performing materials.[27,126,131,132,144,145,147,148] However, it may be beneficial to determine when synthesis in air can produce materials with similar performance, as this can lead to lower processing costs.

An interesting finding from Chapters 5 and 6 is the beneficial impact of including a low temperature step on reducing the Ni content in the Li layer. Increasing the heating temperature, as needed to synthesize SC materials, will increase the Ni content in the Li layer because higher temperatures promote Li/oxygen loss in the material which lowers the average oxidation state of the Ni.[140–143] The low temperature step may be able to reduce the Ni content in the Li layer by allowing Ni^{2+} to migrate back into the TM layer without accelerated Li/oxygen loss.[143,276] There are some reports on the benefits of low temperature steps either right after the initial calcination step[225,227,276] or as a reheating step.[136,143,226] Obviously, having a low temperature step right after the calcination step would be more efficient, but a reheating step may enable material processing such as washing or coating prior to the reheating. Interestingly, the temperature of the beneficial low temperature step has been reported to be within 20-100°C of the initial heating temperature[136,225–227] or ~400°C cooler than the initial heating temperature,[143,276] so more work exploring the various parameters of the low temperature step would be useful. Chapters 5 and 6 showed the success of incorporating a low temperature step in reducing the Ni content in the Li layer. Preliminary work exploring the feasibility of synthesizing Ni-rich materials in air showed that Ni-rich, Mn-substituted materials heated in dry air with excess Li and incorporating a low temperature step may be promising. However, there were concerns about whether the acceptable Ni content in the Li layer was due to the material being Li-rich.

Li-rich materials were briefly discussed in Section 1.3. The metal compositions of Li-rich materials of interest generally contain less Ni and more Mn than Ni-rich materials of interest. However, with the push to reduce or eliminate

Co,[21,24,27,42,149,157,184,196,197,201,202,204–206,210–213] there may be some overlap in the metal compositions. When this is the case, the only difference in the final material is the amount of Li. For example, samples with 50% Ni and 50% Mn can be made as single phases over the range from at least $Li_{1+x}[Ni_{0.5}Mn_{0.5}]_{1-x}O_2$ for $0 < x < 0.25$.[68,71,74,285,286] With higher synthesis temperatures, there needs to be some excess Li due to Li loss during heating.[99,131–143,226,227,286] Additionally, having some excess Li may decrease the amount of Ni in the Li layer.[68,74] There are some reports varying the amount of Li used in synthesis to understand the formation of Li-rich materials.[68,74,285–287] It may be useful to carefully track the Li content in a Ni-rich material to see whether it is Li-rich and understand the conditions needed to form Li-rich materials.

Many reports on Li-rich materials do not measure the amount of Li in their material after synthesis, meaning their results may be attributed to a composition with more Li than in reality due to heating loss.[66,67,69,73–75,285,288] There are some studies that do measure the amount of Li in their material after synthesis,[68,71,286,287] and it is hard to know how prevalent this is for the hundreds of papers on Li-rich materials.[51,70,72] Careful measurements of Li content in the synthesized materials become more important for Ni-rich compositions due to the possibility of the Li existing as a residual Li impurity and not in the material. This section provides a clear and simple method for tracking where the Li went after synthesis.

To better understand the fate of Li in the synthesis of Ni-rich material, this section synthesized various Ni-rich $Li_y[Ni_{1-x}Mn_x]O_2$ (x = ~0.08, 0.2) with excess Li (Li/TM ratio of 1.15 before heating). Syntheses were carried out in either oxygen, dry air or air to explore the impact of oxygen partial pressure (oxygen and dry air) and moisture and CO_2

(dry air and air). Additionally, two series of $Li_{1+x}[Ni_{0.5}Mn_{0.5}]_{1-x}O_2$ samples were synthesized with varying amounts of excess Li (Li/TM ratio in synthesis of 1.00-1.27, leading to $0 \leq x \leq 0.12$) in oxygen and in air to help understand the impact of Mn content (or Ni content). The results in this section were incorporated into a manuscript submitted to Chemistry of Materials.[289]

7.2.1 – Experimental Design

Samples were synthesized using metal hydroxide precursors obtained from Zoomwe. Three precursors were used in this section: $Ni_{0.8}Mn_{0.2}(OH)_2$ (D50 ~16 μm) and $Ni_{0.5}Mn_{0.5}(OH)_2$ (D50 ~4 μm) which will be denoted as NiMn 80/20 and NiMn 50/50, as well as a core shell precursor consisting of an 8 μm $Ni(OH)_2$ core and a 0.75 μm thick $Ni_{0.8}Mn_{0.2}(OH)_2$ shell which will be denoted as NiMn-CS. NiMn-CS has an average Ni content ~92%. Previous work has shown that similar NiMn core shell materials generally lose their core shell structure and have a uniform Mn distribution when heated to 800°C due to interdiffusion.[212,213] This section synthesized the materials at 850°C, so it is assumed that NiMn-CS behaves similarly to a material with ~92% Ni and ~8% Mn. A fourth precursor, $Ni_{0.375}Mn_{0.625}(OH)_2$, was used for thermogravimetric analysis (TGA) and will be denoted as NiMn 37.5/62.5.

The synthesis procedure was carried out as described in Section 3.1. The precursor materials were mixed with Li_2CO_3 in a Li/TM ratio of 1.15 except for NiMn 50/50, which varied from a Li/TM ratio of 1.00 to ~1.27 (corresponding to $0 \leq x \leq 0.12$ in $Li_{1+x}[Ni_{0.5}Mn_{0.5}]_{1-x}O_2$). NiMn 50/50 samples synthesized in oxygen were mixed with $LiOH{\bullet}H_2O$ instead of Li_2CO_3. Samples were heated in a box furnace if synthesized in

air, otherwise samples were heated in a tube furnace with a gas flow of oxygen or dry air. The NiMn-CS and NiMn 80/20 samples were heated in the furnaces at 850°C for 12 hours then at 800°C for 5 hours,[225,227] while NiMn 50/50 samples were heated in the furnaces at 1000°C for 10 hours.

XRD, SEM, acid titrations and ICP-OES measurements were carried out as described in Sections 3.2, 3.3, 3.5 and 3.6, respectively. TGA experiments were conducted on NiMn 37.5/62.5 samples by R. Väli and D. Ouyang. TGA measurements were carried out using a TA Instruments SDT Q600. NiMn 37.5/62.5 precursors were mixed with Li_2CO_3 in a Li/TM ratio of 1.2 and ground before loading into the sample pan. Experiments went from room temperature up to 1050°C at a heating rate of 10°C/min under an air flow rate of 100 mL/min. NiMn-CS samples were separated as described in Section 3.7.1 before electrode preparation. Coin cells for NiMn-CS and NiMn 80/20 samples were assembled as described in Section 3.7 with 1.0 M $LiPF_6$ in FEC:DMC (1:4 v/v) as the electrolyte. Coin cells for NiMn 50/50 samples were assembled for diffusion studies and there were a few differences in the procedure than as described in Section 3.7.[280,282,283] The active material: Super S: PVDF ratio was 84:8:8 and a 40 μm notch bar was used, leading to electrode material loadings of only 0.8-1.0 mg/cm^2. Only one piece of Celgard separator was used during coin cell assembly and 1.2 M $LiPF_6$ in EC:DMC (1:1 v/v, BASF) was used as the electrolyte. Electrochemical testing was carried out as described in Section 3.8. N. Phattharasupakun conducted the material synthesis and characterization of NiMn 50/50. R. Väli and D. Ouyang conducted the TGA characterization of NiMn 37.5/62.5.

7.2.2 – Results and Discussions

Figure 7.6 shows the XRD patterns of the synthesized materials (Figs. 7.6a1-7.6b3, 7.6d1-7.6e3). An expanded view of the (003) and the (104) reflections (Figs. 7.6a2-7.6b2, 7.6d2-7.6e2) and an expanded view of the impurity region (Figs. 7.6a3-7.6b3, 7.6d3-7.6e3) are shown. Rietveld refinement results for the XRD patterns are shown on the rightmost panels (Figs. 7.6c1-7.6c2, 7.6f1-7.6f2). All materials synthesized were single phase materials and peaks associated with short-range ordering between Li and other metals in the TM layer were not observed except in NiMn 50/50 samples.[67,69,73,285] The expanded view of the impurity region (Figs. 7.6a3-7.6b3, 7.6d3-7.6e3) shows that all the synthesized materials did not have an appreciable amount of surface impurities,[110,131,157,172–182] as could be detected by XRD, except for NiMn-CS, which showed some traces of Li_2O for the sample synthesized in dry air as observed in Chapter 6. The materials synthesized in oxygen have the smallest unit cell volumes (Figs. 7.6c1, 7.6f1) and the lowest amount of Ni in the Li layer (Figs. 7.6c2, 7.6f2), although the NiMn 80/20 sample synthesized in dry air and NiMn 50/50 samples synthesized in air show only a small increase compared to oxygen synthesis. Looking only at the materials synthesized in oxygen, as the Mn content of the material increases, the Ni content in the Li layer increases as well. This is due to Mn being in a +4 oxidation state which pushes more Ni to the +2 oxidation state to maintain charge balance, and Ni^{2+} has a similar ionic radii[106] as Li^{+} and is prone to migration into the Li layer.[14,15,17,37,59,110,128,131,140–142,154,170,171] For a given composition, less Ni in the Li layer likely indicates that the material took in more Li, since that would increase the average oxidation state of Ni and reduce the amount of Ni^{2+}.

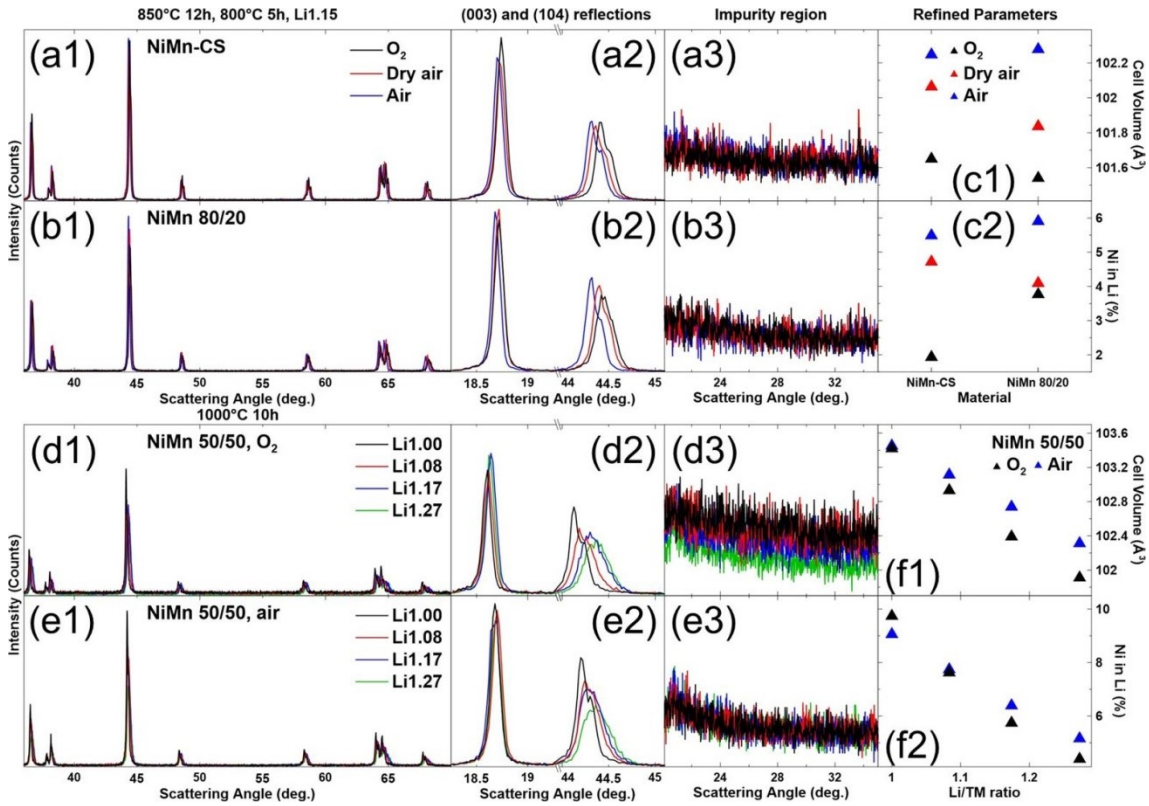

Figure 7.6: XRD patterns (Cu K_α radiation) of NiMn-CS (a1-a3) and NiMn 80/20 (b1-b3) samples synthesized under different atmospheres, collected from 35°-70° (a1-b1) along with the expanded views of the (003) reflection (a2-b2), the (104) reflection (a2-b2) and the Li impurity region (a3-b3). The calculated unit cell volume (c1) and amount of Ni in the Li layers (c2) are shown for the two materials. XRD patterns and expanded views for NiMn 50/50 synthesized in O_2 (d1-d3) and in air (e1-e3), with the calculated unit cell volume (f1) and amount of Ni in the Li layers (f2).

A closer look at Figs. 7.6a2-7.6b2 and 7.6d2-7.6e2 shows that some materials have a broader (104) reflection peak. Figs. 7.6a1-7.6b1 and 7.6d1-7.6e1 show that other reflections of those materials have broader peaks as well. The materials with most noticeable peak broadening are NiMn 80/20 synthesized in oxygen and NiMn 50/50 synthesized in both atmospheres at higher Li amounts. This peak broadening may be indicative of a material being Li-rich, since it has been suggested that the existence of Li in the TM layer may induce non-uniform stress.[99] Later experiments confirm that the

materials experiencing peak broadening are Li-rich, and this may be a qualitative method to identify when a material is Li-rich.

Figure 7.7 shows the SEM images of the NiMn-CS and NiMn 80/20 samples synthesized in oxygen, dry air and air. It appears that the synthesis conditions used in this section formed single crystalline particles for NiMn-CS materials but not for NiMn 80/20 due to lower temperatures needed for materials with higher Ni content to grow particles.[134,135,226,227] However, while NiMn 80/20 retained its polycrystalline morphology, the primary particles have grown. The synthesis atmosphere does not seem to affect the morphology or particle size for both NiMn-CS and NiMn 80/20 materials.

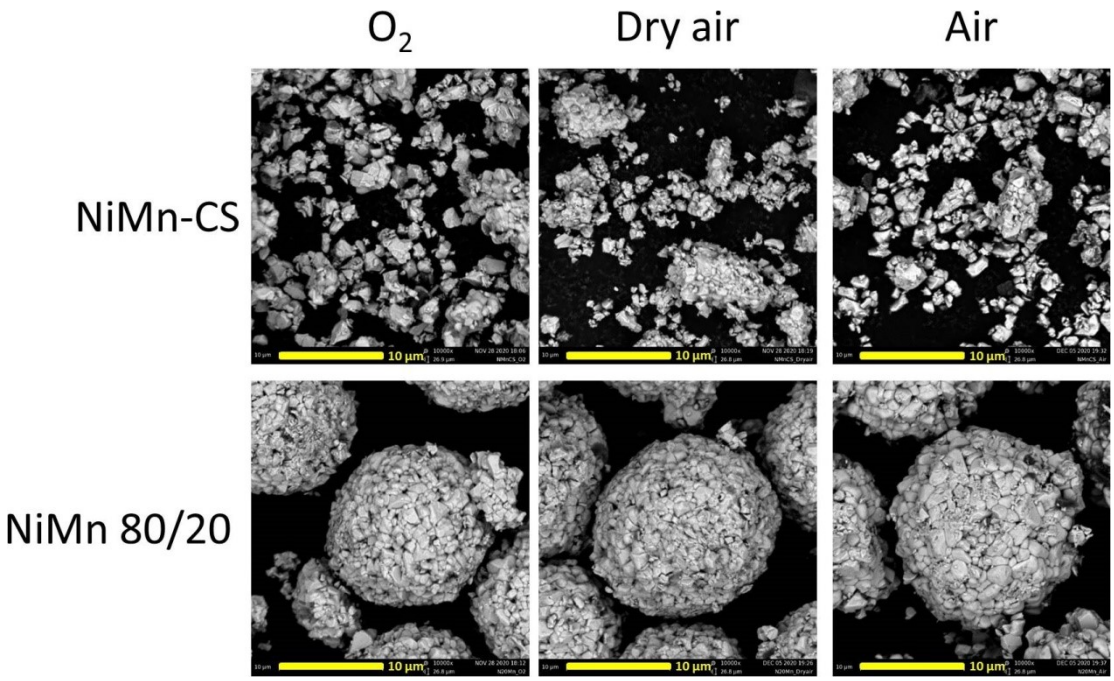

Figure 7.7: SEM images of NiMn-CS and NiMn 80/20 synthesized under different atmospheres. Samples were heated at 850°C for 12 hours then at 800°C for 5 hours.

Table 7.2 shows the normalized atomic ratios of unrinsed and rinsed NiMn-CS and NiMn 80/20 samples as measured by ICP-OES. Atomic ratios were normalized to Ni

+ Mn = 1. Since the Ni and Mn ratios were not expected to change significantly, this method allows the amount of Li to be tracked whether in excess or deficiency. The synthesized samples were used as is for sample preparation and denoted as unrinsed samples, while the rinsed samples were obtained by air drying the residue from the pour method. As can be seen later, the pour method can dissolve residual Li species while minimizing the amount of ion exchange occurring, allowing the determination of the Li content of the material in the absence of residual Li species.

Table 7.2: Elemental analysis of the unrinsed and rinsed samples using ICP-OES. Atomic ratios were normalized to Ni + Mn = 1.

	Unrinsed			Rinsed		
	Li (±0.02)	Ni (±0.02)	Mn (±0.004)	Li (±0.02)	Ni (±0.02)	Mn (±0.004)
NiMn-CS O_2	1.10	0.91	0.088	1.01	0.91	0.088
NiMn-CS dry air	1.11	0.91	0.086	0.93	0.91	0.088
NiMn-CS air	0.98	0.91	0.086	0.91	0.91	0.087
NiMn 80/20 O_2	1.10	0.79	0.211	1.10	0.79	0.214
NiMn 80/20 dry air	1.13	0.79	0.210	1.04	0.79	0.214
NiMn 80/20 air	1.00	0.79	0.211	0.98	0.79	0.214

The minimal deviation of normalized Ni and Mn atomic ratios for NiMn-CS and NiMn 80/20 samples give confidence to the Li/TM ratio determination of the samples. The Li/TM ratios of the unrinsed samples can serve as an estimate of the amount of Li that was lost during the synthesis procedure. Samples were prepared with a Li/TM ratio of 1.15 before heating and samples synthesized in oxygen and dry air were measured to have a Li/TM ratio of ~1.10. Materials synthesized in air had a much lower Li/TM ratio, suggesting that Li loss during synthesis is much higher when synthesizing in air.[132] The Li/TM ratios of the rinsed samples are indicative of the Li content of the electrode material, since residual Li species are expected to be dissolved during the pour method

rinse.[184] For rinsed NiMn-CS samples, only the sample synthesized in oxygen was fully lithiated, the samples synthesized in dry air and in air were both Li-deficient. The Li/TM ratios for rinsed NiMn 80/20 samples were all higher than the NiMn-CS sample synthesized in the same atmosphere. Rinsed NiMn 80/20 samples synthesized in oxygen and dry air appeared to be Li-rich, while the sample synthesized in air was slightly Li-deficient at a Li/TM ratio of 0.98. The Li/TM ratios for rinsed materials support earlier observations (Fig. 7.6c2) that Li uptake affects the Ni content in the Li layer, with Li-deficient NiMn-CS and NiMn 80/20 samples showing more Ni in the Li layer.

The Li/TM ratios of the rinsed samples show the impact of synthesis temperature and Mn content on the uptake of Li into the material. Samples synthesized in oxygen can take in more Li, likely due to the oxidizing nature of the atmosphere which pushes more Ni to the +3 oxidation state. It seems that a higher Mn content is needed to form Li-rich materials, as the rinsed NiMn-CS sample synthesized in oxygen only has a Li/TM ratio of 1.01. On the other hand, the rinsed NiMn 80/20 sample synthesized in oxygen has a Li/TM ratio of 1.10 and even the rinsed NiMn 80/20 sample synthesized in dry air has a Li/TM ratio of 1.04. It is likely that as the Mn content of a material increases, the synthesis atmosphere required does not have to be as oxidizing since less Ni^{3+} is needed for charge balancing with more Mn^{4+} present. This section supports this idea, as the rinsed NiMn-CS sample synthesized in dry air was Li-deficient but the rinsed NiMn 80/20 sample synthesized in dry air was not. It is expected that synthesis in air and dry air have similarly oxidative atmospheres, but the increased Li loss during air synthesis[132] explains why the Li/TM ratios of rinsed samples synthesized in air are lower than rinsed samples synthesized in dry air.

The difference between the Li/TM ratio of the unrinsed and the rinsed sample is the amount of Li lost during the pour method rinse. The amount of Li lost is assumed to stem from only dissolved residual Li species, with no contribution from H^+/Li^+ ion exchange. In reality, the short exposure time of water to the samples (~5 s) may still allow for some small amount of ion exchange to occur.[174,175,182–184] NiMn-CS samples had more residual Li than NiMn 80/20, which is reasonable since residual Li is known to occur in materials with more Ni.[14,131,174–181] For both NiMn-CS and NiMn 80/20 samples, synthesis under dry air results in the most residual Li.

Figure 7.8 shows the pH titration results for NiMn-CS and NiMn 80/20 samples synthesized under different atmospheres and NiMn 50/50 samples synthesized in air. Titration curves of NiMn-CS (Fig. 7.8a1), NiMn 80/20 (Fig. 7.8a2) and NiMn 50/50 (Fig. 7.8a3) are shown on the left and the initial pH (Fig. 7.8b1) and residual Li content (Fig. 7.8b2) as determined by the titration curves which are sorted by material and synthesis atmosphere are shown on the right. For Figs. 7.8a1-7.8a3, duplicate titration experiments on the same sample are indicated by lines of the same type, replicate samples are indicated by lines of a different shade and the second pour results are indicated by dashed lines. For Fig. 7.8b2, the samples are indicated by the colour, the residual Li species are indicated by the texture, and residual Li contents as determined by ICP-OES (Table 7.2) are indicated by a green cross.

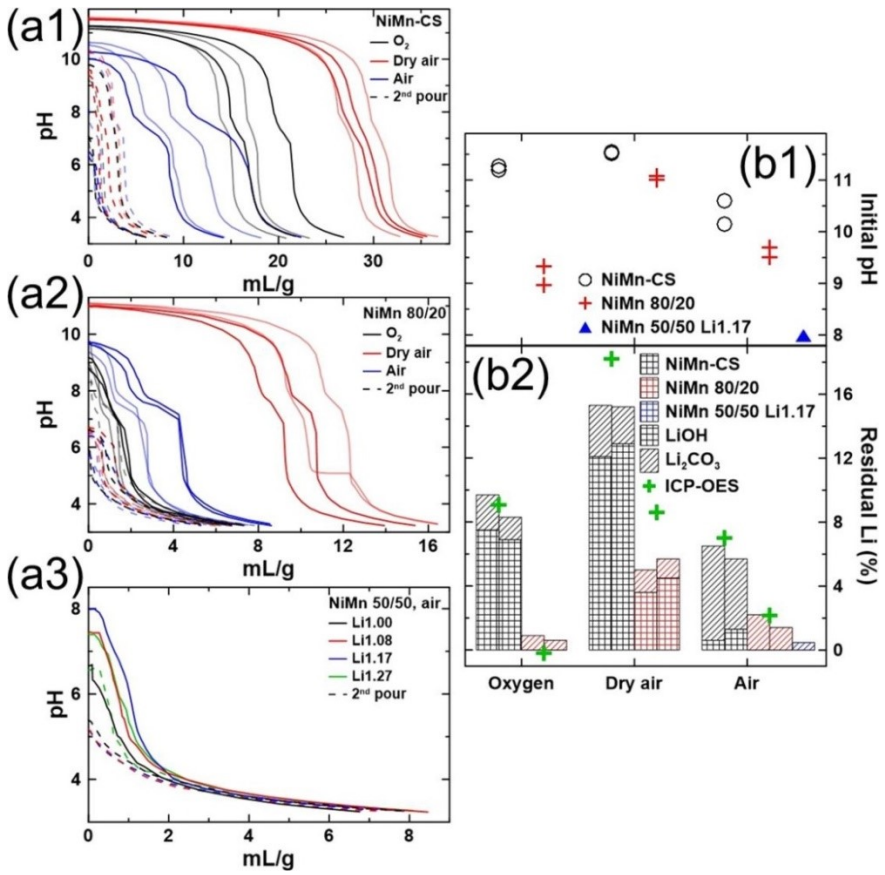

Figure 7.8: Acid titration curves of solutions extracted using the "pour method" from (a1) NiMn-CS, (a2) NiMn 80/20 and (a3) NiMn 50/50 samples. Duplicate experiments on the same sample are indicated by lines of the same type, replicate samples are indicated by lines of a different shade and the second pour results are indicated by dashed lines. The initial pH (b1) and residual Li content (b2) are plotted by synthesis atmosphere and material.

For the samples in Figs. 7.8a1-7.8a3, 2 mL/g corresponds to roughly 1% residual Li by mole fraction compared to the lithium content in $LiMO_2$. It is important to note that the second pour results for all samples showed very little Li in solution (< 1%) regardless of the amount of residual Li in the first pour. This supports previous work that the pour method can sufficiently dissolve residual Li species in just one pour, while the second pour gives an idea of the scale of ion exchange occurring.[182,184] Looking at the

first pour results, there is a clear trend of increasing residual Li content with decreasing Mn content. NiMn-CS samples have a maximum of around 15% residual Li, NiMn 80/20 samples have a maximum of around 6% residual Li and all NiMn 50/50 samples have under 1% residual Li, even for the NiMn 50/50 sample synthesized with a Li/TM ratio of 1.27. In terms of synthesis atmosphere, it is clear that synthesis in dry air results in the highest residual Li content, but NiMn-CS samples synthesized in oxygen have more residual Li than samples synthesized in air, while NiMn 80/20 samples synthesized in air have more residual Li than samples synthesized in oxygen. Titrations on replicate samples and replicate batches give consistent results for the most part, but samples synthesized in air seem to have more variation in residual Li contents.

While it may not be intuitive why NiMn-CS samples synthesized in oxygen have more residual Li than samples synthesized in air but the opposite occurred for NiMn 80/20 samples, the reason can be gleaned by considering ICP-OES results in Table 7.2. It was shown that synthesis in air lost more Li during the heating,[132] so there was less excess Li to form residual Li. Additionally, synthesis in oxygen promotes the uptake of Li by oxidizing Ni. This explains the NiMn-CS residual Li trend (Fig. 7.8a1); synthesis in dry air formed the most residual Li because similar Li loss occurred during syntheses in oxygen and dry air, but more Li was able to go into the sample synthesized in oxygen. A higher Mn content allows the material to take in more Li by requiring less oxidative atmospheres during synthesis, which is why NiMn 80/20 samples contained less residual Li. The rinsed NiMn 80/20 sample synthesized in oxygen took in all the excess Li not lost during heating to form a Li-rich material, leaving minimal Li to form residual Li. The NiMn 80/20 sample synthesized in air lost more Li during heating but some Li still

formed residual Li, which explains the residual Li trend observed for NiMn 80/20 samples (Fig. 7.8a2). For NiMn 50/50 samples (Fig. 7.8a3), all the excess Li went into the material, so all samples showed minimal residual Li amounts.

Figure 7.8b1 shows that the initial pH of a solution can be used as an estimate of the amount of residual Li on a sample. This can be observed in Figs. 7.8a1-7.8a3 as well, the higher the initial pH, the more acid is needed to bring the solution down to pH 3.3. However, the correlation may not be exact, so the initial pH should only be used as a qualitative method to estimate the amount of residual Li.

The equivalence points in the titrations (Figs. 7.8a1-7.8a3) were used to quantitatively determine the amount of residual Li by species,[131,174,175,177,183,184] and the residual Li contents of the samples are shown in Fig. 7.8b2. All titrated samples contained some amount of carbonate impurities (assumed in this section as all Li_2CO_3 for simplicity but not true in reality)[178,179] but not all materials contained quantifiable amounts of LiOH. However, LiOH was the most abundant residual Li species for NiMn-CS samples synthesized in oxygen and dry air and for NiMn 80/20 samples synthesized in dry air. Compared to samples synthesized in other atmospheres, samples synthesized in air have more carbonate species. It may be that the residual Li is reacting with the moisture and CO_2 in the air to form more carbonate species.[176,178,179] If carbonate impurities are mainly formed from reaction with ambient air, then the smaller amounts of carbonate species on other samples may be due to surface reactions when the samples were exposed to air after synthesis or possibly during the titration experiments. A higher carbonates content in NiMn-CS samples support this, since it is known that compositions with more Ni are more sensitive to air and moisture.[14,131,174–181] Further supporting this

idea is the NiMn 80/20 sample synthesized in oxygen, since it is expected that most, if not all, the excess Li was taken in.

As discussed earlier, ICP-OES can also determine the amount of residual Li by taking the difference between the Li/TM ratio of unrinsed and rinsed samples (Table 7.2), and the amounts determined by ICP-OES are also shown in Fig. 7.8b2 as green crosses for the 6 samples. Residual Li amounts determined by ICP-OES agreed with the titration results for the most part, although ICP-OES determined a slightly higher residual Li amount than titrations for samples synthesized in dry air.

Figure 7.9 shows the voltage versus specific capacity (V vs. Q, Figs. 7.9a1-7.9b1) and the differential capacity versus voltage (dQ/dV vs. V, Figs. 7.9a2-7.9b2) for NiMn-CS (Figs. 7.9a1-7.9a2) and NiMn 80/20 (Figs. 7.9b1-7.9b2) samples cycled between 3 V and 4.3 V as well as dQ/dV vs. V for NiMn-CS and NiMn 80/20 cells cycled between 3 V and 4.7 V (Fig. 7.9c) and NiMn 50/50 cells cycled between 3 V and 4.6 V (Fig. 7.9d). Solid and dashed lines represent two duplicate cells.

The V vs. Q curves of NiMn-CS samples (Figs. 7.9a1) show that synthesis atmosphere can impact the capacity of the material by ~25 mAh/g. The ~4.2 V feature in the dQ/dV vs. V curves (Figs. 7.9a2) is broader and occurs at a higher V when the Ni content in the Li layer increases (Fig. 7.6c2) which is also when the material is more Li deficient (Table 7.2). Conversely, the synthesis atmosphere does not affect NiMn 80/20 samples as much, and the V vs. Q (Fig. 7.9b1) and dQ/dV vs. V (Fig. 7.9b2) curves show less noticeable differences.

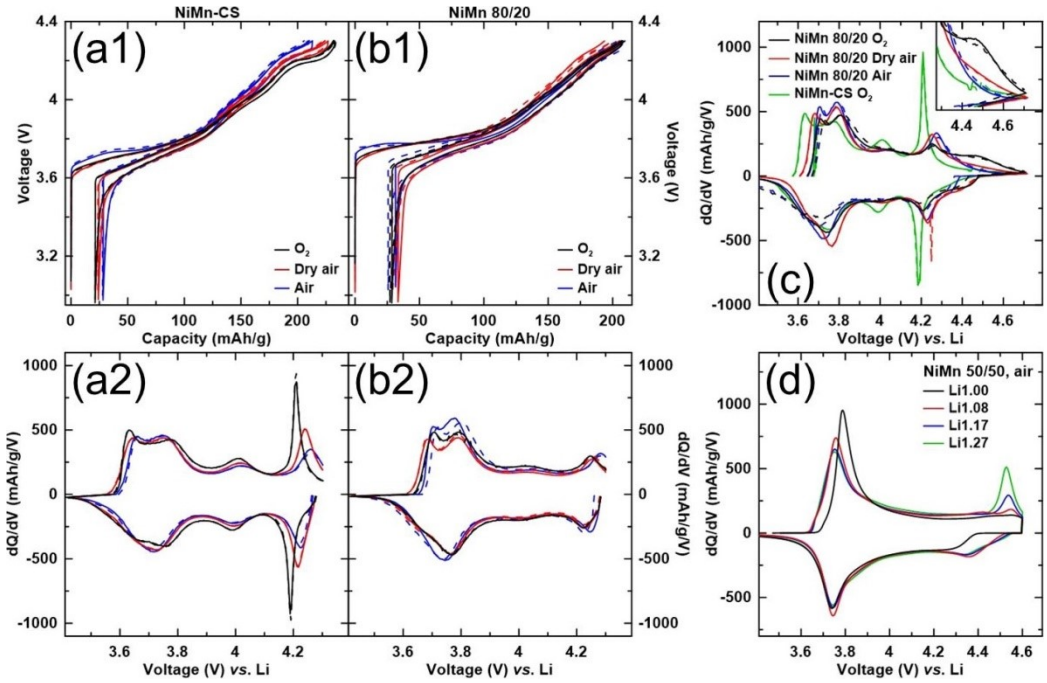

Figure 7.9: Cell voltage as a function of capacity (a1-b1) and differential capacity as a function of cell voltage (a2-b2) for NiMn-CS (a1-a2) and NiMn 80/20 (b1-b2) samples synthesized under different atmospheres and cycled between 3 V and 4.3 V. Differential capacity as a function of cell voltage for NiMn-CS and NiMn 80/20 cells cycled between 3 V and 4.7 V (c) and NiMn 50/50 cells cycled between 3 V and 4.6 V (d). The data was collected at 30°C using a specific current of ~10 mA/g (C/20).

It has been reported that the amount of residual Li can be correlated with the voltage when the cell begins charging,[178–180,227] but that is not observed in Figs. 7.9a1-7.9a2. The NiMn-CS and NiMn 80/20 samples synthesized in dry air contain the most residual Li (Fig. 7.8b2), but the voltages when the cells begin charging are very similar to samples synthesized in oxygen. In fact, for both compositions, the samples synthesized in air have the highest voltage when cells begin charging, even though synthesis in air forms the least amount of residual Li for NiMn-CS samples and the intermediate amount of residual Li for NiMn 80/20 samples (Fig. 7.8b2). However, synthesis in air forms the most carbonate species for both compositions, so perhaps the voltage when the cells

begin charging are more sensitive to carbonates content rather than total residual Li content.

To confirm whether materials are Li-rich and can access oxygen redox capacity,[37,51,66,67,69,70,72,73,75] cells were tested to a higher upper cutoff voltage of 4.7 V for NiMn-CS and NiMn 80/20 cells (Fig. 7.9c) and an upper cutoff voltage of 4.6 V for NiMn 50/50 cells (Fig. 7.9d). NiMn-CS samples synthesized in dry air and air were omitted from Fig. 7.9c because ICP-OES showed the samples were quite Li-deficient (Table 7.2). An expanded view of the region of interest is provided in Fig. 7.9c, and oxygen redox capacity can be observed for NiMn 80/20 samples synthesized in oxygen and dry air but not for the NiMn 80/20 sample synthesized in air and the NiMn-CS sample synthesized in oxygen. This supports the ICP-OES results in Table 7.2, showing that the higher Li ratio of the NiMn 80/20 sample synthesized in oxygen had more oxygen redox capacity than the NiMn 80/20 sample synthesized in dry air. Fig. 7.9d shows that for NiMn 50/50 samples synthesized in air, any excess Li will be result in oxygen redox capacity. This supports earlier observations that all the excess Li atoms were taken in by the material (Fig. 7.8a3) and that less oxidizing atmospheres are required for materials with higher Mn content (Table 7.2).

Figure 7.10 shows the summary of the Li/TM ratio of materials during synthesis and the expected behaviour of materials with various Mn content. Fig. 7.10a shows the relative mass loss as a function of temperature for the TGA experiments on 2 NiMn 37.5/62.5 samples heated to 1050°C in air with a Li/TM ratio of 1.2. Fig. 7.10b shows the maximum amount of Li a material can take in if all the Ni are oxidized to Ni^{3+} as a function of the Mn content. Fig. 7.10c shows the Li/TM ratios of materials before

heating, after heating and after rinsing as a function of Mn content for syntheses in oxygen (top), dry air (middle) and air (bottom). Fig. 7.10c summarizes the expected behaviour, as indicated by dashed lines of the corresponding colour, of materials with a given Mn content starting with a Li/TM ratio of 1.15 and heating at 850°C for 12 h then at 800°C for 5 h.[225,227] Data points for the NiMn 50/50 sample synthesized in air had a starting Li/TM ratio of 1.17 and the sample was heated at 1000°C for 10 h and the heating loss was not measured. Instead, a heating loss estimate based on a starting Li/TM ratio of 1.17 and the expected behaviour is provided.

Figure 7.10a shows TGA experiments of NiMn 37.5/62.5 precursors mixed with Li_2CO_3 in a Li/TM ratio of 1.2 and heated to 1050°C. There are some slight differences in the final relative mass indicating perhaps some small error in the starting Li/TM ratio. However, both samples showed no mass loss from 600°C-1050°C, indicating that there is no Li loss due to heating for these higher Mn materials. Similar TGA studies on precursors with 95% Ni or higher mixed with Li and heated start showing increased mass loss above ~800°C,[130] in contrast to Fig. 7.10a. Fig. 7.10b shows the calculated maximum amount of Li a material can take in if all the Ni is oxidized to Ni^{3+} during synthesis. This could happen during syntheses in oxygen, and may occur for syntheses in dry air or air at higher Mn contents, as suggested earlier. Fig. 7.10b suggests that in this section using a Li/TM ratio of 1.15, materials with a Mn content of > 0.35 will take in all the Li during synthesis.

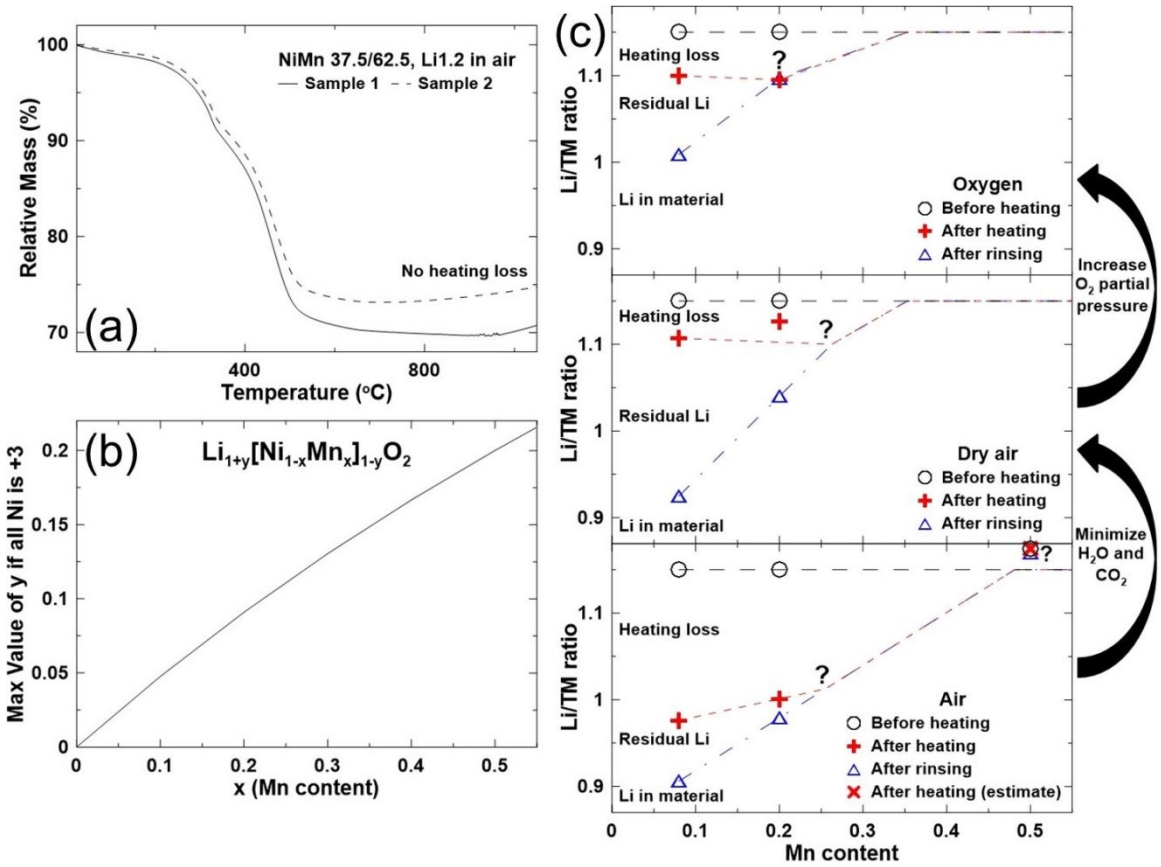

Figure 7.10: Normalized TGA data (a) for 2 NiMn 37.5/62.5 samples heated to 1050°C in air with a Li/TM ratio of 1.2. The maximum amount of Li a material can take in (b) if all the Ni are oxidized to Ni^{3+} as a function of the Mn content. A summary (c) of the Li/TM ratio of materials before heating, after heating (850°C 12h, 800°C 5h) and after rinsing as a function of the Mn content of the material for various synthesis atmospheres. Dashed lines of the corresponding colour indicate the expected behaviour of materials with a given Mn content starting with a Li/TM ratio of 1.15 and heating at 850°C for 12 h then at 800°C for 5 h. The NiMn 50/50 data points were for heating at 1000°C for 10h with an unmeasured amount of heating loss, an estimate based on a starting Li/TM ratio of 1.17 and the expected behaviour is provided.

Figure 7.10c shows the difference between the starting Li/TM ratio and the measured Li/TM ratio of unrinsed samples (Table 7.2) can be seen as the amount of Li loss due to heating. The heating loss is expected to be consistent for a given heating

protocol except for syntheses in air, which may have higher Li loss due to reactions with moisture and CO_2.[132] For syntheses in air, it is assumed that the heating loss decreases as the Mn content increases to account for the fact that many of the NiMn 50/50 materials are Li-rich (Fig. 7.9d). However, it is noted that the Li/TM ratio of unrinsed samples synthesized in dry air and air both saw a similar increase when the Mn content increased, so more work tracking the heating loss would clear up this speculation.

The expected amount of heating loss shown in Fig. 7.10c is quite speculative for materials with higher Mn content. Figures 7.10a and 7.10b support the expectation that Li loss due to heating is reduced for materials with higher Mn. This may occur because all the Li is taken in by the material before the temperature is high enough to start losing Li. However, the authors note that some studies using ICP have measured lower Li/TM ratios in synthesized NiMn 50/50 materials than used in synthesis, likely due to heating loss.[71,286] An interesting report measured no loss of Li in NiMn 50/50 after synthesis, but Li loss was measured for materials with 30%, 40%, 60% and 80% Mn.[68] More work is needed to have a more definitive understanding of the heating loss of Li in various materials.

The difference between the Li/TM ratio of unrinsed samples and rinsed samples (Table 7.2) can be seen as the amount of residual Li on a sample. This is confirmed using titration experiments to show that residual Li amounts as measured by titrations and ICP-OES agree quite well (Fig. 7.8b2). The experiments in this section show that more residual Li forms from materials with higher Ni/lower Mn and this supports literature.[14,131,174–181] Titrations on NiMn 50/50 samples synthesized in air (Fig. 7.8a3) show minimal residual Li amounts, so it is expected that NiMn 50/50 samples

synthesized in other atmospheres will also have minimal amounts of residual Li. The extrapolation of the Li/TM ratio of unrinsed samples (relatively constant for oxygen and dry air synthesis and slightly increasing for air synthesis) and the Li/TM ratio of rinsed samples (increasing for all synthesis atmospheres) shows the lowest Mn content at which residual Li is expected to be minimal for the various synthesis atmospheres, but this is highly speculative and a "?" symbol is labeled at this point to indicate that.

The Li /TM ratio of rinsed samples (Table 7.2) indicates the amount of Li in the material. For all synthesis atmospheres tested, the Li/TM ratio of rinsed samples increased when the Mn content increased. As discussed earlier, this is likely due to more Mn^{4+} requiring less oxidation of Ni^{2+} to Ni^{3+} to accommodate Li. For materials synthesized in oxygen, full uptake of the Li not lost to evaporation occurs at a Mn content of 0.2 or slightly less, and the Li/TM ratio of the synthesized material will depend on the heating loss. Full uptake of the Li occurs at a slightly higher Mn content for materials synthesized in dry air, perhaps around a Mn content of 0.25. For materials with a high enough Mn content, it will not be necessary to synthesize in oxygen since synthesis in dry air is expected to form similar products. Synthesis in air is slightly more complicated. Full uptake of the Li may actually occur at a slightly lower Mn content than synthesis in dry air, but the Li/TM ratio of the synthesized material will be lower due to a higher heating loss.[132] More work is needed to confirm the trends expected in this section and to confirm the suitability of synthesis in air for materials with higher Mn content. As mentioned, Fig. 7.10 shows the expected behaviour of materials with a given Mn content starting with a Li/TM ratio of 1.15 and heating at 850°C for 12 h then at 800°C for 5 h. Similar studies but varying the Li/TM ratios and heating profiles would give a fuller

understanding of the impact of synthesis conditions on the composition and performance of synthesized materials.

7.2.3 – Conclusions

This section synthesized various Ni-rich $LiNiMnO_2$ (Mn contents ~8%, 20% and 50%) with excess Li in oxygen, dry air or air to understand what happens to excess Li during synthesis. The $Li[Ni_{1-x}Mn_x]O_2$ components of the synthesized materials were single phase and synthesis in oxygen produced materials with less Ni in the Li layer. The pour method was confirmed to be a suitable method to dissolve residual Li while minimizing ion exchange. ICP-OES experiments on the unrinsed and rinsed samples are useful in the determination of the amount of Li lost from heating, the amount of Li taken in by the material during synthesis and the amount of residual Li. Materials synthesized in oxygen and dry air lost a similar amount of Li during heating but synthesis in air resulted in more Li loss. Synthesis in oxygen helped the material take in more Li during synthesis and materials with a higher Mn content can take in more Li to form Li-rich materials. Residual Li determination from titrations agrees with ICP-OES results, with the advantage of being able to discern residual Li species. Synthesis in dry air produces the most residual Li but synthesis in air produces the most carbonate impurities, and materials with less Mn content form more residual Li. The electrochemical performance of materials is more impacted by synthesis atmosphere for materials with lower Mn content. Materials determined to be Li-rich by XRD and ICP-OES are confirmed to be able to access oxygen redox capacity. From these experiments, the fate of excess Li can be tracked to heating loss, residual Li or uptake into the material as a function of Mn content and synthesis atmosphere. Figure 7.11 shows a simple summary of expected

behaviour for materials with a given Mn content synthesized with a Li ratio of 1.15 and heated to 850°C for 12 h then 800°C for 5 h.

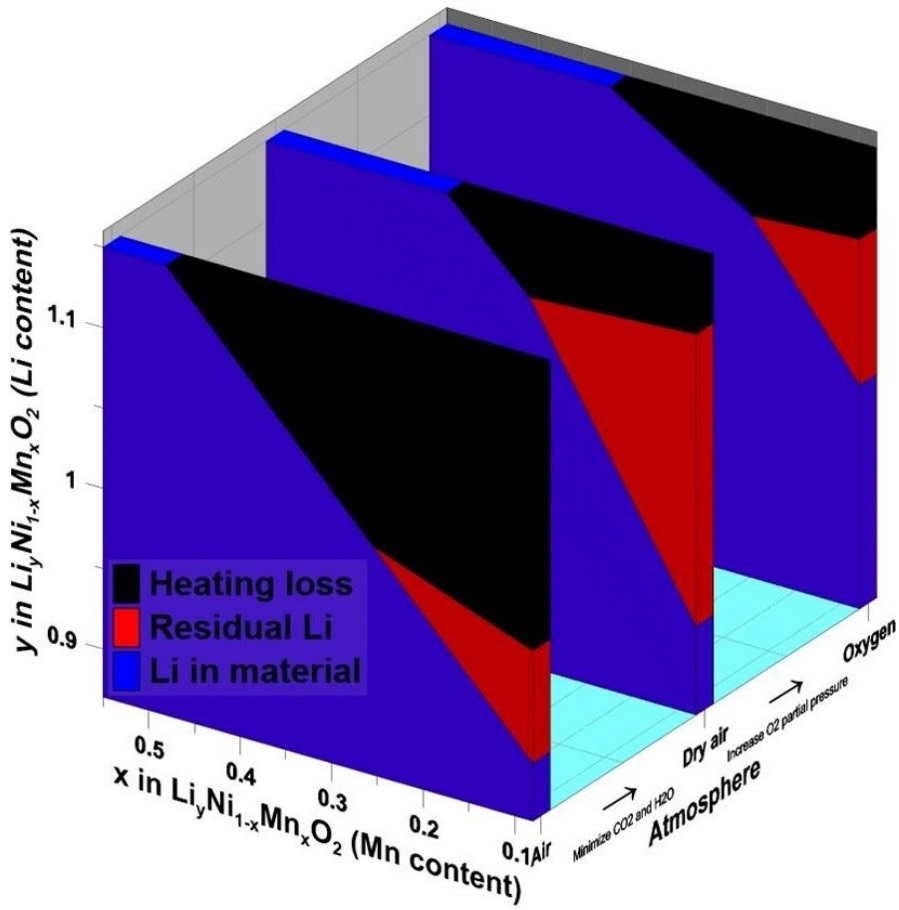

Figure 7.11: A simple summary of expected behaviour for materials with a given Mn content synthesized with a Li/TM ratio of 1.15 and heated to 850°C for 12 h then 800°C for 5 h.

Chapter 8 – Conclusions and Future Work

8.1 – Conclusions

The use of Ni-rich positive electrode materials continue to be a practical direction to further increase the energy density and reduce costs of Li-ion technology for use in electric vehicles. This thesis synthesized and characterized various Ni-rich materials with a focus on Co-free and single crystalline (SC) Ni-rich materials. The effect of Mg substitution in various Ni-rich compositions was studied. Identifying single crystalline materials as a possible solution to overcome the "unavoidable challenge",[157] the synthesis and characterization of Co-free SC LNO substituted with either Al or Mg was carried out as a two-step lithiation or one-step lithiation process. Finally, some miscellaneous studies following up on results from earlier chapters were conducted.

8.1.1 – Mg Substitution in Ni-rich Materials

Chapter 4 studied the effect of Mg substitution in various Ni-rich materials. Materials in four composition series were synthesized with a Mg content of 5% or less. All synthesized materials were single phase, contained no appreciable amount of residual Li impurities and had reasonably low amounts of Ni in the Li layer, even for materials containing no Co. The initial charge and discharge capacity of the material was reduced when increasing the Mg amount and also with increasing Al amount because both substituents are electrochemically inactive. Features in the dQ/dV vs. V curves were smoothed in materials containing more Mg and Al. Increasing the Mg content improved the capacity retention of all composition series and increasing the Al content also improved the capacity retention. An analysis of dQ/dV vs. V curves showed that Mg can

improve the capacity retention by reducing the growth of polarization during cycling. No synergistic effects were observed from co-substitution of Mg with Co and/or Al. Chapter 4 also demonstrated that materials without Co can have comparable performance to materials with Co.

8.1.2 – Synthesis of Co-free Ni-rich Single Crystalline Materials

Chapter 5 studied the synthesis of Co-free single crystalline (SC) Al-substituted LNO and Mg-substituted LNO using a two-step lithiation method. The presence of Li or Mg was shown to be required for grain growth and higher temperatures enhance grain growth as well. Grain growth of rocksalt materials in the first step was found to lead to incomplete lithiation of the material in the second step, resulting in rocksalt impurities, so the first step should contain enough Li to fully convert the material to the layered phase. A first step Li/TM (transition metal or other metal filling the transition metal role) ratio of 0.9-0.975 and heating temperature of 850°C was used to grow particles to a suitable size. While a second step temperature of 700°C can be used to produce decent materials, a higher second step temperature of 750°C was able to reduce the Ni content in the Li layer down to ~2% for NiMg materials. All attempts to synthesize SC NiAl materials in this thesis resulted in the formation of Li_5AlO_4 impurity even at a Li/TM ratio of 0.5.

The two-step lithiation method was introduced to try and avoid the formation of Li_5AlO_4 in Al-substituted materials but the formation of Li_5AlO_4 could not be avoided. Mg-substituted LNO did not form impurities, and was not expected to, even for a one-step lithiation process, so Chapter 6 studied the synthesis of Co-free SC Mg-substituted LNO using a one-step lithiation method. Higher heating temperatures promoted grain

growth, but also increased the Ni content in the Li layer. Increasing the Li/TM ratio did not seem to significantly impact grain growth at lower temperatures (775°C or 800°C) but influenced the formation of Li_2O impurity. The utilization of a low temperature step after the calcination step was found to reduce the Ni content in the Li layer below what would be expected at the calcination temperature, and this can be used to grow larger grains while keeping an acceptable amount of Ni in the Li layer.

8.1.3 – Electrochemical Performance of Co-free Ni-rich Single Crystalline Materials

While synthesis studies on Co-free Ni-rich SC materials were successful in meeting the physical specification targets, the electrochemical performance of SC materials thus far has been below expectations. The capacities of SC materials in Chapters 5 and 6 were significantly lower (~30 mAh/g) than the PC counterparts of the same composition and had a higher irreversible capacity (IRC). Compared to PC samples containing 2.5% Mg, SC cells also had lower capacity retention. A closer look at the dQ/dV vs. V curves revealed that SC cells lost virtually all the capacity around ~3.5 V and some capacity around ~4.2 V compared to PC cells, both regions being associated with kinetic hindrances of Li diffusion in the material. Analysis of dQ/dV vs. V curves from the initial and final cycles showed that SC cells seemed to cycle with less low rate capacity loss than PC cells but experienced more polarization growth, suggesting different modes of failure for SC and PC cells.

Chapter 6 investigated the electrochemical performance of Mg-containing materials further. Better separation of particle aggregates was found to improve the cycling performance of the material. Materials with a higher Mg content had less

capacity with no clear benefit to capacity retention. While SC materials with 2.5% Mg could be synthesized via 3 pathways (two-step, one-step and one-step with low temperature step), all the SC samples had lower capacities, higher IRCs, and similar cycling fade compared to the PC sample. The lower capacities of SC materials were confirmed to stem from increased kinetic hindrances to Li diffusion at ~3.5 V and ~4.2 V compared to PC materials, with primary particle size a much larger factor than secondary particle size in reducing the capacity/increasing the IRC. The SC cells cycled at 55°C were able to recover ~20 mAh/g of discharge capacity and have similar IRC compared with PC cells cycled at 30°C.

8.1.4 – Miscellaneous Investigations of Ni-rich Materials

Stemming partly from the work in Chapters 4 to 6, Section 7.1 studied the impact of various material parameters on the electrochemical performance of three series of Ni-rich materials, specifically focusing on the low voltage kinetic hindrance region related to Li diffusion. Increasing the amount of substituents, increasing the secondary particle size and increasing the primary particle size were all variables found to decrease capacity in the ~3.4-3.6 V region and increase the 1st cycle IRC. Capacity in the low voltage kinetic hindrance region can be increased significantly when cycling at a higher temperature and when cycling to a lower cut-off voltage of 2 V. Combining the two variables to cycle at 55°C and to a low cut-off voltage of 2 V reduced the 1st cycle IRC to 2 mAh/g, or <1% in SC materials containing 2.5% Mg heated at 775°C. A follow up study by N. Phattharasupakun to measure Li chemical diffusion coefficients of PC and SC NiMg 97.5/2.5 (Section 7.1.3) showed that lattice diffusion is much slower than grain boundary diffusion. This supports the expectation that Co-free Ni-rich SC materials will be

intrinsically limited by the larger primary particle size hindering Li diffusion due to increasing lattice diffusion path lengths.

Chapters 5 and 6 showed the success of incorporating a low temperature step in reducing the Ni amount in the Li layer during syntheses of SC materials, so the utilization of a low temperature step in syntheses of materials under different atmospheres was studied. Section 7.2 synthesized various $Li_yNi_{1-x}Mn_xO_2$ (Mn contents ~8%, 20% and 50%) with excess Li in oxygen, dry air or air to understand what happens to excess Li during synthesis. The $LiNi_{1-x}Mn_xO_2$ components of the synthesized materials were single phase and synthesis in oxygen produced materials with less Ni in the Li layer. The pour method was confirmed to be a suitable method to dissolve residual Li while minimizing ion exchange. ICP-OES experiments on the unrinsed and rinsed samples were useful in the determination of the amount of Li lost from heating, the amount of Li taken in by the material during synthesis and the amount of residual Li impurities. Materials synthesized in oxygen and dry air lost a similar amount of Li during heating but synthesis in air resulted in more Li loss. Synthesis in oxygen helped the material take in more Li during synthesis and materials with a higher Mn content can take in more Li to form Li-rich materials. Residual Li determination from titrations agreed with ICP-OES results, with the advantage of being able to discern residual Li species. Materials containing less Mn formed more residual Li impurities. Synthesis in dry air produced the highest amount of residual Li impurities but synthesis in air produced the most carbonate impurities. The electrochemical performance of materials was more impacted by synthesis atmosphere for materials with lower Mn content. Materials determined to be Li-rich by XRD and ICP-OES were confirmed to be able to access oxygen redox capacity. From these

experiments, the fate of Li after synthesis can be tracked to heating loss, residual Li or uptake into the material as a function of Mn content and synthesis atmosphere.

8.1.5 – Main Conclusions from this Thesis

Work in this thesis has achieved understanding of several factors that impact grain growth and the trade-offs of parameters such as heating temperature. This thesis has shown that the synthesis of Co-free Ni-rich SC materials that meet physical specification targets is achievable via various synthesis routes. However, the electrochemical performance of the synthesized SC materials is subpar, and this has been shown to mainly be a Li diffusion issue. Diffusion studies by N. Phattharasupakun indicate that SC materials were limited by the larger primary particle size hindering Li diffusion due to increasing lattice diffusion path lengths. This means that the rate capability and capacity will be inherently limited by the larger primary particles of Co-free Ni-rich SC materials, and advances overcoming these limitations will be needed before Co-free Ni-rich SC materials become viable.

8.2 – Future work

While some conclusions can be made from the studies detailed in this thesis, there are still many questions to answer stemming from this work. This section will describe various directions future work can head towards, four of which will directly build on this work and the last direction focusing on improving Co-free Ni-rich materials in general.

8.2.1 – Improving the Electrochemical Performance of Co-free Ni-rich Single Crystalline Materials

Current materials cannot overcome the "unavoidable challenge"[157] of having a high capacity while maintaining a high capacity retention, since the decrease in capacity retention is related to the volume change experienced from high degrees of delithiation. The "unavoidable challenge" is expected to mainly affect PC materials due to anisotropic volume change intrinsic to PC materials, causing large amounts of stress and strain within a secondary particle. Therefore, work on Co-free Ni-rich SC materials was carried out in this thesis in hopes of synthesizing a material that has a high capacity that could avoid the drop in capacity retention. Chapters 5 and 6 showed success in synthesizing Co-free Ni-rich SC materials that met the physical specification targets via different synthesis pathways, but the poor electrochemical performance of the materials needs to be improved before it can be seen whether SC materials can be a viable solution to overcome the "unavoidable challenge".

Chapter 6 showed the impact of particle separation on improving the cycling retention. The best method for particle separation reported in Chapter 6 and used in Chapters 5 to 7 was milling the material with 20S balls in a planetary mixer for 3 x 100 s. However, SEM images (Fig. 6.5) showed that particle aggregates were still present, meaning that complete separation of particle aggregates was not achieved. Therefore, further work on improving the separation method would likely improve the capacity retention of the material. Studies varying the ball size, milling time, ball to material ratio and milling speeds could further improve particle separation. Other milling methods

such as high energy ball milling[290] and jet milling[291] can be explored to see if particles can be completely separated.

Analysis of the PC and SC NiMg dQ/dV vs. V curves suggests that the main mode of degradation during cycling for PC and SC NiMg cells is different. The degradation of PC NiMg during cycling seems to be related to structural change, specifically in the low V kinetic hindrance region, while the structure of the SC material is more stable. Instead, the main mode of degradation for SC NiMg cells during cycling seems to be polarization growth. SC NiMg cells also have worse rate capability compared to PC NiMg cells, owing to the large primary particles hindering Li diffusion. It may be possible to counter the poor rate capability and polarization growth of the material by tweaking the carbon additive in the electrode. Single-walled carbon nanotubes (SWCNT) have been shown to improve the performance of Si-based negative electrodes.[292,293] The use of SWCNT in the electrode formulation of SC materials may help maintain a conductive network, especially for particle aggregates that were not separated.

While better separation of particle aggregates and the use of SWCNT may improve the capacity retention, the initial capacity of SC materials is not expected to increase from these advances. The initial capacity of the Co-free Ni-rich SC materials in this thesis are below the threshold for overcoming the "unavoidable challenge", so increasing the initial capacity should be a focus. While it is believed that the capacity reduction is intrinsic to Co-free Ni-rich SC materials, efforts should still made to synthesize SC materials of various compositions to confirm this expectation. Some suggested compositions can include materials containing Mn, W or F.

A big portion of the capacity reduction experienced by SC materials in this work occurred in the low voltage kinetic hindrance region, leading to a lower initial discharge capacity and a higher IRC. SC materials likely exacerbate this kinetic hindrance due to longer Li diffusion pathways for the Li to diffuse in and out of the larger grains and it is expected that Ni-rich SC materials may be intrinsically limited, especially if the material is Co-free. It has been observed that the IRC of a material increases quite linearly as the substituent content of LNO increases, except when Co is the substituent.[21,149,200,205] Therefore, it may be valuable to synthesize some Co-containing Ni-rich SC materials, perhaps LNO containing 2.5% or 5% Co, and test electrochemically to see if the SC material experiences significant capacity reduction or increased IRC compared to its PC counterpart. While the suggested composition is not ideal for safety and costs reasons, it would help allow further understanding of the limitations of Ni-rich SC materials. Compositional optimization can be carried out if Co was found to enable Ni-rich SC materials to attain capacities competitive to its PC counterparts.

Ni-rich SC materials are expected to be intrinsically limited by the larger grains increasing the Li diffusion pathway, but an unexplored avenue to overcoming this barrier is to try and grow the SC particle in a shape that minimizes the Li diffusion pathway length. There have been some reports on control of particle shape for SC synthesis.[134,137,275,294–296] Synthesis of octahedral particles seem to be the most commonly reported shape, but truncated octahedrons, polyhedrons and platelet shapes have been achieved as well. All the reported particle shapes do not minimize Li diffusion pathway lengths except the platelet shape, which has not been reported for a Ni-rich composition. Synthesizing a platelet shaped SC material with a Ni-rich composition may be a solution

to avoid the capacity reduction experienced from lengthening the Li diffusion pathway. However, the majority of the reports of SC particle shape control utilize a salt flux to control the morphology and that is less desirable for Ni-rich SC syntheses because it requires a water wash.[17,99,110,131,157,176,178,179,181–183] One report that did not utilize flux synthesized disk-like (platelet shaped) Sr-substituted SC NMC 532 using nanosized $SrCO_3$.[275] The synthesis procedure should be repeated with a higher Ni composition to see if a simple one-step synthesis could form platelet shaped SC particles.

Recent advances in PC materials have reported on the benefits of having a radial rod-like microstructure but no attempts, as far as is known, have been made to create rod-like SC particles. Rod-like particles would also have short Li diffusion pathways to avoid large capacity reductions. The formation of this microstructure seems to stem from the use of substituents like Ta, W, B, and others,[42,49,207,208,297] but have also been reported for an NMC material with a concentration gradient but no substituents.[298,299] Understanding how the rod-like primary particles form may enable synthesis of this shape for SC materials, either by forming the rod-like particles within a secondary particle and separating them somehow or by growing separate, larger primary particles first before shaping into rods. It is anticipated that the synthesis of rod-like SC particles would be more complicated than the synthesis of platelet shaped SC particles.

8.2.2 – Further work on Co-free Ni-rich Single Crystalline Materials

The focus of the work in Chapters 5 and 6 was to synthesize Co-free Ni-rich SC material that can meet the physical specifications target and perform well electrochemically. For the most part, only the basic suite of characterization techniques

was used to screen the materials. As the search for a promising SC material continues, there are other measurements that would be valuable for those candidate materials. EBSD mapping of a cross-sectional SEM image can be used to show crystal orientation to confirm if the materials consist of single crystal particles.[90,137,218] The amount of residual Li impurities in SC materials can be quantified by acid titration and/or ICP-OES as described in Section 7.2.[14,110,131,157,174–176,178,179,181–184] The tap density of the SC materials can be measured using a tap density tester.[114–116,118,228,229] The specific surface area of SC materials can be measured by the Brunauer-Emmett-Teller (BET) method.[24,99,123,228,229] The thermal stability of charged electrode materials can be measured by accelerating rate calorimetry (ARC).[12,21,24,169,300–302] As mentioned, these measurements would only be valuable for candidate materials that have competitive electrochemical performances. All of the mentioned measurements, except EBSD mapping, should be compared with measurements for the PC counterparts. The amount of residual Li impurity and the tap density of the materials are parameters related to the processing of the materials, while the specific surface area and thermal stability are parameters related to the safety of the materials.

If the electrochemical performance of Ni-rich SC materials can be improved enough to be considered for practical use, there are some process considerations for the materials. Two common processing steps for commercial Ni-rich materials are washing and coating. Some of these processes require a reheating step, which may work better with a two-step lithiation process. For example, a fully lithiated Ni-rich material would be sensitive to a water washing/wet coating step,[17,99,110,131,157,176,178,179,181–183] but a SC material after the first step would be Li-deficient and perhaps less sensitive to water

owing to the Ni in the material being less oxidized on average than in a fully lithiated material. While the focus in this thesis was on a one-step lithiation for a simpler process, the flexibility of a two-step lithiation to accommodate further processing steps should be investigated.

Most of the electrochemical characterization suggested in this section and the previous section will be done using half cell experiments, using Li metal as the counter and reference electrode. Half cell experiments are useful for electrode material evaluation since only one electrode will have a varying potential during cycling. However, it's possible that full cells may experience issues that were hidden in half cell experiments, due to an excess of Li in half cells or influences from the choice of negative electrode.[303,304] Therefore, it is important to carry out full coin cell experiments on promising SC materials to ensure performance in realistic conditions.[305]

Once the promising SC materials have been validated by half cell and full cell experiments and found to perform, further improvements can be made by optimizing the electrolyte package for the material. This would require the candidate SC materials be used in machine-made pouch cells to ensure a high level of consistency in cell construction. SC materials can have further improved cycling performance when appropriate electrolyte additives are used.[90–92,97,99] However, the best electrolyte packages can differ for different materials, so candidate SC materials should undergo screening of electrolyte packages to optimize the lifetime improvement gained.

8.2.3 – Diffusion Studies of Ni-rich Materials

As research continues to increase the Ni content of SC materials, the capacity reductions and increased IRC shown in this thesis will become more significant, therefore further understanding of kinetic hindrances related to Li diffusion and reliable measurements of Li chemical diffusion coefficients are important. Additionally, materials have worse rate capability without Co, so charge rates of Co-free Ni-rich materials may become a concern. Therefore, the Dahn lab is undertaking some studies analyzing the Li chemical diffusion coefficients of materials using a reinvented approach inspired by a classic paper by Atlung et al.[281] to better understand kinetic hindrance and rate performance. Section 7.1 makes up a portion of a manuscript connecting the kinetic hindrances to Li diffusion to the introduction of this approach to measure chemical diffusion coefficients and an excerpt of the measurements by N. Phattharasupakun of the Li chemical diffusion coefficients of PC and SC NiMg samples was included in Section 7.1.3.[280] Cross validation of the method to other established methods is being conducted, as well as studies on the impact of particle size and Ni content in the Li layer on Li chemical diffusion coefficients.[282,283]

The use of a low temperature step could be very useful for synthesizing a series of materials for Li chemical diffusion coefficient measurements that have the same primary particle size but varying Ni contents in the Li layer. All the materials can be heated to the same temperature that promotes grain growth, and the low temperature step (at a temperature with minimal grain growth) can be held for different amounts of time to progressively reduce the Ni content in the Li layer. Conversely, materials could be

heated to different temperatures with a low temperature step to attain similar amounts of Ni in the Li layer to study the impact of primary particle size.

Once the method is cross validated and the impact of primary particle size and Ni content in the Li layer on Li chemical diffusion coefficient well understood, the method can be used to evaluate different materials. The impact of various substituents, coatings and prolonged cycling/microcracking could be tested. Measurements on a wide range of materials and parameters would gain understanding of the factors that significantly impact diffusion, enabling the design of Co-free Ni-rich materials with acceptable rate capability.

8.2.4 – Lowering the Costs of Co-free Ni-rich Material Synthesis

Chapters 5 and 6 showed the success of incorporating a low temperature step in reducing the Ni content in the Li layer. Section 7.2 briefly mentioned that preliminary work was carried out to explore the feasibility of synthesizing Ni-rich materials in air. If a Ni-rich material synthesized in air can have similar performance as a material synthesized in oxygen, this can lead to lower processing costs. Work should be continued to determine where the threshold is in terms of composition for when air and oxygen synthesis produces similar materials. Synthesis in dry air may be considered as well if synthesis in a dry room is a viable consideration. The study of a low temperature step should continue to understand how to best reduce the Ni content in the Li layer and understand the limitations to the low temperature step.

Section 7.2 and other studies showed the benefits of using oxygen during synthesis especially for higher Ni compositions.[27,126,131,132,144–148] The role of oxygen in

the synthesis is to ensure oxidation of the Ni to the +3 oxidation state to maximize Li uptake. This likely becomes increasingly significant near the latter part of the heating process. However, a gas flow is still required to evacuate gasses formed during decomposition of the precursor and Li source, such as H_2O and CO_2.[111,125,127–130] These decompositions occur earlier in the heating process, below the temperature used for the preheating step. In the Dahn lab, the preheating step is followed by a regrinding step, so a study investigating the impact, if any, of conducting the preheating step in air then heating in oxygen may be useful. For syntheses not using a preheat step, such as syntheses using Li_2CO_3 as the Li source, the use of a mass flow controller can control the flow rate of different gasses, like oxygen and dry air. Parameters such as gas flow rate, the time/temperature at which oxygen is used and oxygen partial pressure could be studied to enable a synthesis procedure that produces materials performing similarly to those synthesized in oxygen but at a reduced oxygen usage.

Results from Chapters 5 and 6 suggest that the diffusivity of a substituent may impact the rate of grain growth for SC material synthesis. It is speculated that Mg is a good diffuser in Ni-rich materials, which led to the ease in grain growth.[210,273] It may be interesting to try and synthesize SC materials using a Li source with separate Ni and Mg precursors, instead of $Ni_{1-x}Mg_x(OH)_2$. The synthesized SC materials need to be characterized by PSA to ensure an acceptably narrow size distribution. The distribution of Mg in the final product would need to be confirmed to be homogenous by energy-dispersive X-ray spectroscopy (EDS) mapping. Using nanosized Mg precursors that are mixed well with the Ni source, for example by dry particle fusion,[306,307] may aid in the success of the synthesis. An all dry method to synthesize SC NMC 622 was recently

reported using either ball milling for a week or high energy ball milling to promote atomic mixing of the metal oxide precursors.[308] Using Mg may allow synthesis to occur without needing to atomically mix the metals beforehand. If a solid state method to synthesize decent SC materials can be achieved, it has the potential to reduce costs by skipping the precursor co-precipitation step.

8.2.5 – Pushing the Performance of Co-free Ni-rich Materials

While SC materials are a potential solution to overcome the "unavoidable challenge", there are many challenges facing Co-free Ni-rich SC materials, as shown in this thesis, and there is still a long journey before the technology becomes viable. There is still room for improvement for PC materials to push against the boundaries of the "unavoidable challenge", and these improvements are achievable in the near-term.

Compositional studies have shown that materials with a high Ni content are able to reach high capacities but the capacity retention is not very good.[14,15,17,22,26,27,42,49,157,216] On the other hand, there are compositions that do not experience much long term fading, but they usually start with a lower capacity. Core shell type materials, with the high capacity material as the core and the long lifetime material as the shell, can combine the two compositions to realize the benefits of both compositions.[52,117,118,210,212,213,309] Similarly, concentration gradient type materials are very similar to core shell type materials and have been shown to perform impressively.[15,17,42,49,298,310–312] Recent work in the Dahn lab has shown the success of using a Mn-rich shell for a Co-free material.[210,212,213] Optimization of composition, synthesis parameters and electrolyte

formulation can improve the safety, energy density and lifetime of the material even further.

Another way to improve the lifetime of Co-free Ni-rich materials is to apply a surface coating, which is done in many commercial cells. Coatings act like an artificial SEI for the material, shielding the surface from side reactions with the electrolyte.[15,17,22,37,49,53,229,313] Dry particle fusion is a coating method that is more attractive than conventional wet coating methods, which require more processing steps and produce more waste, and deposition methods, which are more expensive and hard to scale up.[66,73,306,307,313,314] The Dahn lab has had success using an in-house dry particle fusion machine to improve the performance of Ni-rich and Li-rich materials.[66,73,306,307] Further work on coating Co-free Ni-rich materials is being conducted and this investigation would complement the core-shell studies to achieve the best cell lifetime possible for PC materials.

For the most part, this thesis has acknowledged the presence of residual Li impurities but little work was done to wash materials and remove these impurities. This was a decision made to minimize the complexity of the studies, as there are many variables to consider for the washing process. Instead, a qualitative method to estimate the amount of residual Li impurities (by looking at the 1st charge voltage curve)[178–180,227] was used to ensure there was not excessive amounts of impurities. These residual Li impurities have been shown to reduce the capacity, rate capability and capacity retention of materials.[14,110,131,157,172–183] For promising Ni-rich PC and SC materials, it would be valuable to study the washing process to best remove the residual Li impurities while minimizing the damage to the water-sensitive materials. The post-washing drying

process and subsequent storage should be investigated as well to ensure longevity of the material.

With the search for materials with higher energy density continuing, the thermal stability of the material when delithiated is of utmost importance, since this is related to the safety of Li ion batteries. Multiple studies have shown that charged LNO and Ni-rich derivatives are more thermally unstable than other materials such as LCO, LMO and LFP,[11–16,19–21,23,31] with the instability increasing as Ni content increases.[12,13,15,18,26–28,30] The state of charge, or degree of delithiation, also factors into the decomposition temperature.[11,12,14,18,24,25,29] Therefore, the thermal stability of promising SC and PC materials should be tested using ARC or experiments in full Li-ion cells to ensure the safety would not be compromised.

References

(1) World Meteorological Organisation. *State of the Global Climate 2020*; WMO-No. 1264, 2021.

(2) *Linden's Handbook of Batteries*; 5th Ed. Beard, K., Ed.; McGraw Hill Professional, 2019.

(3) Pillot, C. *The Rechargeable Battery Market and Main Trends 2020-2030*; 2021.

(4) Masias, A.; Marcicki, J.; Paxton, W. A. *ACS Energy Lett.* **2021**, *6*, 621–630.

(5) Tesla. Tesla | Model S, Tesla | Model 3. https://www.tesla.com/en_CA (accessed Jun 11, 2021).

(6) Geller, S.; Durand, J. L. *Acta Cryst.* **1960**, *13*, 325–331.

(7) Mizushima, K.; Jones, P. C.; Wiseman, P. J.; Goodenough, J. B. *Mater. Res. Bull.* **1980**, *15*, 783–789.

(8) Orman, H. J.; Wiseman, P. J. *Acta Crystallogr. Sect. C Cryst. Struct. Commun.* **1984**, *40*, 12–14.

(9) Ohzuku, T.; Kitagawa, M.; Hirai, T. *J. Electrochem. Soc.* **1990**, *137*, 769–775.

(10) Julien, C. M.; Mauger, A.; Zaghib, K.; Groult, H. *Inorganics* **2014**, *2*, 132–154.

(11) Dahn, J. R.; Fuller, E. W.; Obrovac, M. N.; von Sacken, U. *Solid State Ionics* **1994**, *69*, 265–270.

(12) MacNeil, D. D.; Lu, Z.; Chen, Z.; Dahn, J. R. *J. Power Sources* **2002**, *108*, 8–14.

(13) Yu, X.; Hu, E.; Bak, S. M.; Zhou, Y. N.; Yang, X. Q. *Chinese Phys. B* **2016**, *25*, 018205(1-10).

(14) Xu, J.; Lin, F.; Doeff, M. M.; Tong, W. *J. Mater. Chem. A* **2017**, *5*, 874–901.

(15) Myung, S. T.; Maglia, F.; Park, K. J.; Yoon, C. S.; Lamp, P.; Kim, S. J.; Sun, Y. K. *ACS Energy Lett.* **2017**, *2*, 196–223.

(16) Mauger, A.; Julien, C. M. *Ionics* **2017**, *23*, 1933–1947.

(17) Kim, J.; Lee, H.; Cha, H.; Yoon, M.; Park, M.; Cho, J. *Adv. Energy Mater.* **2018**, *8*, 1702028(1-25).

(18) Tian, C.; Lin, F.; Doeff, M. M. *Acc. Chem. Res.* **2018**, *51*, 89–96.

(19) Liu, K.; Liu, Y.; Lin, D.; Pei, A.; Cui, Y. *Sci. Adv.* **2018**, *4*, eaas9820(1-11).

(20) Ren, D.; Liu, X.; Feng, X.; Lu, L.; Ouyang, M.; Li, J.; He, X. *Appl. Energy* **2018**, *228*, 633–644.

(21) Li, H.; Cormier, M.; Zhang, N.; Inglis, J.; Li, J.; Dahn, J. R. *J. Electrochem. Soc.* **2019**, *166*, A429–A439.

(22) Bianchini, M.; Roca-Ayats, M.; Hartmann, P.; Brezesinski, T.; Janek, J. *Angew. Chemie - Int. Ed.* **2019**, *58*, 10434–10458.

(23) Guilmard, M.; Croguennec, L.; Delmas, C. *Chem. Mater.* **2003**, *15*, 4484–4493.

(24) Cormier, M.; Zhang, N.; Liu, A.; Li, H.; Inglis, J.; Dahn, J. R. *J. Electrochem. Soc.* **2019**, *166*, A2826–A2833.

(25) Bak, S. M.; Nam, K. W.; Chang, W. Y.; Yu, X.; Hu, E.; Hwang, S. Y.; Stach, E. A.; Kim, K. B.; Chung, K. Y.; Yang, X. Q. *Chem. Mater.* **2013**, *25*, 337–351.

(26) Noh, H. J.; Youn, S. J.; Yoon, C. S.; Sun, Y. K. *J. Power Sources* **2013**, *233*, 121–130.

(27) Sun, Y. K.; Lee, D. J.; Lee, Y. J.; Chen, Z.; Myung, S. T. *ACS Appl. Mater. Interfaces* **2013**, *5*, 11434–11440.

(28) Konishi, H.; Yoshikawa, M.; Hirano, T.; Hidaka, K. *J. Power Sources* **2014**, *254*, 338–344.

(29) Benmayza, A.; Lu, W.; Ramani, V.; Prakash, J. *Electrochim. Acta* **2014**, *123*, 7–13.

(30) Bak, S. M.; Hu, E.; Zhou, Y. N.; Yu, X.; Senanayake, S. D.; Cho, S. J.; Kim, K. B.; Chung, K. Y.; Yang, X. Q.; Nam, K. W. *ACS Appl. Mater. Interfaces* **2014**, *6*, 22594–22601.

(31) Golubkov, A. W.; Scheikl, S.; Planteu, R.; Voitic, G.; Wiltsche, H.; Stangl, C.; Fauler, G.; Thaler, A.; Hacker, V. *RSC Adv.* **2015**, *5*, 57171–57186.

(32) Goodenough, J. B.; Mizushima, K. Electrochemical Cell with New Fast Ion Conductors. US4302518, 1981.

(33) Ozawa, K. *Solid State Ionics* **1994**, *69*, 212–221.

(34) Tukamoto, H.; West, A. R. *J. Electrochem. Soc.* **1997**, *144*, 3164–3168.

(35) Fathi, R.; Burns, J. C.; Stevens, D. A.; Ye, H.; Hu, C.; Jain, G.; Scott, E.; Schmidt, C.; Dahn, J. R. *J. Electrochem. Soc.* **2014**, *161*, A1572–A1579.

(36) Shim, J. H.; Han, J. M.; Lee, J. H.; Lee, S. *ACS Appl. Mater. Interfaces* **2016**, *8*, 12205–12210.

(37) Radin, M. D.; Hy, S.; Sina, M.; Fang, C.; Liu, H.; Vinckeviciute, J.; Zhang, M.; Whittingham, M. S.; Meng, Y. S.; Van der Ven, A. *Adv. Energy Mater.* **2017**, *7*, 1602888(1-33).

(38) Cho, J.; Kim, G. *Electrochem. solid-state Lett.* **1999**, *2*, 253–255.

(39) MacNeil, D. D.; Dahn, J. R. *J. Electrochem. Soc.* **2002**, *149*, A912–A919.

(40) Amnesty International. *"This is what we die for": Human rights abuses in the Democratic Republic of the Congo power the global trade in cobalt*; AFR 62/3183/2016, 2016.

(41) Li, W.; Erickson, E. M.; Manthiram, A. *Nat. Energy* **2020**, *5*, 26–34.

(42) Ryu, H. H.; Sun, H. H.; Myung, S. T.; Yoon, C. S.; Sun, Y. K. *Energy Environ. Sci.* **2021**, *14*, 844–852.

(43) United States Geological Survey. *Mineral Commodity Summaries 2021*; 2021.

(44) Turcheniuk, K.; Bondarev, D.; Amatucci, G. G.; Yushin, G. *Mater. Today* **2021**, *42*, 57–72.

(45) Kim, Y.; Seong, W. M.; Manthiram, A. *Energy Storage Mater.* **2021**, *34*, 250–259.

(46) Pillot, C. The Rechargeable Battery Market and Main Trends 2015-2025. Presented at the the 18th International Meeting on Lithium Batteries, Chicago, USA, 2016.

(47) Ohzuku, T.; Makimura, Y. *Chem. Lett.* **2001**, *30*, 642–643.

(48) Lu, Z.; MacNeil, D. D.; Dahn, J. R. *Electrochem. Solid-State Lett.* **2001**, *4*, A200–A203.

(49) Sun, H. H.; Ryu, H. H.; Kim, U. H.; Weeks, J. A.; Heller, A.; Sun, Y. K.; Mullins, C. B. *ACS Energy Lett.* **2020**, *5*, 1136–1146.

(50) MacNeil, D. D.; Lu, Z.; Dahn, J. R. *J. Electrochem. Soc.* **2002**, *149*, A1332–A1336.

(51) Rozier, P.; Tarascon, J. M. *J. Electrochem. Soc.* **2015**, *162*, A2490–A2499.

(52) Li, J. Study and Development of Layered Li-Ni-Mn-Co Oxide Positive Electrode Materials for Lithium Ion Batteries. PhD Thesis, Dalhousie University, 2016.

(53) Kim, J.; Cha, H.; Lee, H.; Oh, P.; Cho, J. *Batter. Supercaps* **2020**, *3*, 309–322.

(54) Ohzuku, T.; Ueda, A.; Kouguchi, M. *J. Electrochem. Soc.* **1995**, *142*, 4033–4039.

(55) Ohzuku, T.; Nakura, K.; Aoki, T. *Electrochim. Acta* **1999**, *45*, 151–160.

(56) Pouillerie, C.; Croguennec, L.; Biensan, P.; Willmann, P.; Delmas, C. *J. Electrochem. Soc.* **2000**, *147*, 2061–2069.

(57) Pouillerie, C.; Croguennec, L.; Delmas, C. *Solid State Ionics* **2000**, *132*, 15–29.

(58) Pouillerie, C.; Perton, F.; Biensan, P.; Pérès, J. P.; Broussely, M.; Delmas, C. *J. Power Sources* **2001**, *96*, 293–302.

(59) Delmas, C.; Ménétrier, M.; Croguennec, L.; Saadoune, I.; Rougier, A.; Pouillerie, C.; Prado, G.; Grüne, M.; Fournes, L. *Electrochim. Acta* **1999**, *45*, 243–253.

(60) Madhavi, S.; Rao, G. V. S.; Chowdari, B. V. R.; Li, S. F. Y. *J. Power Sources* **2001**, *93*, 156–162.

(61) Albrecht, S.; Kümpers, J.; Kruft, M.; Malcus, S.; Vogler, C.; Wahl, M.; Wohlfahrt-Mehrens, M. *J. Power Sources* **2003**, *119–121*, 178–183.

(62) Chen, C. H.; Liu, J.; Stoll, M. E.; Henriksen, G.; Vissers, D. R.; Amine, K. *J. Power Sources* **2004**, *128*, 278–285.

(63) Sasaki, T.; Godbole, V.; Takeuchi, Y.; Ukyo, Y.; Novák, P. *J. Electrochem. Soc.* **2011**, *158*, A1214–A1219.

(64) Li, W.; Liu, X.; Celio, H.; Smith, P.; Dolocan, A.; Chi, M.; Manthiram, A. *Adv. Energy Mater.* **2018**, *8*, 1703154(1-11).

(65) Zhou, K.; Xie, Q.; Li, B.; Manthiram, A. *Energy Storage Mater.* **2021**, *34*, 229–240.

(66) Phattharasupakun, N.; Geng, C.; Johnson, M. B.; Väli, R.; Sawangphruk, M.; Dahn, J. R. *J. Electrochem. Soc.* **2020**, *167*, 160545(1-9).

(67) Lu, Z.; MacNeil, D. D.; Dahn, J. R. *Electrochem. Solid-State Lett.* **2001**, *4*, A191–A194.

(68) Li, J.; Camardese, J.; Glazier, S.; Dahn, J. R. *Chem. Mater.* **2014**, *26*, 7059–7066.

(69) Shunmugasundaram, R.; Arumugam, R. S.; Dahn, J. R. *J. Electrochem. Soc.* **2016**, *163*, A1394–A1400.

(70) Nayak, P. K.; Erickson, E. M.; Schipper, F.; Penki, T. R.; Munichandraiah, N.; Adelhelm, P.; Sclar, H.; Amalraj, F.; Markovsky, B.; Aurbach, D. *Adv. Energy Mater.* **2018**, *8*, 1702397(1-16).

(71) Ku, K.; Hong, J.; Kim, H.; Park, H.; Seong, W. M.; Jung, S. K.; Yoon, G.; Park, K. Y.; Kim, H.; Kang, K. *Adv. Energy Mater.* **2018**, *8*, 1800606(1-8).

(72) Hu, S.; Pillai, A. S.; Liang, G.; Pang, W. K.; Wang, H.; Li, Q.; Guo, Z. *Electrochem. Energy Rev.* **2019**, *2*, 277–311.

(73) Phattharasupakun, N.; Geng, C.; Johnson, M. B.; Väli, R.; Liu, A.; Liu, Y.; Sawangphruk, M.; Dahn, J. R. *J. Electrochem. Soc.* **2020**, *167*, 120531(1-8).

(74) Bian, X.; Zhang, R.; Yang, X. *Inorg. Chem.* **2020**, *59*, 17535–17543.

(75) Lu, Z.; Dahn, J. R. *J. Electrochem. Soc.* **2002**, *149*, A815–A822.

(76) Lee, M. J.; Lee, S.; Oh, P.; Kim, Y.; Cho, J. *Nano Lett.* **2014**, *14*, 993–999.

(77) Padhi, A. K.; Nanjundaswamy, K. S.; Goodenough, J. B. *J. Electrochem. Soc.* **1997**, *144*, 1188–1194.

(78) Zaghib, K.; Charest, P.; Dontigny, M.; Guerfi, A.; Lagacé, M.; Mauger, A.; Kopec, M.; Julien, C. M. *J. Power Sources* **2010**, *195*, 8280–8288.

(79) Zheng, T.; Reimers, J. N.; Dahn, J. R. *Phys. Rev. B* **1995**, *51*, 734–741.

(80) Obrovac, M. N.; Chevrier, V. L. *Chem. Rev.* **2014**, *114*, 11444–11502.

(81) Weber, R.; Louli, A. J.; Plucknett, K.; Dahn, J. R. *J. Electrochem. Soc.* **2019**, *166*, A1779–A1784.

(82) Yang, Z.; Choi, D.; Kerisit, S.; Rosso, K. M.; Wang, D.; Zhang, J.; Graff, G.; Liu, J. *J. Power Sources* **2009**, *192*, 588–598.

(83) Ohzuku, T.; Ueda, A.; Yamamoto, N. *J. Electrochem. Soc.* **1995**, *142*, 1431–1435.

(84) Xu, K. *Chem. Rev.* **2004**, *104*, 4303–4417.

(85) Xu, K. *Chem. Rev.* **2014**, *114*, 11503–11618.

(86) Fong, R.; von Sacken, U.; Dahn, J. R. *J. Electrochem. Soc.* **1990**, *137*, 2009–2013.

(87) Peled, E. *J. Electrochem. Soc.* **1979**, *126*, 2047–2051.

(88) Peled, E.; Golodnitsky, D.; Ardel, G. *J. Electrochem. Soc.* **1997**, *144*, L208–L210.

(89) Li, J.; Li, W.; You, Y.; Manthiram, A. *Adv. Energy Mater.* **2018**, *8*, 1801957(1-11).

(90) Li, H.; Li, J.; Zaker, N.; Zhang, N.; Botton, G. A.; Dahn, J. R. *J. Electrochem. Soc.* **2019**, *166*, A1956–A1963.

(91) Harlow, J.; Ma, X.; Li, J.; Logan, E.; Liu, Y.; Zhang, N.; Ma, L.; Glazier, S.; Cormier, M.; Genovese, M.; Buteau, S.; Cameron, A.; Stark, J.; Dahn, J. R. *J. Electrochem. Soc.* **2019**, *166*, A3031–A3044.

(92) Logan, E.; Hebecker, H.; Ma, X.; Quinn, J.; HyeJeong, Y.; Kumakura, S.; Paulsen, J.; Dahn, J. R. *J. Electrochem. Soc.* **2020**, *167*, 060530(1-14).

(93) Abe, K.; Miyoshi, K.; Hattori, T.; Ushigoe, Y.; Yoshitake, H. *J. Power Sources* **2008**, *184*, 449–455.

(94) Nie, M.; Chalasani, D.; Abraham, D. P.; Chen, Y.; Bose, A.; Lucht, B. L. *J. Phys. Chem. C* **2013**, *117*, 1257–1267.

(95) Madec, L.; Petibon, R.; Xia, J.; Sun, J. P.; Hill, I. G.; Dahn, J. R. *J. Electrochem. Soc.* **2015**, *162*, A2635–A2645.

(96) Xia, J.; Nelson, K. J.; Lu, Z.; Dahn, J. R. *J. Power Sources* **2016**, *329*, 387–397.

(97) Li, J.; Cameron, A.; Li, H.; Glazier, S.; Xiong, D.; Chatzidakis, M.; Allen, J.; Botton, G. A.; Dahn, J. R. *J. Electrochem. Soc.* **2017**, *164*, A1534–A1544.

(98) Yu, X.; Manthiram, A. *Energy Environ. Sci.* **2018**, *11*, 527–543.

(99) Li, H.; Li, J.; Ma, X.; Dahn, J. R. *J. Electrochem. Soc.* **2018**, *165*, A1038–A1045.

(100) Thomas, M. G. S. R.; David, W. I. F.; Goodenough, J. B.; Groves, P. *Mater. Res. Bull.* **1985**, *20*, 1137–1146.

(101) Dahn, J. R.; von Sacken, U.; Michal, C. A. *Solid State Ionics* **1990**, *44*, 87–97.

(102) Dahn, J. R.; von Sacken, U.; Juzkow, M. W.; Al-Janaby, H. *J. Electrochem. Soc.* **1991**, *138*, 2207–2211.

(103) Metalary. Latest and Historical Metal Prices. https://www.metalary.com/ (accessed Jun 17, 2021).

(104) Scrap Monster. Metal Prices - Base Metals, Minor Metals, Rare Earth, High Purity Metals, Stable Isotopes Prices. https://www.scrapmonster.com/metal-prices (accessed Jun 17, 2021).

(105) Li, W.; Reimers, J. N.; Dahn, J. R. *Phys. Rev. B* **1992**, *46*, 3236–3246.

(106) Shannon, R. D. *Acta Crystallogr. Sect. A* **1976**, *32*, 751–767.

(107) Deb, A.; Bergmann, U.; Cramer, S.; Cairns, E. *J. Appl. Phys.* **2005**, *97*, 113523(1-11).

(108) Ohzuku, T.; Ueda, A.; Nagayama, M. *J. Electrochem. Soc.* **1993**, *140*, 1862–1870.

(109) Li, W.; Reimers, J. N.; Dahn, J. R. *Solid State Ionics* **1993**, *67*, 123–130.

(110) Li, H.; Zhang, N.; Li, J.; Dahn, J. R. *J. Electrochem. Soc.* **2018**, *165*, A2985–A2993.

(111) Bai, J.; Sun, W.; Zhao, J.; Wang, D.; Xiao, P.; Ko, J. Y.; Huq, A.; Ceder, G.; Wang, F. *Chem. Mater.* **2020**, *32*, 9906–9913.

(112) Rossen, E.; Jones, C. D. W.; Dahn, J. R. *Solid State Ionics* **1992**, *57*, 311–318.

(113) Lee, K. S.; Myung, S. T.; Moon, J. S.; Sun, Y. K. *Electrochim. Acta* **2008**, *53*, 6033–6037.

(114) van Bommel, A.; Dahn, J. R. *J. Electrochem. Soc.* **2009**, *156*, A362–A365.

(115) van Bommel, A.; Dahn, J. R. *Chem. Mater.* **2009**, *21*, 1500–1503.

(116) van Bommel, A. Lithium-rich Transition Metal Oxides as Positive Electrode Materials in Lithium-ion Batteries. PhD Thesis, Dalhousie University, 2010.

(117) Camardese, J.; Abarbanel, D.; McCalla, E.; Dahn, J. R. *J. Electrochem. Soc.* **2014**, *161*, A890–A895.

(118) Camardese, J. Core-Shell Materials as Positive Electrodes in Lithium-Ion Batteries. PhD Thesis, Dalhousie University, 2015.

(119) Yoon, S. H.; Lee, C. W.; Bae, Y. S.; Hwang, I.; Park, Y. K.; Song, J. H. *Electrochem. Solid State Lett.* **2009**, *12*, A211–A214.

(120) Kim, Y.; Kim, D. *ACS Appl. Mater. Interfaces* **2012**, *4*, 586–589.

(121) Xie, H.; Du, K.; Hu, G.; Duan, J.; Peng, Z.; Zhang, Z.; Cao, Y. *J. Mater. Chem. A* **2015**, *3*, 20236–20243.

(122) Duan, J.; Hu, G.; Cao, Y.; Tan, C.; Wu, C.; Du, K.; Peng, Z. *J. Power Sources* **2016**, *326*, 322–330.

(123) Duan, J.; Wu, C.; Cao, Y.; Huang, D.; Du, K.; Peng, Z.; Hu, G. *J. Alloys Compd.* **2017**, *695*, 91–99.

(124) He, K.; Ruan, Z.; Teng, X.; Zhu, Y. *Mater. Res. Bull.* **2017**, *90*, 131–137.

(125) Liu, A.; Zhang, N.; Li, J.; Casagrande, T.; Butcher, C.; Martinez, J.; Korinek, A.; Botton, G. A.; Dahn, J. R. *J. Electrochem. Soc.* **2018**, *165*, A2781–A2791.

(126) Purwanto, A.; Yudha, C. S.; Ubaidillah, U.; Widiyandari, H.; Ogi, T.; Haerudin, H. *Mater. Res. Express* **2018**, *5*, 122001(1-22).

(127) Liu, A.; Dahn, J. R. *ChemEngineering* **2019**, *3*, 38(1-14).

(128) Zhao, J.; Zhang, W.; Huq, A.; Misture, S. T.; Zhang, B.; Guo, S.; Wu, L.; Zhu, Y.; Chen, Z.; Amine, K.; Pan, F.; Bai, J.; Wang, F. *Adv. Energy Mater.* **2017**, *7*, 1601266(1-13).

(129) Bianchini, M.; Fauth, F.; Hartmann, P.; Brezesinski, T.; Janek, J. *J. Mater. Chem. A* **2020**, *8*, 1808–1820.

(130) Weber, R.; Li, H.; Chen, W.; Kim, C. Y.; Plucknett, K.; Dahn, J. R. *J. Electrochem. Soc.* **2020**, *167*, 100501(1-9).

(131) Li, J.; Zhang, N.; Li, H.; Liu, A.; Wang, Y.; Yin, S.; Wu, H.; Dahn, J. R. *J. Electrochem. Soc.* **2018**, *165*, A3544–A3557.

(132) McCalla, E.; Carey, G. H.; Dahn, J. R. *Solid State Ionics* **2012**, *219*, 11–19.

(133) Li, J.; Li, H.; Stone, W.; Weber, R.; Hy, S.; Dahn, J. R. *J. Electrochem. Soc.* **2017**, *164*, A3529–A3537.

(134) Zhu, J.; Chen, G. *J. Mater. Chem. A* **2019**, *7*, 5463–5474.

(135) Fan, X.; Hu, G.; Zhang, B.; Ou, X.; Zhang, J.; Zhao, W.; Jia, H.; Zou, L.; Li, P.; Yang, Y. *Nano Energy* **2020**, *70*, 104450(1-11).

(136) Huang, B.; Wang, M.; Zuo, Y.; Zhao, Z.; Zhang, X.; Gu, Y. *Solid State Ionics* **2020**, *345*, 115200(1-8).

(137) Qian, G.; Zhang, Y.; Li, L.; Zhang, R.; Xu, J.; Cheng, Z.; Xie, S.; Wang, H.; Rao, Q.; He, Y.; Shen, Y.; Chen, L.; Tang, M.; Ma, Z. F. *Energy Storage Mater.* **2020**, *27*, 140–149.

(138) Wang, T.; Ren, K.; He, M.; Dong, W.; Xiao, W.; Pan, H.; Yang, J.; Yang, Y.; Liu, P.; Cao, Z.; Ma, X.; Wang, H. *Front. Chem.* **2020**, *8*, 747(1-8).

(139) Zhang, M.; Shen, J.; Li, J.; Zhang, D.; Yan, Y.; Huang, Y.; Li, Z. *Ceram. Int.* **2020**, *46*, 4643–4651.

(140) Duan, Y.; Yang, L.; Zhang, M. J.; Chen, Z.; Bai, J.; Amine, K.; Pan, F.; Wang, F. *J. Mater. Chem. A* **2019**, *7*, 513–519.

(141) Kong, D.; Zhang, M.; Xiao, Y.; Hu, J.; Zhao, W.; Han, L.; Pan, F. *Nano Energy* **2019**, *59*, 327–335.

(142) Zheng, J.; Ye, Y.; Liu, T.; Xiao, Y.; Wang, C.; Wang, F.; Pan, F. *Acc. Chem. Res.* **2019**, *52*, 2201–2209.

(143) Wang, T.; Ren, K.; Xiao, W.; Dong, W.; Qiao, H.; Duan, A.; Pan, H.; Yang, Y.; Wang, H. *J. Phys. Chem. C* **2020**, *124*, 5600–5607.

(144) Lee, D. G.; Gupta, R. K.; Cho, Y. S.; Hwang, K. T. *J. Appl. Electrochem.* **2009**, *39*, 671–679.

(145) Shim, J. H.; Kim, C. Y.; Cho, S. W.; Missiul, A.; Kim, J. K.; Ahn, Y. J.; Lee, S. *Electrochim. Acta* **2014**, *138*, 15–21.

(146) Liu, B. S.; Wang, Z. B.; Yu, F. Da; Xue, Y.; Wang, G. J.; Zhang, Y.; Zhou, Y. X. *RSC Adv.* **2016**, *6*, 108558–108565.

(147) Nie, Y.; Xiao, W.; Miao, C.; Xu, M.; Wang, C. *Electrochim. Acta* **2020**, *334*, 135654(1-11).

(148) Mesnier, A.; Manthiram, A. *ACS Appl. Mater. Interfaces* **2020**, *12*, 52826–52835.

(149) Liu, A.; Zhang, N.; Li, H.; Inglis, J.; Wang, Y.; Yin, S.; Wu, H.; Dahn, J. R. *J. Electrochem. Soc.* **2019**, *166*, A4025–A4033.

(150) Chen, Z.; Lu, Z.; Dahn, J. R. *J. Electrochem. Soc.* **2002**, *149*, A1604–A1609.

(151) Liu, A.; Li, J.; Shunmugasundaram, R.; Dahn, J. R. *J. Electrochem. Soc.* **2017**, *164*, A1655–A1664.

(152) Liu, A. Synthesis and Characterization of Magnesium and Manganese Doped $LiCoO_2$. MSc Thesis, Dalhousie University, 2017.

(153) Croguennec, L.; Pouillerie, C.; Delmas, C. *J. Electrochem. Soc.* **2000**, *147*, 1314–1321.

(154) Delmas, C.; Pérès, J. P.; Rougier, A.; Demourgues, A.; Weill, F.; Chadwick, A.; Broussely, M.; Perton, F.; Biensan, P.; Willmann, P. *J. Power Sources* **1997**, *68*, 120–125.

(155) Li, H. Studies of Ni-rich Positive Electrode Materials for Lithium Ion Batteries. PhD Thesis, Dalhousie University, 2019.

(156) Sun, H. H.; Manthiram, A. *Chem. Mater.* **2017**, *29*, 8486–8493.

(157) Li, H.; Liu, A.; Zhang, N.; Wang, Y.; Yin, S.; Wu, H.; Dahn, J. R. *Chem. Mater.* **2019**, *31*, 7574–7583.

(158) Ryu, H. H.; Park, N. Y.; Noh, T. C.; Kang, G. C.; Maglia, F.; Kim, S. J.; Yoon, C. S.; Sun, Y. K. *ACS Energy Lett.* **2021**, *6*, 216–223.

(159) Liu, X.; Zhan, X.; Hood, Z. D.; Li, W.; Leonard, D. N.; Manthiram, A.; Chi, M. *J. Mater. Chem. A* **2021**, *9*, 2111–2119.

(160) Makimura, Y.; Zheng, S.; Ikuhara, Y.; Ukyo, Y. *J. Electrochem. Soc.* **2012**, *159*, A1070–A1073.

(161) Zhang, H.; Omenya, F.; Yan, P.; Luo, L.; Whittingham, M. S.; Wang, C.; Zhou, G. *ACS Energy Lett.* **2017**, *2*, 2607–2615.

(162) Xiong, D.; Ellis, L.; Li, J.; Li, H.; Hynes, T.; Allen, J.; Xia, J.; Hall, D. S.; Hill, I.; Dahn, J. R. *J. Electrochem. Soc.* **2017**, *164*, A3025–A3037.

(163) Erickson, E. M.; Li, W.; Dolocan, A.; Manthiram, A. *ACS Appl. Mater. Interfaces* **2020**, *12*, 16451–16461.

(164) Strehle, B.; Friedrich, F.; Gasteiger, H. A. *J. Electrochem. Soc.* **2021**, *168*, 050512(1-15).

(165) Li, J.; Liu, H.; Xia, J.; Cameron, A.; Nie, M.; Botton, G. A.; Dahn, J. R. *J. Electrochem. Soc.* **2017**, *164*, A655–A665.

(166) Hatchard, T. D.; MacNeil, D. D.; Stevens, D. A.; Christensen, L.; Dahn, J. R. *Electrochem. Solid-State Lett.* **2000**, *3*, 305–308.

(167) MacNeil, D. D.; Larcher, D.; Dahn, J. R. *J. Electrochem. Soc.* **1999**, *146*, 3596–3602.

(168) Wang, L.; Maxisch, T.; Ceder, G. *Chem. Mater.* **2007**, *19*, 543–552.

(169) MacNeil, D. D.; Dahn, J. R. *J. Electrochem. Soc.* **2001**, *148*, A1205–A1210.

(170) Rougier, A.; Gravereau, P.; Delmas, C. *J. Electrochem. Soc.* **1996**, *143*, 1168–1175.

(171) Iqbal, A.; Li, D. *Chem. Phys. Lett.* **2019**, *720*, 97–106.

(172) Huang, X.; Duan, J.; He, J.; Shi, H.; Li, Y.; Zhang, Y.; Wang, D.; Dong, P.; Zhang, Y. *Mater. Today Energy* **2020**, *17*, 100440(1-9).

(173) Su, Y.; Chen, G.; Chen, L.; Li, L.; Li, C.; Ding, R.; Liu, J.; Lv, Z.; Lu, Y.; Bao, L.; Tan, G.; Chen, S.; Wu, F. *Front. Chem.* **2020**, *8*, 573(1-11).

(174) Seong, W. M.; Kim, Y.; Manthiram, A. *Chem. Mater.* **2020**, *32*, 9479–9489.

(175) Kim, Y.; Park, H.; Warner, J. H.; Manthiram, A. *ACS Energy Lett.* **2021**, *6*, 941–948.

(176) Liu, H. S.; Zhang, Z. R.; Gong, Z. L.; Yang, Y. *Electrochem. Solid-State Lett.* **2004**, *7*, A190–A193.

(177) Cho, D. H.; Jo, C. H.; Cho, W.; Kim, Y. J.; Yashiro, H.; Sun, Y. K.; Myung, S. T. *J. Electrochem. Soc.* **2014**, *161*, A920–A926.

(178) Faenza, N.; Bruce, L.; Lebens-Higgins, Z. W.; Plitz, I.; Pereira, N.; Piper, L. F. J.; Amatucci, G. G. *J. Electrochem. Soc.* **2017**, *164*, A3727–A3741.

(179) Jung, R.; Morasch, R.; Karayaylali, P.; Phillips, K.; Maglia, F.; Stinner, C.; Shao-Horn, Y.; Gasteiger, H. A. *J. Electrochem. Soc.* **2018**, *165*, A132–A141.

(180) Lin, Y.; Xu, M.; Tian, Y. Y.; Fan, W.; Yu, L.; Li, W. *Mater. Chem. Phys.* **2018**, *211*, 200–205.

(181) You, Y.; Celio, H.; Li, J.; Dolocan, A.; Manthiram, A. *Angew. Chemie - Int. Ed.* **2018**, *57*, 6480–6485.

(182) Pritzl, D.; Teufl, T.; Freiberg, A. T. S.; Strehle, B.; Sicklinger, J.; Sommer, H.; Hartmann, P.; Gasteiger, H. A. *J. Electrochem. Soc.* **2019**, *166*, A4056–A4066.

(183) Hamam, I.; Zhang, N.; Liu, A.; Johnson, M. B.; Dahn, J. R. *J. Electrochem. Soc.* **2020**, *167*, 130521(1-14).

(184) Zhang, N.; Stark, J.; Li, H.; Liu, A.; Li, Y.; Hamam, I.; Dahn, J. R. *J. Electrochem. Soc.* **2020**, *167*, 080518(1-10).

(185) Hwang, S. Y.; Kim, S. M.; Bak, S. M.; Cho, B. W.; Chung, K. Y.; Lee, J. Y.; Chang, W. Y.; Stach, E. A. *ACS Appl. Mater. Interfaces* **2014**, *6*, 15140–15147.

(186) Levasseur, S.; Ménétrier, M.; Delmas, C. *J. Power Sources* **2002**, *112*, 419–427.

(187) Yin, R. Z.; Kim, Y. S.; Shin, S. J.; Jung, I.; Kim, J. S.; Jeong, S. K. *J. Electrochem. Soc.* **2012**, *159*, A253–A258.

(188) Wang, Z.; Wang, Z.; Guo, H.; Peng, W.; Li, X. *Ceram. Int.* **2015**, *41*, 469–474.

(189) Shim, J. H.; Lee, J. H.; Han, S. Y.; Lee, S. *Electrochim. Acta* **2015**, *186*, 201–208.

(190) Luo, W.; Zhou, F.; Zhao, X.; Lu, Z.; Li, X.; Dahn, J. R. *Chem. Mater.* **2010**, *22*, 1164–1172.

(191) Zhang, B.; Li, L.; Zheng, J. *J. Alloys Compd.* **2012**, *520*, 190–194.

(192) Huang, Z.; Li, X.; Liang, Y.; He, Z.; Chen, H.; Wang, Z.; Guo, H. *Solid State Ionics* **2015**, *282*, 88–94.

(193) Kondo, H.; Takeuchi, Y.; Sasaki, T.; Kawauchi, S.; Itou, Y.; Hiruta, O.; Okuda, C.; Yonemura, M.; Kamiyama, T.; Ukyo, Y. *J. Power Sources* **2007**, *174*, 1131–1136.

(194) Huang, B.; Li, X.; Wang, Z.; Guo, H.; Xiong, X. *Ceram. Int.* **2014**, *40*, 13223–13230.

(195) Xie, Q.; Li, W.; Manthiram, A. *Chem. Mater.* **2019**, *31*, 938–946.

(196) Mu, L.; Zhang, R.; Kan, W. H.; Zhang, Y.; Li, L.; Kuai, C.; Zydlewski, B.; Rahman, M. M.; Sun, C. J.; Sainio, S.; Avdeev, M.; Nordlund, D.; Xin, H.; Lin, F. *Chem. Mater.* **2019**, *31*, 9769–9776.

(197) Seong, W. M.; Manthiram, A. *ACS Appl. Mater. Interfaces* **2020**, *12*, 43653–43664.

(198) Guilmard, M.; Rougier, A.; Grüne, M.; Croguennec, L.; Delmas, C. *J. Power Sources* **2003**, *115*, 305–314.

(199) Majumder, S. B.; Nieto, S.; Katiyar, R. S. *J. Power Sources* **2006**, *154*, 262–267.

(200) Lee, K. K.; Kim, K. B. *J. Electrochem. Soc.* **2000**, *147*, 1709–1717.

(201) Aishova, A.; Park, G. T.; Yoon, C. S.; Sun, Y. K. *Adv. Energy Mater.* **2020**, *10*, 1903179(1-9).

(202) Zhang, S.; Gao, P.; Wang, Y.; Li, J.; Zhu, Y. *J. Alloys Compd.* **2021**, *885*, 161005(1-9).

(203) Ma, R.; Zhao, Z.; Fu, J.; Lv, H.; Li, C.; Wu, B.; Mu, D.; Wu, F. *ChemElectroChem* **2020**, *7*, 2637–2642.

(204) Zhang, J. T.; Tan, X. H.; Guo, L. M.; Jiang, Y.; Liu, S. N.; Wang, H. F.; Kang, X. H.; Chu, W. G. *J. Alloys Compd.* **2019**, *771*, 42–50.

(205) Ryu, H. H.; Park, G. T.; Yoon, C. S.; Sun, Y. K. *J. Mater. Chem. A* **2019**, *7*, 18580–18588.

(206) Yoon, C. S.; Choi, M. J.; Jun, D. W.; Zhang, Q.; Kaghazchi, P.; Kim, K. H.; Sun, Y. K. *Chem. Mater.* **2018**, *30*, 1808–1814.

(207) Ryu, H. H.; Park, N. Y.; Yoon, D. R.; Kim, U. H.; Yoon, C. S.; Sun, Y. K. *Adv. Energy Mater.* **2020**, *10*, 2000495(1-8).

(208) Kim, U. H.; Park, G. T.; Son, B. K.; Nam, G. W.; Liu, J.; Kuo, L. Y.; Kaghazchi, P.; Yoon, C. S.; Sun, Y. K. *Nat. Energy* **2020**, *5*, 860–869.

(209) Cui, Z.; Xie, Q.; Manthiram, A. *ACS Appl. Mater. Interfaces* **2021**, *13*, 15324–15332.

(210) Zhang, N.; Zaker, N.; Li, H.; Liu, A.; Inglis, J.; Jing, L.; Li, J.; Li, Y.; Botton, G. A.; Dahn, J. R. *Chem. Mater.* **2019**, *31*, 10150–10160.

(211) Li, W.; Lee, S.; Manthiram, A. *Adv. Mater.* **2020**, *32*, 2002718(1-6).

(212) Liu, Y.; Wu, H.; Li, K.; Li, H.; Ouyang, D.; Arab, P.; Phattharasupakun, N.; Rathore, D.; Johnson, M. B.; Wang, Y.; Yin, S.; Dahn, J. R. *J. Electrochem. Soc.* **2020**, *167*, 120533(1-8).

(213) Liu, Y.; Wu, H.; Wang, Y.; Li, K.; Yin, S.; Dahn, J. R. *J. Electrochem. Soc.* **2021**, *167*, 160556(1-8).

(214) Logan, E.; Hebecker, H.; Eldesoky, A.; Luscombe, A.; Johnson, M. B.; Dahn, J. R. *J. Electrochem. Soc.* **2020**, *167*, 130543(1-16).

(215) McKinsey & Company. *The future of nickel: A class act*; 2017.

(216) Nam, G. W.; Park, N. Y.; Park, K. J.; Yang, J.; Liu, J.; Yoon, C. S.; Sun, Y. K. *ACS Energy Lett.* **2019**, *4*, 2995–3001.

(217) Li, W.; Asl, H. Y.; Xie, Q.; Manthiram, A. *J. Am. Chem. Soc.* **2019**, *141*, 5097–5101.

(218) Lee, S. H.; Sim, S. J.; Jin, B. S.; Kim, H. S. *Mater. Lett.* **2020**, *270*, 127615(1-4).

(219) Wang, L.; Wu, B.; Mu, D.; Liu, X.; Peng, Y.; Xu, H.; Liu, Q.; Gai, L.; Wu, F. *J. Alloys Compd.* **2016**, *674*, 360–367.

(220) Huang, B.; Wang, M.; Zhang, X.; Xu, G.; Gu, Y. *Ionics* **2020**, *26*, 2689–2698.

(221) Liang, R.; Wu, Z. Y.; Yang, W. M.; Tang, Z. Q.; Xiong, G. G.; Cao, Y. C.; Hu, S. R.; Wang, Z. B. *Ionics* **2020**, *26*, 1635–1643.

(222) Zhang, H.; Fang, H. *Ionics* **2020**, *26*, 3185–3192.

(223) Zhu, J.; Zheng, J.; Cao, G.; Li, Y.; Zhou, Y.; Deng, S.; Hai, C. *J. Power Sources* **2020**, *464*, 228207(1-11).

(224) Yang, C.; Zhu, Z.; Wei, W.; Zhou, L. *Int. J. Electrochem. Sci.* **2020**, *15*, 5031–5041.

(225) Qian, G.; Li, Z.; Meng, D.; Liu, J.; He, Y.-S.; Rao, Q.; Liu, Y.; Ma, Z.-F.; Li, L. *J. Electrochem. Soc.* **2021**, *168*, 010534(1-6).

(226) Liu, A.; Zhang, N.; Stark, J.; Arab, P.; Li, H.; Dahn, J. R. *J. Electrochem. Soc.* **2021**, *168*, 040531(1-15).

(227) Liu, A.; Zhang, N.; Stark, J.; Arab, P.; Li, H.; Dahn, J. R. *J. Electrochem. Soc.* **2021**, *168*, 050506(1-12).

(228) Ryu, H. H.; Namkoong, B.; Kim, J. H.; Belharouak, I.; Yoon, C. S.; Sun, Y. K. *ACS Energy Lett.* **2021**, *6*, 2726–2734.

(229) Langdon, J.; Manthiram, A. *Energy Storage Mater.* **2021**, *37*, 143–160.

(230) Wang, D.; Kou, R.; Ren, Y.; Sun, C. J.; Zhao, H.; Zhang, M. J.; Li, Y.; Huq, A.; Ko, J. Y. P.; Pan, F.; Sun, Y. K.; Yang, Y.; Amine, K.; Bai, J.; Chen, Z.; Wang, F. *Adv. Mater.* **2017**, *29*, 1606715(1-8).

(231) Bi, Y.; Tao, J.; Wu, Y.; Li, L.; Xu, Y.; Hu, E.; Wu, B.; Hu, J.; Wang, C.; Zhang, J. G.; Qi, Y.; Xiao, J. *Science* **2020**, *370*, 1313–1317.

(232) Cha, H.; Kim, J.; Lee, H.; Kim, N.; Hwang, J.; Sung, J.; Yoon, M.; Kim, K.; Cho, J. *Adv. Mater.* **2020**, *32*, 2003040(1-10).

(233) Zhao, Z.; Huang, B.; Wang, M.; Yang, X.; Gu, Y. *Solid State Ionics* **2019**, *342*, 115065(1-10).

(234) Liu, G.; Li, M.; Wu, N.; Cui, L.; Huang, X.; Liu, X.; Zhao, Y.; Chen, H.; Yuan, W.; Bai, Y. *J. Electrochem. Soc.* **2018**, *165*, A3040–A3047.

(235) Zhang, X.; Hu, G.; Peng, Z.; Cao, Y.; Li, L.; Tan, C.; Wang, Y.; Wang, W.; Du, K. *Ceram. Int.* **2021**, In Press.

(236) Liu, Y.; Harlow, J.; Dahn, J. R. *J. Electrochem. Soc.* **2020**, *167*, 020512(1-9).

(237) Ge, M.; Wi, S.; Liu, X.; Bai, J.; Ehrlich, S.; Lu, D.; Lee, W.-K.; Chen, Z.; Wang, F. *Angew. Chemie Int. Ed.* **2021**, *60*, 1–7.

(238) Zhou, H.; Xin, F.; Pei, B.; Whittingham, M. S. *ACS Energy Lett.* **2019**, *4*, 1902–1906.

(239) Van der Ven, A.; Ceder, G. *J. Power Sources* **2001**, *97–98*, 529–531.

(240) Li, J.; Harlow, J.; Stakheiko, N.; Zhang, N.; Paulsen, J.; Dahn, J. R. *J. Electrochem. Soc.* **2018**, *165*, A2682–A2695.

(241) Peres, J. P.; Delmas, C.; Rougier, A.; Broussely, M.; Perton, F.; Biensan, P.; Willmann, P. *J. Phys. Chem. Solids* **1996**, *57*, 1057–1060.

(242) Arai, H.; Okada, S.; Sakurai, Y.; Yamaki, J. I. *Solid State Ionics* **1997**, *95*, 275–282.

(243) Mueller-Neuhaus, J. R.; Dunlap, R. A.; Dahn, J. R. *J. Electrochem. Soc.* **2000**, *147*, 3598–3605.

(244) Kang, S. H.; Yoon, W. S.; Nam, K. W.; Yang, X. Q.; Abraham, D. P. *J. Mater. Sci.* **2008**, *43*, 4701–4706.

(245) Grenier, A.; Reeves, P. J.; Liu, H.; Seymour, I. D.; Märker, K.; Wiaderek, K. M.; Chupas, P. J.; Grey, C. P.; Chapman, K. W. *J. Am. Chem. Soc.* **2020**, *142*, 7001–7011.

(246) Kasnatscheew, J.; Evertz, M.; Streipert, B.; Wagner, R.; Klöpsch, R.; Vortmann, B.; Hahn, H.; Nowak, S.; Amereller, M.; Gentschev, A. C.; Lamp, P.; Winter, M. *Phys. Chem. Chem. Phys.* **2016**, *18*, 3956–3965.

(247) Yoshio, M.; Brodd, R. J.; Kozawa, A. *Lithium-Ion Batteries: Science and Technologies*; Springer Science & Business Media, 2009.

(248) Warren, B. E. *X-Ray Diffraction*; Dover Ed. Dover Publications, 1990.

(249) Cullity, B. D.; Stock, S. R. *Elements of X-Ray Diffraction*; 3rd Ed. Prentice Hall, 2001.

(250) Rietveld, H. M. *J. Appl. Crystallogr.* **1969**, *2*, 65–71.

(251) Hunter, B. A. *Rietica for Windows*; Version 2.1, 2007.

(252) Hunter, B. A. *Int. Union Crystallogr. Comm. Powder Diffr. Newsl.* **1998**, *20*, 21.

(253) Hunter, B. A.; Howard, C. J. *A Computer Program for Rietveld Analysis of X-Ray and Neutron Powder Diffraction Patterns*; Australian Nuclear Science and Technology Organization, 2000.

(254) Crystal Impact. *Match!*; Version 1.11h, 2013.

(255) The International Centre for Diffraction Data. ICDD Products - PDF-4+. http://www.icdd.com/products/pdf4.htm (accessed Jun 23, 2021).

(256) Wyckoff, R. W. G. *Crystals Structures*; Interscience Publishers, 1958.

(257) National Institute of Standards and Technology. X-Ray Form Factor, Attenuation, and Scattering Tables. https://www.nist.gov/pml/x-ray-form-factor-attenuation-and-scattering-tables (accessed Jun 23, 2021).

(258) Peng, L. M.; Ren, G.; Dudarev, S. L.; Whelan, M. J. *Acta Crystallogr. Sect. A Found. Crystallogr.* **1996**, *52*, 456–470.

(259) Toby, B. H. *Powder Diffr.* **2006**, *21*, 67–70.

(260) Kim, H. S.; Ko, T. K.; Na, B. K.; Cho, W. Il; Chao, B. W. *J. Power Sources* **2004**, *138*, 232–239.

(261) Kriegner, D.; Matej, Z.; Kuzel, R.; Holy, V. *J. Appl. Crystallogr.* **2015**, *48*, 613–618.

(262) Widjonarko, N. *Coatings* **2016**, *6*, 54.

(263) Brundle, C. R.; Evans, C. A.; Wilson, S. *Encyclopedia of Materials Characterization*; Butterworth-Heinemann, 1992.

(264) Skoog, D. A.; Holler, F. J.; Crouch, S. R. *Principles of Instrumental Analysis*; 6th Ed. Brooks/Cole, 2007.

(265) Boss, C. B.; Fredeen, K. J. *Concepts, Instrumentation and Techniques in Inductively Coupled Plasma Optical Emission Spectrometry*; 3rd Ed. PerkinElmer Life and Analytical Sciences, 2004.

(266) Marks, T.; Trussler, S.; Smith, A. J.; Xiong, D.; Dahn, J. R. *J. Electrochem. Soc.* **2011**, *158*, A51–A57.

(267) Xiao, P.; Lv, T.; Chen, X.; Chang, C. *Sci. Rep.* **2017**, *7*, 1408(1-8).

(268) Zhang, N.; Zhang, X.; Shi, E.; Zhao, S.; Jiang, K.; Wang, D.; Wang, P.; Guo, S.; He, P.; Zhou, H. *J. Energy Chem.* **2018**, *27*, 1655–1660.

(269) Tang, Z. F.; Wu, R.; Huang, P. F.; Wang, Q. S.; Chen, C. H. *J. Alloys Compd.* **2017**, *693*, 1157–1163.

(270) Zhang, H. Z.; Liu, C.; Song, D. W.; Zhang, L. Q.; Bie, L. J. *J. Mater. Chem. A* **2017**, *5*, 835–841.

(271) Zhao, X.; Zhou, F.; Dahn, J. R. *J. Electrochem. Soc.* **2008**, *155*, A642–A647.

(272) Luo, W.; Dahn, J. R. *Chem. Mater.* **2009**, *21*, 56–62.

(273) Zhao, Y.; Li, J.; Dahn, J. R. *Chem. Mater.* **2017**, *29*, 5239–5248.

(274) Kim, Y.; Kim, D.; Kang, S. *Chem. Mater.* **2011**, *23*, 5388–5397.

(275) Hu, G.; Li, L.; Lu, Y.; Cao, Y.; Peng, Z.; Xue, Z.; Zhang, Y.; Fan, J.; Du, K. *J. Electrochem. Soc.* **2020**, *167*, 140505(1-9).

(276) Sun, G.; Yin, X.; Yang, W.; Song, A.; Jia, C.; Yang, W.; Du, Q.; Ma, Z.; Shao, G. *Phys. Chem. Chem. Phys.* **2017**, *19*, 29886–29894.

(277) Han, S.; Park, J.; Lu, W.; Sastry, A. M. *J. Power Sources* **2013**, *240*, 155–167.

(278) Yang, S.; Yan, B.; Lu, L.; Zeng, K. *RSC Adv.* **2016**, *6*, 94000–94009.

(279) Yang, S.; Yan, B.; Wu, J.; Lu, L.; Zeng, K. *ACS Appl. Mater. Interfaces* **2017**, *9*, 13999–14005.

(280) Liu, A.; Phattharasupakun, N.; Cormier, M.; Zsoldos, E.; Zhang, N.; Lyle, E.; Arab, P.; Sawangphruk, M.; Dahn, J. R. *J. Electrochem. Soc.* **2021**, *168*, 070503(1-10).

(281) Atlung, S.; West, K.; Jacobsen, T. *J. Electrochem. Soc.* **1979**, *126*, 1311–1321.

(282) Phattharasupakun, N.; Lyle, E.; Cormier, M.; Zsoldos, E.; Liu, A.; Liu, Y.; Li, H.; Sawangphruk, M.; Dahn, J. R. *Submitted to J. Electrochem. Soc.*

(283) Zsoldos, E.; Cormier, M.; Phattharasupakun, N.; Liu, A.; Dahn, J. R. *Manuscript in Preparation*.

(284) Wang, C.; Yu, R.; Hwang, S.; Liang, J.; Li, X.; Zhao, C.; Sun, Y.; Wang, J.; Holmes, N.; Li, R.; Huang, H.; Zhao, S.; Zhang, L.; Lu, S.; Su, D.; Sun, X. *Energy Storage Mater.* **2020**, *30*, 98–103.

(285) Thackeray, M. M.; Kang, S. H.; Johnson, C. S.; Vaughey, J. T.; Hackney, S. A. *Electrochem. commun.* **2006**, *8*, 1531–1538.

(286) Myung, S. T.; Komaba, S.; Kurihara, K.; Hosoya, K.; Kumagai, N.; Sun, Y. K.; Nakai, I.; Yonemura, M.; Kamiyama, T. *Chem. Mater.* **2006**, *18*, 1658–1666.

(287) Hua, W.; Wang, S.; Knapp, M.; Leake, S. J.; Senyshyn, A.; Richter, C.; Yavuz, M.; Binder, J. R.; Grey, C. P.; Ehrenberg, H.; Indris, S.; Schwarz, B. *Nat. Commun.* **2019**, *10*, 5365(1-11).

(288) Johnson, C. S.; Kim, J. S.; Lefief, C.; Li, N.; Vaughey, J. T.; Thackeray, M. M. *Electrochem. commun.* **2004**, *6*, 1085–1091.

(289) Liu, A.; Phattharasupakun, N.; Väli, R.; Ouyang, D.; Dahn, J. R. *Submitted to J. Electrochem. Soc.*

(290) Hatchard, T. D.; Genkin, A.; Obrovac, M. N. *AIP Adv.* **2017**, *7*, 045201(1-12).

(291) Li, G.; You, L.; Wen, Y.; Zhang, C.; Huang, B.; Chu, B. Bin; Wu, J. H.; Huang, T.; Yu, A. *ACS Appl. Mater. Interfaces* **2021**, *13*, 10952–10963.

(292) Kirner, J.; Qin, Y.; Zhang, L.; Jansen, A.; Lu, W. *J. Power Sources* **2020**, *450*, 227711(1-8).

(293) Dressler, R. A.; Dahn, J. R. *Manuscript in Preparation*.

(294) Ariyoshi, K.; Maeda, Y.; Kawai, T.; Ohzuku, T. *J. Electrochem. Soc.* **2011**, *158*, A281–A284.

(295) Kimijima, T.; Zettsu, N.; Teshima, K. *Cryst. Growth Des.* **2016**, *16*, 2618–2623.

(296) Chen, B.; Ben, L.; Chen, Y.; Yu, H.; Zhang, H.; Zhao, W.; Huang, X. *Chem. Mater.* **2018**, *30*, 2174–2182.

(297) Kim, U. H.; Park, N. Y.; Park, G. T.; Kim, H.; Yoon, C. S.; Sun, Y. K. *Energy Storage Mater.* **2020**, *33*, 399–407.

(298) Noh, H. J.; Chen, Z.; Yoon, C. S.; Lu, J.; Amine, K.; Sun, Y. K. *Chem. Mater.* **2013**, *25*, 2109–2115.

(299) Sun, H. H.; Weeks, J. A.; Heller, A.; Mullins, C. B. *ACS Appl. Energy Mater.* **2019**, *2*, 6002–6011.

(300) Xia, X. Studies of the Safety of Materials for Metal-Ion Batteries. PhD Thesis, Dalhousie University, 2013.

(301) Ma, L. Studies of the Effects of Electrolyte Additives on the Reactivity Between Charged Electrodes and Electrolytes in Li-Ion Batteries Using Accelerating Rate Calorimetry. MSc Thesis, Dalhousie University, 2014.

(302) Zhang, N.; Li, J.; Li, H.; Liu, A.; Huang, Q.; Ma, L.; Li, Y.; Dahn, J. R. *Chem. Mater.* **2018**, *30*, 8852–8860.

(303) Björklund, E.; Hahlin, M.; Younesi, R.; Brandell, D.; Edström, K. *J. Electrochem. Soc.* **2017**, *164*, A3054–A3059.

(304) Xu, W.; Kim, H. T.; Yu, L.; Engelhard, M. H.; Ren, X.; Xiao, J.; Lee, J. H.; Liu, J.; Lim, H. S.; Zhang, J. G.; Lee, H. K.; Han, K. S. *ACS Energy Lett.* **2018**, *3*, 2921–2930.

(305) Murray, V.; Hall, D. S.; Dahn, J. R. *J. Electrochem. Soc.* **2019**, *166*, A329–A333.

(306) Geng, C.; Trussler, S.; Johnson, M. B.; Zaker, N.; Scott, B.; Botton, G. A.; Dahn, J. R. *J. Electrochem. Soc.* **2020**, *167*, 110509(1-7).

(307) Geng, C.; Liu, A.; Dahn, J. R. *Chem. Mater.* **2020**, *32*, 6097–6104.

(308) Zheng, L.; Bennett, J. C.; Obrovac, M. N. *J. Electrochem. Soc.* **2020**, *167*, 130536(1-7).

(309) Park, B. C.; Bang, H. J.; Amine, K.; Jung, E.; Sun, Y. K. *J. Power Sources* **2007**, *174*, 658–662.

(310) Liao, J. Y.; Oh, S. M.; Manthiram, A. *ACS Appl. Mater. Interfaces* **2016**, *8*, 24543–24549.

(311) Kim, U. H.; Ryu, H. H.; Kim, J. H.; Mücke, R.; Kaghazchi, P.; Yoon, C. S.; Sun, Y. K. *Adv. Energy Mater.* **2019**, *9*, 1803902(1-11).

(312) Kim, U. H.; Park, G. T.; Conlin, P.; Ashburn, N.; Cho, K.; Yu, Y. S.; Shapiro, D. A.; Maglia, F.; Kim, S. J.; Lamp, P.; Yoon, C. S.; Sun, Y. K. *Energy Environ. Sci.* **2021**, *14*, 1573–1583.

(313) Zheng, L.; Hatchard, T. D.; Obrovac, M. N. *MRS Commun.* **2018**, *9*, 245–250.

(314) Zheng, L.; Wei, C.; Garayt, M. D. L.; MacInnis, J.; Obrovac, M. N. *J. Electrochem. Soc.* **2019**, *166*, A2924–A2927.

Appendix – Copyright Permissions

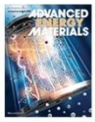

Narrowing the Gap between Theoretical and Practical Capacities in Li-Ion Layered Oxide Cathode Materials

Author: Maxwell D. Radin, Sunny Hy, Mahsa Sina, et al
Publication: Advanced Energy Materials
Publisher: John Wiley and Sons
Date: Jul 4, 2017

© 2017 WILEY-VCH Verlag GmbH & Co. KGaA, Weinheim

Order Completed

Thank you for your order.

This Agreement between Mr. Aaron Liu -- Aaron Liu ("You") and John Wiley and Sons ("John Wiley and Sons") consists of your license details and the terms and conditions provided by John Wiley and Sons and Copyright Clearance Center.

Your confirmation email will contain your order number for future reference.

Printable Details

License Number	5092100336129
License date	Jun 18, 2021

Licensed Content

Licensed Content Publisher	John Wiley and Sons
Licensed Content Publication	Advanced Energy Materials
Licensed Content Title	Narrowing the Gap between Theoretical and Practical Capacities in Li-Ion Layered Oxide Cathode Materials
Licensed Content Author	Maxwell D. Radin, Sunny Hy, Mahsa Sina, et al
Licensed Content Date	Jul 4, 2017
Licensed Content Volume	7
Licensed Content Issue	20
Licensed Content Pages	33

Order Details

Type of use	Dissertation/Thesis
Requestor type	University/Academic
Format	Print and electronic
Portion	Figure/table
Number of figures/tables	4
Will you be translating?	No

About Your Work

Title	Synthesis and Characterization of Co-free Ni-rich Single Crystalline Positive Electrode Materials for Li-ion Batteries
Institution name	Dalhousie University
Expected presentation date	Jul 2021

Additional Data

Portions	Figs. 5, 6, 10 and 19

Requestor Location

Requestor Location	Mr. Aaron Liu 6274 Coburg Road Halifax, NS B3H 4R2 Canada Attn: Mr. Aaron Liu

Tax Details

Publisher Tax ID	EU826007151

$ Price

Total	0.00 CAD

Would you like to purchase the full text of this article? If so, please continue on to the content ordering system located here: Purchase PDF
If you click on the buttons below or close this window, you will not be able to return to the content ordering system.

Total: 0.00 CAD

CLOSE WINDOW

ORDER MORE

CCC | RightsLink®

Home | Help | Email Support | Aaron Liu

SPRINGER NATURE

Heuristic solution for achieving long-term cycle stability for Ni-rich layered cathodes at full depth of discharge

Author: Un-Hyuck Kim et al
Publication: Nature Energy
Publisher: Springer Nature
Date: Sep 21, 2020

Copyright © 2020, The Author(s), under exclusive licence to Springer Nature Limited

Order Completed

Thank you for your order.

This Agreement between Mr. Aaron Liu -- Aaron Liu ("You") and Springer Nature ("Springer Nature") consists of your license details and the terms and conditions provided by Springer Nature and Copyright Clearance Center.

Your confirmation email will contain your order number for future reference.

Printable Details

License Number	5096710515766
License date	Jun 26, 2021

Licensed Content

Licensed Content Publisher	Springer Nature
Licensed Content Publication	Nature Energy
Licensed Content Title	Heuristic solution for achieving long-term cycle stability for Ni-rich layered cathodes at full depth of discharge
Licensed Content Author	Un-Hyuck Kim et al
Licensed Content Date	Sep 21, 2020

Order Details

Type of Use	Thesis/Dissertation
Requestor type	academic/university or research institute
Format	print and electronic
Portion	figures/tables/illustrations
Number of figures/tables /illustrations	1
High-res required	no
Will you be translating?	no
Circulation/distribution	1 - 29
Author of this Springer Nature content	no

About Your Work

Title	Synthesis and Characterization of Co-free Ni-rich Single Crystalline Positive Electrode Materials for Li-ion Batteries
Institution name	Dalhousie University
Expected presentation date	Jul 2021

Additional Data

Portions	Figure 1

Requestor Location

Requestor Location	Mr. Aaron Liu 6274 Coburg Road Halifax, NS B3H 4R2 Canada Attn: Mr. Aaron Liu

Tax Details

$ Price

Total	0.00 USD

Total: 0.00 USD

CLOSE WINDOW | ORDER MORE

CCC | RightsLink®

Home | Help | Email Support | Sign in | Create Account

ACS Publications
Most Trusted. Most Cited. Most Read.

An Unavoidable Challenge for Ni-Rich Positive Electrode Materials for Lithium-Ion Batteries

Author: Hongyang Li, Aaron Liu, Ning Zhang, et al
Publication: Chemistry of Materials
Publisher: American Chemical Society
Date: Sep 1, 2019

Copyright © 2019, American Chemical Society

PERMISSION/LICENSE IS GRANTED FOR YOUR ORDER AT NO CHARGE

This type of permission/license, instead of the standard Terms and Conditions, is sent to you because no fee is being charged for your order. Please note the following:

- Permission is granted for your request in both print and electronic formats, and translations.
- If figures and/or tables were requested, they may be adapted or used in part.
- Please print this page for your records and send a copy of it to your publisher/graduate school.
- Appropriate credit for the requested material should be given as follows: "Reprinted (adapted) with permission from {COMPLETE REFERENCE CITATION}. Copyright {YEAR} American Chemical Society." Insert appropriate information in place of the capitalized words.
- One-time permission is granted only for the use specified in your RightsLink request. No additional uses are granted (such as derivative works or other editions). For any uses, please submit a new request.

If credit is given to another source for the material you requested from RightsLink, permission must be obtained from that source.

BACK | CLOSE WINDOW

© 2021 Copyright - All Rights Reserved | Copyright Clearance Center, Inc. | Privacy statement | Terms and Conditions
Comments? We would like to hear from you. E-mail us at customercare@copyright.com

CCC | RightsLink®

Home | Help | Email Support | Sign in | Create Account

ACS Publications
Most Trusted. Most Cited. Most Read.

Collapse of LiNi1−x−yCoxMnyO2 Lattice at Deep Charge Irrespective of Nickel Content in Lithium-Ion Batteries

Author: Wangda Li, Hooman Yaghoobnejad Asl, Qiang Xie, et al
Publication: Journal of the American Chemical Society
Publisher: American Chemical Society
Date: Apr 1, 2019

Copyright © 2019, American Chemical Society

PERMISSION/LICENSE IS GRANTED FOR YOUR ORDER AT NO CHARGE

This type of permission/license, instead of the standard Terms and Conditions, is sent to you because no fee is being charged for your order. Please note the following:

- Permission is granted for your request in both print and electronic formats, and translations.
- If figures and/or tables were requested, they may be adapted or used in part.
- Please print this page for your records and send a copy of it to your publisher/graduate school.
- Appropriate credit for the requested material should be given as follows: "Reprinted (adapted) with permission from {COMPLETE REFERENCE CITATION}. Copyright {YEAR} American Chemical Society." Insert appropriate information in place of the capitalized words.
- One-time permission is granted only for the use specified in your RightsLink request. No additional uses are granted (such as derivative works or other editions). For any uses, please submit a new request.

If credit is given to another source for the material you requested from RightsLink, permission must be obtained from that source.

BACK | CLOSE WINDOW

© 2021 Copyright - All Rights Reserved | Copyright Clearance Center, Inc. | Privacy statement | Terms and Conditions
Comments? We would like to hear from you. E-mail us at customercare@copyright.com

CCC Marketplace™

This is a License Agreement between Aaron Liu ("User") and Copyright Clearance Center, Inc. ("CCC") on behalf of the Rightsholder identified in the order details below. The license consists of the order details, the CCC Terms and Conditions below, and any Rightsholder Terms and Conditions which are included below.

All payments must be made in full to CCC in accordance with the CCC Terms and Conditions below.

Order Date	30-Jun-2021	Type of Use	Republish in a thesis/dissertation
Order License ID	1129884-1		
ISSN	17545692	Publisher	Royal Society of Chemistry
		Portion	Chart/graph/table/figure

LICENSED CONTENT

Publication Title	Energy & environmental science	Rightsholder	Royal Society of Chemistry
		Publication Type	Journal
Article Title	Reducing cobalt from lithium-ion batteries for the electric vehicle era	Start Page	844
		End Page	852
Author/Editor	Royal Society of Chemistry (Great Britain)	Issue	2
		Volume	14
Date	01/01/2008		
Language	English		
Country	United Kingdom of Great Britain and Northern Ireland		

REQUEST DETAILS

Portion Type	Chart/graph/table/figure	Distribution	Worldwide
Number of charts / graphs / tables / figures requested	1	Translation	Original language of publication
		Copies for the disabled?	No
Format (select all that apply)	Print, Electronic	Minor editing privileges?	No
Who will republish the content?	Academic institution	Incidental promotional use?	No
		Currency	CAD
Duration of Use	Life of current edition		
Lifetime Unit Quantity	Up to 499		
Rights Requested	Main product		

NEW WORK DETAILS

Title	Synthesis and Characterization of Co-free Ni-rich Single Crystalline Positive Electrode Materials for Li-ion Batteries	Institution name	Dalhousie University
		Expected presentation date	2021-08-12
Instructor name	Aaron Liu		

ADDITIONAL DETAILS

Order reference number	N/A	The requesting person / organization to appear on the license	Aaron Liu

REUSE CONTENT DETAILS

Title, description or numeric reference of the portion(s)	Figure 1	Title of the article/chapter the portion is from	Reducing cobalt from lithium-ion batteries for the electric vehicle era
Editor of portion(s)	Ryu, Hoon-Hee; Sun, H. Hohyun; Myung, Seung-Taek; Yoon, Chong S.; Sun, Yang-Kook	Author of portion(s)	Ryu, Hoon-Hee; Sun, H. Hohyun; Myung, Seung-Taek; Yoon, Chong S.; Sun, Yang-Kook
Volume of serial or monograph	14	Issue, if republishing an article from a serial	2
Page or page range of portion	844-852	Publication date of portion	2021-01-01

CCC Terms and Conditions

CCC | RightsLink®

Home | Help | Email Support | Aaron Liu

ELSEVIER

Single-crystal nickel-rich layered-oxide battery cathode materials: synthesis, electrochemistry, and intra-granular fracture

Author:
Guannan Qian,Youtian Zhang,Linsen Li,Ruixin Zhang,Junmeng Xu,Zhenjie Cheng,Sijie Xie,Han Wang,Qunli Rao,Yushi He,Yanbin Shen,Liwei Chen,Ming Tang,Zi-Feng Ma

Publication: Energy Storage Materials

Publisher: Elsevier

Date: May 2020

© 2020 Elsevier B.V. All rights reserved.

Order Completed

Thank you for your order.

This Agreement between Mr. Aaron Liu -- Aaron Liu ("You") and Elsevier ("Elsevier") consists of your license details and the terms and conditions provided by Elsevier and Copyright Clearance Center.

Your confirmation email will contain your order number for future reference.

Printable Details

License Number	5096701424437
License date	Jun 26, 2021

Licensed Content

Licensed Content Publisher	Elsevier
Licensed Content Publication	Energy Storage Materials
Licensed Content Title	Single-crystal nickel-rich layered-oxide battery cathode materials: synthesis, electrochemistry, and intra-granular fracture
Licensed Content Author	Guannan Qian,Youtian Zhang,Linsen Li,Ruixin Zhang,Junmeng Xu,Zhenjie Cheng,Sijie Xie,Han Wang,Qunli Rao,Yushi He,Yanbin Shen,Liwei Chen,Ming Tang,Zi-Feng Ma
Licensed Content Date	May 1, 2020
Licensed Content Volume	27
Licensed Content Issue	n/a
Licensed Content Pages	10

Order Details

Type of Use	reuse in a thesis/dissertation
Portion	figures/tables/illustrations
Number of figures/tables /illustrations	1
Format	both print and electronic
Are you the author of this Elsevier article?	No
Will you be translating?	No

About Your Work

Title	Synthesis and Characterization of Co-free Ni-rich Single Crystalline Positive Electrode Materials for Li-ion Batteries
Institution name	Dalhousie University
Expected presentation date	Jul 2021

Additional Data

Portions	Figure 2

Requestor Location

Requestor Location	Mr. Aaron Liu 6274 Coburg Road Halifax, NS B3H 4R2 Canada Attn: Mr. Aaron Liu

Tax Details

Publisher Tax ID	GB 494 6272 12

$ Price

Total	0.00 USD

Total: 0.00 USD

CLOSE WINDOW | ORDER MORE

CCC | RightsLink®

Home | Help | Email Support | Aaron Liu

High performance well-developed single crystal LiNi0.91Co0.06Mn0.03O2 cathode via LiCl-NaCl flux method

Author: Seung-Hwan Lee,Seong-Ju Sim,Bong-Soo Jin,Hyun-Soo Kim
Publication: Materials Letters
Publisher: Elsevier
Date: 1 July 2020

© 2020 Published by Elsevier B.V.

Order Completed

Thank you for your order.

This Agreement between Mr. Aaron Liu -- Aaron Liu ("You") and Elsevier ("Elsevier") consists of your license details and the terms and conditions provided by Elsevier and Copyright Clearance Center.

Your confirmation email will contain your order number for future reference.

Printable Details

License Number	5096701014774
License date	Jun 26, 2021

Licensed Content

Licensed Content Publisher	Elsevier
Licensed Content Publication	Materials Letters
Licensed Content Title	High performance well-developed single crystal LINi0.91Co0.06Mn0.03O2 cathode via LiCl-NaCl flux method
Licensed Content Author	Seung-Hwan Lee,Seong-Ju Sim,Bong-Soo Jin,Hyun-Soo Kim
Licensed Content Date	Jul 1, 2020
Licensed Content Volume	270
Licensed Content Issue	n/a
Licensed Content Pages	1

Order Details

Type of Use	reuse in a thesis/dissertation
Portion	figures/tables/illustrations
Number of figures/tables /illustrations	1
Format	both print and electronic
Are you the author of this Elsevier article?	No
Will you be translating?	No

About Your Work

Title	Synthesis and Characterization of Co-free Ni-rich Single Crystalline Positive Electrode Materials for Li-ion Batteries
Institution name	Dalhousie University
Expected presentation date	Jul 2021

Additional Data

Portions	Figure 1

Requestor Location

Requestor Location	Mr. Aaron Liu 6274 Coburg Road Halifax, NS B3H 4R2 Canada Attn: Mr. Aaron Liu

Tax Details

Publisher Tax ID	GB 494 6272 12

$ Price

Total	0.00 USD

Total: 0.00 USD

CLOSE WINDOW | ORDER MORE